Fakultät für
Mathematik, Informatik
und Naturwissenschaften

RWTHAACHEN
UNIVERSITY

Molecular Beam Epitaxy of Magnetic Topological Insulators and their Integration into Superconducting Hybrid Devices

Von der Fakultät für Mathematik, Informatik und Naturwissenschaften der
RWTH Aachen University zur Erlangung des akademischen Grades eines
Doktors der Naturwissenschaften genehmigte Dissertation

vorgelegt von

Michael Schleenvoigt, Master of Science (M.Sc.)

aus

Elsdorf, Deutschland

Berichter: Univ.-Prof. Dr. rer. nat. Detlev Grützmacher
Univ.-Prof. Dr. rer. nat. Markus Morgenstern

Tag der mündlichen Prüfung: 12.12.2024

Eidesstattliche Erklärung

Ich, Michael Schleenvoigt, erkläre hiermit, dass diese Dissertation und die darin dargelegten Inhalte die eigenen sind und selbstständig, als Ergebnis der eigenen originären Forschung, generiert wurden.

Hiermit erkläre ich an Eides statt

1. Diese Arbeit wurde vollständig oder größtenteils in der Phase als Doktorand dieser Fakultät und Universität angefertigt;

2. Sofern irgendein Bestandteil dieser Dissertation zuvor für einen akademischen Abschluss oder eine andere Qualifikation an dieser oder einer anderen Institution verwendet wurde, wurde dies klar angezeigt;

3. Wann immer andere eigene oder Veröffentlichungen Dritter herangezogen wurden, wurden diese klar benannt;

4. Wenn aus anderen eigenen oder Veröffentlichungen Dritter zitiert wurde, wurde stets die Quelle hierfür angegeben. Diese Dissertation ist vollständig meine eigene Arbeit, mit der Ausnahme solcher Zitate;

5. Alle wesentlichen Quellen von Unterstützung wurden benannt;

6. Wann immer ein Teil dieser Dissertation auf der Zusammenarbeit mit anderen basiert, wurde von mir klar gekennzeichnet, was von anderen und was von mir selbst erarbeitet wurde;

____

(Datum)

____

(Unterschrift)

Table of Contents

Abstract

Among the few approaches towards quantum computing (QC) as the future of computing in a post-Moore's-law time, the recent push for topological QC is one of the most auspicious. It promises fault tolerant QC by employing exotic Majorana zero mode (MZM) quasiparticle states, which build the basis of the topological QC qubit. Intrinsic protection against relaxation and dephasing distinguishes those elusive qubits from other platforms, like superconducting and spin qubits. Nanowires of 3D topological insulator (TI) – superconductor (SC) hybrid structures are predicted to exhibit MZM at each end of the wire. The one-dimensional confinement however leads to a loss of the topological phase needed to realize the MZMs. An alternative capable of avoiding this problem has gotten much traction lately, which are magnetic topological insulators (MTI), which incorporate magnetic dopants into the TI itself. This thesis focuses on the growth of magnetic TIs via molecular beam epitaxy (MBE) from established recipes for non-magnetic TIs. It will show how complex MTI-SC hybrid devices can be fabricated *in situ* and will illustrate the difficulties that arise when trying to combine MTIs with SC.

First, the growth of 3D TI $(BiSb)_2Te_3$ via MBE is optimized to reach a low level of charge carrier density and a high mobility, signifying an appropriate host material for the magnetic dopants. By supplying Cr during thin film growth, high quality magnetically doped films are deposited. First films exhibit an anomalous Hall effect, indicating homogeneous and strong magnetism. In similar Mn-doped films, investigated in parallel, the magnetization is found to less homogeneous, ultimately leading to an focusing onto the more reliable Cr doped MTI films. By creating a trilayer film of CBST and thinning it down to <8 nm a quantization in the Hall resistance is observed, signaling a transition into a quantum anomalous Hall insulator.

To investigate the interaction of the MTI and SC, Josephson junction (JJ) devices are created via a stencil lithography process established in our group. The JJ devices show no supercurrent over the junctions, but rather indications for a barrier at the MTI-SC interface due to bad interface transparency between MTI and SC. To rule out *ex situ* contaminations and to relate the barrier height to the magnetization, a new device layout is developed. It allows for full *in situ* deposition and enables Hall and JJ measurements in one device. While the low transparency issue persists, indications of induced superconductivity are found when decreasing the magnetic doping in these devices.

To further investigate the interplay of topology, magnetism and superconductivity on atomic scales, a novel process is developed in the last chapter: a fully *in situ* process utilizing removable large-scale ultra-high vacuum lithography (LUL). With LUL, (M)TI and SC films can be grown selectively *in situ* and aligned to each other with nm precision. Soft cappings of Tellurium or Selenium are investigated to protect the functional surfaces. By exfoliating the stencil mask layer, samples suitable for investigations in scanning tunneling microscopes (STM) are created. In STM, atomic resolution is achieved after capping removal. Tunneling spectra of the SC gap, the TI surface and the magnetic gap are obtained after successful mask and capping removal, showing a short-ranged SC gap profile on the TI.

In conclusion, this thesis establishes multiple new material systems in our institute, showcases novel UHV lithography methods for the combination of (M)TIs and SCs, paving the way for the creation of MZMs in hybrid devices, and lastly, by utilizing LUL, provides an innovative process for creating structures and devices of combinations of arbitrary quantum materials *in situ* that enables measurements in ways unprecedented in STM.

Kurzfassung

Unter den verschiedenen Materialplattformen für Quantencomputing (QC) ist das noch junge topologische QC eine der vielversprechendsten Routen in eine Zeit nach dem Mooreschen Gesetz. Es verspricht fehlertolerantes QC mittels der exotischen Majorana Null Moden (MZM), die die Grundlage des topologischen QC-Qubits bilden. Ihr intrinsischer Schutz gegen Relaxation und Verlust der Phasenkohärenz unterscheidet sie von anderen Qubit-Ansätzen, wie supraleitende oder Spin-Qubits. Für Nanodrähte aus 3D-Hybridstrukturen aus topologischem Isolator (TI) und Supraleiter (SC) wird vorausgesagt, dass je eine Mode eines MZM-Paares an den Enden des Drahtes entstehen soll. Die eindimensionale Begrenzung des TIs führt jedoch zu einem Verlust seiner topologischen Phase, die für die Realisierung der MZMs erforderlich sind. Eine Alternative, die dieses Problem umgehen kann, sind magnetische topologische Isolatoren (MTI), bei denen magnetische Dotierstoffe in den TI selbst eingefügt werden. Diese Doktorarbeit konzentriert sich auf das Wachstum magnetischer TIs mittels Molekularstrahlepitaxie (MBE), zeigt, wie komplexe MTI-SC-Hybrid-Bauelemente *in situ* hergestellt werden können, und veranschaulicht die Schwierigkeiten, die auftreten, wenn MTIs mit SC kombiniert werden.

Zunächst wird der 3D-TI $(BiSb)_2Te_3$ als Grundlage mittels MBE gewachsen und optimiert, um so niedrige Ladungsträgerdichten und hohe Mobilitäten in den Filmen zu erreichen. Durch die Zufuhr von Cr während des optimierten Wachstums werden qualitativ hochwertige, magnetisch dotierte Schichten abgeschieden. Die ersten Filme weisen einen anomalen Hall-Effekt auf, der auf eine homogene Magnetisierung des Films hindeutet. In Mn-dotierten Filmen, die parallel untersucht werden, ist diese Homogenität schwieriger zu erreichen, was letztlich zu einer Fokussierung auf die zuverlässigeren Cr-dotierten MTI-Filme führt. Durch das Einführen eines drei-lagigen Films und einer Reduktion der Filmdicke auf <8 nm wird eine Quantisierung des Hall-Widerstands beobachtet, was auf einen Übergang zu einem anomalen Quanten-Hall-Isolator hindeutet.

Um die Wechselwirkung zwischen MTI und SC zu untersuchen, werden Josephson-Kontakte (JJ) mit einem in unserer Gruppe etablierten Vakuum-Lithografie-Verfahren hergestellt. Messungen zeigen keinen Suprastrom über den Josephson Kontakt, sondern ein Verhalten, das auf niedrige Transparenz an der MTI-SC-Grenzfläche hinweist. Um *ex situ* Verunreinigungen auszuschließen und einen Zusammenhang zwischen Transparenz und Stärke der Magnetisierung zu finden, wird ein neues Design entwickelt, das vollständige *in situ* Fabrikation und Hall- und JJ-Messungen in einem einzigen Bauelement ermöglicht. Zwar bleibt die niedrige Transparenz bestehen, es zeigen sich in diesen Bauelementen jedoch Signaturen induzierter Supraleitung bei niedriger Cr-Dotierung.

Um das Zusammenspiel von Topologie, Magnetismus und Supraleitung auf atomarer Skala weiter zu untersuchen, wird im letzten Kapitel ein neuartiges, vollständig *in situ* verlaufendes, Verfahren entwickelt, welches eine entfernbare, großflächige Vakuum-Lithografie-Maske (LUL) nutzt. Mit LUL können (M)TI- und SC-Schichten selektiv *in situ* gewachsen und mit nm-Präzision zueinander ausgerichtet werden. Durch Hitze entfernbare Schichten aus Tellur und Selen werden auf ihre Anwendbarkeit als Schutzschicht für die funktionalen Oberflächen untersucht. Durch Exfolieren der Maskenschicht werden Proben erzeugt, die für Untersuchungen in Rastertunnelmikroskopen (STM) geeignet sind. Nach dem Entfernen der Schutzschichten wird im STM eine atomare Auflösung erreicht. Tunnelspektren der SC- und der magnetischen Bandlücke und der TI-Oberfläche können gemessen werden und zeigen ein kurzreichweitiges SC-Bandlückenprofil auf dem TI.

Im Laufe dieser Arbeit wurden somit neue Materialsysteme in unserem Institut etabliert und neuartige UHV-Lithografiemethoden für die Kombination von (M)TIs und SCs vorstellt, die den Weg für die Kreation und Entdeckung von MZMs in hybriden Bauelementen ebnen. Zu guter Letzt wird durch die Etablierung von LUL ein innovatives Verfahren für die *in situ* Fabrikation von Strukturen und Bauelementen aus Kombinationen beliebiger Quantenmaterialien bereitgestellt, welches Messungen in einer Weise ermöglicht, wie sie im STM bisher nicht *in situ* möglich waren.

List of Publications

Phase-coherent transport in topological insulator nanocolumns and nanoribbons
T. Schäpers, C. Weyrich, D. Rosenbach, J. Kölzer, T. W. Schmitt, P. Schüffelgen, G. Mussler, **M. Schleenvoigt**, A. R. Jalil, H. Lüth and D. Grützmacher
SPIE Proceedings Volume 10732, Spintronics XI, 107320V (2018)

Exploiting topological matter for Majorana physics and devices
P. Schüffelgen, T. W. Schmitt, **M. Schleenvoigt**, D. Rosenbach, P. Perla, A. R. Jalil, G. Mussler, M. Lepsa, T. Schäpers and D. Grützmacher
Solid-State Electronics, **155**, pp. 99-104 (2019)

Selective area growth and stencil lithography for in situ fabricated quantum devices
P. Schüffelgen, D. Rosenbach, C. Li, T. W. Schmitt, **M. Schleenvoigt**, A. R. Jalil, S. Schmitt, J. Kölzer, M. Wang, B. Bennemann, U. Parlak, L. Kibkalo, St. Trellenkamp, T. Grap, D. Meertens, M. Luysberg, G. Mussler, E. Berenschot, N. Tas, A. A. Golubov, A. Brinkmann, T. Schäpers and D. Grützmacher
Nature Nanotechnology, **14**, pp. 825-831 (2019)

Exploiting topological matter for Majorana physics and devices via molecular beam epitaxy (conference presentation)
P. Schüffelgen, D. Rosenbach, C. Li, T. W. Schmitt, **M. Schleenvoigt**, S. Schmitt, A. R. Jalil, J. Kölzer, L. Kibkalo, M. Luysberg, B. Bennemann, U. Parlak, D. Meertens, St. Trellenkamp, G. Mussler, T. Grap, M. Wang, E. Berenschot, N. Tas, A. A. Golubov, A. Brinkmann, T. Schäpers and D. Grützmacher
SPIE Proceedings Volume 11090, Spintronics XII, 110902D (2019)

Room temperature in-situ measurement of the spin voltage of a $BiSbTe_3$ *thin film*
A. Leis, **M. Schleenvoigt**, A. R. Jalil, V. Cherepanov, G. Mussler, D. Grützmacher, F. S. Tautz and B. Voigtländer
Scientific Reports **10**, 2816 (2020)

Phase-coherent loops in selectively-grown topological insulator nanoribbons
J. Kölzer, D. Rosenbach, C. Weyrich, T. W. Schmitt, **M. Schleenvoigt**, A. R. Jalil, P. Schüffelgen, G. Mussler, V. E. Sacksteder IV and D. Grützmacher
Nanotechnology **31**, 325001 (2020)

Quantum spin-valley Hall kink states: From concepts to materials design
T. Zhou, S. Cheng, **M. Schleenvoigt**, P. Schüffelgen, H. Jiang, Z. Yang and I. Žutić
Phys. Rev. Lett. **127**, 116402 (2021)

Reappearance of first Shapiro step in narrow topological Josephson junctions
D. Rosenbach, T. W. Schmitt, P. Schüffelgen, M. P. Stehno, C. Li, **M. Schleenvoigt**, A. R. Jalil, G. Mussler, E. Neumann, St. Trellenkamp, A. A. Golubov, A. Brinkmann, D. Grützmacher and T. Schäpers
Science Advances **7** (26), pp. 1-10 (2021)

Lifting the spin-momentum locking in ultra-thin topological insulator films
A. Leis, **M. Schleenvoigt**, V. Cherepanov, F. Lüpke, P. Schüffelgen, G. Mussler, D. Grützmacher, B. Voigtländer and F. S. Tautz
Advanced Quantum Technologies **4**, 11, 2100083 (2021)

Probing edge state conductance in ultra-thin topological insulator films
A. Leis, **M. Schleenvoigt**, K. Moors, H. Soltner, V. Cherepanov, P. Schüffelgen, G. Mussler, B. Voigtländer, F. Lüpke and F. S. Tautz
Advanced Quantum Technologies **5**, 9, 2200043 (2022)

Integration of topological insulator Josephson junctions in superconducting qubit circuits
T. W. Schmitt, M. R. Connolly, **M. Schleenvoigt**, C. Liu, O. Kennedy, J. M. Chávez-Garcia, A. R. Jalil, B. Bennemann, St. Trellenkamp, F. Lentz, E. Neumann, T. Lindström, S. E. de Graaf, E. Berenschot, N. Tas, G. Mussler, K. D. Petersson, D. Grützmacher and P. Schüffelgen
Nano Lett. **22**, 7, pp. 2595-2602 (2022)

Anomalous temperature dependence of multiple Andreev reflections in a topological insulator Josephson junction
T. W. Schmitt, B. Frohn, W. Wittl, A. R. Jalil, **M. Schleenvoigt**, E. Zimmermann, A. Schmidt, T. Schäpers, J. C. Cuevas, A. Brinkmann, D. Grützmacher and P. Schüffelgen
Supercond. Sci. Technol. **36**, 2, 024002 (2023)

Universal conductance fluctuations in a $Bi_{1.5}Sb_{0.5}Te_{1.8}Se_{1.2}$ topological insulator nano-scaled Hall bar structure
E. Zimmermann, J. Kölzer, **M. Schleenvoigt**, D. Rosenbach, G. Mussler, P.Schüffelgen, T. Heider, L. Plucinski, J. Schubert, H. Lüth, D. Grützmacher and T. Schäpers
Semicond. Sci. Technol. **38**, 3, 035010 (2023)

Selective area epitaxy of quasi-1-dimensional topological nanostructures and networks
A. R. Jalil, P. Schüffelgen, H. Valencia, **M. Schleenvoigt**, C. Ringkamp, G. Mussler, M. Luysberg, J. Mayer and D. Grützmacher
Nanomaterials **13**, 2, 354 (2023)

Fourier transformation based analysis routine for intermixed longitudinal and transversal hysteretic data for the example of a magnetic topological insulator
E. Zimmermann, **M. Schleenvoigt**, A. Rupp, G. Behner, J. Karthein, J. Teller, P. Schüffelgen, H. Lüth, D. Grützmacher and T. Schäpers
J. Phys. Mater. **7,** 015015 (2024)

Current-induced magnetization switching in a magnetic topological insulator heterostructure
E. Zimmermann, J. Teller, **M. Schleenvoigt**, G. Behner, P. Schüffelgen, H. Lüth, D. Grützmacher and T. Schäpers
Phys. Rev. Materials **8**, 025201 (2024)

In-plane magnetic field-driven conductance modulations in topological insulator kinks
G. Behner, K. Moors, Y. Zhang, **M. Schleenvoigt**, A. Rupp, E. Zimmermann, A. R. Jalil, P. Schüffelgen, H. Lüth, D. Grützmacher and T. Schäpers
Phys. Rev. B **109**, 155429 (2024)

Single In-Situ Interface Characterization Composed of Niobium and a Selectively Grown Topological Insulator Nanoribbon
K. Janßen, P. Rüßmann, S. Liberda, **M. Schleenvoigt,** X. Hou, A. R. Jalil, F. Lentz, St. Trellenkamp, B. Bennemann, E. Zimmermann, G. Mussler, P. Schüffelgen, C.-M. Schneider, S. Blügel, D. Grützmacher, L. Plucinski and T. Schäpers
Phys. Rev. Materials **8**, 034205 (2024)

Topological insulator based axial DC SQUID quantum interferometer structures
E. Zimmermann, A. R. Jalil, **M. Schleenvoigt**, B. Frohn, T. W. Schmitt, J. Karthein, G. Behner, F. Lentz, St. Trellenkamp, E. Neumann, P. Schüffelgen, H. Lüth, D. Grützmacher and T. Schäpers
Supercond. Sci. Technol. **37**, 085028 (2024)

List of Presentations

International Conference on Molecular Beam Epitaxy, Shanghai, China, September 2018

Presentation

“Patterned In Situ MBE Growth on Topological Insulators Using Stencil Lithography”

Sino-German Workshop on Cooperation (Jülich-SIMIT), Shanghai, China, May 2019

Presentation

„Majorana Zero Modes In Hybrid Networks of 3D Topological Insulators and s-Wave Superconductors”

German MBE Workshop (DEMBE), Würzburg, Germany, December 2019

Presentation

“UHV Lithography for STM Investigations of 3D Topological Insulators-Superconductor Hybrid Arrays”

Conference on Micro and Nano Engineering (MNE), Leuven, Belgium, September 2022

Presentation

“UHV Lithography for Investigations of Topological Insulator-Superconductor Hybrid Structures and Devices”

1 Introduction

In 2019 a calamity disturbed the world community and the process of globalization that had been building up rather undisturbed since the end of the cold war, the COVID-19 pandemic. A pandemic of this extent had not occurred for 100 years, when the Spanish flu had come down upon a world that was already on its knees due to the repercussions of the first world war. Although the world and technology in the 2020s had developed farther than anyone in 1918 might have imagined, the higher connectivity between vast amounts of people created fertile soil for an infectious respiratory disease, thus impacting every facet of everyday life. All over the world scientists hurried to find medications or vaccines to combat the spread of COVID-19 and to avert medical complications to protect the global health systems. Luckily, vaccine research, especially mRNA research, driven by earlier breakouts of SARS and other coronavirus diseases brought first countermeasures in record times. But at the same time the world had to wonder, what if the next virus is not as well known? How can the development of medication and vaccines be accelerated to combat pandemics as soon as possible?

It comes to no surprise that two ventures experienced unprecedented publicity during the search for COVID-19 vaccines: *Folding@Home* and *Alphafold.* Both are initiatives to decipher the folding of proteins like those building up the spike proteins of viruses, for example those of the SARS-CoV-2 virus causing COVID-19. Therefore, both ventures actively allocated resources towards the unfolding of SARS-CoV-2 proteins in hope of finding binding sites, to which medication-provided molecules could couple to render the proteins harmless. *Folding@Home* relies on a vast network of private computers provided by volunteers, creating the world's first exaflop computing system [1], [2], each solving small parts of simulation which are later recombined. On the other hand, *Alphafold* [3], a subsidiary of *Alphabet* daughter *Deepmind*, is an AI machine learning tool. Both approaches show promising results, are however impeded by the limitations of state-of-the-art, but traditional computer architectures. The next awaited evolution of computing using quantum computers could open up new possibilities in speed as well as capabilities in protein unfolding, potentially protecting us all when the next pandemic endangers the world [4].

Instead of using only the binary 0s and 1s, the fundamental building blocks of all information technology surrounding us, quantum computation utilizes the unintuitive physics of quantum mechanics to create entangled superpositions of the two states. The resulting simulations of molecules are much closer to reality, since the physics in molecules is governed by the same quantum mechanical processes also governing these quantum bits, or qubits for short. While the material basis of classical computers is Silicon due to its abundance and chemical as well as physical viability, the medium providing the foundation for quantum computing has not yet been decided. Multiple candidates are currently in a global tight race towards establishing themselves as the future platform of quantum computing. While qubits built from superconducting loops and those made from silicon quantum dots profit from their origin in the semiconductor industry, their low stability while requiring to be cooled permanently is one of the main factors hindering successful scaling. Trapped ions on the other hand promise high stability, in turn providing only slow operation. On the other hand, vacancies in diamond lattices could operate at room temperatures, but the entanglement of states to create superpositions of 1 and 0 remains a challenge [5].

A further approach towards quantum computing is the relatively new field of topological quantum computing [6], [7], [8]. It relies on the manipulation of anyons, a third type of particle next to fermions and bosons, whose spin is neither an integer (bosons) or multiple of half integers (fermions) but can lay in between [9]. Anyon quasiparticles can only exist in two dimensions and are categorized further into abelian and non-abelian anyons, wherein the latter are the foundation of topological quantum computing. The signature quality of non-abelian anyons is that when they are moved in respect to each other or made to switch places, the accumulated Berry phase along a closed path does not necessarily yield a multiple of 2π [10]. The original and final state thus are neither equal nor differ by a factor of (-1), as it would be the case for fermions, but the traveled path is encoded in the accumulated phase. Therefore, also the order and direction of switching matters. By measuring the phase of the anyon before and after a switching process, computation can be performed, as was proposed by Friedman, Kitaev *et al.* [6]. Since this type of computing is performed by twisting of anyons in space-time, the computation is also referred to as “braiding”. Braiding can be used to create superposition and entanglement, capable of creating all quantum gates necessary for a universal gate set [11], [12], [13].

But how does one obtain anyons or can we create them? One particle possessing non-abelian anyon properties is the Majorana. Majorana particles, originally devised in the field of particle physics by Ettore Majorana in 1937 are their own antiparticles, existing at zero energy [14]. When discussing topological quantum computing the involved particles are however not Majoranas themselves, but rather an equivalent quasiparticle state existing in special solid-state systems at zero energy [15]. These always appear as pairs of quasiparticles, which are separated in space and are thus more protected from local decoherence [16]. The topologically protected nature of the braiding operations causes topological quantum computing to be more error-proof in contrast to superconducting or quantum dot qubits, due to the absence of dephasing and relaxation since the qubit states have the same energy [10], [17], [18]. However, the operations must still be performed at cryogenic temperatures and some error correction is still needed due to quasiparticle poisoning effects [19], [20].

With Majorana quasiparticles providing the non-abelian statistics needed for topological quantum computing, the next step is now to realize these Majorana states. A system proposed to host the exotic quasiparticles is a 2D p-type (p_x+ip_y) superconductor (SC), providing triplet-pairing [15], [21]. However, there is no known p-type superconductor in existence. A proposed way to artificially create a p-type superconductor is by combining a normal s-wave superconductor with a topological insulator (TI) [16], [22], [23]. As will be detailed further in the next chapter, a TI is a material with a peculiar band structure. The band structures in trivial systems are periodic up to the interface, where the bands need to realign to transition into the adjacent material's band structure. The band structure in TIs is however inverted and thus topologically different, similar to the difference between a ribbon and a Möbius strip [24], [25]. To realign, the inverted bands need to cross at the materials' interface, creating metallic topologically protected surface states, which are moreover spin momentum locked due to strong spin orbit coupling in the TI systems [25]. Coupling these extraordinary surface states with s-wave superconductivity, a process called proximization, is proposed to artificially create p-wave superconductivity in the topologically superconducting region, hosting the Majorana quasiparticle states [15].

Proposals of devices incorporating these TI-superconductor hybrid systems utilize a network of proximitized, quasi-1-dimensional topological wires [18], [26], [27], in which the pair of Majorana quasiparticles is localized separately at the ends of each wire [28], [29]. This approach, together with electrostatic-gate- or magnetic-flux-control creates scalable devices [26], however creates a new problem. Shrinking the TI-wires into a quasi-1D configuration causes the formation of a confinement gap, which lifts the topological protection of the wires, rendering them topologically trivial [30], [31]. By applying a magnetic flux along the wire, the wires can be re-topologized, in turn diminishing the scalability due to the need for more complex layouts [28]. Additionally, varying wire diameters and problems regarding flux control when applying a global in-plane magnetic field for re-topologization cause concern for this approach. This is where this thesis comes into play. Instead of "normal" TIs, it is proposed to use magnetically doped TIs, hosting the exotic quantum anomalous Hall effect (QAHE). In quasi-1D wires of magnetically doped or QAH systems no in-plane field is needed to re-topologize the spatially confined systems [32], [33].

Scope of this Thesis

The goal of this thesis is thus to fabricate magnetic TI systems via molecular beam epitaxy in order to achieve a QAH system, to combine this QAH insulator with superconductors to locally create artificial p-type superconductivity and lastly to find definitive signatures of the Majorana quasiparticle state in quasi-1D devices. Majorana modes have not been unambiguously identified yet and would provide a great leap in the future of topological quantum computing. Moreover, the proximation of superconductivity into magnetically doped TIs, or any dilute magnetic semiconductor for that matter, has not been established before, with a very recent exception utilizing Mn-doped HgTe [34]. This thesis follows a holistic approach, combining material growth, cleanroom fabrication, various characterization techniques, cryogenic measurements and highly specialized *in situ* fabrication techniques in cooperation with partners from the University of California Los Angeles, the Jiao Tong University Shanghai, the RWTH Aachen, the University of Cologne and multiple institutes at the Jülich Research Center to achieve a step toward the realization of Majorana devices. And such a step is currently of great necessity, since the field of topological quantum computing is facing multiple setbacks due to ambiguous and doubted results [35], [36], [37].

In chapter 2, the theoretical framework of TIs is shortly introduced, followed by a more in-depth explanation of magnetism in TIs and the physics behind the formation of the QAH phase. This is followed by an introduction to superconductivity and the phenomena regarding superconducting weak links, so called Josephson junctions, which are one tool to investigate the signatures of Andreev bound states and Majorana physics in devices. Lastly, a closer look is taken to the interplay of magnetism and superconductivity, which are in fact counteracting phenomena. With this, the theoretical foundations of this thesis are laid, continuing with the experimental work.

Chapter 3 focusses on the realization of the first QAHI system at the Research Center Jülich. In section 3.1, routine growth and fabrication steps are introduced to grow an optimized non-magnetic topological insulator, which will be used as the foundation for incorporating magnetic dopants. Next, growth, structural and transport characterizations of magnetic TIs (MTIs) will be detailed, however separated into two parts. First, the established magnetic TI $Cr_x(Bi_ySb_{1-y})_{2-x}Te_3$ will be grown and examined utilizing MTI films thicker than 10 nm to determine the optimal stoichiometry and growth procedure, before moving to quasi-2D sub-10 nm films culminating in the first magnetic TI system fabricated in the Jülich Research Center exhibiting quantized Hall resistance in a trilayer heterostructure. Moreover, a second approach utilizing the rather new intrinsic MTI systems $MnBi_2Te_4$ and $MnSb_2Te_4$ is pursued in parallel. These promise a homogeneous distribution of magnetic moments and thus a more stable magnetization. It will however become clear that $MnBi_2Te_4$ is not capable of providing the ferromagnetic qualities needed for the realization of Majorana physics, while first experiments on $MnSb_2Te_4$ do not show signs of quantization. Therefore, the growth and characterization of the intrinsic MTIs are moved to the appendix in chapter 7.1.

The MTIs established in chapter 3 will be combined with superconductors in chapter 4 using a technique for patterned thin film growth developed in our institute. First a device grown in cooperation with the UCLA will be examined, whose ambiguous results will lead to the development of an *in situ* fabricated device allowing for the investigation of superconducting as well as magnetic effects. These devices will be prepared with magnetic TI thin film and superconductors grown in a molecular beam epitaxy chamber in Jülich, which is commissioned in the scope of this thesis. In the thusly *in situ* fabricated Josephson junctions no induced superconductivity spanning the full device will be measured, owing to a bad interface transparency caused by a high magnetic exchange energy in the MTI films. However, multiple indications of a short ranged induced SC will be found in the devices, pointing towards solutions for the bad transparency effect and towards the need for an atomistic study of the proximity effect itself, forming the motivation for the last chapter.

In the last part, chapter 5, an alternative, more direct, path towards the investigation of the interplay of superconductivity and magnetic topological insulators is pursued. Utilizing scanning electron microscopy and spectroscopy, the behavior of the involved energy gaps at the MTI/SC interface can be locally examined. In order to create samples capable of measuring the interplay of the unequal phenomena of SC and magnetism at the interfaces, a new sample preparation technique needs to be developed. It will need to entail *in situ* patterning of the desired structures while yielding pristine and unobstructed surfaces viable for scanning electron microcopy. After multiple arduous optimization steps, this technique will be acquired in the form of large-scale ultra-high vacuum lithography (LUL).

2 Theory on Magnetic Topological Insulators and Superconductivity

In this chapter, the physical concepts behind the characteristics of the remarkable materials investigated in this thesis will be shortly explained. Commencing with the introduction of magnetic topological insulators and the quantum anomalous Hall effect, which is one of the main objectives of this thesis, next the prospects of using quasi one-dimensional magnetic topological insulator systems will be detailed. Then the concept of superconductivity will be illustrated, shortly introducing Majorana quasiparticles that may arise at the interface of superconductors and topological materials. Finally, concepts of the interaction of superconductivity and magnetism and the possible proximization of superconductivity into topological magnetic systems will be detailed.

2.1 Introduction into Topological Insulators

After von Klitzing had encountered the Quantum Hall Effect (QHE) in two-dimensional electron gases in 1980, Thouless, Kohomoto, Nightingale and den Nijs in their publication from 1982 developed a theoretical framework to describe the findings of von Klitzing, revealing the connection between the QHE and topological concepts known from mathematics [38] [39]. In 2005 Kane and Mele and in 2006 Bernevig and Zhang established another topological Hall effect, the Quantum Spin Hall Effect (QSHE) [40], [41], [42]. The main difference between the QHE and the QSHE lies in the fate of the time reversal symmetry (TRS) in the examined systems. While the external magnetic field needed for the QHE breaks the TRS, for the QSHE no external fields are needed, preserving the TRS and rendering the QSHE a time reversal invariant 2D topological system. Instead of the magnetic field, inherent strong spin orbit coupling (SOC) causes the spin of the electrons in the system to be coupled to their momentum, an effect called spin momentum locking. Due to the spin momentum locking two spin-polarized channels propagate in opposite directions along the system's edges, forming a so-called helical edge state. This phenomenon was first realized in 2007 in HgTe/CdTe quantum wells [42]. The fact that these inherently topological systems are only conductive at their interface, i.e. in 2D the edge, but insulating otherwise earned them the name of 2D topological insulators (TI).

Also in 2007, Fu, Kane and Mele succeeded in expanding the topological formalism to the three-dimensional regime [24]. While the 2D TIs possess topologically non-trivial bulk band gaps, which have to close at the interface to a trivial insulator, resulting in highly conductive 1D edge channels surrounding the TI, in three dimensions, the logical consequence of a 3D TI with an inverted band gap are topologically non-trivial 2D surfaces, giving rise to topologically protected surface states. The first realization of a 3D TI came shortly after Fu, Kane and Mele's publication in the form of $Bi_{1-x}Sb_x$ in 2008 [43]. The field started to gain traction with the material systems Bi_2Te_3, Bi_2Se_3 and Sb_2Te_3 introduced and realized in the following year [44], [45]. These X_2Y_3-compounds are characterized by their heavy elements, inversion symmetry and a large bulk band gap up to 0.3 eV, the latter of which was not given in $Bi_{1-x}Sb_x$. The topological nature in these materials is provided by an inverted band gap, resulting from the strong SOC deriving from the heavy elements in the compounds. The SOC leads to an exchange of the highest filled orbital and the lowest empty orbital state across the Fermi energy, yielding an inverted band gap. Simultaneously spin and orbital momentum are connected by SOC, thus lifting spin degeneracy [46]. The result is an inverted band gap, similar to the one in HgTe quantum wells, which needs to be closed at the interface to a trivial insulator creating topologically protected surface states and a spin polarized Fermi surface. In a three-dimensional picture of the energy dispersion this creates a spin polarized cone, also called a Dirac cone, with a Dirac point at its center, see figure 2.1 a). A consequence of spin momentum locking is that backscattering is heavily suppressed in the surface states of 3D TIs. If an electron were to backscatter at an impurity, it would need to fulfill a half rotation along the Dirac cone to reverse its momentum. This is accompanied by a spin flip and thus an accumulation of a Berry phase of π, which leads to destructive interference, effectively suppressing backscattering and rendering strong TIs highly robust against disorder. [25]

Magnetic topological insulators (MITs) were developed and investigated alongside non-magnetic TIs as early as 2008, when Liu *et al.* investigated HgTe quantum well systems doped with Mn [47]. Soon after TIs were found to host the QHE and QSHE as described above, the question arose whether TIs could also host the remaining effect known from the Hall effect family, the Anomalous Hall Effect (AHE). The latter was discovered shortly after the ordinary Hall effect by Edwin Hall, when he investigated the Hall behavior of magnetic cobalt and nickel films in 1981 [16]. Due to the inherent remnant magnetic field in the materials, a Hall effect can also be measured when no external field is applied. A quantum version of the AHE would entail conductive edge channels in a topological material, similar to the edge channels in the QSHE but without an external field, a system first proposed by Haldane in 1988 [49]. The prospect of topological edge channels without the need of an external magnetic field promises an attractive platform for realizing more elaborate circuits and quantum computational applications, which is why the discovery of the QAHE in magnetically doped TIs attracted remarkable interest. The next sections will thus elaborate on the QAHE and magnetism in TIs in general.

2.1.1 The Quantum Anomalous Hall Effect in Magnetic Topological Insulators

There are multiple ways to magnetize TIs, one of which is the approach of Liu *et al.* to use magnetic doping, but also magnetic proximity effects and lately intrinsic magnetic TIs are investigated. Their advantages and disadvantages will be discussed in chapter 3, however they have in common that they break the time reversal symmetry of the TI system they are incorporated into. For 3D TIs, the surface states of each of the 3 surface pairs can be described by

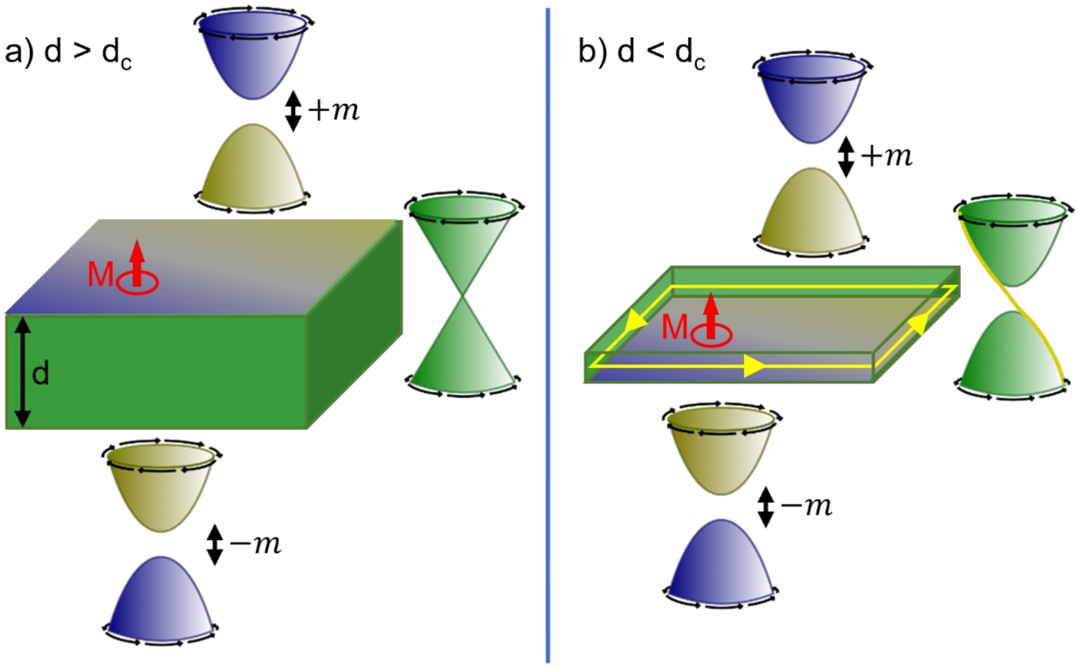

Figure 2.1: Thickness dependent surface dispersion configurations. When the MTI thickness d is larger than the critical thickness in a), the surfaces threaded by the magnetization M exhibit a magnetization gap $\pm m$*, while the side facet stays gapless with a Dirac-cone dispersion. When decreasing the thickness to a quasi-2D system, the side facets are gapped, but threaded by a single state (yellow), yielding a chiral edge state along the sample edge.*

$$\mathcal{H} = v_F\left(-k_y\sigma_x + k_x\sigma_y\right), \tag{2.I}$$

here exemplarily for the surfaces with the surface normal parallel to the z direction and with the spin matrices σ_i. This Hamiltonian describes the Dirac cone introduced previously. Introducing an inherent magnetic field via magnetization into the 3D TI or next to it adds a mass term m to the equation in 2.I, characterizing the effect of the exchange interaction of the conduction electrons with the magnetic field yielding

$$\mathcal{H} = v_F\left(-k_y\sigma_x + k_x\sigma_y\right) \pm m\sigma_z\,. \tag{2.II}$$

In the Dirac cone dispersion picture, the mass term leads to the formation of a magnetic gap as shown in figure 2.1. It must however be taken into account that the magnetic field penetrates the two considered surfaces of the TI either parallel or antiparallel to the surface normal, yielding either +*m* or -*m*. This has direct consequences for the Chern numbers of the surfaces, yielding $C = \pm 1$ for the respective surfaces [50]. The side surfaces are therefore similar to domain walls and thus the magnetic gap has to close, exhibiting a topological Dirac cone without a magnetic gap as shown in figure 2.1 a) [51]. When confining the 3D TI into a quasi-2D regime by decreasing the thickness d, the gapless side surfaces states become quantized. By tuning the Fermi energy to the Dirac point only a single 1D edge channel is present (which will be elaborated on in section 2.1.3). The result is a chiral edge state supplying a quantized Hall conductance of $\sigma_{xy} = e^2/h$ in Hall measurements at zero external magnetic field, together with zero longitudinal conduction

$\sigma_{xx} = 0$. Insulators showing this behavior are therefore called Quantum Anomalous Hall Insulators (QAHI). [52]

2.1.2 Magnetism in Topological Insulators

In the previous section it was shown how magnetism in TIs breaks the TRS and how, as a result, the last member of the Hall effect family could be realized [53], [54], [55]. As previously mentioned, the magnetism can be introduced into the TI either via doping, proximity or intrinsically by incorporation into the lattice. The fundamental mechanisms evoking the ferromagnetic magnetic order in the TI have been found to be the Ruderman-Kittel-Kasuya-Yosida interaction (RKKY) and the Van Vleck interaction. In this section, the two mechanisms will be shortly introduced. [50], [51]

2.1.2.1 Ruderman-Kittel-Kasuya-Yosida (RKKY) interaction

The RKKY interaction in TI compounds was already investigated before topological insulators had been discovered. The TIs were viewed as dilute magnetic semiconductors, in which ferromagnetism via RKKY interaction is a common feature [56], [57]. RKKY is an indirect interaction between the lattice atoms, which possess magnetic moments themselves, but due to only miniscule overlap of orbitals cannot establish long range order. The exchange interaction is thus mediated via itinerant electrons, which are polarized at the lattice atoms and convey their magnetization over a long range in an oscillatory fashion. This entails that the type of magnetism, ferro- or antiferromagnetism, depends on the distance between lattice atoms. [38]

RKKY has been shown to be the cause for magnetism in various MTIs and can be verified by investigating the response of the Hall conductance to a gate voltage, since the exchange interaction is dependent on the charge carriers and their density [50]. For the realization of the QAHE, the free charge carriers of the RKKY interaction are however detrimental, since they provide a parallel conduction channel which would replace the QAHE channel conduction. [58]

2.1.2.2 Van Vleck Mechanism

The second interaction potentially responsible for ferromagnetic order in MTIs is the Van Vleck mechanism. Its existence in tetradymite crystal structures doped with 3d transition metals, for example Chromium, which will be used in this thesis, was shown by Yu *et al.* [59]. Most importantly, the magnetic order in this interaction is not mediated by itinerant carriers, but by the band electrons. Yu *et al.* showed this by assuming that the whole system can be divided into two subsystems, describing the local magnetic moments and the band electrons, which are connected via a magnetic exchange term, resulting in a term for the free energy F of the system

$$F_{total} = \frac{1}{2}\chi_L^{-1}M_L^2 + \frac{1}{2}\chi_e^{-1}M_e^2 - J_{eff}M_LM_e - (M_L + M_e)H\,, \tag{2.III}$$

with χ the susceptibility of either the electrons e or the local moments L, M the magnetization of the respective subsystem and J_{eff} the magnetic coupling term. For ferromagnetism to exist in this system, F needs to be minimized without an external magnetic field H, yielding as a condition

$$\chi_L > \left(J_{eff}^2 \cdot \chi_e\right)^{-1}, \tag{2.IV}$$

which is fulfilled for large χ_e, giving rise to stronger local coupling. Via the Van Vleck mechanism large band electron spin susceptibilities χ_e can be achieved, following the equation

$$\chi_e^{zz} = \sum_{E_{nk}\langle E_F;E_{mk}\rangle E_F} 4\mu_0\,\mu_B^2\,\frac{\langle nk|\widehat{S_z}\,|mk\rangle\langle mk|\widehat{S_z}\,|nk\rangle}{E_{mk} - E_{nk}} \tag{2.V}$$

for temperatures lower than the band gap energy with μ_0 the vacuum permeability, μ_B the Bohr magneton, $\widehat{S_z}$ the electron spin operator and $|mk\rangle$, $|nk\rangle$ the Bloch functions in the conduction and valence bands, respectively. Due to an inverted band structure in strongly spin orbit coupled tetradymite TIs, the matrix element $\langle nk|\widehat{S_z}\,|mk\rangle$ is considerably large, in contrast to trivial insulators, where it is minimal [59], [60]. This causes a high susceptibility, which in turn minimizes the total free energy and enables the existence of ferromagnetism without an external magnetic field. In contrast to RKKY interaction, this effect does not depend on free carriers and is therefore not influenced by gating and depletion of free carriers as witnessed by Chang *et al.*[61]. Therefore, no parallel channel overshadowing the QAHE is formed, granting better access to the latter effect. Moreover, this interaction should be the dominant one when considering a QAHI with the Fermi level in the band gap, yielding low charge carrier densities.

2.1.3 MTIs as a Platform for Topological Quantum Computing

In the previous section, it has been shown that in quasi-2D magnetic topological insulators the QAHE can be realized, yielding a chiral spin polarized edge channel in a quasi-2D film with quantized conduction and otherwise insulating bulk. This entails that a magnetic field needs to be applied only once perpendicular to the sample to magnetize it, the QAHE state is maintained by the remnant field when the external field is turned off.

In chapter 1, it was stated that to utilize Majorana modes for quantum computing, the modes need to be braided to make use of their non-Abelian exchange statistics [62]. With braided Majorana modes information can be encoded and quantum algorithms are proposed to be performed. This braiding however is executed with zero dimensional Majorana modes, behaving as a pair of quasiparticles. In 2012, van Heck *et al.* proposed multiple layouts to perform braiding operations with Majorana quasiparticles using Cooper pair boxes, containing a quasi-1D nanowire covered with a superconductor [13]. Via the superconducting proximity effect in the surface of the nanowire, which has to be a material with strong SOC (for example InAs or TI materials), a p-wave superconductor is created and 0-dimensional Majorana modes at the ends of the wires arise (see also section 2.2.3) [22], [63]. In [26], Hyart *et al.* show the various quantum computational operations possible with networks of such Cooper pair boxes in more detail.

The usage of TI nanowires or -ribbons however requires the presence of a precise in-plane magnetic field to close the trivial confinement gap which arises when narrowing TI materials into the quasi-1D regime [64], [65]. For solely perpendicular arrangements of nanoribbons this is achievable, however arrangements as shown in [26] and [30] with non-perpendicular layouts complicate the realization, not to mention the impact of the external in-plane magnetic field on the superconductor and necessary read-out components. In his publication from 2013, Beenakker proposes using magnetic insulators to locally create Majorana modes on 2D topological insulators edge channels with superconducting electrodes [15]. Thus, no external field would be needed to create the desired Majorana modes. With the first realization of a QAHI in the form of a quasi-2D TI doped with chromium by Chang *et al.* another approach opened up of realizing the quasi-1D structures [53]. Shortly after, Chen *et al.* proposed utilizing a QAH compound, proximitized by a superconductor but narrowed into the quasi-1D limit forming a QAHI nanoribbon [66].

To realize Majorana modes, a superconducting gap has to be opened in topologically protected, spin polarized bands creating a p_x+ip_y spinless superconductor (c.f. section 2.2.3) [8]. In figure 2.2 a) a 2D QAH compound on a SC layer is shown with yellow arrows indicating the chiral edge state. The corresponding dispersion of states, not including an induced superconducting gap, is shown in figure 2.2 c), similar to the dispersion indicated in figure 2.1. Instead of only one state threading the band gap, two states are shown here between higher order surface states, they however illustrate the two counterpropagating channels on opposite sides of the QAHI film. Including the induced superconductivity in this case would open a superconducting gap at the chemical potential. Following the argumentation of Chen, this gap will be topological and capable of the creation of Majorana modes when the chemical potential intersects the QAH state.

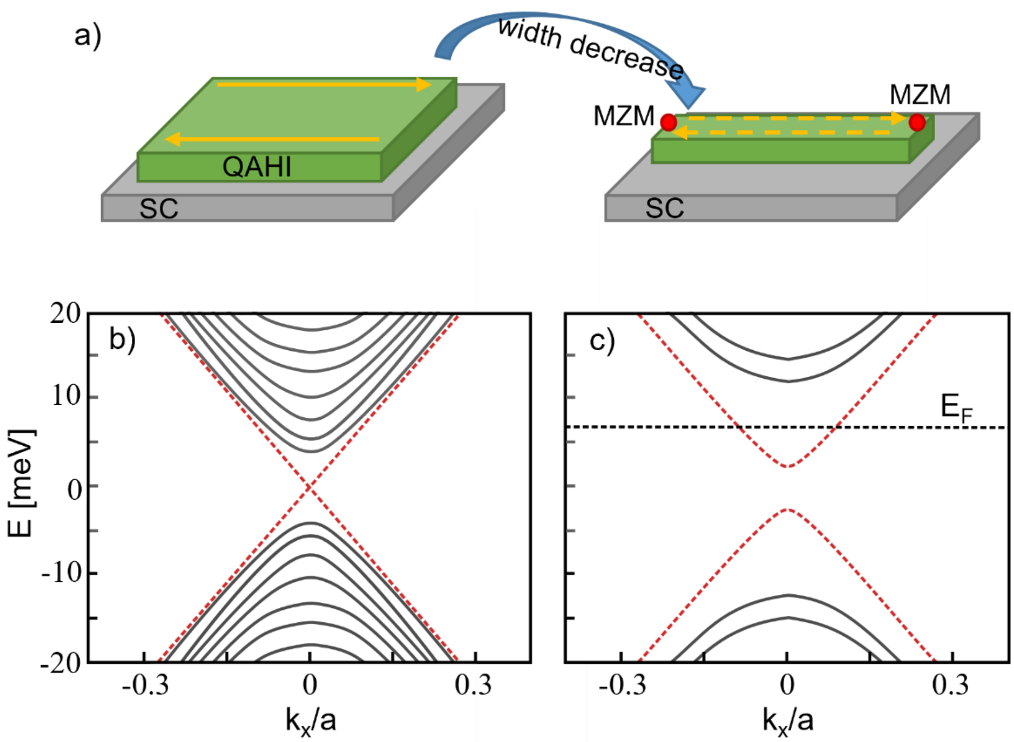

Figure 2.2: Creation of localized Majorana modes via narrowing of a quasi-2D QAHI on a SC. When decreasing the width of the QAHI going from wide shown in b) to narrow in c), the edge channels (yellow) can scatter into each other, creating a gap in the dispersion. b) shows a cut through the Dirac cone at $k_y=0$ with the topological state in red and other surface states in grey. At the opposite ends of the quasi-1D structure in c), localized Majorana zero modes (MZMs) arise when a superconducting gap is induced at the chemical potential crossing the topological state. Figure adapted from [66].

When the QAHI film is confined in one direction to form a quasi-1D system smaller than the localization length of the chiral channels, the counterpropagating channels start to overlap. Due to their chiral nature with aligned spins, carriers can scatter between the channels, creating a gap in the topological edge state. Thus, the chiral edge mode transforms into a single helical channel of superpositioned spin, indicated by the dotted yellow lines in figure 2.2 b). Concurrently, the confinement gap enlarges, pushing the higher order surface states to higher energies and therefore increasing the topologically non-trivial gap. Through this, a large energy window is opened, in which the gap is topological, enabling the creating of Majorana modes when incorporating a SC gap at the chemical potential over a much broader energy region. Simulations in our group suggest that it suffices, for the existence of Majorana modes, for the chemical potential to intersect the QAHI states in the bulk band gap. That entails that higher order surface states (grey in figure 2.2 b) and c)) may also be intersected.

This finding is one of the main motivations for this thesis. By confining MTIs or QAHI systems to quasi-1D nanoribbons instead of ordinary TIs, the necessity of an in-plane magnetic field with its complications can be avoided utilizing the inherent magnetism, topological chiral edge mode and enlarged topological gap to realize 0-dimensional Majorana states when combining the ribbons with a superconductor. Therefore, the Cooper pair box devices proposed by Hyart *et al.* or other Majorana devices [32] could be realized more straightforwardly and, due to the larger topological energy window, more stably. The three requirements to realize such devices, fabrication of a QAHI, its structuring or patterned growth and the combination with a superconductor are the tasks set to be solved in this work. Thus, in the next section, superconductivity and the physics of Majorana modes will be detailed.

2.2 Superconductivity

This chapter will illustrate the phenomenon of superconductivity, first on a microscopic scale in intrinsic superconductors, then in materials adjacent to superconductors, covering the proximity effect, Andreev reflections and Andreev bound states, culminating in Josephson junctions and Shapiro physics. Lastly, the interplay of superconductivity and the magnetism covered in the previous section will be discussed.

2.2.1 Intrinsic Superconductivity

Since their first discovery by Kamerlingh Onnes in 1911 [67], superconductors (SCs) have been the focus of many physicists from various disciplines. Their peculiar properties of perfect diamagnetism, zero resistivity and expulsion of magnetic fields up to specific temperatures opened up a plethora of research fields and many modern technologies could not be realized if not for superconductivity. Only in 1957 Bardeen, Cooper and Schrieffer (BCS) managed to describe the concepts behind superconductivity on a microscopic level [68]. They were able to show that if there is a small attractive force between the valence electrons in a material, this can lead to the formation of electron pairs, even though the particles would otherwise repel each other. In 1952, Fröhlich [69] and in 1955 Bardeen [70] proposed that an interaction mediated by lattice phonons is responsible for the attractive force between electrons. The pairs formed via this Fröhlich-interaction at low temperatures are called Cooper pairs and exhibit a net spin of zero, consisting of two electrons with opposite momentum $\boldsymbol{k}_1 = -\boldsymbol{k}_2$ and antiparallel spin. In reference to the orbitals in atoms, the zero-spin state following an antisymmetric wave function is called s-type SC. Other superconductive ground states, like the previously mentioned p_x+ip_y state are not covered by the BCS theory and will be examined later. Since the Cooper pairs have effectively zero spin, they can be treated as bosons and thus form a bosonic state that can be described with a macroscopic ground state following the wave function

$$\Psi_\mathrm{S} = \sqrt{n_{CP}} \cdot e^{i\Theta_\mathrm{S}}\,, \qquad 2.VI$$

where n_{CP} is the density of Cooper pairs and Θ_S is the complex phase of the macroscopic state.

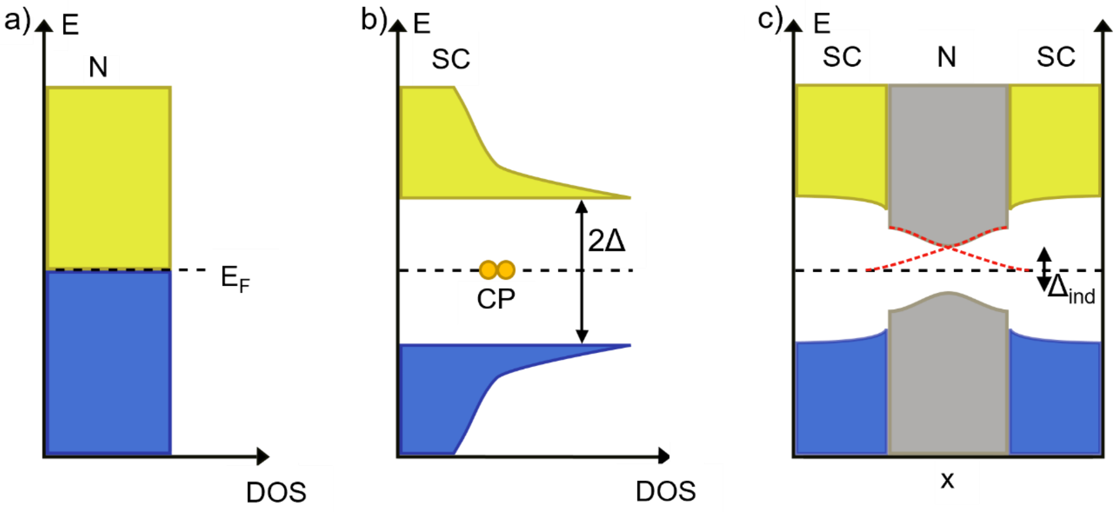

Figure 2.3: In a), the schematic of a density of states diagram of a normal metal (N) is shown, with the valence (blue) and conduction (yellow) band separated at the Fermi energy E_F. When the material is cooled below the critical superconducting temperature a superconducting gap Δ opens at the Fermi level, with the bosonic state hosting the Cooper pairs at E_F. When two SCs are separated by a non-SC (grey), the superconducting gap is induced into the non-SC. If the gap profiles of the SCs (red) overlap, the normal metal becomes superconducting with a diminished induced superconducting gap Δ_{ind}.

In fact, the pair wise configuration or condensation of the electrons into Cooper pairs is energetically favorable for the electrons in the free electron gas, resulting in a transition of all electrons in a material-specific interval around the Fermi energy into Cooper pairs. This creates a gap Δ_S above and below the Fermi energy, in which no quasiparticle states exist as shown in figure 2.3 b). Since no quasiparticle states for the Cooper pairs to scatter into are thus available, the Cooper pairs exhibit dissipationless transport up to excitations exceeding the SC gap Δ. These excitations can be caused by high temperatures, leading to the critical temperature T_C, high currents, yielding the critical current I_C, or high magnetic fields B_C, which break the Cooper pairs. The latter case of the critical magnetic fields has to be specified for different superconducting materials, however. In so called type-I-SC, SC is maintained up to a specific field B_C, in type-II-SCs there are two such fields. For $B < B_{c,1}$ and $B > B_{c,2}$, type-II-SC behave like type-I-SC, for fields between the two critical fields magnetic fluxes can penetrate the SC locally in the form of magnetic vortices without inhibiting SC in the surrounding material.[38]

Not all materials exhibit SC in practical environments, some need extremely low temperatures, high pressures or both to transition into a superconducting state. It is however possible to achieve SC also in materials that themselves do not show SC. This is especially of interest for TIs, which do not intrinsically turn superconductive, with some exceptions that are still the focus of ongoing investigation like $Cu_xBi_2Se_3$ ([71], [72]) and $Nb_xBi_2Se_3$ ([73], [74]). When a superconducting material is adjacent to a non-SC compound, Cooper pairs are not confined to the SC itself, but can diffuse into the bordering material given a high enough transparency for the correlated electron pairs. Therefore, a superconducting gap is opened in the compound, which decreases

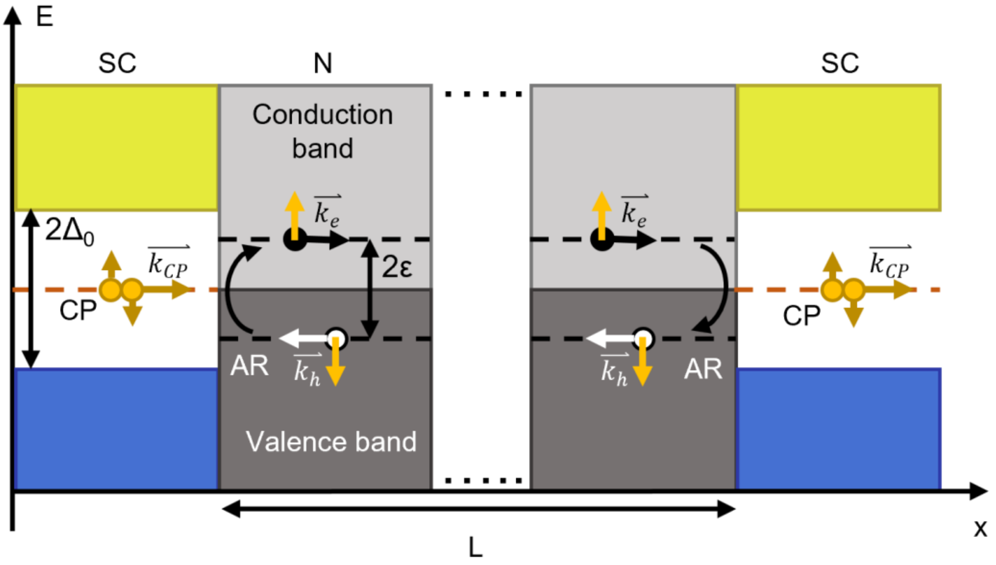

Figure 2.4: When a SC is adjacent to a non-SC (N) material, incoming electrons from the N must go through the process of Andreev reflection (AR) to enter the SC as a Cooper pair (CP), since there are no states available for the electrons in the SC gap. By combining with an opposite spin electron at -ε from the Fermi-sea, leaving a counterpropagating hole in the valence band, a CP is formed. At the opposite interface, the hole can recombine with a CP, to allow conduction from the SC into the N. If the distance L between the interfaces is smaller than the dephasing length l_ϕ*, the two AR couple to a loop. This loop is called an Andreev bound state, effectively carrying 2e of charge over the N region. Figure adapted from* [75]

over a length scale ξ_N referred to as coherence length or penetration depth of the Cooper pairs. This effect is shown in figure 2.3 c), with the extended gap profiles penetrating the non-SC compound given in red. Since the strength of the SC relies mostly on the Cooper pair density n_{CP}, the superconductivity's strength at the interface and in the proximitized compound is reduced compared to the bulk value. For "dirty" materials, in which the mean free path of the electrons l^* is smaller than the size of a Cooper pair ξ_0, the coherence length is given by

$$\xi_N = \sqrt{\frac{\hbar D_N}{2\pi k_B T}}, \tag{2.VII}$$

with the diffusion constant $D = \frac{1}{3} v_F l^*$. The depth of Cooper pair penetration is however not only dependent on the temperature and mean free path, but also on the density of states in the two materials as well as interface transparency or roughness, to name a few factors. The induced gap Δ_{ind} is therefore always smaller than the original SC gap as illustrated in figure 2.3 c). [76], [77]

When a current is applied from a SC to a non-proximitized normal metal or insulator (N), charge carriers are bound to flow from one compound into the other. To do so, at the interface the charge carriers generally scatter into unoccupied states in the other material. In the superconductor however there is a gap without states to scatter into around the Fermi energy. In a microscopic picture this means charge carriers with energies lower than the gap size Δ_S need to team up to build Cooper pairs, which can scatter into the bosonic ground state in the superconductor. The scattering process describing this behavior is called Andreev reflection and shown in figure 2.4. In the following, the Andreev process illustrated at the right interface in figure 2.4 (N→SC) is described. When an electron with $\boldsymbol{k}_{\uparrow}$ at energy ε is propagating towards the N-SC interface from the normal metal, it needs a second electron with $-\boldsymbol{k}_{\downarrow}$ to form a Cooper pair as stated previously. In the SC however, no such electrons are available at the given energy E_A. The second electron is therefore extracted from the Fermi-sea of the normal metal, creating a hole $-\boldsymbol{k}_{h,\downarrow}$ at $-\varepsilon$, travelling in the opposite direction, away from the interface. The process is thus retro-reflecting an incoming electron as a hole while creating a Cooper pair, yielding a net charge transfer of 2e per scattering process. The reversal of the process at an inverse SC→N boundary is called inverse Andreev reflection and involves the breaking of a Cooper pair into two electrons, one of which combines with a fitting hole in the Fermi-sea (see left interface in figure 2.4).

Superconducting proximity and the Andreev reflection are the phenomena involved when a single SC-N interface is considered. Combining two such interfaces with a distance $L < 2\xi_N$ between them creates an overlapping region, through which Cooper pairs can be exchanged between the SC. If $L > 2\xi_N$, Andreev bound states between two Andreev reflections can exist in the non-superconducting region. These phenomena will be detailed in the next section.

2.2.2 Andreev Bound States and Josephson Junctions

The previous section showed how superconductivity can leak from a superconductor into an adjacent non-SC compound and how charge transfer takes place at the interface of the SC region to the non-SC region. In this section the focus will be put on the effects that occur when two SC materials are brought in close contact with each other, but still separated by a non-SC normal (N) region, forming a so-called Josephson junction. [78]

The process of (inverse) Andreev reflection shown in figure 2.4 can lead to a bound state when two reverse interfaces, SC-N and N-SC, are involved. If the interfaces are closer than the dephasing length l_ϕ of the electron and hole quasiparticles in the N-region, the electron that is created by breaking the Cooper pair at the SC-N interface can, at the other interface, be employed to create a new pair at the opposite N-SC surface. A hole would in turn be created there, traveling back towards the SC-N surface where it would combine with the second electron arising from the Cooper pair splitting. After such a process, the initial conditions are reestablished, enabling a continuous bound state transferring 2e over the junction without a voltage drop.

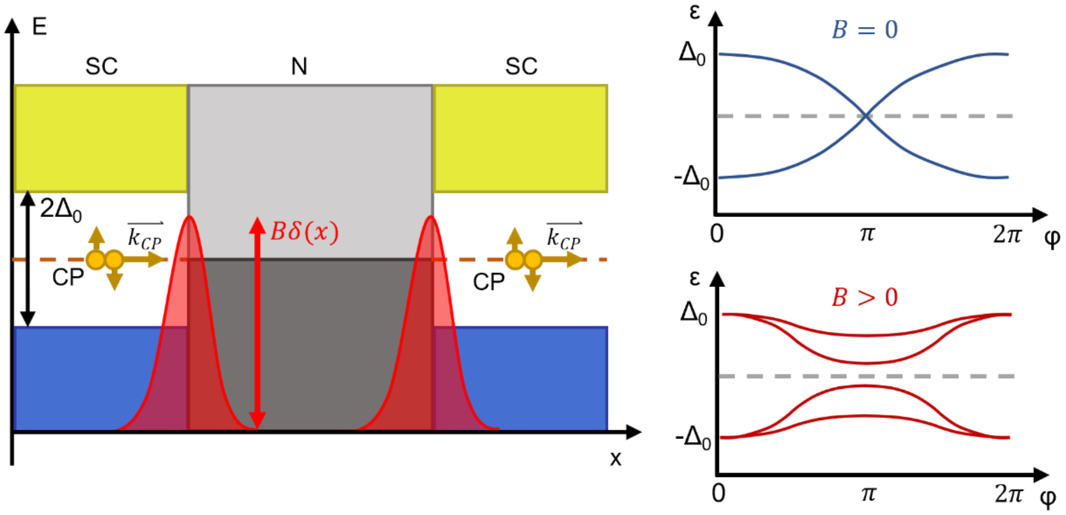

Figure 2.5: Josephson junction with suboptimal interfaces. If at the interface of the superconducting to the non-SC region a barrier B (red) is present, the process of Andreev reflection is imperfect. This influences the phase periodicity of the junction. At zero barrier strength (top right), the periodicity is 4π *periodic, while with increasing barrier height* $B\delta(x)$ *the periodicity becomes more and more* 2π *periodic. This in turn influences the step periodicity in Shapiro measurements directly, which therefore is a way to investigate the nature of the phase period present in the sample. Figure adapted from* [75].

The bound state energy ε can be calculated following Kulik by $\varepsilon = \pm\Delta_0 \cos\left(\frac{\varphi}{2}\right)$ with $\varphi = \theta_{NS} - \theta_{SN}$ being the difference between the superconductors' global phases, see equation 2.VI, for the short junction limit [79]. In figure 2.5, the resulting states depending on the phase difference are shown for ideal and for realistic surfaces with barriers at the SC-N interface. The equation for ε would suggest a 4π periodicity of the Andreev bound states (ABS) as in figure 2.5 for $B = 0$, in reality however, imperfect interfaces with barrier strengths $B > 0$ and non-perpendicular incidence of the ABS causes the spectrum to be dominated by an additional 2π periodic contribution [80], [81]. It will later be shown that in S-TI-S junctions, the 4π periodicity can be reestablished.

When the two SC regions are closer than $2\xi_N$ and separated by an insulator (I), Cooper pairs can tunnel through the I compound. This effect was first proposed by Josephson in 1962, earning him the Nobel prize in 1973 [78]. In a SC-normal metal-SC (SNS) junction as considered before, the involved process is not tunneling but the previously explained ABS, leading to dissipationless transport through the junction, which is also referred to as a weak link due to the weakened superconductivity in the N compound. As stated in equation 2.VI, a superconductor possesses a macroscopic wavefunction with a phase θ. Josephson discovered that the tunneling current density J_S depends on the difference in phase between the superconductors, yielding the first Josephson equation

$$J_S = J_c \sin(\varphi_{1,2}) = J_c \sin\left(\theta_1 - \theta_2 - \frac{2\pi}{\Phi_0}\int_1^2 \boldsymbol{A}d\boldsymbol{l}\right), \qquad 2.VIII$$

with the phases $\theta_1$and θ_2 corresponding to the 1st and 2nd SC. J_c denotes the maximum current density over the junction, $\boldsymbol{A}$ a vector potential and $\boldsymbol{l}$ the path over the junction [38].

When taking the time derivative of the phase difference $\varphi_{1,2}$, the second Josephson equation is acquired in the form of

$$\frac{\partial\varphi_{1,2}}{\partial t}=\frac{2\pi}{\Phi_0}\int_1^2 \boldsymbol{E}d\boldsymbol{l}\,, \tag{2.IX}$$

where the integral of the electrical field $\boldsymbol{E}$ over the junction length $\boldsymbol{l}$ corresponds to the voltage drop over the junction. Applying a direct voltage U_D over the junction structure would thus yield a phase difference

$$\varphi_{1,2}(t)=\varphi_0+\frac{2\pi}{\Phi_0}U_D\cdot t\,. \tag{2.X}$$

Adding an alternating voltage $U_A\cdot\cos\left(\omega_A t\right)$ to the direct component results in an oscillating phase difference given by

$$\varphi_{1,2}(t)=\varphi_0+\frac{2eU_D}{\hbar}t+\frac{2eU_A}{\hbar\omega_A}\sin(\omega_A t), \tag{2.XI}$$

which, when inserted into equation 2.VIII and using Fourier-Bessel-series, can be rewritten as

$$J_S=J_c\sum_{n=0}^{\infty}\mathcal{J}_n\left(\frac{2eU_A}{\hbar\omega_A}\right)\sin\left[\varphi_0+\frac{2eU_D}{\hbar}t\pm n\omega_A t\right], \tag{2.XII}$$

with $\mathcal{J}_n$ the Bessel-functions of the first degree and the integer n. Interestingly, the direct current contribution of J_S, which is measured in most experiments, is only finite for certain values of U_D, at which the sine becomes time independent, namely

$$U_D=n\cdot\frac{\hbar\omega_A}{2e}\,. \tag{2.XIII}$$

The result are steps in the current-voltage relation when measuring over a Josephson junction at voltages given by equation 2.XIII. These steps are called Shapiro steps after their discoverer [82].

With this, the processes at S-N-S and S-I-S interfaces in the form of tunneling, ABS and Josephson junctions have been illustrated. The next section will now illuminate the differences when substituting the N or I by a TI and show why this S-TI-S junction piqued the interest of many scientists regarding the possibility of the existence of Majorana modes in these junctions.

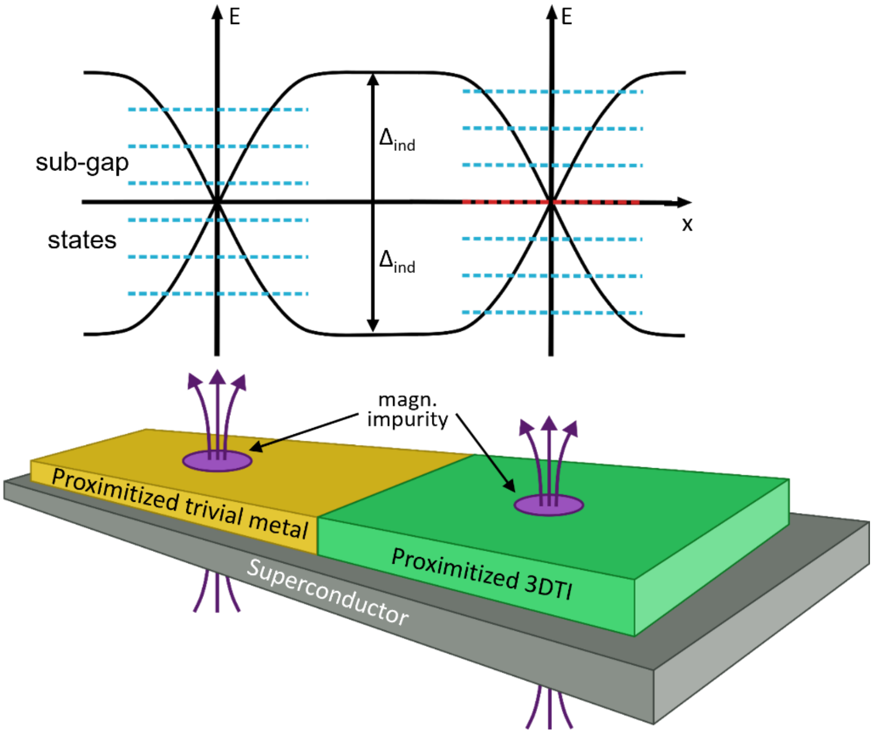

Figure 2.6: The induced superconductive gap in proximitized materials may host multiple sub-gap states (blue lines). In trivial materials (yellow), these sub-gap states are distributed symmetrically around the superconductive ground state at E = 0 because of electron-hole symmetry. For proximitized 3DTIs the non-trivial topology leads to an additional phase, yielding constructive interference at E = 0 and thus a (Majorana) state (red). One can access this state by closing the SC gap locally, for example with magnetic flux from an impurity or a vortex. Figure adapted from [15].

2.2.3 SC-TI-SC Josephson Junctions

In SC-TI-SC junctions, the previously discussed proximity effect causes Cooper pairs to diffuse into the surface states of the TI, which in turn are topologically protected and spin-momentum locked. The resulting phenomena will be detailed in this section.

By transferring the terminology of SC into the Bogliubov-de Gennes (BdG) formalism, which is often used when describing inhomogeneous SC and unconventional SC pairings, the creation of an excitation in the SC gap can be written using second quantization as $u(\boldsymbol{r}) = vc_{k,\uparrow} + wc^{\dagger}_{-k,\downarrow}$, with c and $c^{\dagger}$ the annihilation and creation operators, showing that excitation states in the gap are a combination of electron and hole excitations. In 2008, Fu and Kane realized that when the induced superconductivity in TI is written in the BdG-formalism, the resulting equations correspond to that of a $p_x + ip_y$ superconductor, in which Read and Green in 2000 had postulated the existence of Majorana quasiparticles or Majorana bound states [16], [83]. The Majorana fermion, which had been proposed by Ettore Majorana in 1931, is a concept from particle physics describing a particle which is its own anti-particle. Its creation and annihilation operators are therefore identical, obeying $\gamma(E) = \gamma^{\dagger}(-E)$ [14]. The Majorana particle can be understood as an equal mixture of particle and hole, which would translate to $\gamma = c + c^{\dagger}$ and is clearly similar to the expression found for the quasiparticle excitations in the SC gap for $v = w = 1$. The latter condition of equal weight is only given for a quasiparticle state at zero energy. In standard s-wave superconductors, no such quasiparticle state at $E = 0$ exists due to electron-hole symmetry, as exemplified in figure 2.6, and the Cooper pairs consist of electrons with antiparallel spins.

In the topological Dirac surface states of TIs, spin momentum locking creates an effectively spin-less state by removing the spin degree of freedom and creating Cooper pairs reliant on spin-triplets, which causes the superconducting surface of the TI to behave like a $p_x + ip_y$ superconductor [16], [84]. Meanwhile the non-trivial Berry phase adds a π phase shift to the shift of π given by the Bohr-Sommerfeld quantization rule, leading to constructive interference at $E = 0$ and thus allowing for a zero-energy state while maintaining TRS as is depicted in figure 2.6 [15], [16]. Locally breaking TRS by a magnetic vortex or impurity closes the SC gap, giving access to the sub gap states, including the zero-energy state for which the Majorana condition is fulfilled. These quasiparticle states or Majorana zero modes can be viewed as solid state realizations of the Majorana fermion proposed by Majorana [15]. Sun, Jia *et al.* showed in 2016 via spin selective Andreev tunneling first indications of Majorana states bound to vortices [85], [86].

A definitive proof of the Majorana state will only be achieved when a braiding process with Majorana bound states (MBS) can be shown, utilizing their non-Abelian statistics to distinguish them from other possible quasiparticle modes [87]. There are however multiple approaches to find indications of Majorana states in electrical transport experiments, for example in tunneling experiments [88], but their traces can also be found in the current phase relations of SC-TI-SC junctions [15], [89]. In Josephson junctions (JJs) with TIs as the proximitized interlayer, a p-type superconductor as introduced previously should form due to the induction of a SC gap into the topological spin-momentum locked surface states in the weak link. In SC-N-SC junctions, imperfect interfaces and incidences of oncoming carriers cause the Andreev reflection to turn 2π periodic instead of 4π periodic. In the case of perpendicular incidence, an electron that does not form an CP via AR would be retroreflected, diminishing the 4π ratio. For a TI however, this incoming electron is spin-momentum locked and the reflection would therefore require a spin-flip. The high energy cost for the spin-flip involved in the backscattering strongly suppresses the process, leading to almost perfect transmission into the SC for modes perpendicular to the interface. These perfect transmissions manifest themselves in a restoration of 4π periodicity. Thus, evaluating the ratio of $I_{2\pi}$ and $I_{4\pi}$ to the full supercurrent can yield insight on the extent of ABS corresponding to p-wave superconductivity in the proximitized region. [89]

2.2.4 Interaction of Superconductivity and Magnetism

When magnetic fields and superconductors interact, two distinctly different macroscopic ordering phenomena collide. On the one hand, in magnetic materials as illustrated in section 2.1.2, long range order of aligned spins is achieved via various interactions. On the other hand, in the most common s-wave superconductors, electrons with opposite spin condensate into a bosonic Cooper pair. The discrepancy in combining the two concepts is thus obvious, however there are possibilities to combine both materials, or rather to create mixtures of both, via the proximity effect.

Two main issues affect the electrons in a Cooper pair when magnetism is considered, firstly the orbital effect and secondly the Pauli paramagnetic limitation. The former describes the effect of the Lorentz force arbitrated by the magnetic field on the electrons in a Cooper pair which have opposite momenta, causing the CP to break if the field reaches a specific value, the critical field B_c. The Pauli limitation takes effect when the Zeeman field induced by the magnetic flux is strong enough to align the spins, destroying the spin-singlet states [90]. The latter effect is the predominant reason for the destruction of SC in proximity to a ferromagnet, which will be covered in this thesis, while the orbital pair breaking is more common in bulk SC systems.[91]

An SC proximity effect into a ferromagnetic material, and vice versa, is however possible. In contrast to the AR at the interface to a non-magnetic material, in the ferromagnet the electronic bands are each shifted by the exchange field E_{ex} depending on the spin direction as shown in figure 2.7 a). This directly influences the momenta values of the opposite spin electrons available at the Fermi energy to form Cooper pairs, resulting in $\boldsymbol{k}_{F\uparrow,\downarrow} = \boldsymbol{k}_F \pm \boldsymbol{Q}/2$, which results in a CP with a center of mass momentum $\pm\boldsymbol{Q}$. The CP is therefore not in an ordinary singlet state, but a mixture of singlet $(\uparrow\downarrow - \downarrow\uparrow)$ and triplet $(\uparrow\downarrow + \downarrow\uparrow)$ states called the FFLO phase, after its discoverers Fulde, Ferrell, Larkin and Ovchinnikov (FFLO), described by

$$\begin{aligned}(\uparrow\downarrow - \downarrow\uparrow) &\rightarrow \left(\uparrow\downarrow e^{i\boldsymbol{Q}\cdot\boldsymbol{r}} - \downarrow\uparrow e^{-i\boldsymbol{Q}\cdot\boldsymbol{r}}\right) \\ &= (\uparrow\downarrow - \downarrow\uparrow)\cos(\boldsymbol{Q}\cdot\boldsymbol{r}) + (\uparrow\downarrow + \downarrow\uparrow) i\sin(\boldsymbol{Q}\cdot\boldsymbol{r})\,.\end{aligned} \qquad \text{2.XIV}$$

In figure 2.7 b), the effect of the singlet-triplet mixing on the proximity effect is shown and compared to a non-FM material N. In the N material, only the singlet state exists, which penetrates far into the compound. In spin polarized materials the strength of the two superconductive pairing amplitudes in the FM oscillate with the wave number $Q/\hbar$, but the correlation decay length ξ_F decreases with increasing spin-polarization and is commonly much smaller than in SC-N interfaces ($\xi_N \gg \xi_F$). The triplet state in c) exhibits zero spin projection onto the magnetization axis. It should be noted that the adjacency to the FM also influences the SC itself, where the pairing amplitudes of the singlet state decreases towards the interface while the strength of the triplet state increases, even more so with strongly polarized FM. [92], [93]

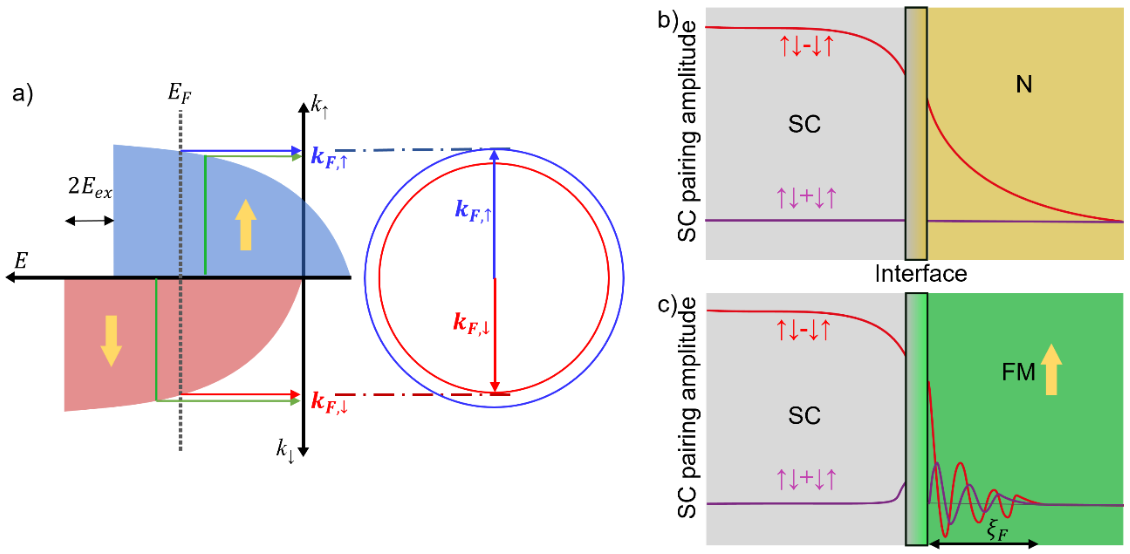

Figure 2.7: The formation of Cooper pairs at the interface of FM and SCs involves shifted momenta compared to the SC-N (green arrows) case. As shown in a), due to the exchange energy influencing the spin directions differently, the available electrons at the Fermi level for the CP formation have slightly different momenta. A CP of these electrons retains a center of mass momentum $\boldsymbol{Q}$*. This leads to a mixture of singlet and triplet CP at the interface. In b) the pairing amplitude of the CP at the trivial SC-N interface is shown. No triplet state is present, the singlet state can penetrate into the N material, decreasing exponentially with distance from the SC. In the non-trivial case of a SC-FM interface, a triplett state is present, giving an alternatively oscillating pairing amplitude in the FM material up to a correlation decay length* ξ_F*. Adapted from* [92].

When building a JJ with SC and FM, the two FFLO states exuding from the SC-FM interfaces can connect and form a SC-FM-SC Josephson junction. Due to the oscillatory behavior of the induced pairing however, two types of junctions exist, the 0- and the π-junction, which depend on the alignment of the pair amplitudes. By varying temperature and width of the junction, the states can be switched, leading to minima in the junction-characteristic $I_c R_N$, with R_N the resistance of the junction in the non-SC state [92], [94].

As explained before, the proximity effect in the FM is rather weak and generally short-ranged compared to the proximity effect into ordinary metals. There is however the possibility of a “long-range proximity effect” (LRPE) as detailed by Bergeret, Volkov and Efetov [93], [95]. In their paper, they describe an SC-FM interface with an inhomogeneous magnetization. There, the $S_z = 0$ triplet states ($\uparrow\downarrow + \downarrow\uparrow$) can be transferred into $S_z = \pm 1$ triplet states (↑↑ or ↓↓, respectively). When comparing the formation of such CP with that of the $S_z = 0$ pairs in figure 2.7 a), it becomes clear that the former do not experience a center of mass momentum shift and thus are not proportional to an exponential factor, which in turn means that there is no oscillatory behavior of the pairing amplitude. The penetration width of the triplet states with finite total spin thus increases from $\xi_{S_z=0} = \sqrt{D/b}$, with D the diffusion constant and b the strength of the magnetic exchange field, to the order of $\xi_{S_z=\pm 1} = \xi_T = \sqrt{D/2\pi T}$, where T denotes the temperature. Nonetheless, the creation of these CPs necessitates an inhomogeneous magnetization, for example non-aligned ferromagnetic multilayers [96], [97] or interfaces with magnetic disorder [98].

Most notably, Houzet and Buzdin show that the LRPE can be optimized when employing a trilayer FM'-FM-FM' structure [97]. With a (anti-)parallel magnetization in the FM' layers and a magnetization shifted by θ = 90° respectively in the FM layer, the LRPE can be maximized. Furthermore, by controlling the magnetization in each layer, the supercurrent can be switch on and off [99]. The enhanced range of the LRPE in these structures can be explained by a rotation of the basis of the shorted ranged triplet component given in equation 2.XIV. The triplet $(\uparrow\downarrow+\downarrow\uparrow)$ is aligned to the magnetization in the FM' layer, for example along the z-direction, but the shifted magnetization in the FM layer will transform this triplet into

$$(\uparrow\downarrow+\downarrow\uparrow)_z = \frac{\sin(\theta)}{\sqrt{2}}(\uparrow\uparrow)_\theta + \cos(\theta)\,(\uparrow\downarrow+\downarrow\uparrow)_\theta - \frac{\sin(\theta)}{\sqrt{2}}\,(\downarrow\downarrow)_\theta\,. \qquad 2.XV$$

$(\uparrow\uparrow)_\theta$ and $(\downarrow\downarrow)_\theta$ are long range triplet components, which carry the triplet supercurrent through the FM layer. [100], [101]

The discovery of LRPE in CrO_2 however, a strong ferromagnet, caused some surprise [102], [103]. The previous requirements for the LRPE were not obviously given, a spin-active layer at the interface could only be suspected. In 2014, Bergeret and Tokatly introduced a theoretical framework capable of explaining the LRPE in CrO_2 without magnetic inhomogeneities, but with the presence of spin-orbit coupling in the proximitized layer [104]. Their approach describes a layerstack of SC/FM/N and Josephson junctions in a SC/FM(SOC)/SC setup. The SOC is assumed to be linear in momentum, finite and small in relation to the disorder strength. SOC and exchange field can then be described perturbatively by an effective SU(2) potential. To account for the perturbations, covariant derivatives are incorporated into the quasiclassical equations, implicating the SU(2) gauge field. This results in a spin-precession akin to that caused by magnetic inhomogeneities, creating all possible triplet projections. Moreover, the singlet-triplet conversion might even be enhanced in the lateral junctions employed later in this thesis and in earlier works of our group [104], [105], [106].

Although the framework developed by Bergeret and Tokatly shows that LRPE in homogenous magnetic layers is possible, they focused on small SOC and exchange fields compared to the disorder strength. Thus, Lu and Heikkilä developed the concept of LRPE via SOC further, examining the case of strong SOC and high exchange fields [107]. There, both effects cannot be treated as perturbations and thus the SU(2) ansatz is invalid. They find that there is no LRPE when the SOC strength $\alpha \cdot k_F$ is comparable to the exchange field strength b, since in this case both spin rotation symmetry and TRS are broken, allowing for spin-flip scattering at non-magnetic impurities, strongly suppressing the proximity effect. If however $\alpha \cdot k_F \ll b$ or $\alpha \cdot k_F \gg b$, one of the respective symmetries is preserved, allowing for LRPE. Examples of a 3D TI weak link covered with a FM to proximitize the TI, i.e. a SC/QAHI/SC structure, are explicitly mentioned to host LRPE under these conditions.

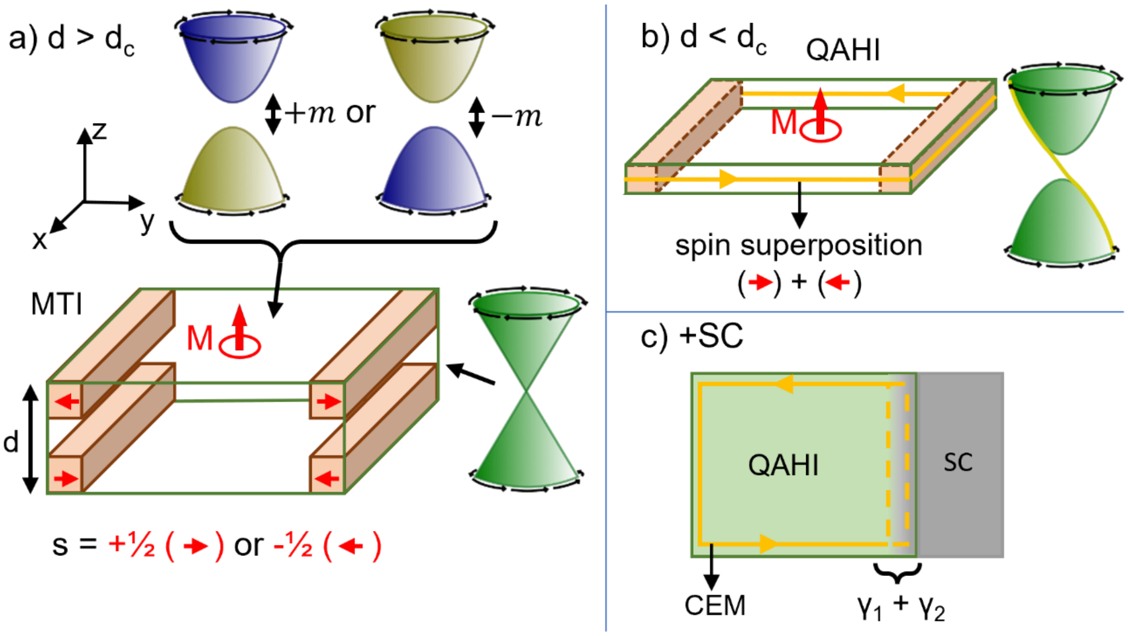

Figure 2.8: Reevaluation of figure 2.1, specifically the spin arrangement. In a), a 3D MTI is considered with gapped surface states on the faces threaded perpendicularly by the magnetization. The side facets, not gapped by the magnetization, exhibit increased density of spin polarization towards the edge to the topologically different x-y-planes (not shown for the y-z-planes). This is also the case for certain non-magnetic TIs [108]. *The corner-localized spin polarization is aligned in the x-y-plane. b) Decreasing the thickness d below a critical level d_c causes the edge channel wave functions to overlap and form a single QAH edge state. The edge channel exhibits a superposition of the spins, averaging the spin to 0. In c) a superconducting material is added at one side to the QAHI. The proximitized SC gap induced into the QAHI transforms the chiral fermionic QAH state into two topologically equivalent chiral Majorana fermions γ_1/γ_2, with non-coinciding energy dispersions separating them* [109].

Thus, in theory triplet SC in proximitized MTIs is possible, giving access to the elusive Majorana modes proposed to exist in these p-wave SC compounds [15], [16]. The microscopic mechanism of the Andreev reflection giving rise to the induced superconductivity in such systems is however not yet clear. Consider a lateral 2D QAHI/SC interface, where only one spin state is available coupled to the momentum. For the formation of a (↑↑) triplet state, two electrons with $\boldsymbol{k}_\uparrow$ and $-\boldsymbol{k}_\uparrow$ are needed to form the triplet CP, however due to spin-momentum locking the antiparallel momenta are situated on the opposite sides of the thin film. Thus, there is no available hole state for the AR at one side of the interface [110].

Simulations by Kristof Moors in our group on MTIs suggest a process taking the side surfaces of the MTI into account, elaborating on what is established in figure 2.1. The sides are parallel to the film's magnetization and therefore exhibit a shifted electronic structure, but no magnetic gap in the surface Dirac states. The TRS on the side surfaces is thus maintained, leading to two channels of opposite spin at the corners of the x-z-planes (and y-z-planes, not shown) to the x-y-planes as shown in grey in figure 2.8 a), which would allow for AR processes [111]. However, the thusly created CPs would be singlet CPs, not the triplet states needed for Majorana investigations. In contrast to that, in the limit of the quasi-2D QAHI no side surfaces are available as shown in figure 2.8 b). In this case, the corner states with antiparallel spin alignment will coalesce to form the 1D edge channel.

The resulting channel consists of a superposition of both spins, yielding a vanishing spin when averaged over the channel.

Furthermore, [109], [112] state that when the QAHI is proximitized by a superconductor as shown in figure 2.8 c), the single QAHI edge state is split into two chiral Majorana edge mode states (CMEM), related to each other by particle-hole symmetry, but with differing energy dispersions [109]. While they propagate along the interface to a trivial superconductor as shown in figure 2.8 c), they can penetrate into a topological SC with the same topological variant. By applying magnetic fields this variant can be changed locally, so that only one CMEM is permitted through the TSC. The other CMEM is reflected and again propagates along the interface to the opposite edge, rejoining with the transmitted CMEM of the other edge [113], [114]. This yields only one well-separated CMEM in the topological SC needed for the realization of chiral Majorana zero modes. In this approach however, no attention is given to the nature of the induced proximity and how it is conveyed, leaving some uncertainties regarding the microscopic processes concerning AR and the proximity effect at SC/QAHI interfaces.

With this, the theoretical background on topological insulators, superconductivity, magnetism and their combinations concludes, showing that although SC in QAHIs, consisting of thin 3D MTIs, via the proximity effect is theoretically possible, its microscopic texture, strength and reach is however not fully explored. Moreover, the Majorana modes proposed at the interface of a topological p-wave superconductor are still being sought after, with each indication of MZM bringing us closer to the proof of their existence via braiding. This thesis aims to elaborate on the foundations to reach the proof of Majorana states and thus aims to investigate the proximity effect in Josephson junctions of MTIs and QAHIs. To do so, in the next chapter the equipment necessary to fabricate, manipulate and investigate thin films of MTIs will be detailed, followed by the characterization of MTI films grown by molecular beam epitaxy.

3 Growth and Characterization of Magnetic Topological Insulators

In this chapter, the fabrication and characterization of magnetic topological insulator thin films will be performed. However, it is mandatory to first establish high-quality non-magnetic TI with low charge carrier density and a Fermi level close to the Dirac point in order to lay the foundations for optimal later incorporation of magnetic dopants for MTIs. This optimization will be performed on $(Bi_ySb_{1-y})_2Te_3$ in the next section 3.1. To examine the grown films, structural characterization techniques like X-ray diffractometry, transmission electron microscopy and Rutherford backscattering spectroscopy as well as Hall measurements for transport characterization will be utilized and explained. Examining non-magnetic TI first also helps identifying the differing features when shifting to magnetic TIs.

Magnetic TI material configurations will be investigated thereafter: in section 3.2, magnetically doped MTIs containing Chromium, which was one of the first compounds in which the QAHE was established [53], will be grown and examined. After establishing suitable, structurally high-quality MTI thin films, electronic transport experiments in the form of Hall measurements will be performed to characterize the films further and to identify the quantum anomalous Hall effect promised to arise in thin MTI films. This will first be performed on films with thicknesses above 10 nm, before moving to sub-10 nm films entering into the quasi-2D regime. The investigation of superconductivity and Josephson junctions on the MTI films will then be treated separately in chapter 4.

A second MTI material system in the form of intrinsically magnetic MTI is also explored in the scope of this thesis. Intrinsic MTIs are rather new compounds in the field of TIs employing a specific position of the magnetic atoms in the crystal as opposed to the random distribution in doped MTIs [115]. While the results on the intrinsic MTIs are remarkable, they will not show the same drive toward the QAHE as the Chromium compounds and will hence only feature occasionally to compare with Cr-BST results. Their growth and characterization are therefore shifted to the appendix (see chapter 7.1). There, the intrinsic MTIs will be further separated into Mn-*Bi*-Te (7.1.1) and Mn-*Sb*-Te (7.1.2), both with their own advantages and disadvantages.

3.1 Laying the Foundations for the QAH phase: Optimizing $(Bi_ySb_{1-y})_2Te_3$

To realize the devices needed to investigate the QAH phase and its interaction with superconductivity in this thesis, the necessary thin films of topological insulators need to be of a high crystal quality in order to meet requirements regarding Fermi level positioning, mobility and carrier density magnitude. All thin films evaluated in this thesis are deposited by molecular beam epitaxy (MBE). MBE is a technique of growing thin films in the nano- to micrometer thickness range with high control over thickness and

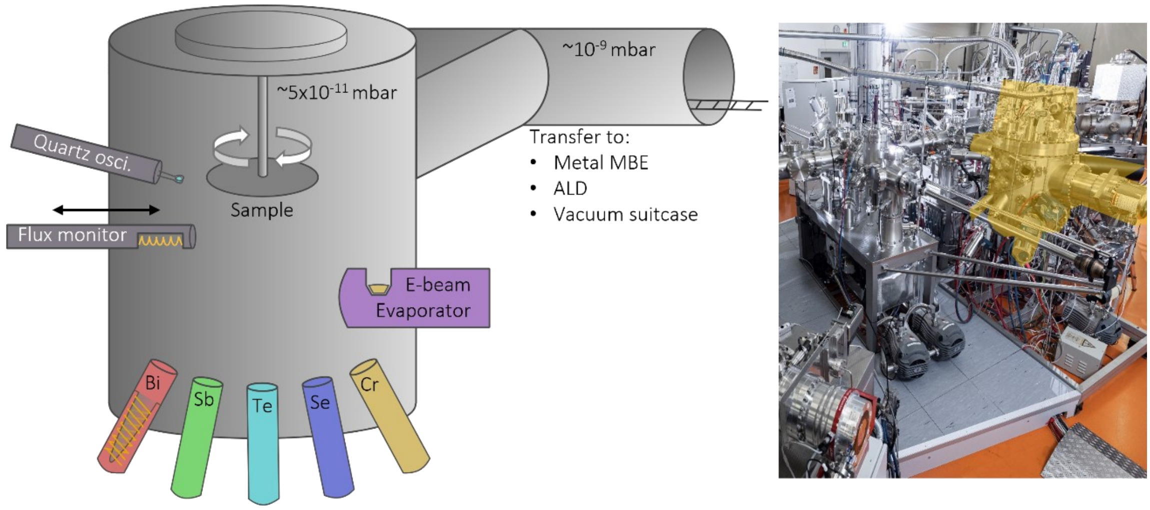

Figure 3.1: Schematic of the MBE chamber setup and its position in the Nanocluster. Two pumps, not depicted, create a vacuum in the 10^{-11} mbar range in the MBE chamber with liquid nitrogen cooled walls. The sample is mounted on a rotatable mount, above which the heating is positioned, heating the samples from the backside. Material sources are positioned on the bottom towards the substrate. In each source a crucible wrapped in heating wires is filled with the respective material. A separate electron beam evaporator can be utilized to deposit high temperature materials. A retractable quartz oscillator and a beam flux monitor can be inserted to measure the material fluxes. The chamber is connected to the transfer system of the Nanocluster, from where samples can be transferred to the load lock, other MBE chambers, an atomic layer deposition system and a vacuum suitcase port for access to other systems.

composition. The general set-up of an MBE chamber is shown in figure 3.1, depicting the ultra-high vacuum (UHV) chamber, effusion cells, substrate holder and other included devices like an electron beam evaporator, a quartz oscillator and a beam flux monitor.

The process of MBE was developed in the late 1950s and relies on evaporation of materials from heated evaporation cells, so called Knudsen cells [116]. The material to be evaporated is stored in crucibles of a temperature resistant material, which is chosen specifically for the evaporation material inside. In this thesis, the used materials are evaporated form boron nitride and stainless-steel crucibles. To reach the necessary temperatures to evaporate the elements, heating wires are coiled around the crucibles, allowing for precise temperature regulation. Two liquid nitrogen cooled MBE systems have been employed in this thesis to fabricate the TI thin films. A stand-alone MBE chamber, in the following called BST-MBE, and a refurbished chamber designed by Dr. Eberl MBE Komponenten GmbH, in the following referred to as M13, as it is the thirteenth module attached to the Helmholtz Nano Facility's (HNF) Nanocluster, which will be detailed later. The latter chamber shown in figure 3.1 was assembled and put into operation as a part of the defined tasks of this dissertation. The BST-MBE contains only standard Knudsen effusion cells for each of the used materials, M13 is equipped with cracker cells for antimony, tellurium and selenium. In cracker cells, the beam of evaporated molecules is funneled through a separately heated region, in which the molecules are "cracked" into smaller molecules or single atoms, influencing the growth mechanisms on the substrate. Each cell is provided with a shutter plate, interrupting the beam if necessary. In the Te and Se cracker cells, the shutter is substituted by an adjustable valve, providing a possibility to seamlessly set the material flow. A quartz oscilloscope and a beam flux monitor can be inserted into the beam lines to measure the growth rate or beam partial pressure of the evaporated material, respectively. In both chambers the materials to fabricate the TI (Antimony, Bismuth, Tellurium and Selenium) are constantly contained in separate effusion cells. The BST-MBE additionally provides slots for Manganese (see chapter 7.1), Aluminum, Tin and Germanium, M13 contains an additional Chromium effusion cell (see chapter 3.2).

In the BST-MBE the pressure is maintained below 10^{-9} mbar, in the M13 an additional cryogenic pump decreases the pressure to levels below 10^{-10} mbar. The mean free path of the evaporated molecules in these UHVs ranges from meters to kilometers, providing a direct and focused beam onto the substrate mounted facing downwards in the middle of the chamber. MBE is a process capable of accommodating a large range of substrates. To understand the choice of substrate in this thesis, first a look at the crystal structure of the TIs has to be taken. The TIs investigated in this thesis are of the tetradymite crystal class, forming rhombohedral crystals with a trigonal symmetry. Distinctly, the TI crystals consisting of Bi, Sb, Te and Se form layers following the composition $Bi_{2-x}Sb_xTe_{3-y}Se_y$, with a stacking of VI-V-VI-V-VI referring to the main group notation of the periodic system. This quintuple layer (QL) stacking is shown in figure 3.2 a). Each QL layer of ~1 nm height is stable in itself but bound only weakly to neighboring QL via van-der-Waals (vdW) forces between the outer group VI elements, which renders the materials easily cleavable, similar to graphene [117]. For MBE growth on a given substrate the vdW-gaps between the QL provide a great benefit, in that they compensate strain given by a lattice mismatch of the TI and substrate crystal lattice parameters. TIs can thus be successfully grown on hexagonal substrates like InP, which is closely lattice matched to Bi_2Se_3, sapphire or $SrTiO_3$ ([118], [119]), but also on the silicon (111) surface, which can exhibit a lattice mismatch up to 17% to the TI materials, as shown in figure 3.2. Though lattice matched substrates promise some suppression of crystal defects, the strain relaxation over the vdW-gaps also enables high quality TI crystal growth on non-matched substrates via this so-called vdW-epitaxy [120]. For this thesis, silicon (111) was chosen as a substrate due to its availability, cleanroom compatibility, established cleanroom processes and the possibility to use differently doped Si to have conductive and non-conductive substrates with similar growth parameter sets. This variability enables electrical transport measurements, requiring insulating substrates, as well as tunneling measurements with the necessity of conductive substrates. In the MBE chambers, the substrate is mounted in a rotatable set-up under a graphite heater with a temperature range between 14°C and 1000°C in the M13 and down to temperatures < 0°C in the BST-MBE chamber.

For materials that require higher vapor pressures and thus evaporation temperatures, the mounted Knudsen cells might not be adequate, as the maximum cell temperature in both chambers is 1500°C. In M13, an electron beam evaporation (EBV) system is therefore additionally employed. In separate crucibles Niobium, Vanadium, Platinum, Palladium, Tungsten and Aluminum oxide are provided. The crucibles are embedded into a movable water-cooled copper block. To heat the material, electrons are extracted from a cathode

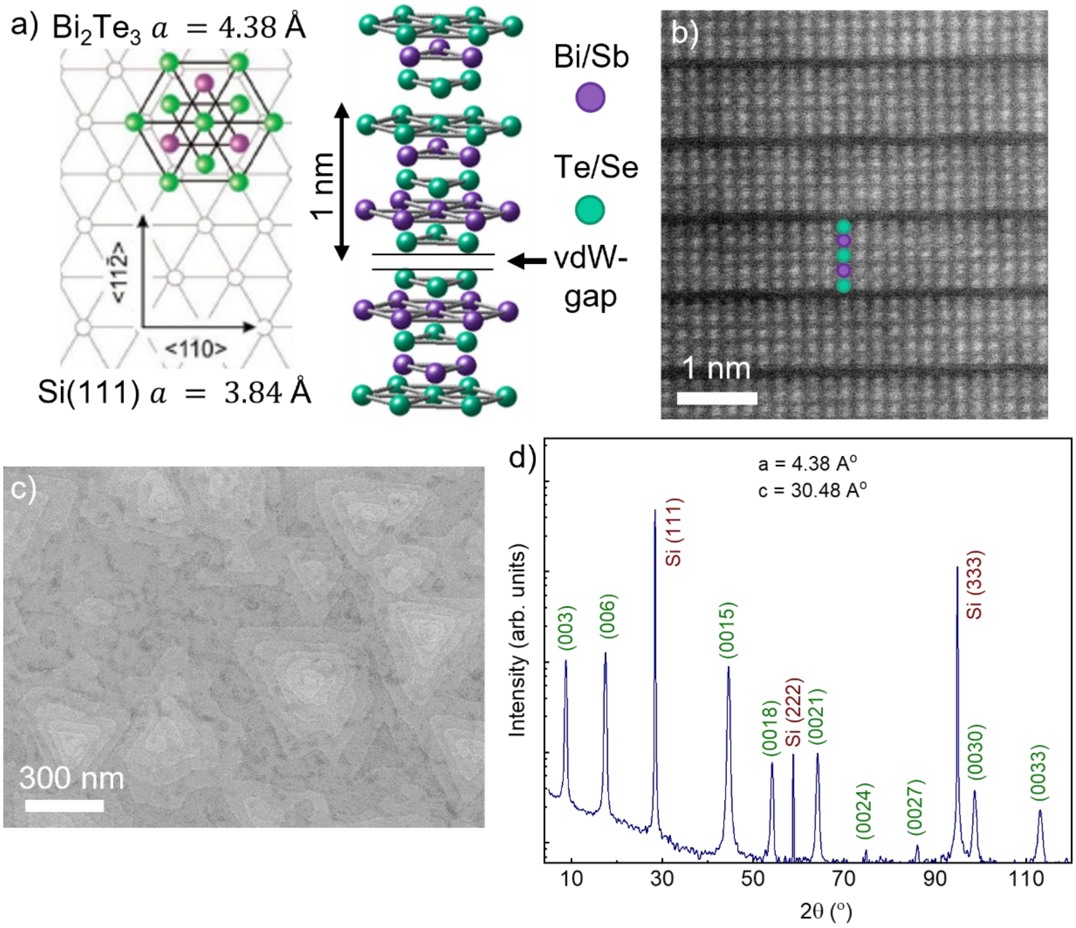

Figure 3.2: TI growth overview. In a) the crystal structure of tetradymite TI grown on a Si (111) surface is shown. The large lattice mismatch is compensated by the vdW gaps, shown in the side view. The QL arrangement and the vdW gaps can also be seen clearly in the bright field transmission electron micrograph in b), $(BiSb)_2Te_3$ in this case. Each QL has a height of ~1 nm, with three QL building one unit cell. In a top view of the grown crystal film illustrated in c), the underlying trigonal crystal structure is clearly discernable, also exhibiting some 180° rotated domains (rotational twins). In d) a X-ray diffractometry curve of Bi_2Te_3 is shown, exhibiting the typical tetradymite TI peaks at (0,0,3n) with n = 0, 1, 2, 3… . Figure a) adapted from [121].

with a voltage of 10kV, focused with magnetic fields and directed onto the evaporation material. At the point of impact, the material is heated depending on the set beam current. Using high currents, Tungsten can be molten locally, therefore providing a minimum achievable temperature of about 3400°C. During this thesis, Niobium and Aluminum oxide will be evaporated via EBV to create superconducting and capping layers, respectively.

The process of creating a TI thin film sample proceeds as follows: First, the substrates need to be cleaned from organic contaminations. Therefore, the samples are inserted for 10 minutes into a Piranha-solution bath consisting of one part 33% H_2O_2 mixed with two parts 96% sulfuric acid. While removing organic contaminations, this process also creates a continuous oxide on the Si surface. To deposit high quality TI thin films, the surface of the Si is required to be pristine, exhibiting no oxides. Hence, after rinsing the sample with deionized water for at least 5 minutes, a 5-minute dip in 1% hydrofluoric (HF) acid is performed, which removes native and other present oxides while additionally passivating the dangling bonds of the silicon, which form during oxide removal, with hydrogen. The hydrogen passivation acts as a semi-stable protection from environmental influences during sample transfer from the HF bath (after a water rinse) into the load lock of the MBE system.

In both chambers, the sample manipulation systems are designed to accommodate sample sizes up to 4” wafers. Smaller samples are inserted into adapters made from Si or Molybdenum, capable of holding up to five substrate pieces in equivalent pockets of the sizes 6x6, 7x7 and 10x10 mm². The chosen sample holder is moved from the load lock into the growth chamber via an UHV transfer system. In the chamber, the substrate is annealed to 700°C for 10 minutes. Thus, the hydrogen passivation is removed, exposing the dangling bonds of the silicon for TI growth. Over a period of minimum 30 minutes, the substrate is cooled to the desired growth temperature T_{sub}, while the cells temperatures are simultaneously set to the required values. These T_{sub} differ strongly between the two MBE chambers, between the desired TI compounds, substrates and the used sample holders, requiring constant monitoring. When all set temperatures are established, TI growth can commence. First, the Te or Se shutter are opened (or both, if the compound so requires) to provide group VI elements to saturate the dangling bonds on the Si surface. The saturated surface forms the initial layer from which the vdW growth can start with an vdW gap, immediately compensating part of the possible strain induced by the substrate-TI lattice mismatch. To counter common antisite defects, where group VI elements lattice positions are occupied by group V elements, increasing the carrier density and thus the conductivity in the technically insulating bulk, the group VI elements can be provided excessively. This is helped by the fact that the 2:3 ratio is highest V:VI ratio viable in the TI phase diagram, thus there is no danger to switch to other stoichiometries [122]. In contrast, higher group V contents create undesired phases. Excess group VI elements are re-evaporated from the sample surface due to the substrate temperature, while the group V elements, requiring higher evaporation temperatures, adhere to the sample and form the tetradymite TI structure. The growth of the TI compounds therefore proceeds in a Te or Se overpressure regime, with beam equivalent pressures (BEP) of ~10^{-6} and $5*10^{-7}$ mbar, respectively. The group V elements, which are provided after a minute of VI surface saturation, are evaporated with BEPs of the order of 10^{-8} up to low 10^{-7} mbar and control the TI growth rates due to their relative scarcity. The BEPs of the evaporants are controlled by their respective effusion cell temperatures, or in the case of the cracker sources by material reservoir and cracker temperatures both.

3.1.1 Characterizing the Crystal Quality of TI Thin Films

On plain Si (111) surfaces, TI crystal island as shown in figure 3.2 c) form via the Volmer-Weber growth mode, growing in width and height and coalescing, thus creating continuous layers of TI thin films. To provide optimal TI quality, structural investigations are performed to identify the crystal structure of the fabricated TI. There are three methods frequently employed for structural investigations in this thesis, scanning electron microscopy (SEM), transmission electron microscopy (TEM) and X-ray diffractometry. Figure 3.2 b) - d) show examples of the three methods, respectively. In SEM, electrons are accelerated onto the sample surface and reflected electrons are collected. Due to the much smaller wavelength of electrons compared to visible light, the minimum resolution is far greater and much smaller structures can be examined, providing magnifications up to 1000000x. In figure 3.2 c), features like step edges and the triangular grain structure of a $(BiSb)_2Te_3$ (BST) thin film can be identified in a SEM micrograph.

3.1.1.1 Transmission Electron Microscopy (TEM)

For internal structural information, TEM provides direct access down to an atomic level as shown in figure 3.2 b). In TEM the samples are not examined from the top, but from the side. To do so, rectangular lamellas with a width of a few hundred nanometers are cut from a sample via focused ion beam (FIB) etching, transferred to an ion mill and further thinned by mild Ar-ion sputtering to create TEM specimen with thicknesses of the order of 10 nm. In the TEM chamber the specimen are exposed to a high voltage electron beam, which penetrates the thin lamellas entirely. Evaluating the energy loss and diffraction that took place during the translation through the specimen, the internal structure of the lamella can be resolved. It has to be taken into account however that the picture depicts an average over the width of the lamella. In regular crystal structures spanning the full lamella width, resolutions on the atomic scale can be achieved, as shown in figure 3.2 b). The QL structure with vdW gaps of the BST TI is clearly discernable. The brightness of the atoms in TEM depends on the weight of the atoms involved. In the dark field mode, the Bi as the heaviest atom appears as the brightest in the TI compound. Due to the similarity in Sb and Te weight only limited statements can be made on the distribution of these elements. If multiple grain orientations are present in the lamella, the atom positions are averaged and the resolution is diminished. The TEM analysis will be applied extensively in chapter 7.1 to evaluate the stacking of quintuple- and septuplelayers in TIs containing Manganese.

3.1.1.2 X-ray Diffractometry (XRD)

An indirect and less invasive method to examine the crystal structure of the grown TI thin films is X-ray diffractometry. The system used for XRD analysis in this thesis is a RIGAKU SmartLab XRD (Ge(220) 2-bounce monochromator). The thin film samples are mounted on a rotatable sample holder and illuminated with X-rays stemming from the $K\alpha$ Bremsstrahlung of electrons that have been accelerated with 9 kV voltage towards an aligned copper block. Incident X-rays on the sample surface interfere constructively when they fulfill the Bragg equation

$$n \cdot \lambda = \frac{2c \cdot \sin(\theta)}{\sqrt{h^2 + k^2 + l^2}}, \qquad 3.I$$

where λ denotes the wavelength of the X-rays, c is the velocity of light, $(h\ k\ l)$ the Miller indices and θ the angle of the X-ray to the sample surface normal. In the scope of this thesis three measurements are frequently performed: X-ray diffraction, X-ray reflection and φ-scans. With X-ray diffraction, the sample is rotated by θ with the detector following along with double the angle, 2θ . The rotation of the plate about 1° leads to a diffraction angle of 2°, which is why XRD measurements are plotted as intensity over 2θ as shown in figure 3.2 d). A peak in the measurement indicates an angle for which the Bragg equation is fulfilled for a given set of $(h\ k\ l)$. In the tetradymite crystal class of the TIs investigated in this thesis with QL layer stacking along the surface normal direction, the peaks in the XRD are given by the Miller indices $(0\ 0\ l)$ where $l = 3n, n \in \mathbb{Z}$, as denoted in figure 3.2 d). Rocking curves can be performed on single XRD peaks to evaluate the thin film quality. The width to height ratio and therefore the full width at half maximum (FWHM) value of a peak is on one hand increased by the measurement time and the film thickness, on the other hand many differently oriented grains lead to a simultaneous widening and shrinking of the peak. Hence, at comparable thicknesses and measurement times the FWHM value gives an indication on the homogeneity of the grown TI thin film. High quality TI with large and homogenous crystal grains exhibit FWHM values below the order of 100 arcsec. X-ray reflection (XRR) covers only the range of 2θ up to 5°, leading to grazing incidence measurements. The X-rays penetrate the sample surface partially and are reflected at interfaces of regions with differing electron density. The path difference of the reflected rays leads to interference and creates an oscillating pattern. The oscillations can be simulated, employing the stacking order, the layer thicknesses, roughness and densities as parameters, providing a non-intrusive way to access these values. Lastly, φ-scans can be performed. For these the angle θ is set to a specific XRD peak, whereafter the sample plate is rotated around the sample's surface normal along φ. Due to the trigonal symmetry of the rhombohedral TI crystals, the XRD peak will arise every 120°. If however twin domains are present in the thin films, which are 180° rotations of the original crystal also compatible with the substrate lattice, peaks in the φ-scan will arise every 60°. A suppression of twin domains is desired, since the domain walls between twin domains lead to an increase in charge carriers in the insulating bulk, decreasing the contribution of the more important TI surface states [123].

3.1.1.3 Stoichiometry evaluation

With the previous methods, the crystal structure and quality can be investigated and evaluated, the stoichiometry of the TI films is however not yet measurable. For the ternary and quaternary tetradymite TI compounds the ratio of Bi:Sb and Te:Se and later the amount of magnetic elements in the MTIs is a crucial factor. While the importance of the correct amount of magnetic atoms in the TI compounds will be explained in the next sections, for ordinary TIs the ratio of Bi:Sb and Te:Se already influences the position of the Fermi level and the position of the Dirac cone in comparison to the bulk bands, respectively. Bi_2Te_3 exhibits frequent Te_{Bi} antisite defects, leading to n-type doping, while Sb_2Te_3 exhibits intrinsic p-type doping by Sb_{Te} [124], [125]. The mixture of both thus can lead to a carrier compensated compound $(Bi_ySb_{1-y})_2Te_3$, where y needs to be carefully chosen and is reported to be $y = 0.06$ or $y = 0.53$ to achieve a Fermi level close to the Dirac point or bulk insulating ternary compounds respectively, depending on the referred source [126], [127], [128]. Similarly, a mixture between Te and Se can be employed to include the advantages of both Bi_2Se_3 and Bi_2Te_3 while mitigating their disadvantages. Bi_2Se_3 provides a very well accessible Dirac point in the band gap center but tends to be n-type due to Se vacancies. These can be filled with the Te in compounds containing both, where the Se helps suppressing the Bi_{Te} antisite defects, the results however remain n-type [120].

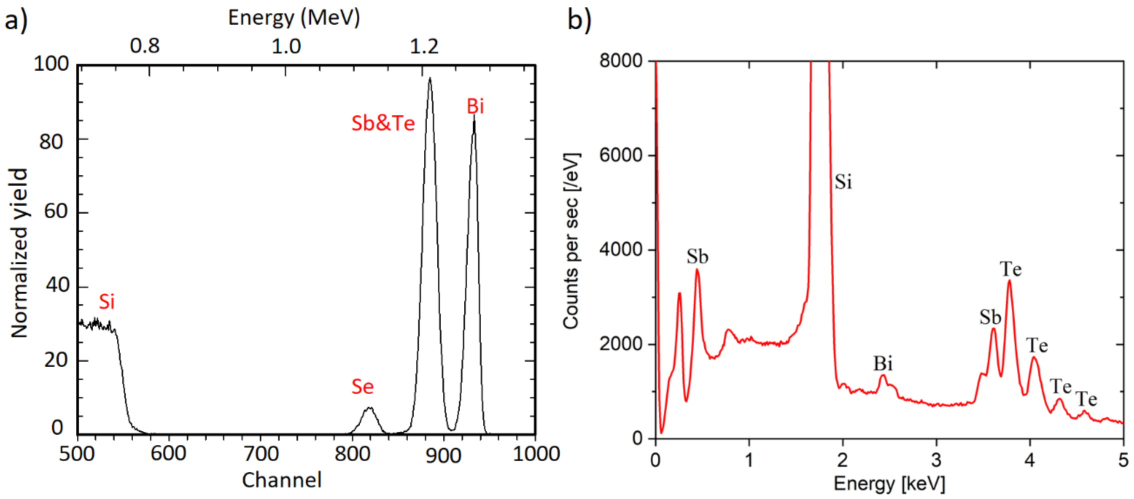

Figure 3.3: Methods to determine the stoichiometry of deposited thin films. a) depicts an RBS measurement, illustrating the characteristic energy loss after backscattering and the respective counts, from which the ratio of elements can be calculated. In EDX (b), the energy spectrum of X-rays originating from electrons filling lower holes in the investigated elements is shown. Each element exhibits specific peaks, the count yield is used to obtain the given stoichiometry.

It is thus mandatory to investigate the films stoichiometry, which in the scope of this thesis will be performed with three methods. Firstly, the different TI compounds exhibits slightly different in-plane lattice parameters of $a = 0.418$ nm for Bi_2Se_3, over Sb_2Te_3 with 0.425 nm to 0.437 nm for Bi_2Te_3, which leads to a shift of the peaks in the XRD pattern of (qua-)ternary compounds [129], [130]. The relation between peak position and compound ratio can be linearly approximated, providing an easily accessible way to investigate the stoichiometry in ternary compounds. For quaternary compounds however the two peak shift components cannot be distinguished, while in Cr MTIs the Cr doping cannot be accessed via this method, as it does not noticeably influence the lattice parameters. Moreover, thick and high-quality films are needed to provide clear and narrow XRD peaks to diminish the measurement error. This method however plays an important role in Manganese containing MTI (see appendix section 7.1).

In figure 3.3, the more direct methods to determine the stoichiometry are depicted. Figure 3.3 a) shows a Rutherford backscattering spectroscopy (RBS) graph for a quaternary BiSbTeSe compound, in which peaks at distinct energy levels can be attributed to specific elements [131]. In RBS, He ions are fired onto a thin film surface, leading to elastic scattering of the incoming ions. The energy loss factor k due to the scattering process can be calculated via

$$k = \left(\frac{m_1 \cos(\theta) \pm \sqrt{m_2^2 - m_1^2 \sin^2(\theta)}}{m_1 + m_2} \right), \qquad 3.II$$

where m_1 and m_2 are the masses of the accelerated ion and target atom, respectively, and θ is the scattering angle. The latter is set to approximately 180° (backscattering) to provide the highest energy losses and thus greatest resolution. The mass of the investigated atom can hence be connected to the measured peak by inserting the measured k and known m_1. The yield for a specific element can be extracted by integrating over a given peak resulting in an atom density, which is then set into relation with other incorporated materials' densities to directly reflect the stoichiometry of the investigated film.

A result of the third method of determining the thin film stoichiometry is shown in figure 3.3 b). The depicted spectrum was created via energy dispersive X-ray spectroscopy (EDX). This technique utilizes the electromagnetic emission spectrum unique to every element. Similar to SEM and TEM, a focused beam of electrons is applied to the sample surface. The electrons can excite an electron on the inner shells of the target atoms, which can thereby exit its position, leaving a vacancy on a lower shell. This vacancy will be quickly filled by an electron from a higher shell, emitting the surplus energy as a characteristic radiation in the X-ray regime assigned to an atom as shown in figure 3.3 b). The stoichiometry of the investigated film is then identified similar to the process in RBS by comparing the relative yield of each element.

3.1.2 Identifying a Suitable BiSbTe Candidate for Magnetic Doping

The previous methods are used to structurally and chemically investigate the fabricated TI thin films. To make definite statements about the quality of the TI thin film, electrical transport measurements need to be undertaken to identify the charge carrier density, mobility and Fermi level position, which are important values to find the ideal TI-composition basis for the later incorporation of magnetic doping. Furthermore, the magnetic response of the MTIs fabricated in the next sections will be investigated similarly to evaluate the progress towards achieving a QAH state. A standard measurement to reveal the described properties is the Hall measurement utilizing a Hall bar device set up. The Hall bar fabrication and device layout are given in the appendix (chapter 7.2) as well as in figure 7.12. A gate electrode covering the TI Hall bar can be used to induce an electric field into the TI stripe, supplying or depleting the stripe of charge carriers to alter the Fermi level in the device. The Hall measurement itself is performed by applying a current between electrodes at opposite ends of a TI stripe while simultaneously sweeping a magnetic field B_z perpendicular to the device plane. Thus, a Lorentz force $F_{L,y} = -q \cdot v_x \cdot B_z$ acts on the charge carriers q travelling with a velocity v_x in the bar, accumulating carriers at one side of the Hall bar with width d and thickness b. This creates an internal, capacitor-like in-plane electric field with a specific voltage, the Hall voltage $U_H = {}^{F_L}\!/_{q} \cdot d$. U_H is connected over the current $I = nqbd \cdot v_x$, with n, the 3D charge carrier density, to the Hall resistance R_H given by

$$R_H = R_{xy} = \frac{U_H}{I} = -\frac{1}{q \cdot n_{2D}} B_z. \qquad 3.III$$

The sign of the slope of R_H is given by the type of charge carrier involved, enabling a differentiation between electron- and hole-type carriers. Therein the assumption

$n_{3D} \cdot b = n_{2D}$ is made, which is provided by the b = 1 nm thick layers of the present TI materials, yielding an n_{2D} for each quintuple layer [128].

Employing the characterization methods detailed in the last paragraphs, multiple optimization cycles were performed to create a structurally and chemically favorable $(Bi_ySb_{1-y})_2Te_3$ TI compound. A suitable candidate for magnetic doping should exhibit high mobility, low carrier concentration and a Fermi level close to the charge neutrality point, to facilitate gate tuning between the carrier types. These features will help decrease the risk of bulk contributions overshadowing the QAHE. However, the inclusion of, for example, Chromium doping will again influence the Fermi level, which needs to be considered later.

The result is a Hall bar device made from $Bi_{0.55}Sb_{1.45}Te_3$ with a thickness of 6 nm and a width of 10 µm, covered with Al_2O_3 capping. The thin film is grown with a rate of 0.27 nm/min and by applying molecular fluxes of Bi:Sb:Te of the ratio 1:3:42, ensuring Te overpressure. It is inserted into a variable temperature insert cryostat (VTI), where the sample in the chip carrier can be cooled to 1.2 K while applying magnetic fields up to 14 T. The Hall measurements are shown in figure 3.4. Firstly, in a) and b), the longitudinal resistance R_{xx} and the Hall resistance R_{xy} are depicted, respectively, when applying a fixed AC current of 1 µA along the bar and sweeping the out-of-plane magnetic field B_z from -13 to 13 T while applying gate voltages from -10 to +10 V. For non-magnetic compounds, the Hall resistance is expected to follow a linear behavior as shown in equation 3.III. Due to possible contact electrode misalignments and crystal defects in the TI thin film, the Hall slope, antisymmetric around the origin, can exhibit symmetric features. These stem from a mixture with the symmetric longitudinal resistance. The Hall resistance can however be symmetrized and from a fit to the slope the charge carrier density can be extracted.

The longitudinal signal exhibits a dip in resistance towards 0 T, which is a common feature in TIs and stems from the weak antilocalization effect (WAL). WAL describes a quantum mechanical effect that affects electrons encircling closed loops in the presence of a magnetic field. If an electron scatters in a way that a closed loop is formed, while the loop circumference is smaller than the phase coherence length l_φ of the electrons in the material, the electron particle wave will interfere with itself. In weak localization (WL), the interference is constructive, leading to an enhanced resistance at zero magnetic field. If a magnetic field is applied, an additional phase is added during a loop depending on its size, inhibiting the constructive interference and thus leading to an averaging out of the additional resistance. In WAL the spin momentum locking of the electrons in the TI surface states needs to be considered. During a loop, the spin is forced to rotate by 2π for the anti- and the clockwise path through the loop simultaneously, resulting in destructive interference in respect to the 4π periodicity of the fermionic wave function. WAL manifests itself as a dip in resistance at zero magnetic field, which is corrected by applying a magnetic field threading the electron loops [30]. As shown in figure 3.4 a), the Hall bar exhibits pronounced WAL. The overall resistance of the longitudinal signal decreases with increasing gate voltages due to the increase of charge carriers at higher electric fields as

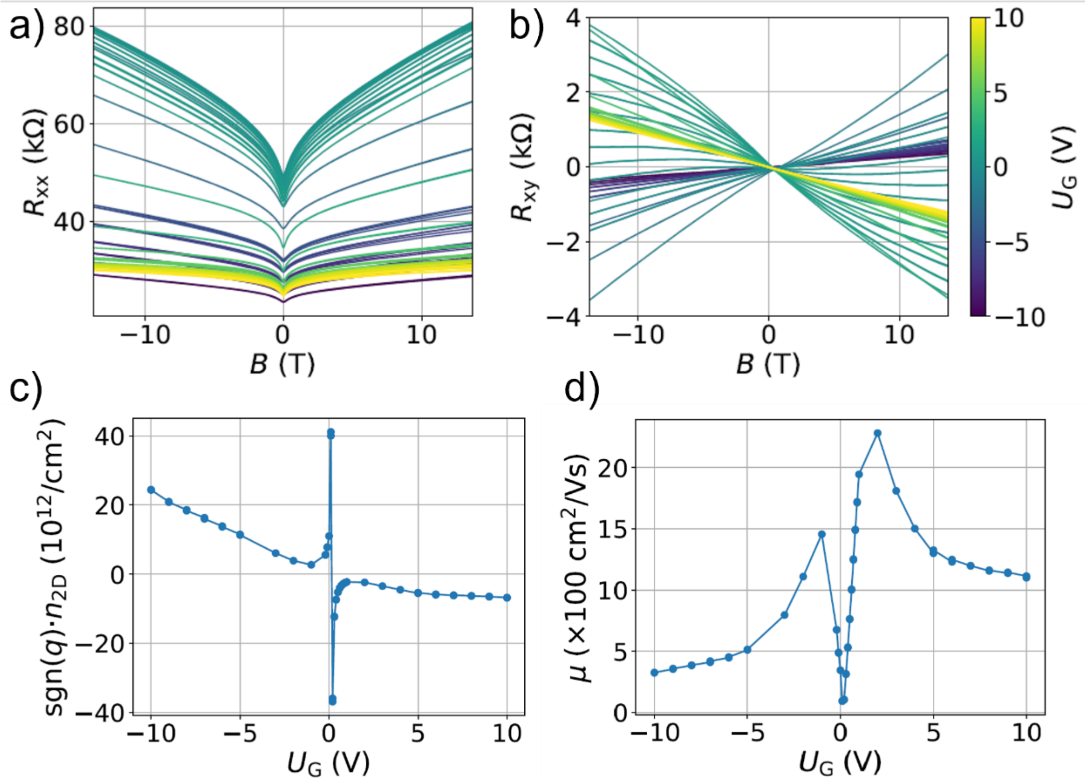

Figure 3.4: Hall measurements performed on a 6 nm thin $Bi_{0.55}Sb_{1.45}Te_3$ Hall bar capped with Al_2O_3 and covered with 15 nm HfO_2 and a gate. a) and b) show the magnetic field dependent longitudinal and Hall resistance when sweeping the gate voltage from -10 to +10 V. The Hall slope in b) changes sign, indicating a shift through the full gap, thus changing the carrier type. The change of slope is however not monotonous, caused by a competing influence of p- and n-type carriers in the semiconductor-like material. Calculating the charge carrier density n_{2D} from the Hall slope in c) shows the main carrier change by the sign change. The switch occurs very close to $U_G = 0$ V, putting the Fermi level very close to the Dirac point. The increase of carriers towards higher $|U_G|$ also explains the decrease in R_{xx} in a), as more carriers lead to lower longitudinal resistance. With R_{xx} and n_{2D} the mobility is calculated, resulting in a record mobility of 2300 cm²/Vs. Measurements taken by Justus Teller.

given in c). The charge carrier type can be extracted from the Hall slope, as q is $\pm e$ in 3.III depending on the carrier type. In figure 3.4 b) a change of sign of the slope is clearly visible. The slope however does not monotonously in- or decrease with the gate voltage, pointing towards a participation of p- as well as n-type carriers. This is usual for semiconductor-like materials, but unusual for metals, for which the Hall equation was derived. Therefore, the equation for the Hall resistance in 3.III must be adjusted. As was shown by Smith *et al.* [132], if both types of carriers are present, both need to be represented in the Hall resistivity, which additionally explains the non-linearity of the Hall slopes in figure 3.4 a). The adjusted equation is

$$R_H = \frac{B}{e} \cdot \frac{(p - nb^2) + b^2 \mu_p^2 B^2 (p - n)}{(p + nb)^2 + b^2 \mu_p^2 B^2 (p - n)^2}, \qquad 3.IV$$

where p (n) denotes the hole (electron) concentration, $b = \mu_n / \mu_p$ and $\mu_{p/n}$ the hole/electron mobility. The shift of slope can be explained by a change in dominant carriers dependent on gate voltage. For a more detailed explanation of these findings the reader is directed to the Master's thesis of Justus Teller [133].

In figure 3.4 c) the 2D charge carrier density is plotted against the gate voltage. The sign of the density references the type of majority carrier, with negative values indicating electrons and positive values indicating holes. Close to $U_g = 0\,V$, the sign switches, indicating a change of majority carriers. In the Hall data, this point is reached when the slope is 0. The low charge carrier density of $\sim 10^{12} \cdot 1/cm^2$ and the change of majority carriers at almost $U_g = 0\,V$ indicate that the TI's Fermi level is in the gap and close to the charge neutrality point (CNP) without much gating [54], as desired for the later magnetic doping. This contrasts with measurements from literature however, which measured the charge neutrality point to be at distinctly different stoichiometries [127], [128], [134]. The investigated film shown here is however unusually thin, close to the hybridization limit [135], which will also be the case for the MTI films of the following chapters. Thereby, almost no bulk is present, suppressing the probability of antisite defects and the number of bulk carriers in total, giving more dominance to the surface. The Hall mobility of the given sample is shown in figure 3.4 d). The standard approach to calculating the mobility in Hall measurements does not apply to the present majority carrier switching case, leading to a dip at $U_g = 0$ V due to the jump in n_{2D}. While close to $U_g = 0$ V the values could reach even higher considering the real n_{2D}, the exhibited values of up to $2300\,\frac{cm^2}{Vs}$ already set a record mobility in our institute and are attributable to the sample's high crystal quality and low thickness, thereby suppressed bulk contribution. The difference in mobility between positive and negative gate voltages can be attributed to the difference in Fermi velocity above and below the Dirac point [136]. Depending on the position of the Dirac point in the band gap, the valence bands can be situated closely, meaning gating can lead to the Fermi level intersecting bulk states one-sidedly, leading to asymmetric mobility [137].

In this section, the general process of growing TIs and the methods involved have been discussed. This includes the structural internal evaluation, as well as the characterization of the electronic features of the TI thin film. The result is a non-magnetic BST TI with a record mobility and low charge carrier density as well as a Fermi level in the gap close to the CNP, giving an optimal starting point to fulfill one of the aims of this thesis, to combine TI thin films with magnetic dopants. How and which magnetic TIs will be created, resulting in the first fabrication of a QAHI in Jülich, will be discussed in detail in the following subchapters, building up on the results given in the last paragraphs.

3.2 Magnetization via Chromium Incorporation

There are three main routes to integrate magnetic interaction into topological insulator materials. They are magnetic doping, induction of magnetism by proximation and the newest route, intrinsic magnetic TIs [50], [115]. During this thesis, the first and last approach are studied in detail, the proximation will only be treated in special cases. This chapter will illustrate how chromium was used to achieve the first magnetic TIs in the Research Center Jülich, what measures were taken to approach the QAH limit and lastly how a QAHI film was established by extensive Hall measurements. The first part of this chapter was acquired together with Max Vaßen-Carl in the scope of his master's thesis, in which we established the initial growth of Cr doped TIs.

Incorporating Cr as a highly concentrated dopant into $(Bi,Sb)_2Te_3$ TIs was the first approach to realize magnetic TIs in the tetradymite crystal class and also the basis for the first QAHI by Chang *et al.* in 2013 [53], [138]. Not much later, also Vanadium and Manganese were introduced as magnetic dopants [139], [140], [141]. While QAH was also found in V-$(Bi,Sb)_2Te_3$, no anomalous Hall phase could be detected in the Manganese-doped compounds. It took until the discovery of the intrinsic magnetic TIs with Mn to realize the QAH in these compounds (see chapter 7.1).

In order to establish the QAHI in Jülich, the Cr-MTI system was chosen, as it is considered to be the relatively easiest to establish, compared to the V QAHI compounds, which are known to be difficult to fabricate in MBE, due to the fact that VTe_2 is easily formed, suppressing the QAHI phase. When doping TIs with magnetic material, two factors need to be considered, the amount of Cr in the compound and the ratio of Bi to Sb, where both factors also rely on each other. The amount of Cr influences the magnetic characteristics, while the Bi:Sb ratio determines the position of the Fermi level, also in respect to influences of the Cr doping. Literature gives a large scope of stoichiometries to realize the QAHI in $Cr_x(Bi_ySb_{1-y})_{2-x}Te_3$ (CBST) systems, ranging from (x, y) = (0.15, 0.1) [53] to (0.27, 0.43) [142]. Most literature recommends a Cr level of about $x = 0.2$, with a ratio of Bi at about $y = 0.2$ to 0.25 to have a strong magnetic response while maintaining charge neutrality by the Bi:Sb ratio [52]. The results of the previous chapter showed that a somewhat higher Bi ratio of about $y = 0.275$ provided a BST film with optimal qualities. Therefore, combining our results with literature, the (0.2, 0.25) ratio was chosen to realize the QAHI in Jülich.

To grow the desired CBST compounds, the growth recipe illustrated in the previous chapter is adjusted to account for the desired Bi:Sb ratio. The incorporation of Cr is performed by providing a Cr flux during the TI growth at a cell temperature of about $T_{Cr} =$ 1030-1050°C, depending on the desired Cr amount. Since the Cr tends to collect material from the chamber vacuum and binds it to the chamber walls because of its high vapor pressure (gettering), flux measurements with the beam flux monitor were not successful. Instead of an increase in partial pressure indicating the molecular flux, the flux decreased, inhibiting the measurement of the Cr flux itself [143]. The films are grown on highly resistive Si (111) chips as done in the previous section. Although an additional element with a high sticking coefficient evaporated at comparably high temperatures is introduced for the TI growth, it is not necessary to change the substrate temperature from the optimal temperature of ordinary TIs. For the growth of plain CBST films on the highly ohmic Si a substrate temperature of 225°C provided the films of the highest achieved quality, compared to 215-225°C for regular TIs. Similar to the growth of non-magnetic TIs, first Te is evaporated onto the substrate to saturate the dangling bonds, before supplying the other elements. For

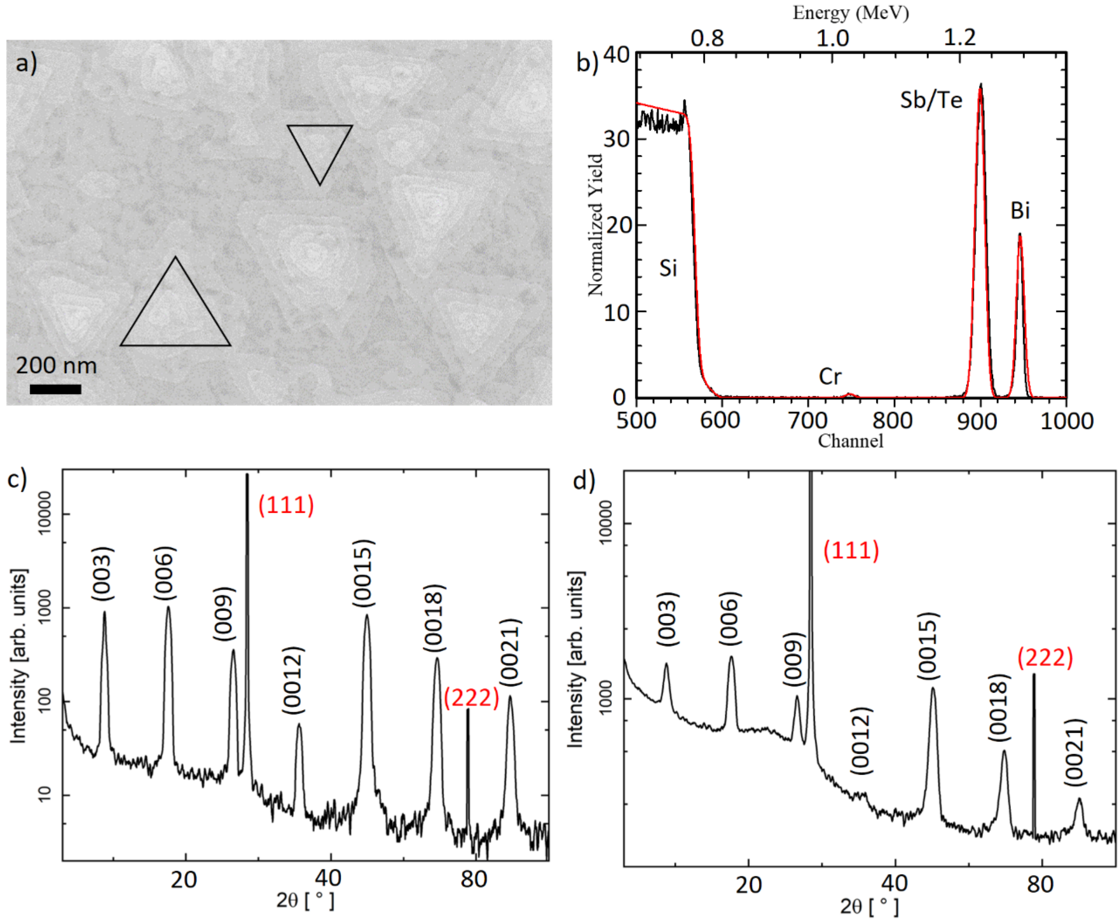

Figure 3.5: Characterization of deposited CBST thin films. In a) the SEM micrograph reveals the triangular structure of the deposited crystals, also showing rotated twin domains. To evaluate the stoichiometry, RBS is performed and a layer-stack profile fitted to the data (red), yielding the stoichiometry. Information about the crystal structure is obtained via XRD, exhibiting the tetradymite crystal peaks (0 0 3n). Thicker films (80 nm, c)) yield more prominent peaks, however later thinner films (21 nm, d) will be needed for QAHI investigations.

the growth of CBST, this is done for 30 seconds after the substrate has cooled down from 700°C annealing temperature to the growth temperature after 30 to 40 minutes, before Bi is supplied for another 1-2 minutes. Sb and Cr are provided directly thereafter.

An SEM micrograph of the resulting thin films is shown in figure 3.5 a), showing the triangular crystallite structure known from the tetradymite crystal class. The presence of twin domains is clearly visible by the two triangular islands facing opposite directions. The suppression of one of these domains might be possible by going to extremely low growth rates, this was however not examined in the scope of this thesis [123]. That Cr is incorporated into the otherwise seemingly ordinary TI thin film is verified by RBS measurements as shown in figure 3.5 b). The discernable peak of the Cr mass can be integrated as explained in the previous section, yielding the concentration of Cr in the thin film. This method is employed for most MTI films investigated in this thesis. In EDX the low signals from the minute magnetic compound concentrations in the thin films are overshadowed by noise or the other elements' characteristic peaks.

The Cr doping does not change the overall crystal structure, which can be extracted from the XRD measurements in figure 3.5 c) and d), which show XRD data for two films of different thickness, 80 nm for c) and 21 nm for d), and stoichiometries, (0.33, 0.57) and (0.19, 0.54), respectively. Thicker films provide more signal in XRD, leading to higher intensity peaks in XRD at the same measurement time. The XRD peaks follow the (0 0 3n) pattern of the tetradymite crystals, however the inclusion of Cr in the ternary TI compound leads to a decrease of the lattice parameter c along the out-of-plane z-axis as shown by Zhou *et al.* [144]. The different Cr concentrations do not differ greatly between each other in c (30.15 Å for c) and 30.17 Å for d)), but greatly from comparable samples with no Cr. For (0, 0.2) BST c = 30.28 Å [145], while for pure Sb_2Te_3 and Bi_2Te_3 only larger lattice parameters are reported. Thus, the Cr contracts the QL to give smaller unit cells in z axis direction.

The position of the Cr in the lattice is difficult to determine. While clusters of pure Cr or Cr_xTe_y could form additionally incorporated into the vdW layer structure, the Cr can also be a substituent of Sb or Bi in the QL or it may accumulate in the vdW gaps. The latter is unlikely, since this would potentially lead to wider vdW gaps and larger c, contradicting the measured values. Substitution and Cr_xTe_y are thus more likely. The former is the best configuration to provide a homogenous magnetization in the film and is aspired. Any interlayer or cluster would consist of a non-topological material, creating an interface in the material with perturbing Dirac states. In contrast to clusters or interlayers, the substitution would result in XRD patterns following those of the ordinary TI, which is what is observed in the films even for high Cr concentrations as in figure 3.5 c). When adding Cr to the BST crystal, the ratio of the Bi:Sb changes in that the amount of Bi increases slightly in comparison to Sb at constant material fluxes. This suggests that both elements are substituted, however Sb is substituted more than Bi in the QL structure.

At high Cr concentrations as in figure 3.5 c), a slightly broadened (006) peak can be observed in some samples, which might point towards the existence of a Cr_xTe_y layer. To investigate this feature, high angle annular dark-field (HAADF) TEM measurements are performed by Jin-Hee Bae of PGI-9 to check the sample for large-scale Cr clusters or interlayers. As shown in figure 3.6 a) and b), the QL structure of the MTI can be clearly resolved and resolutions down to the atomistic level are possible. The vdW gaps, the Si substrate on the bottom and a Pt protective layer on the top are easily discernable, without any signs of non-QL interlayers or large Cr clusters. However, since TEM is only a very locally resolved measurement and contaminations with a low density might just be overlooked, investigations utilizing a Superconducting Quantum Interferometry Device (SQUID) are also performed. CBST is a ferromagnetic material, Cr_xTe_y and pure Cr form anti-ferromagnetic compounds, which should therefore be well distinguishable in the SQUID, a measurement system highly sensitive to magnetic moments in thin films. SQUID measurement results were however not convincing, slightly indicating ferromagnetism, but being overshadowed by substrate paramagnetic effects and thus yielding Curie temperatures not assignable to any sole compound and far from literature values (see figure 7.17 in the appendix). In the following sections T_{Curie} values closer to those expected from literature will be extracted from Hall measurements.

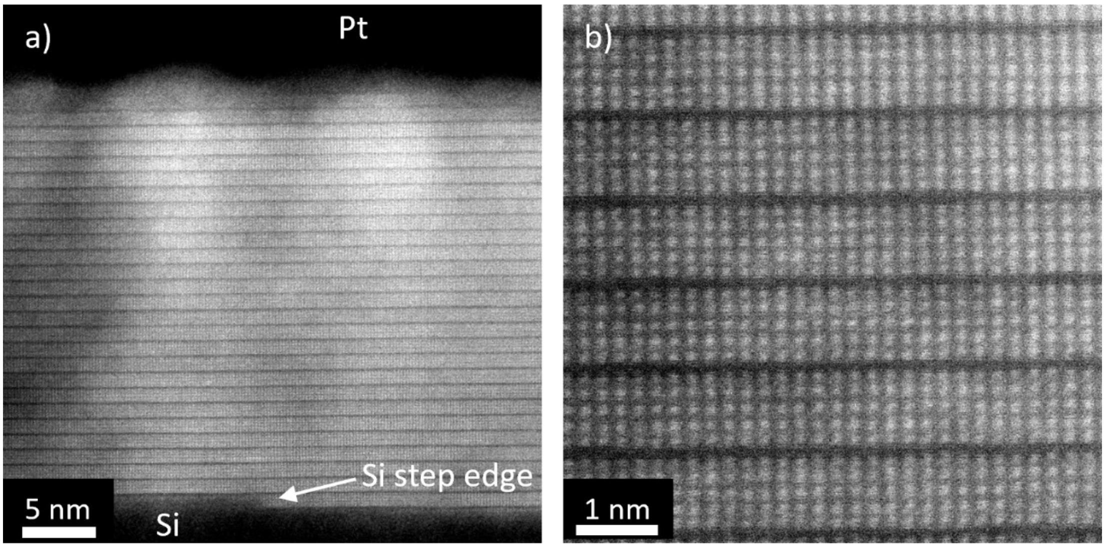

Figure 3.6: HAADF TEM investigation of $Cr_{0.16}(Bi_{0.1}Sb_{0.82})_2Te_3$ *layers. In a) the full film is depicted, showing the layered structure and the vdW gaps of the TI compound. A step edge in the Si and the continued growth of the TI over this edge can also be observed. b) shows a zoom in onto the atomistic level, revealing the atomic order in the crystal. Due to the direction of lamella preparation in respect to the TI crystal not possible rotational twin domains can be distinguished. However overall, no trilayered* Cr_xTe_y *or pure Cr clusters can be identified in this sample.*

3.2.1 Investigating the Magnetism in Hall Devices

SQUID investigations suggested that a magnetization is present, but no clear evidence for or against antiferromagnetic (aFM) phases is discernable. To clear up the ambiguous results of the SQUID measurements, the magnetic response of the CBST MTI thin films is next investigated in Hall measurements. Since the applications of the MTIs in future experiments rely on electrical transport investigations, the examination of the magnetic response via Hall measurements is closer to the realistic experiments following after the realization of the QAHI. Similar to the investigations in the previous section, Hall devices are structured from plain MTI thin films via optical resist and RIE processes. An Al_2O_3 capping is provided to protect the surface states as was done with the regular TI thin films.

First measurements were conducted on films of $Cr_x(Bi_ySb_{1-y})_{2-x}Te_3$ with (x, y) = (0.1, 0.2) and a thickness of 11 nm determined via XRR. The low Cr content was chosen to avoid the formation of aFM phases while also testing the strength of the magnetic response and coercive field. The measurements were performed together with Erik Zimmermann and Alina Rupp in the VTI cryostat of Prof. Thomas Schäpers at PGI-9. As shown in figure 3.7, a clear ferromagnetic hysteresis loop is formed when decreasing the temperature below 30 K. The loop forms due to the collective switching of the film's magnetization when the externally applied field is higher than the internal coercive field of the MTI, forcing a magnetization flip. In a R_{xy} measurement of a MTI film, the hysteresis stemming from the anomalous Hall effect is combined with the Hall slope of the ordinary Hall effect. The shown data was anti-symmetrized via a fast Fourier transformation to filter out longitudinal

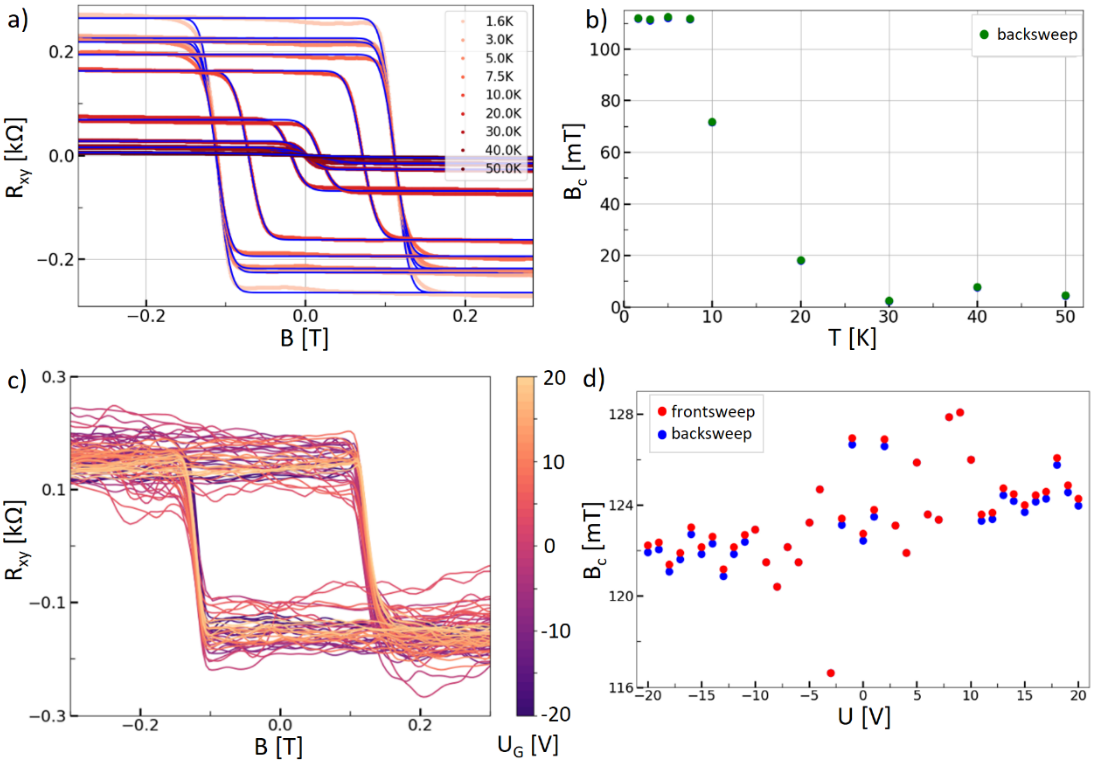

Figure 3.7: Hall measurements of a CBST Hall bar and evolution of the coercive field with temperature and top gate voltage. a) exhibits the formation of a ferromagnetic hysteresis when cooling the sample below 30 K. The slope of the Hall resistance has been subtracted from the data. The width of the hysteresis, the coercive field B_c *is given in b), extracted from the blue lined fits in a). Fitting performed according to* [146]*. The Curie temperature is thus estimated to lie between 20K and 30K. Gating a comparable Hall sample at the base temperature of 1.4 K shows only little influence on the height of the hysteresis (c) or on the coercive field (d), suggesting a carrier independent magnetism arbitrated by the Van-Vleck mechanism.*

signals and the Hall slope of the ordinary Hall effect was corrected to put emphasis solely on the hysteresis behavior. Only below the Curie temperature, the long-range ordering temperature of a ferromagnet, can such a behavior be observed. The Curie temperature is thus estimated to lie between 20 and 30 K, close to the literature values [51], [53]. An antiferromagnetic hysteresis curve would exhibit multiple steps in the magnetization flip, one according to each flipping domain or layer in the antiferromagnetic compound, which cannot be observed in figure 3.7 [147], [148].

The width of the hysteresis, and therefore the coercive field, is fitted, shown in blue in figure 3.7 a), and the evolution with temperature is shown in figure 3.7 b). Information on the fitting procedure can be found in [146], where samples fabricated in the scope of this thesis were used to establish the hysteresis fitting procedure. The field saturates at about 110 mT, which is in good accordance with literature values measured on similar MTI thin films [53], [54], [149]. B-field sweeps to higher magnetic fields of 14 T allow for fitting a slope to the high field ordinary Hall signal without influences of the AHE hysteresis around zero magnetic field. The fits provide a charge carrier density of $n_{2D} = 6.7 \cdot 10^{13} \mathrm{cm}^{-2}$ and a mobility of $\mu = 71.3\ \mathrm{cm}^2/\mathrm{Vs}$. The charge carrier density is an order of magnitude higher than values recorded on other (QAH) CBST systems, suggesting a Fermi level position closer to the valence or conduction band than the Dirac point. The mobility is within the expected order of magnitude, slightly lower than comparable literature values.

The most important feature when examining the MTI Hall hysteresis is the height of the AHE amplitude, the deviation from $R_{xy} = 0\ \Omega$ at $B_{ext} = 0$ T. For a QAHI, this value is expected to quantize to $R_{xy} = {}^{h}/_{e^2} = 25.812\ k\Omega$, the von-Klitzing constant, while the longitudinal resistance R_{xx} in a perfectly quantized case approaches 0 Ω. At the lowest measured temperature of $1.6\ K$, R_{xy} reaches only about $0.26\ k\Omega$, showing no quantization or QAH phase was realized in this CBST sample. Since the examined film exhibits a thickness of 11 nm and a relatively low Cr content, the QAH was also not expected to arise in this sample. For the QAH phase, a thickness of less than 10 nm is required to minimize the perturbing bulk contribution and enter a quasi-2D regime [150]. Film thicknesses below 6 nm also inhibit a robust QAHE [150], [151]. The measurements however reveal that long range magnetic order is present in the films and no indications of aFM order are found. A comparable second Hall bar with a gate is used to inspect the AHE and the coercive field when depleting or increasing the charge carrier density via gating. The evolution of the hysteresis is shown in figure 3.7 c), with the coercive field of the up (red) and down (blue) field sweep shown in figure 3.7 d). Over a range of $U_G = -20$ to 20 V, B_c remains largely constant, deviating only slightly at low gate voltages, however only by $3 - 4$ mT, with the average at $B_c = 123$ mT. This small deviation suggest that the magnetism is not largely influenced by the amount of free charge carriers, which would mediate the magnetism in the RKKY interaction. Thus, the magnetism in the samples is dominantly arbitrated by the Van Vleck mechanism, which, as explained in chapter 2.1.2, provides magnetism without the necessity of free carriers overshadowing the QAHI.

3.2.2 Sub-10 nm Films to Approach the 2D Regime

	Lower Cr	Medium Cr	High Cr	Sandwich
Thickness [nm]	6.14±0.12	6.42±0.51	6.13±0.19	7 (nominally)
Stoichiometry	(0.15, 0.29)	(0.21, 0.29)	(0.24, 0.3)	-

Tab 3.1: Thickness and stoichiometry of the thin CBST films used for QAHI Hall device investigations. The Cr content in the sandwich sample is that of the medium compound, however only in the CBST layers at the top and bottom.(X,Y) relates to $Cr_x(Bi_ySb_{1-y})_{2-x}Te_3$.

With ferromagnetic order on the basis of the Van Vleck mechanism established, Hall bar (HB) devices with film thicknesses below 10 nm are prepared to decrease the influence of bulk contributions, approach the 2D regime and investigate the QAHE. Four cases are studied, CBST thin films with a lower, medium and higher Cr (lowCr, medCr and hiCr) content, while maintaining constant Bi:Sb flux ratio during growth, and lastly a sandwich structure. In the latter, the Cr flux of the medium sample is provided for the first 2 QL of thin film, followed by undoped BST for 4 nm, concluding with another 2 nm of CBST

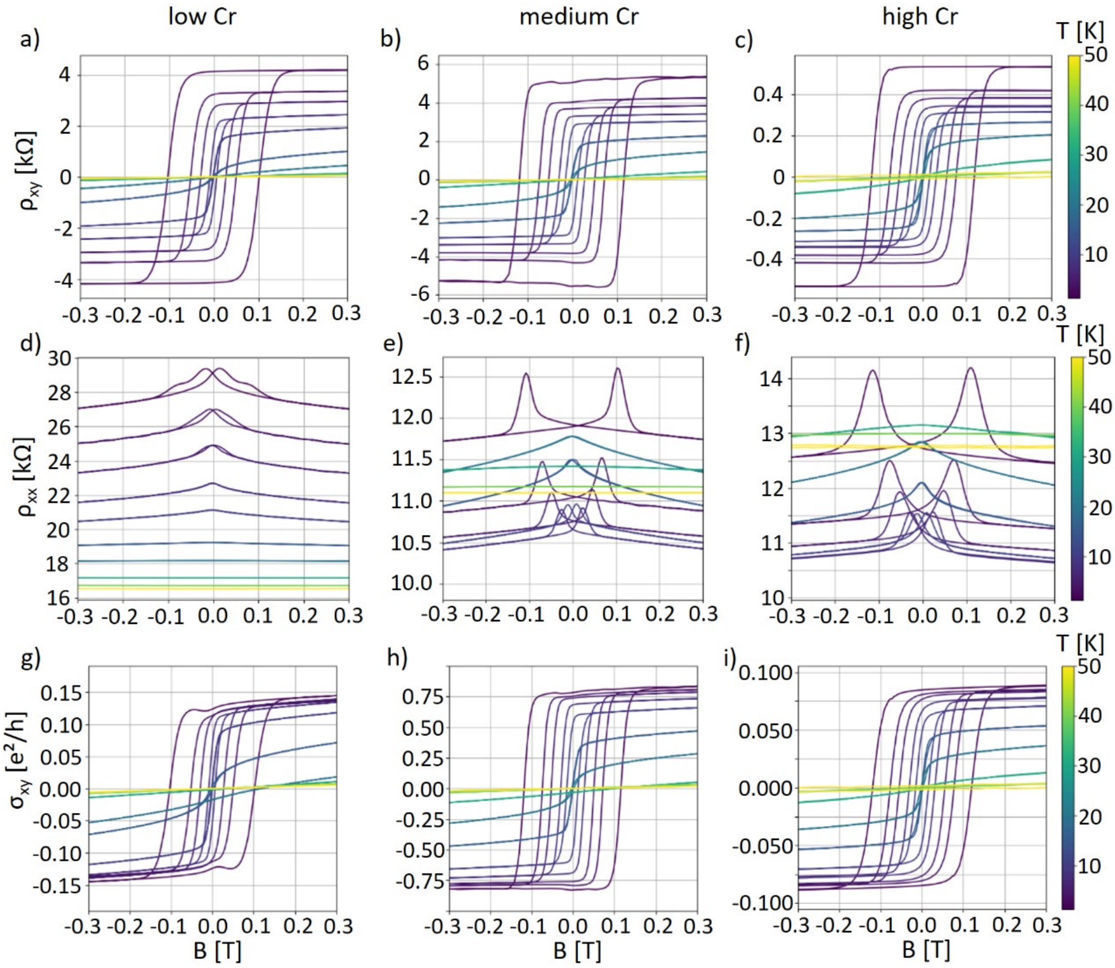

Figure 3.8: Hall characterization of the devices made from the CBST MTI thin films. Stoichiometries are given in table 3.1, increasing Cr content from left to right. a)-c) show temperature dependent Hall sheet resistivity ρ_{xy}*, exhibiting the hysteresis of the AHE, d)-f) depict longitudinal resistivity. The weak localization peaks are shifted, respective to the net zero magnetic field value. g)-i) exhibit the sheet conductivity* σ_{xy}*, calculated via equation 3.V in units of the conductance quantum* e^2/h*. For the medium Cr device, the conductivity approaches the desired value of* $1\,e^2/h$ *for negative gate voltages.*

before applying a Al_2O_3 capping via electron beam evaporation. Sandwich structures have been shown to consistently exhibit the QAHE over a wide range of gating [54].

The lowCr, medCr and hiCr film's stoichiometries measured via RBS are given in table 3.1 with the corresponding thicknesses. The plain MTI films show great reproducibility in film quality and thickness, with an easily adjustable Cr content via temperature variation of the Cr effusion cell. The according temperatures are 1037°C, 1045°C and 1050°C, respectively. The flux ratio of Bi:Sb:Te is readjusted to the values established in section 3.1.2, which is 1:3:42, which yields y = 0.27. The slight preference of Cr to substitute Sb can be seen in the minute shift of the Bi:Sb ratio towards Bi, bringing y to 0.29 and 0.3.

The thin films are patterned into Hall devices following the recipe described in the appendix (chapter 7.2) and supplied with a dielectric and gate. The devices are characterized together with Justus Teller, in the scope of his master's thesis, and Erik Zimmermann in the VTI cryostat. Measurements of the Hall and longitudinal resistance behavior of the three continuously doped samples are shown in figure 3.8 a)-c), with extracted Hall data given in table 3.2. Similar to the previously measured thicker Hall devices, a magnetic hysteresis originating from the AHE is observed in all three samples. The coercive field increases with decreasing temperature, saturating at around 95 mT for the lowCr and 120 mT for the medCr and hiCr stoichiometries, indicating a comparably stable ferromagnetic order in all investigated Cr concentrations. The onset of ferromagnetism, the Curie temperature, however varies. In the lowCr sample, only below 10 K an opening of the hysteresis loop and thus coercive field is observed. For medCr and hiCr, the T_{Curie} is more elevated, showing a hysteresis starting below 15 K. The temperatures lie within the range of reported T_{Curie} of CBST films with various Cr-concentrations [149], [152]. As was expected, the T_{Curie} increases with higher Cr content.

At T=1.2K	Lower Cr	Medium Cr	High Cr
$n_{2D}[10^{12} \cdot 1/cm^2]$	3.7	5.2	51
$\mu\ [\frac{cm^2}{Vs}]$	57.83	98.8	9
$R_{AH}\ [\Omega]$	4423	5542	535
$B_c\ [mT]$	94.9	120	120

Tab 3.2: Hall device characteristics derived from the measurements shown in figure 3.8.

In contrast to the measurements on the thicker Hall device the anomalous Hall resistance reaches values much closer to the desired conductance quantum even without gating. Previously $0.26\ k\Omega = 0.01\ e^2/h$ were accomplished, in the lowCr and medCr devices this is enhanced to about $4.4\ k\Omega = 0.17\ e^2/h$ and $5.5\ k\Omega = 0.21\ e^2/h$ at the base temperature of 1.2 K, closing in on the quantized value. The hiCr sample exhibits the lowest AHE amplitude, only $0.5\ k\Omega = 0.02\ e^2/h$ suggesting that the higher Cr content creates greater disorder and thereby more charge carriers, suppressing the resistivity. This claim is supported by the measured charge carrier density and mobility given in table 3.2, each being one magnitude higher or lower, respectively, than in the lowCr and medCr HBs. The low charge carrier densities in the lowCr and medCr samples are linked to the negligible bulk of the 6 nm thin films, together with a Fermi level proposedly less close to the bulk states compared to the thicker HB devices.

The longitudinal resistance of the three devices shows varying behavior. In QAHI devices the longitudinal resistance should approach zero with decreasing temperature in the optimal case. Moreover weak (anti-)localization peaks are expected, which will be split according to the sweep direction of the magnetic field. The peak of the W(A)L is situated where the magnetic field is zero, therefore in the case of a magnetic film where the external and internal field are equal, which is in the switching points of the hysteresis curve. In figure 3.8 d)-f) the longitudinal resistivities are depicted. The films show weak localization peaks, with more pronounced features for the medCr and hiCr compounds. This differs from ordinary TIs measured in our group, where WAL is mostly present in the samples. It has however been shown that in Cr-doped Bi_2Se_3 there is a transition from predominantly WAL effects to WL effects with increasing magnetization, which can be linked to an opening of a TRS-breaking magnetic gap at the Dirac point, as expected for the QAHE [153]. The more pronounced WL can thus be linked to the more stable FM in these samples. Interestingly, the resistivity of the samples is in the range of $k\Omega$ over the full temperature window. In the lowCr sample in figure 3.8 d) ρ_{xx} increases steadily with decreasing temperature, contrary to the expected behavior. In the medCr and hiCr case, ρ_{xx} shows a steep decrease going below 20 K, possibly connected to the formation of magnetic behavior below the Curie temperature. Below 10 K however, ρ_{xx} increases again, not fitting to the expected behavior of a QAHI.

To further analyze the Hall devices, the sheet Hall conductivity σ_{xy} is calculated following [53]. σ_{xy} and σ_{xx} are thus given by

$$\sigma_{xy} = \frac{\rho_{xy}}{\rho_{xy}^2 + \rho_{xx}^2} \ , \qquad \sigma_{xx} = \frac{\rho_{xx}}{\rho_{xy}^2 + \rho_{xx}^2} . \qquad 3.V$$

The sheet conductivity relies on both the Hall as well as the longitudinal resistivity of the film. In a perfect QAHI thin film, where ρ_{xx} approaches 0 Ω and $\rho_{xy} = h/e^2$, $\sigma_{xx} = 0\ \Omega^{-1}$ and $\sigma_{xy} = 1\ e^2/h$ following these equations. The data calculated for the measured devices is shown in figure 3.8 g) - i). In g) and i), the resulting conductivity for the lowCr an hiCr does not approach the conductivity quantum, however in h) σ_{xy} reaches up to $0.75\ e^2/h$ at the base temperature of 1.2 K. While this value is pointing into the right direction, the only slowly decreasing ρ_{xx}, which is still in the $k\Omega$ range at 1.2 K for all stoichiometries, does not follow the expected behavior of a QAHI. This distorts the values for σ_{xy}. However, measurements at lower temperatures might show a further decrease of ρ_{xx} and increase of ρ_{xy}, as was reported by other groups, which showed that towards the mK range the longitudinal resistivity can decrease drastically [53].

While the temperature dependent behavior of $\rho_{xy}, \rho_{xx}\ and\ \sigma_{xy}$ might already indicate the sample's quality and possible capability of exhibiting the QAHE, gated measurements are imperative to manipulate the Fermi level to enter or leave the magnetic gap. In figure 3.9, gated measurements of the devices of figure 3.8 are shown, measured at the VTI base temperature of 1.2 K. Figure 3.9 a) - c) show the gate dependence of the coercive field B_c over a range of -10 to 10 V (13 V for medCr) applied via the top gate. The size of B_c is affected by the gating, especially in a) (lowCr), which might indicate an interplay of Van Vleck and RRKY interaction in the samples. In all three devices however the amplitudes of the AHE are more strongly affected by the gating. Higher amplitudes are achieved by applying positive gate voltages compared to the ungated values, most notably in the medCr device, where $R_{AH,medC} \approx 15\ k\Omega = 0.58 \frac{e^2}{h}$.

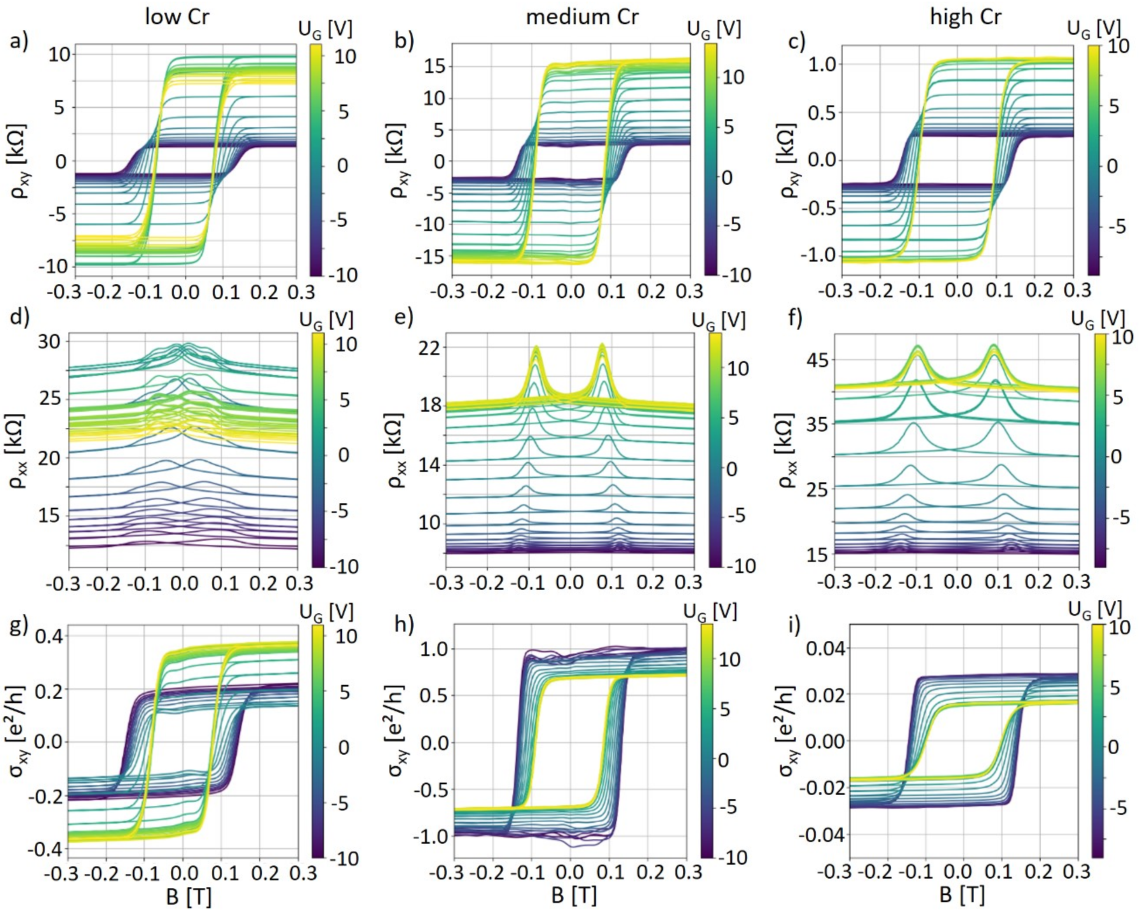

Figure 3.9: Gate dependent measurements of ρ_{xy} *(a-c),* ρ_{xx} *(d-f) and* σ_{xy} *(g-i) over magnetic field, emphasizing on the influence of gating on the hysteresis and anomalous Hall effect. Gating with high positive gating voltages shows an increase in both resistivities (and vice versa) (a-f), which is however unwanted for the longitudinal resistivity. The medCr sample exhibits the most promising results of high AHE with the lowest* ρ_{xx}*. While in g) and i) the conductivity does not reach the desired value of* e^2/h*, in h) the value reaches the desired level at high negative gate voltages. This is in contrast to b), where low* U_G *results in low AHE amplitudes.*

The gating also shows a strong effect on ρ_{xx}. By applying high positive gate voltages, the resistivity increases by a factor of x2 (medCr) to x3 (lowCr, hiCr). In the medCr and hiCr compound, ρ_{xx} increases monotonously until leveling off to a value of 18 $k\Omega$ and 40 $k\Omega$ respectively. In the lowCr case, the resistivity decreases again after reaching its highest point at $+2.5\ V$, suggesting that in this case the Fermi level has crossed the Dirac point without exhibiting QAH insulation. In the medCr and hiCr compounds the Dirac point was not explicitly crossed, as no decrease in resistance due to higher charge carrier concentrations is detected. Higher gating voltages were not applied as not to provoke a shortcut by a gate leakage, destroying the sample. The gating leads to a more pronounced WL effect with increasing positive gate voltages for medCr (e) and hiCr (f), suggesting an increase in phase coherence length, facilitating higher probabilities of the underlying interference effects.

When calculating σ_{xy} via the equation in 3.V, figure 3.9 h) exhibits a peculiar behavior, with an AH sheet conductivity approaching the quantized conduction value closely for high negative gate voltages. It is however a coincidence that the combined value of ρ_{xx} and ρ_{xy} following equation 3.V add up to the desired value for σ_{xy}. ρ_{xy} is decreasing strongly instead of increasing to R_{AH} for negative voltages, at which ρ_{xx} shows the desired trend of approaching lower resistivities and vice versa. This contradicts the expected behavior of a QAHI device and already indicates a problem with the conductivities given by equation 3.V, which will become more obvious in the next section. The lowCr and hiCr samples exhibit alike developments with the gate shifting the resistivities antiparallel to each other, however on scales that do not range in the magnitudes desired for the QAHE.

The fact that at high U_G the charge neutrality point was not reached for higher Cr compounds, but the samples remain p-type throughout, points towards a strong p-type doping of Cr overshadowing the counter doping by the n-type Bi in the compound. By utilizing a Bi:Sb ratio with more Bi, the Fermi level in samples could be tuned into closer to charge neutrality in the gap, facilitating the QAHE.

In conclusion, the medCr compound was chosen to further investigate the Cr-doped TI films due to its AHE resistivity closer to quantization and a comparably lower ρ_{xx}. Later it was found that the applied current along the Hall bar of 1 µA was chosen too high, as the QAHE is prone to breakdown in the presence of high currents [154], [155]. But before, considering the results of the thin CBST devices, a sandwich sample consisting of two 2 nm layers of the medCr compound with pure BiSbTe sandwiched between is grown and Hall devices are prepared, which will be shown in the next section.

3.2.3 The CBST Sandwich Stack

As was shown in [54], layer stacks of doped and undoped (C)BST QL provide access to the QAHE over a wide range. To investigate this, a sandwich stack as shown in figure 3.10 a) was grown by closing the Cr cell shutter for a set time during thin film growth. The resulting film in figure 3.10 b) does not differ structurally from the continuously doped CBST films investigated before.

After Al_2O_3 capping Hall devices are processed with 15 nm ALD HfO_2 dielectric and Pt contacts and Au gate as before. The measurements are shown in figure 3.10 c) and d). Here, the gate was first investigated at base temperature of 1.2 K with a current of 1 μA before the temperature dependence in order to first check the important gating capabilities of the device. When examining ρ_{xy} (corrected for the Hall slope) and ρ_{xx} it stands out that at gate voltages U_G around 2 V the longitudinal resistivity is at its lowest point while the Hall resistivity is at its highest, which is what is expected for the QAHE. Increasing the gate voltage in either direction causes the resistivities to deteriorate respectively, exemplarily shown for ρ_{xy} in figure 3.11 a). ρ_{xy} reaches as high as $25\ k\Omega = 0.97\ h/e^2$, approaching the quantized value closely even at 1.2 K, which is an elevated temperature for QAH measurements when compared to literature values [53], [149]. In figure 3.11 b) the gate dependent resistivity ρ at $B = 0.1\,T$ is given for both xx and xy direction, showing the

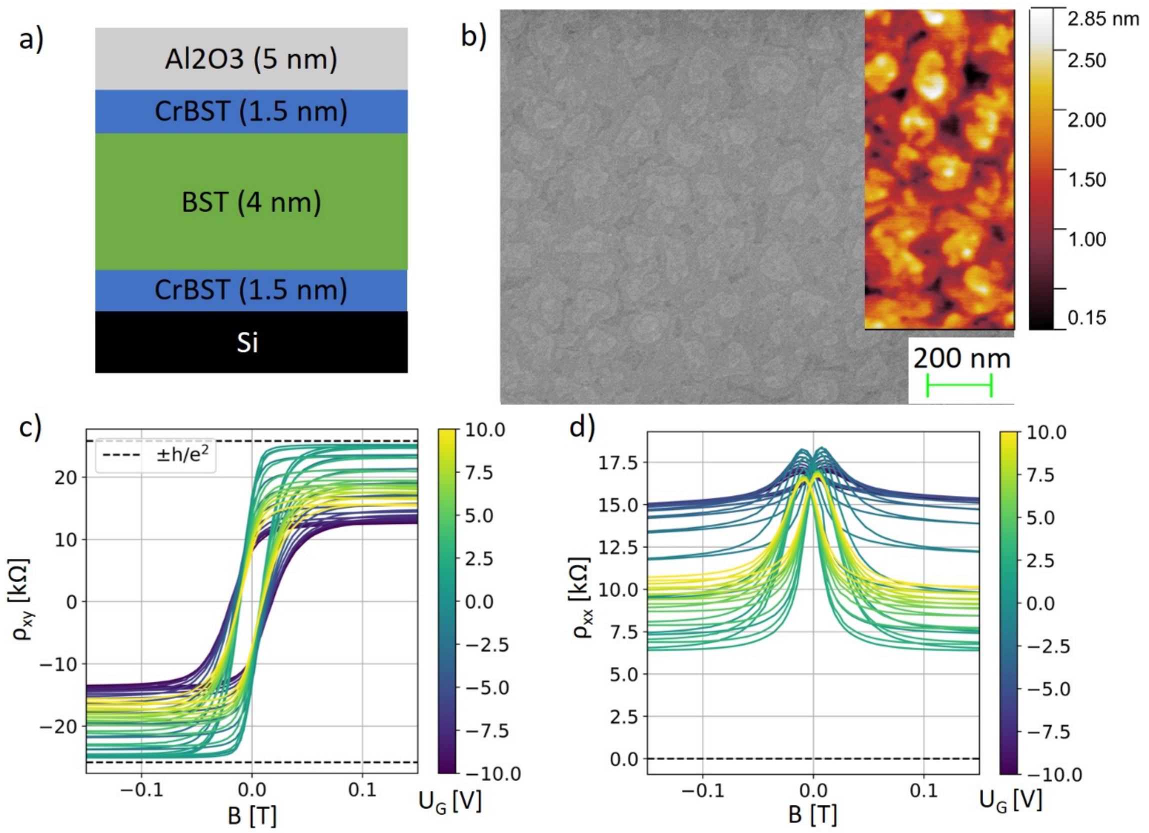

Figure 3.10: Sandwich sample characterization. The trilayered sample as depicted in a) exhibits growth in crystallite islands of roughly 100 nms in size, with only slight variations in heights as given by the atomic force microscopy (AFM) inset in b). The measurement suggests height differences of 1nm steps. The Hall resistivity ρ_{xy} (c) and the longitudinal resistivity ρ_{xx} (d) vary with the applied gate voltage, with extrema at approximately 2 V gate voltage, measured at 1.2 K.

evolution of the resistivities, which, at a specific gate voltage, should show $\rho_{xy} \rightarrow h/e^2$ and $\rho_{xx} \rightarrow 0\ \Omega$. The data follows this trend close to $U_G = 2$ V. Strikingly, figure 3.11 b) is very similar to a graph given by Chang *et al.* in [32] depicting the same measurements on the first CBST sample to ever show the QAHE but at $90 - 400\ mK$. In the measurement of Chang *et al.* the longitudinal resistivity for $T > 90\ mK$ is $\sim 0.25\ h/e^2$, almost equal to the data in the measurement in figure 3.10 d) at $1.2\ K$ and $U_G = 2\ V$, $\sim 6.4\ k\Omega = 0.248\ h/e^2$, suggesting that at even lower temperatures ρ_{xx} close to $0\ \Omega$ might be possible. $U_G = 2\ V$ is chosen because at that value the charge carrier density changes sign, implying a position close to the charge neutrality point. The carrier density during gating does not exceed $2.5 \cdot 10^{12}/cm^2$, ranging closely to the low level of the previous samples. This finding supports the assumption of the last section, that Cr in the continuous samples causes strong p-type doping. In the trilayer structure a “p-n-p”-like stack is formed by the (M)TI layers, with the BST layer providing a more n-type structure, effectively creating a compound with a Fermi level closer to charge neutrality, similar to Sb_2Te_3-Bi_2Te_3 p-n structures [156]. The QAHI regime in the topological gap is thus more accessible and stable with low gate voltages. In [54], Mogi *et al.* postulate that a confined Cr layer forms a more homogeneous concentration of the Cr which results in a larger magnetic gap in the surface

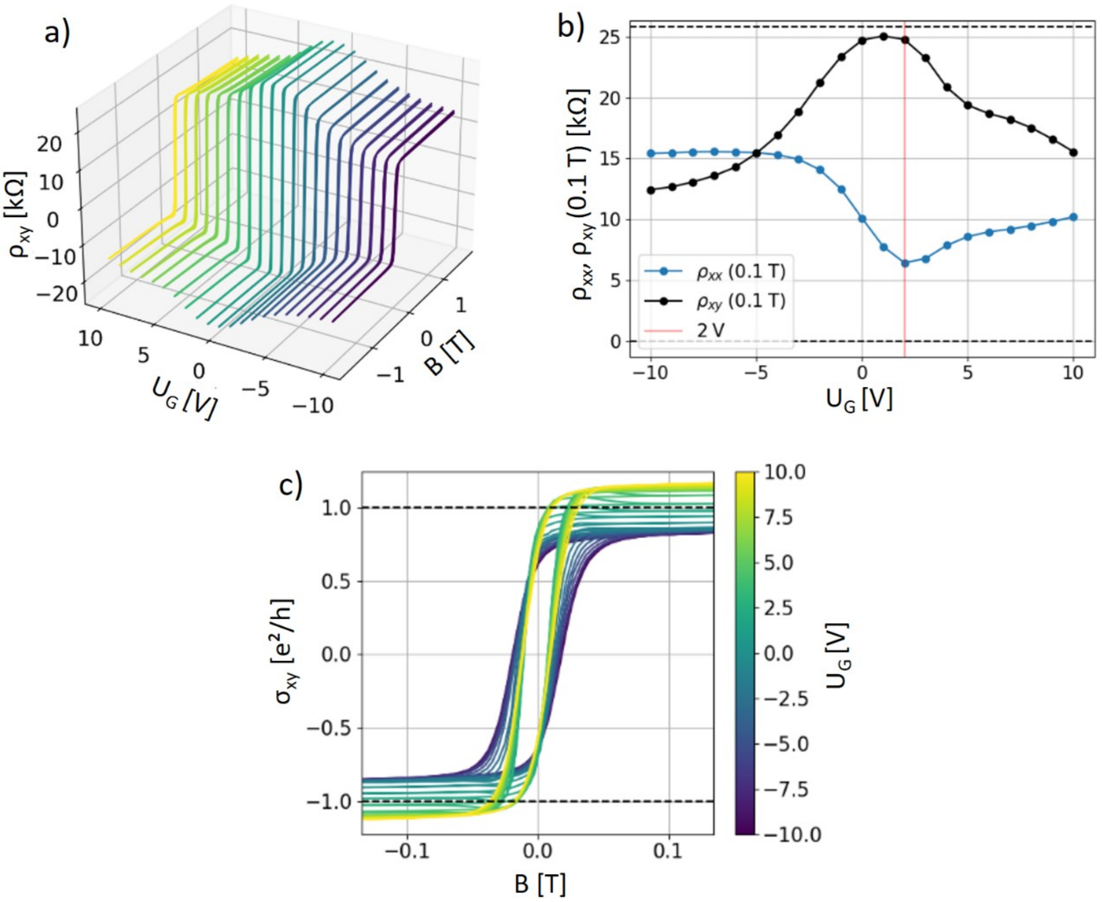

Figure 3.11: In a) the development of the AHE amplitude is shown in 3D, illustrating the maximum in the AHE at $U_G = 2$ V. b) Plotting the values for ρ_{xy} and ρ_{xx} at 0.1 T for different U_G reveals the desired dip in ρ_{xx} with a simultaneous peak in ρ_{xy} to almost the quantized value, suggesting a QAHI behavior at lower temperatures. In c) the Hall conductivity, calculated from data in figure 3.10 via equations 3.V, is plotted at 1µA bias current. Due to the elevated $\rho_{xx} \neq 0\,\Omega$ in figure 3.10 d), σ_{xy} in c) exceeds the quantized value at gate voltages above 2 V. Thus, σ_{xy} is not a reliable value when evaluating the QAHI combabilities.

states while simultaneously suppressing bulk conduction. This creates a larger energy window for the QAHE, which in their work is even enhanced by a pentalayer design.

Although the resistivities of the sample show the desired behavior, the conductivity σ_{xy} calculated via 3.v shown in figure 3.11 c) exceeds the limit of e^2/h at positive U_G due to the still elevated $\rho_{xx} \neq 0\,\Omega$ (figure 3.11 b)). While close to the charge neutrality point at $U_G = 2\,V$ the R_{AH} amplitude is approaching the quantized value and does not exceed the limit, the validity of σ_{xy} and σ_{xx} is still questionable. This was already indicated in the previous section, where σ_{xy} approached quantization in the medCr compound (figure 3.9 b), e) & h)), while ρ_{xx} and ρ_{xy} showed a distinctly different behavior. The calculation of σ, while applicable when ρ_{xx} approaches 0 Ω, can skew the interpretation if $\rho_{xx} > 0\,\Omega$. Thus, only the resistivities are considered in the further analysis.

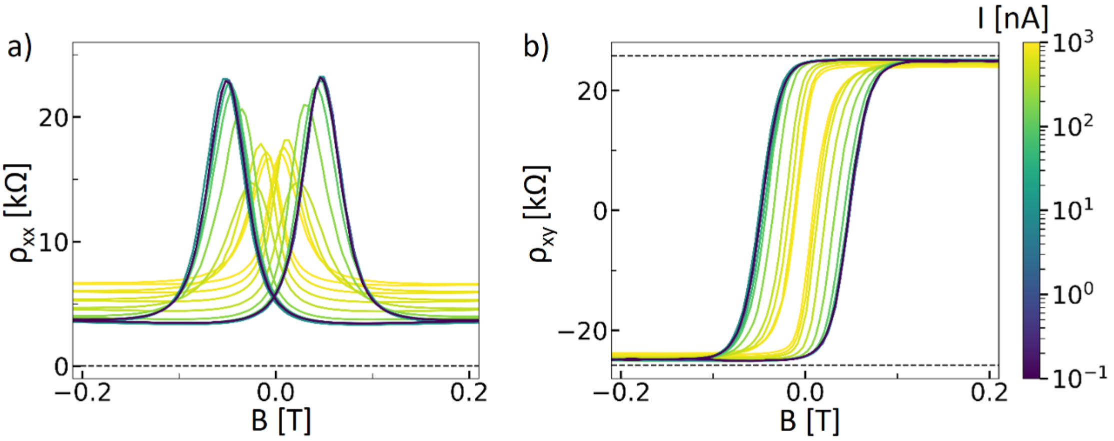

Figure 3.12: Progression of ρ_{xx} *(a) and* ρ_{xy} *(b) when decreasing the applied bias current from 1 µA to 0.1 nA, while maintaining* $U_G = 2\ V$ *and* $T = 1.2\ K$*. Diminishing bias currents exhibit a strong influence on the coercive field, leading to a pronounced shift in the WL peaks for* ρ_{xx} *(a) and a widening of the hysteresis in (b). The dotted lines in b) indicate the quantized value of e/h². Data as published by Erik Zimmermann in [157], figure adapted.*

As mentioned before, the resistivity of the trilayer is expected to decrease further towards temperatures below 100 mK, reaching in the quantized values for both resistivities. The measurement in figure 3.11 b) alone would however not support the claim that the trilayer sandwich has formed a QAHI system. Comparison with results of other groups suggest another reason for the elevated resistivities apart from the elevated temperatures: the applied AC current. As shown in [154], [155], elevated currents inhibit the QAHI. Especially the longitudinal resistivity suffers greatly from increased currents even in the mK range, causing ρ_{xx} to never reach the theorized 0 Ω . In figure 3.12 a) and b) the evolution of ρ_{xx} and ρ_{xy} when decreasing the current is depicted. The measurements were performed at $T = 1.2$ K and $U_G = 2$ V.

Two developments are shown in figure 3.12, ρ_{xx} on the one hand decreases when lower currents down to 0.1 nA are applied and on the other hand the coercive field is increased for ρ_{xy}. Moreover, $\rho_{xx}(B = 0\ T)$ decreases due to the shifting of the magnetization reversal peaks, while $\rho_{xy}(B = 0\ T) \rightarrow e^2/h$. In [158] Kawamura *et al.* show that the maximal current to maintain the QAHE correlates to the width of the Hall bar. In their argumentation, applying higher currents leads to higher effective temperatures in the device, causing a breakdown of the QAHE. Moreover, they argue that the low characteristic current still providing QAH features originates from a diminished magnetic gap due to a disordered Cr distribution [158]. As was shown in [159], Cr disorder in the CBST can lead to the formation of in-gap states, enabling variable range hopping, effectively coupling the effective temperature to the applied current strength. ρ_{xx} and ρ_{xy} thus show better behavior with smaller currents, fitting closely to what has been reported in literature for similar samples. However, these measurements were performed at lower temperatures, in which our extent of quantization at 1.2 K was only reached at temperatures below 500 mK [32]. It is therefore highly plausible that the investigated trilayer Hall device exhibits the sought after QAHE when moving towards the mK range.

While it has been shown that the QAHE can also exist at higher temperatures in CBST sandwich samples as well as other magnetic TIs ([54], [160]), in our samples Fermi level fluctuations might be a possible reason for the elevated ρ_{xx}. These would cause QAH areas, interrupted by normal MTI, resulting in resistive hopping between QAH patches, increasing ρ_{xx}. Moreover, if the edges of the Hall bar are too close, exchange between the channels via bulk states is possible, diminishing QAH features. Going from 10 µm to wider Hall bars with high quality thin films might therefore show better results [149]. A peculiar current-induced switching of the magnetization is also observed in the layered samples fabricated in the scope of this thesis, which are investigated in detail in [157].

In conclusion, high quality Chromium doped tetradymite BiSbTe thin films are successfully fabricated with varying Cr-concentrations. The compounds show variable strengths of the magnetization in Hall measurements, but consistently provide strong ferromagnetic order. Thicker MTI thin films $d > 10$ nm exhibit low ρ_{xy} and high ρ_{xx}, as opposed to the behavior in the QAHE, which is expected samples with large bulk contributions. When thinning the films to $6-7$ nm and thus diminishing the bulk, the resistivities show trends towards the desired quantized values. A sandwich sample utilizing the best continuously doped CBST thin film enclosing an undoped film finally leads to an observation of clear indications of the QAHE at the charge neutrality point, with ρ_{xy} and ρ_{xx} approaching the desired quantized values. These trends are in line with literature, especially in comparison to [148], where a similar trilayer structure shows very similar values for 1-2 K and exhibits clear quantization in the mK range. Decreasing the bias current improves the approach towards quantization even further. Hall measurements in the < 1 K temperature regime should be performed to further examine the suspected QAHI, emphasizing on the development of ρ_{xx} towards lower temperatures. Additionally, low bias current measurements are planned on the continuously doped devices to investigate their current dependency, too.

The CBST MTI thin films investigated in this section promise to exhibit the QAHE at lower temperatures while being close to the charge neutrality point. They are therefore predestined to be combined with a superconductor to search for Majorana signatures due to the formation of triplet superconductivity in proximitized regions. This will be performed in chapter 4, however as mentioned before, CBST films exhibit a random magnetic gap size correlating to the distribution of the Cr atoms in the compound. Clusters and more sparsely doped regions create a potential landscape exhibiting large differences in magnetic gap size, which can cause a local breakdown of the QAHE. It is therefore beneficial to also consider alternatives with a more ordered and constant magnetic structure. In the course of this thesis, the first intrinsic magnetic topological insulator was discovered in the form of $MnBi_2Te_4$, promising some advantages searched for when considering the shortcomings of CBST. Therefore, various $MnBi_xTe_y$ and the even more recent $MnSb_2Te_4$ compound have been grown and characterized in parallel to CBST, however in the scope of this thesis no breakthrough towards a QAHE in the intrinsic MTIs could be achieved. Therefore, the focus is put on the promising CBST devices, information on the intrinsic MTIs can be found in chapter 7.1 in the appendix.

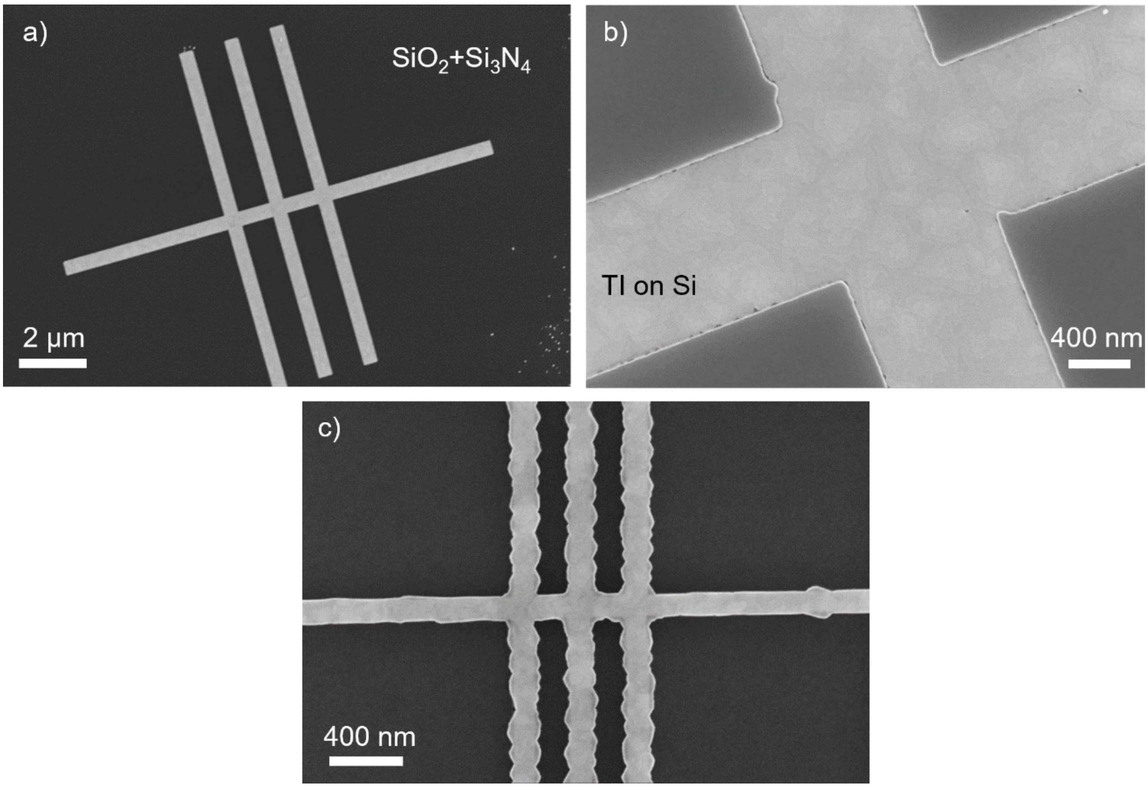

Figure 3.13: Examples of selectively grown TI films in Hall bar patterns. a) illustrates the high selectivity of the process, showing only minute crystallites in a large area around the intended trench. A closer look into the trench reveals the crystalline structure of the grown film, exhibiting the characteristic trigonal structure of the TI film, in this sample $(BiSb)_2Te_3$. If the growth is not stopped in time, the TI will start to protrude from the trench, forming crystalline overshoots onto the Si_3N_4 hard mask. The phenomenon can be identified by the ragged edges of the TI as in c), not following the etched straight edges.

3.3 Selective Area Growth of MTI

All Hall devices examined up to this point were fabricated via clean room processes, however, these involve a risk of contaminating the thin film surfaces while simultaneously exposing the functional surfaces to ambient conditions and oxidation, thus creating possibly conductive layers or band bending effects overshadowing the TI surface states. Therefore, in our group a method was developed which enables the growth of TI only in prepatterned regions [161], [162], [163]. To do so, the silicon substrate is covered before the cleaning and growth procedures with a layer stack of SiO_2 and Si_3N_4 via low pressure or plasma enhanced chemical vapor deposition (LPCVD/PECVD). The layer thicknesses are chosen depending on the intended use of the layers. For selective growth, 5 nm of SiO_2 are deposited, covered with 20 nm of Si_3N_4. The nitride layer is then covered with optical or electron beam resists, which are accordingly patterned and structured. In a RIE step, similar to the one used to create the TI Hall mesa, the exposed, non-resist covered, nitride is removed, baring the SiO_2/Si surface. The oxide acts as a stopping layer during the nitride patterning and is etched in the substrate cleaning process within the HF dip. These patterned samples can then be standard cleaned and transferred to the growth chamber. If the right substrate temperature is given, only the crystalline surface of the Si allows for TI nucleation, while material deposited on the amorphous Si_3N_4 layer is re-evaporated, inhibiting growth on that surface. Examples of TI films grown into such patterned trenches are shown in figure 3.13, where the bright TI crystal is depicted to only have grown in the patterned trench etched into the darker Si_3N_4 layer. Via this method, structures down to widths of 30-40 nm have been realized with non-magnetic TI thin films.

Utilizing the SAG also for MTIs like CBST and $MnSb_2Te_4$ (MST) would promise more clean, efficient and reproducible device fabrication. Thus, SAG substrates were fabricated with trenches of varying width in a Hall bar mesa design. As is established for non-magnetic TIs grown in the PGI-9, the substrate temperature for selective area deposition is chosen slightly higher than for plain thin film growth. This is done to ensure that no crystallites form on the mask surface. First tests on the selectivity of MTI are performed with CBST, in which the high effusion cell temperature of the chromium is a source of concern. If Cr needs high temperatures to desorb from the cell material, the substrate temperature during growth is too low to inhibit growth on the amorphous mask. Higher substrate temperatures are limited by TI re-evaporation. Therefore, a window of substrate temperature needs to be found in which the TI can be grown with a good quality as well as inhibiting the growth on the mask similar to figure 3.13.

In figure 3.14 a) and b) a test growth of CBST on a prepatterned SAG substrate is shown. The material fluxes are chosen according to the optimal growth conditions for a plain thin film, the substrate temperature is however increased. The optimal temperature for SAG of non-magnetic BST Hall bars in the M13 MBE is known to be at 220°C, with only minor variations to accommodate changing substrate dimensions and the respective holder plates. The growth of CBST requires slightly higher temperatures as was shown in section 3.2, for SAG T_{sub} is additionally increased by 5°C from the standard 225°C to 230°C. As shown in figure 3.14 a) and b), this minorly elevated temperature is enough to negatively impact the quality of the MTI in the trench strongly, showing small crystallite island growth, while simultaneously the growth on the mask is not prevented. A polycrystalline film is deposited on the Si_3N_4 mask, potentially shortcutting the metal pads which would be deposited later via *ex situ* processes for contacting. The most likely explanation is that Cr is deposited on the nitride surface, forming small clusters, which in turn act as nucleation sites for a polycrystalline CBST film growth. Attempts to remove the polycrystalline film by further increasing T_{sub} to remove the Cr clusters however only worsened the MTI quality in the trench. Cr is known to have a large sticking coefficient. Thus, for CBST, no viable temperature window for selective growth with prepatterned stencils could be found.

As is detailed in the appendix in chapter 7.1, Manganese requires much lower effusion cell temperatures than chromium, 750°C compared to 1050°C, which on the one hand could result in better selectivity results, on the other hand these temperatures are still far greater than those used for Sb, Bi or Te, much less T_{sub}. A test with MST in the BST-MBE at an elevated growth temperature of 290°C is depicted in figure 3.14 c). The polycrystalline overgrowth on the mask is clearly visible. In contrast to the CBST compound, the MST is not as negatively impacted by elevated substrate temperatures. Thus, higher temperatures

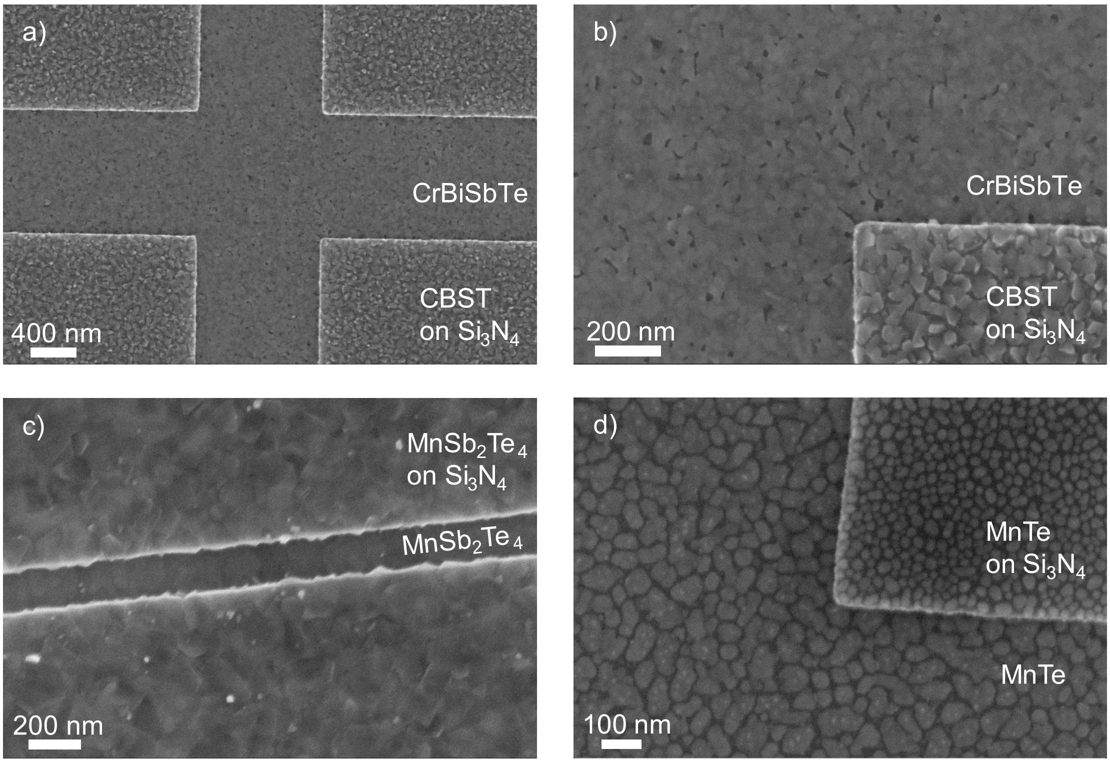

Figure 3.14: MTI selective growth study. For non-magnetic compounds like BST, SAG is performed at temperatures slightly above the optimal growth temperatures of plain film samples. Adopting this recipe for MTIs yields results as shown in a) – c). Growth is not limited to the predefined trenches, but films are also deposited on the Si_3N_4 *mask. While for MST (c) the growth quality in the trench is still acceptable, for CBST (a & b), the film quality in the trench is also negatively affected by the increased* T_{sub}*. Possible accumulations of Cr/Mn on the mask lead to nucleation sites for polycrystalline MTI growth, inhibiting selectivity. This explanation is supported by micrograph d), where only MnTe was grown at elevated temperatures. The compound is not re-evaporated from the* Si_3N_4 *layer and forms crystallites on both surfaces, pointing towards difficulties when employing elements with high effusion temperatures in selective growths.*

could still bring the desired selectivity effect. To investigate this, a MnTe test growth at $T_{sub} = 300°C$ is performed. With Mn as with Cr there is the possibility in the Te overpressure regime that, when Bi or Sb are not able to adhere to the substrate surface anymore due to the high T_{sub}, Cr_xTe_y or Mn_xTe_y are formed. If at an strongly elevated T_{sub} these compounds still form polycrystalline films on the Si_3N_4 mask, there will also be no selectivity for the CBST or M(B/S)T compound. In figure 3.14 d) an SEM micrograph of a MnTe test growth is depicted. The Mn flux is taken over from the MST growth, therefore there is only a minute Mn flux in the 10^{-9} mbar range. As is clearly visible, the low material supply is still enough to create a discontinuous layer of crystallites on the Si as well as the Si_3N_4 surface. If Sb or Bi were additionally evaporated, even at temperatures which are too high for plain high-quality growth of any MTI, polycrystalline films would form on all surfaces. Thus, with higher substrate temperatures there is also no available growth window to achieve selective area growth with MBT or MST, similar to CBST.

These findings may point towards a necessity of clean room fabrication processes when aiming to fabricate MTI devices, however not all hope is lost. There are a few approaches left to realize *in situ* patterned growth with MTIs. Firstly, evaporating the elements separately onto the substrate and then annealing them at moderate temperatures to enable the formation of an ordered MTI crystal out of the available material is a possible process, called *digital alloying* [164]. If each element is deposited at its SAG temperature only in the exposed patterned areas, selective growth is possible. Secondly, for CBST as well as MBT and MST, stoichiometric source material can be equipped in effusion cells and evaporated onto patterned substrates. The Cr and Mn bound in the materials, which themselves could be evaporated at moderate temperatures, might in this configuration not form the temperature-resistant nucleation sites impeding normal SAG growth.

Finally, stencil lithography is a third approach to solving the selectivity problems. Stencil lithography is a technique developed by Peter Schüffelgen during his Ph.D. thesis [165] also utilized during my Master's thesis [163], which uses nitride and oxide masks similar to the ones in SAG. Fabrication of stencil lithography samples, growth of MTI on these samples, devices fabricated from it and measurements of MTI/SC hybrid devices will be shown in the next chapter 4 and a derivative of stencil lithography will be established in chapter 5 in order to create patterned TI/SC hybrid samples suitable of scanning tunneling microscopy and spectroscopy.

4 Combining MTIs and Superconductors

In the last chapter, the growth of Chromium doped TIs has been established and, via Hall investigations, the general magnetic behavior with strong indications of a QAHE in the trilayer sample have been measured. With magnetism in TIs now realized, the next step is to combine the MTIs with superconductors and to investigate the proximity effect in these hybrid devices to venture towards the realization of topological superconductivity in circuits of MTI-SC nanoribbons. As was shown by Burke *et al.* [33], a QAHI is not necessary, but magnetic TI-SC hybrid devices are sufficient to identify Majorana physics. Only when these devices show indications of Majorana quasiparticle states can the transition to quasi-1D structures commence. This chapter will thus address the combination of MTIs with SCs, which, as mentioned in chapter 2.2.4, are two very distinct phenomena. Creating hybrid devices of TIs and SCs like Niobium and Aluminum is an established process in our group ([105], [162]), MTIs however complicate many aspects of sample fabrication and transport measurements. In chapters 4.2 and 4.3 new device layouts will be introduced, which allow for investigation of Hall and Josephson junction characteristics in one device. The measured data will reveal that inducing SC into the present MTIs is difficult, but indications of superconductive behavior will lead to proposals for future promising experiments. First however, the process of stencil lithography, allowing us to grow MTI selectively will be introduced. Utilizing this process, a first sample with an established QAHI, grown by collaborators at the UCLA in the group of Prof. Kang L. Wang, combined with SC from the Research Center Jülich will be explored in chapter 4.1.

4.1 *Ex situ* Devices Utilizing CBST-Nb

As was shown in chapter 3.3, the selective growth of MTIs by adjusting the growth temperature and employing SiO_2/Si_3N_4 hard masks could not be achieved. Due to the high re-evaporation temperatures needed for Cr and Mn, no fitting temperature window could be established in which MTI was only deposited on the exposed Si surface. This means that all devices need to be etched from a plain thin film involving multiple chemical and physical etching processes and lithography steps. The impact of these processes on the topological surface states and on the QAH states will likely not improve the quality. However, the problem of growth on the mask can be circumvented by separating the mask from the functional layer using stencil lithography, a growth process somewhat similar to the Niemayer-Dolan technique [166], [167].

In stencil lithography, instead of a Si_3N_4 mask directly on the Si substrate with only a thin SiO_2 buffer as in chapter 3.3, the patterned Si_3N_4 mask rests on a 300 nm thick layer of oxide, which acts as a sacrificial layer during HF cleaning and etching. Thereby, as shown in figure 4.1 a), parts of the Si_3N_4 mask become free-standing and suspended above the Si surface as soon as the sacrificial SiO_2 underneath is removed. When applying a material flux in the MBE onto such a sample under rotation, the free-standing nitride acts as a stencil

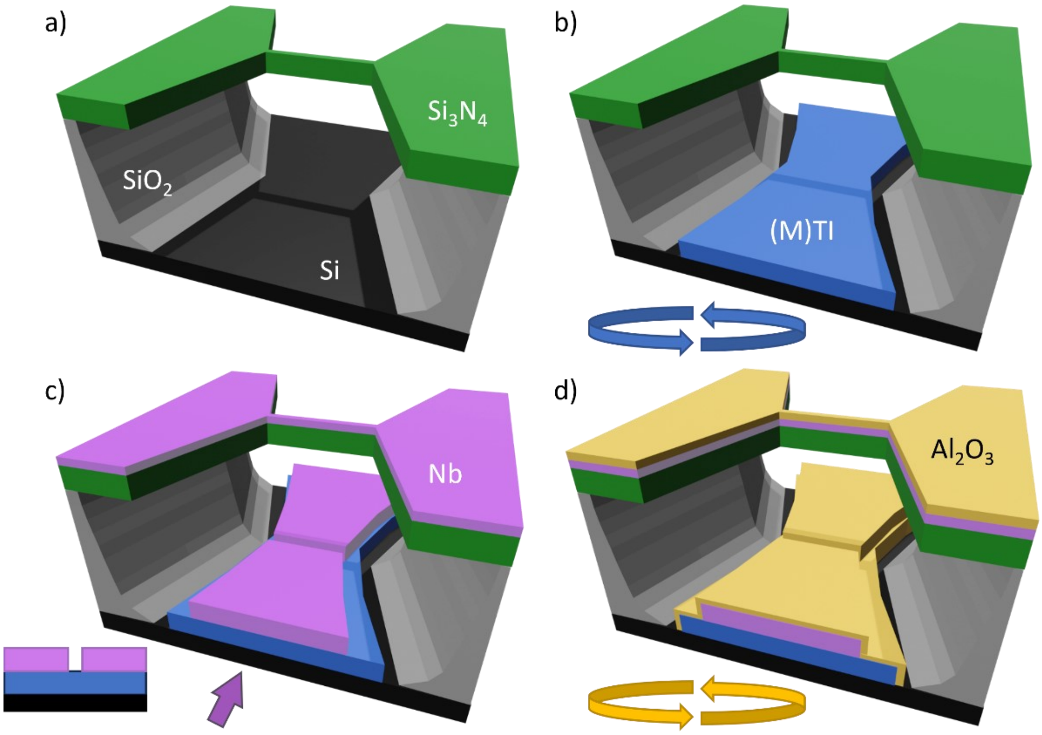

Figure 4.1: Stencil lithography process capable of creating nm-scale devices in situ. On a Si substrate first a layer of 300 nm SiO_2 *and a layer of 100 nm* Si_3N_4 *are deposited via LPCVD. The* Si_3N_4 *layer is then patterned via resist and reactive ion etching processes into the tapered design shown in a). Exposing the substrate to 1% HF acid etches the* SiO_2 *layer isotropically, releasing the* Si_3N_4 *mask layer. These steps are performed before any thin film is grown, effectively shifting the device patterning process before the growth. The substrate is then inserted into the MBE growth chamber, where (M)TI is selectively deposited under rotation (b), creating a continuous film on the exposed Si. Stopping the rotation and evaporating a SC material utilizes the shadow of the suspended mask, creating a gap in the SC film (c). The gap as shown in the inset forms the weak link area of the thusly deposited Josephson junction device. To protect the (M)TI and SC films from ambient conditions, a capping is evaporated under rotation in d), sealing all exposed surfaces.*

similar to those in graffiti art, leading to material deposition only in destined areas not shadowed by the masks as shown in blue in figure 4.1 b). As exhibited in multiple papers from our group, complex structures of the order of 10s to 100s of nanometers can be realized with this technique [105], [106]. It also enables heterostructure fabrication by manipulating the angle under which material is deposited onto the sample. The levels of mask and substrate are separated by up to 400 nm, which means that MTI crystallites on the elevated mask do not influence the functional MTI layer grown on the Si below, promising the realization of SAG also with MTIs.

After (M)TI deposition, the substrate rotation is halted and a superconductor is deposited via electron beam evaporation. This evaporation is directed and translates the shadow of the bridge onto the lower level, creating a lateral gap in the superconductor on the (M)TI surface as shown in figure 4.1 c). This gap forms an *in situ* fabricated SC-(M)TI-SC junction as detailed in section 2.2.2 and will be used to investigate the induced superconductivity into the MTI film underneath. Due to the metallization process

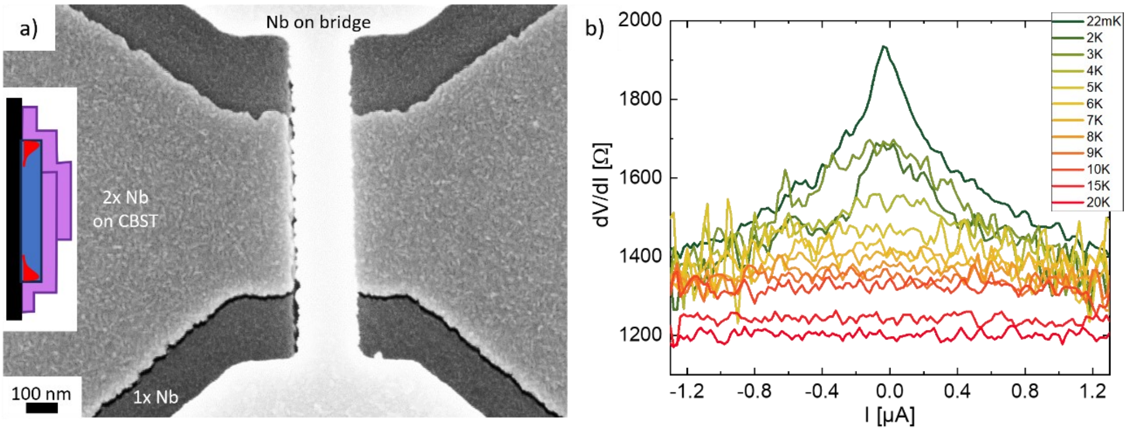

Figure 4.2: First MTI hybrid devices fabricated in cooperation with the group of Prof. Kang Wang from the UCLA. a) SEM micrograph (top view) of a bridge device as described in figure 4.1. Nb is deposited twice from opposite directions parallel to the bridge, creating regions with 25 nm or 50 nm Nb thickness as indicated in the schematic on the left, to ensure contact to both proposed edge channels (red) of the CBST film. Other colors as in figure 4.1. b) Differential resistance measurements over the junction in a) utilizing an DC + AC bias current (3 nA AC amplitude). An increasing resistance towards low bias currents at low temperatures is revealed, indicating no signatures of induced superconductivity.

happening *in situ* in the same chamber immediately after TI deposition, a highly clean interface is known from SC-TI-SC devices created with this fabrication method. To protect the (M)TI-SC structure from oxidation, an aluminum oxide capping is supplied to the sample via electron beam evaporation under rotation to cover all essential surfaces as shown in figure 4.1 d). With this, the SC-MTI-SC device can be bonded and built into the measurement setup without further need for device processing.

A realization of a QAHI-JJ via stencil lithography was planned already at the beginning of this work to evaluate the proximity effect in MTIs early on. At that point no MTI growth had been established at the PGI-9 yet. Earlier collaborations with Prof. Kang L. Wang from the UCLA however enabled a transfer of prestructured substrates to Los Angeles, where the samples were etched with HF to release the bridges. They then deposited their QAHI CBST films [149] and immediately returned the samples, packed in N_2 atmosphere. Upon arrival the samples were inserted into the Nanocluster for Nb and Al_2O_3 deposition. Standard Nb effusion is performed from an electron beam evaporator without rotation at 50°C substrate temperature with an acceleration voltage of 10 kV and a rate of 2 Å/s. 5 nm of Al_2O_3 are deposited after Nb, with 10 rpm rotation at a rate of 1.7 Å/s. The resulting junction is shown in figure 4.2 a). The SEM micrograph reveals the bright Nb covered bridge above the JJ, occluding the weak link. The Nb on the lower-level exhibits two distinct colorations due to a two-step evaporation of Nb. If the deposited CBST is a QAHI, which could not be tested beforehand[1], edge channels would run along the edge of the MTI film deposited on the lower level. To investigate the induced superconductivity into these exotic states, the SC should be positioned on the edge of the MTI film to ensure QAHI-SC

---

[1] In the group of Kang L. Wang, the QAH CBST was exclusively deposited on GaAs substrates. The CBST in figure 4.2 a) is expected to be stoichiometrically comparable to the GaAs/CBST devices, the existence of QAHI in these layers is however not guaranteed.

interaction. As visible in figure 4.1 c) this is however not the case for stencil lithography if the Nb is evaporated perpendicular to the bridge. Thus, 25 nm of Niobium are deposited onto the sample first from the bottom parallel to the bridge, then the sample is rotated by 180° and another 25 nm Nb are deposited. Thereby all edges of the MTI are covered while maintaining the JJ weak link, creating two regions with different Nb thickness. This should however not impact the general measurement of the proximity effect. After capping, the sample is glued into a chip carrier and bonded twice with Al wire on each side of the JJ to facilitate four-point measurements over the junction. The chip carrier is then inserted into an Oxford Triton cryostat and cooled to a base temperature of ~20 mK. The cryostat is equipped with a vector magnet, allowing for in- and out-of-plane magnetic fields.

As a reminder to chapter 2.2, in the present configuration a plateau in the I-V curve is expected for induced superconductivity with a distinct critical current, resulting in a drop of the (differential) resistance to 0 Ω. Due to the magnetism in the CBST film, the critical current can be heavily diminished compared to JJs on non-magnetic BST films. In theory, at the magnetization reversal point the critical current and the conductance should thus show a peak. As shown in section 2.2.4, the induced SC coherence length is diminished in magnetic layers, also for possible p-wave superconductivity, although there are specific arrangements of magnetic layers that again increase the coherence length of p-wave superconductivity [97]. Therefore, in MTIs the penetration depth of the necessary Cooper pairs might not be large enough to yield a substantial overlap, inhibiting induced superconductivity. If induced superconductivity is present the ratio of 2π to 4π signal can be measured (compare chapter 2.2.3) via Shapiro measurements, i.e., supplying a radio frequency into the chamber. Moreover, a π junction as detailed in chapter 2.2.4 might also be present, depending on SC phase, temperature and contact separation.

However, the SC-MTI-SC junction shows a distinctly different behavior as depicted in figure 4.2 b). Instead of zero resistance at low temperatures and low bias currents, a peak in resistance is measured over the junction, decreasing with the magnitude of current applied. The peak feature develops below 7 K and becomes increasingly sharp with lower temperature. The disappearance of the peak above 7 K might be caused by a temperature dependent Fermi-Dirac distribution of the involved states, however the presence of the peak up to the critical temperature of the Nb contacts suggests a relationship of the peak and the superconducting gap forming below 9 K. No supercurrent over the junctions could be measured in any of the devices, however it has to be mentioned that many devices were damaged during the ambient transport. Multiple junctions were shorted by mask debris and dirt particles connecting mask to device level. In all non-shorted devices no SC could be measured, only exhibiting the shown peak. A similar behavior of the resistance approaching zero bias has been found in SC-Insulator-FM-SC junctions in [168], however close to zero current a narrow SC plateau was found in these devices. In our Nb-CBST-Nb junctions on the other hand, no such plateau can be identified. The absence of a supercurrent could stem from a bad interface after surface oxidation during sample transport. An interfacial barrier between SC and MTI would cause bad transparency for Cooper pairs into the MTI layer, inhibiting ABS and thus impeding induced superconductivity.

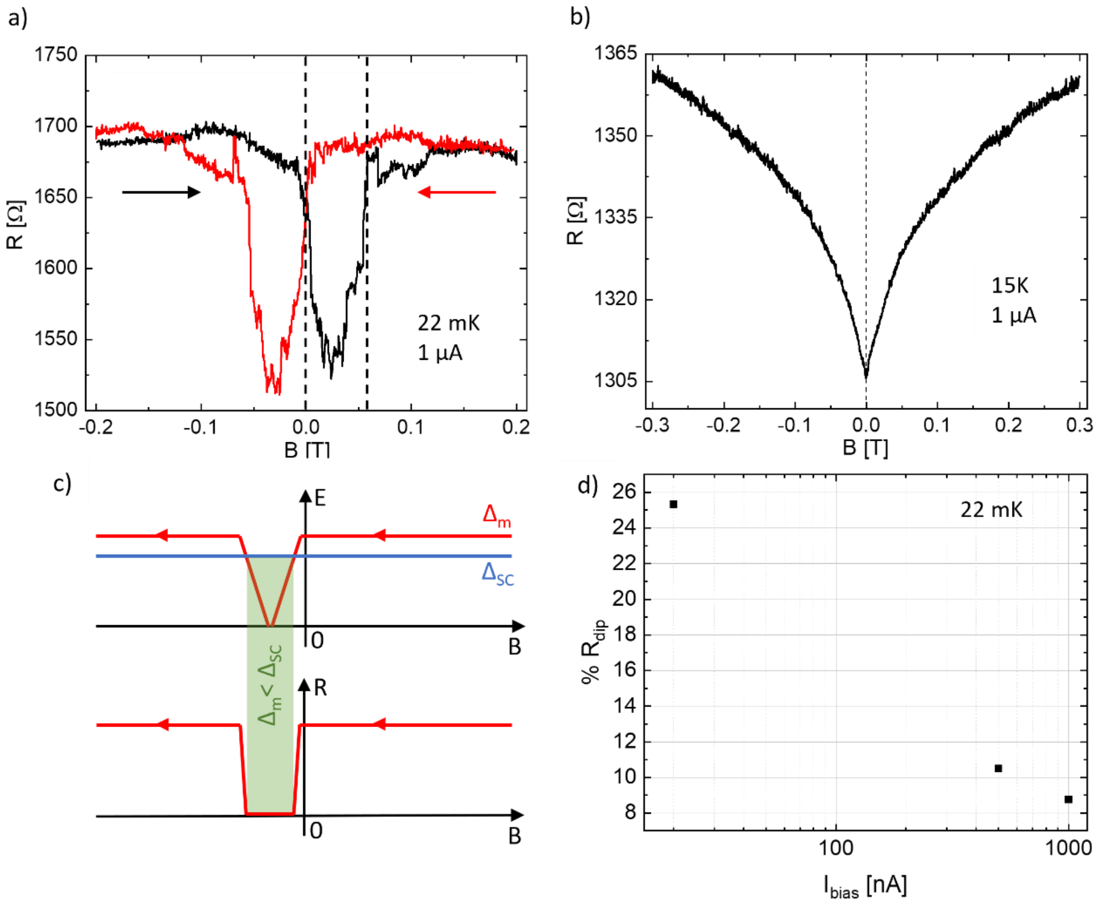

Figure 4.3: When sweeping an external magnetic field perpendicular to the film plane, dips in resistance symmetric around zero magnetic field, but reliant on field sweeping direction, are measured in a). Towards high temperatures (b) the effect is lost and an ordinary WAL peak is found, coinciding with transgression of the critical temperature of Nb and the Curie temperature of the CBST film. The behavior can be explained by comparing the involved gaps as shown in c) (adapted from [169]*). When approaching the coercive field, in c) for the red curve of a), the magnetic gap decreases due to the loss of polarization, resulting in the formation of a superconducting gap, decreasing the resistance. d) At lower bias currents, a possible proximitized region is likely enlarged, causing a shorter non-proximitized weak link and thus an increase in dip depth.* $\%R_{dip}$ *denotes* $100*(\bar{R}-\overline{R_{dip}})/\bar{R}$*, where* $\bar{R}$ *is determined by horizontal fits to the top and dip region.*

Since all available MTI on the sample is covered with a layer of SC, no Hall bar device can be integrated onto the chip. Thus, measuring hysteresis curves or evaluating the (Q)AHE response of the present CBST layer is not possible. Applying a magnetic field at base temperature while applying a constant bias current reveals sharp dips in the resistance over the junction shown in figure 4.3 a). The position of the dip minimum depends on the magnetic field sweep direction and is situated at ±29 mT. This magnetic field is however only the external field, due to flux focusing of the surrounding superconducting material into the junction area the real magnetic flux penetrating the JJ is higher. Evaluating the junction area via Fraunhofer measurements was not possible. The coercive field remains constant when lowering currents but is influenced by increasing the temperature. In figure 4.3 b) the magnetic field sweep at 15 K is shown, exhibiting a WAL peak feature, but no dips symmetric around zero, suggesting a connection of the dips to ferromagnetism and superconductivity.

The low temperature hysteretic dip feature is reminiscent of spin valve devices, where antiparallel magnetizations in the path of spin-polarized currents cause potential differences [30]. While these devices usually entail semiconductors in combination with ferromagnets, experiments have also shown spin valve-like behaviors in FM-SC setups [169], [170]. There, the disordered magnetism during the domain switching decreases the magnetic gap size, causing the superconducting gap to exceed the former and thus leading to superconductivity over the weak link as shown in figure 4.3 c). This configuration of gap sizes, with $\Delta_m > \Delta_{SC}$, would fit to the previously given explanation of the resistance peak-feature in figure 4.2 b). A larger magnetic gap would dissolve any correlated quasiparticle states and therefore not allow Cooper pairs to penetrate into the MTI, effectively acting similar to a barrier causing a low transparency interface for the Cooper pairs.

A prominent difference between Qiu *et al.* and the data in figure 4.3 is the remaining high resistance in the dip. Whereas in [169] the resistance falls to almost zero, it remains on a high level in figure 4.3 a). It has to be noted that in contrast to [169], where a Josephson junction consisting of a single van-der-Waals gap is examined, in the present device the contact separation is of the order of tens of nms. A possible formation of correlated quasiparticles in the weak link might therefore be limited to a small area in direct contact with the SC, diminishing the resistance slightly. As shown in figure 2.7, the superconducting order parameter decreases rapidly in ferromagnets, requiring a much closer configuration of contacts in lateral weak link devices to reach full superconductivity [92]. Lower bias currents show an increase of drop depth. As shown in figure 4.3 d), at 20 nA bias current the drop amounts to 25% of the average high field resistance value. While lower bias currents might lead to a slightly enhanced induced SC coherence length further decreasing the dip resistance, the lower bias currents also coincide with starkly higher resistance over the junction (the peak feature as shown in figure 4.2 b)), which raises the average high field resistance $\bar{R}$ and might explain the increase dip depth.

At higher temperatures, figure 4.3 b), the critical temperature of the Nb is surpassed and no magnetization effects are present (with a Curie temperature of ~15 K in our films, compare chapter 3.2). The weak link is then reverted to a four-point longitudinal measurement. The measured weak antilocalization dip is different from the investigations in the CBST Hall devices of chapter 3.2, where exclusively WL is found. WAL has however been found in earlier samples of the UCLA group [51]. Moreover, additional doping effects of the Nb contacts influencing the small measurement region cannot be ruled out.

In conclusion, the devices built with CBST from the UCLA combined with Nb and Al_2O_3 from Jülich show no clear, thorough induced superconductivity in I-V measurements, but rather the opposite, an increase in resistance at low applied currents. This originates most probably from a barrier at the SC-MTI interface lowering the transparency for Cooper pairs. Possible causes for the low transparency are either the magnetism as mentioned above or a surface oxidation layer that formed before SC deposition. Both would decrease the possibility of Andreev reflections to a minimum and thus cause the incoming electrons to be reflected, inhibiting any transport at low bias voltages. Sweeping the magnetic field reveals hysteretic dips in resistance symmetric around zero external magnetic field. These features are comparable to measurements performed recently in [169], where the superconducting gap dominates in a FM Josephson junction whenever the magnetic gap is diminished due to magnetic disorder at the coercive field. The dips in our data thus can be interpreted as indications of a minute superconducting proximity effect when the magnetic gap is lowered, in turn increasing the transparency. The induced SC coherence length in the MTI is however too short to span the full weak link, lowering the resistance only up to 25%.

To further examine the causes for the low transparency, more information needs to be gathered about the Nb-CBST devices. In a simple Josephson junction layout like the one provided in these samples (see figure 4.2 a)), investigating the magnetic properties of the MTI film, like the coercive field, is difficult, if doable at all. The presence of Nb and the hard mask on the entire sample moreover do not allow for the patterning of an additional Hall device on the sample. Moreover, the possible oxidation layer on the MTI surface that formed before reentering vacuum after transport from the US to Germany is a disadvantage of this sample. Any oxidation needs to be avoided to rule out the oxidation layer as a cause for the bad transparency. Therefore, it is necessary to rework the stencil lithography mask into a design which allows for Hall and JJ measurements, favorably on the same chip or device, with MTI films grown in Jülich. This way, the magnetic properties like Curie temperature and QAH state can be investigated first before continuing with measurements involving superconductivity on a fully *in situ* fabricated device. The result of this design is the “Josephson Junction-Transmission Line Measurement” (JJTLM) device, which will be investigated in the following sections.

4.2 *In situ* Devices Utilizing CBST: The JJTLM Structure

After the *ex situ* combination of superconductivity with MTIs and its ambiguous results, a new design needs to be found to investigate magnetism and SC, preferably in one device. During the development of this JJTLM device layout, the progress shown in chapter 3 of growing our own MTIs was achieved. This enables fabrication of MTI JJTLM structures in Jülich, without the need of (ambient) transfers to or from other groups. The following sections will illustrate the process of JJTLM device fabrication and detail the measurements achieved in the first-generation designs, hampered by etching problems, and the second refined JJTLM generation. A comparison of CBST JJTLMs and MST JJTLM will reveal recurring features when combining MTIs with Nb superconducting contacts.

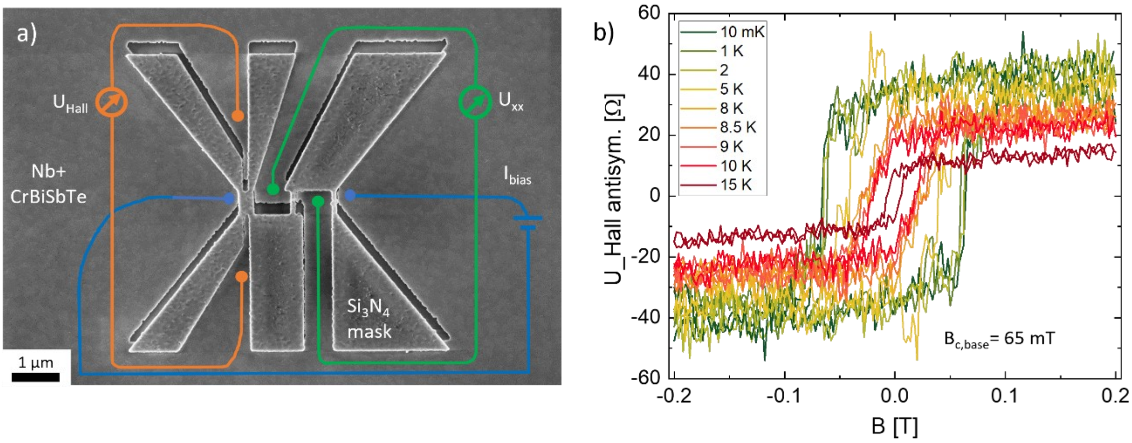

Figure 4.4: First generation JJTLM device. In a), an SEM micrograph of the full JJTLM device layout is depicted. Bias current (I_{bias}, blue), longitudinal (U_{xx}, green) and Hall (U_{xy}, orange) measurement capabilities are indicated. The surrounding circuitry is not yet etched and the mask not yet removed. Nb is deposited from the bottom, creating the shadowed regions seen above the mask. b) Hall measurements (antisymmetrized) on the device in a) reveal a FM hysteresis behavior, with decreasing remanence field towards higher temperatures, in line with plain film Hall devices. The comparably smaller maximal remanence field of 65 mT can be caused by flux focussing effects of the surrounding SC Nb.

4.2.1 First Generation JJTLM

To incorporate a Hall design into a device capable of JJ measurements, utilizing the shadow lithography explained in section 4.1, is complicated. Hall devices usually rely on a relatively long Hall bar of the material to be investigated, contacted with metal contacts at the ends of the bar for current biasing. As shown in chapter 3, at least four more contacts are needed for a longitudinal (xx) and a Hall (xy) signal, measuring the respective resistances. These are commonly spaced further apart, while in JJs a very proximal arrangement of contact is needed to investigate the short-range induced superconductivity. While the layout of the mask for the different contacts is manageable, the larger problem is the realization of a large strip of MTI thin film not covered with SC. Large mask configurations creating a superconductor-free strip would simultaneously degrade the quality of the TI film supposed to be grown under them. Therefore, in cooperation with Max Vaßen-Carl in the scope of his Master's thesis, the first-generation JJTLM is developed to consist of multiple Josephson junctions via thin bridges in succession, as shown on the right part of the device in figure 4.4 a). The bridges create two Josephson junctions, which can be used for the longitudinal measurements (green circuit) in a Hall configuration or as a JJ below the critical temperature of the SC. The current is applied between the left most and right most parts of the shown device (blue circuit). For the Hall measurement (orange circuit) a wider bridge is used, still allowing for MTI growth underneath it. The two SC fingers deposited on the top and bottom of the wider bridge shown in figure 4.4 a) act as the contacts for Hall measurements when a magnetic field is applied, with a contact separation the size of the bridge length. In figure 4.4 a) this amounts to 500 nm.

In contrast to the sample layout in the device in section 4.1, in the JJTLM design the insulating mask layer is reduced greatly. As shown in figure 4.4 a), only the protruding SiO_2/Si_3N_4 structure is left after sample fabrication, on the remainder of the sample the silicon nitride has been removed, leading to a plain Si surface after the silicon oxide release. This method yields three advantages. Firstly, since the Nb on the mask contributes to the flux focusing immediately at and above the JJ it is desired to remove the mask, which is facilitated by the decreased mask area. Secondly, when the SC on the mask and the mask itself is to be etched to remove the mask, in the same step the contact pads to the six contacts of the JJTLM device can be patterned from the surrounding excess Nb. Lastly, less mask leads to fewer possibilities to create short circuits by mask debris or contamination accumulations at the mask edge, which was a detrimental factor for the first investigated devices.

The fabrication of the JJTLM mask layers can be found in the appendix in section 7.3. For the device in figure 4.4 a) 20 nm CBST were deposited with rotation, following the recipe of the “lowCr” sample in chapter 3.2.1. The “lowCr” recipe is chosen in expectation of better transparency to the SC due to its lower magnetic doping. Unlike the previous sample, where two Nb depositions were used to ensure contact with possible edge channels, on this JJTLM sample only one 30 nm Nb layer is deposited after the CBST, followed by 5 nm Al_2O_3 capping. Strunz *et al.* [171] state that the edge channels in quantum spin Hall systems extends over about 50 to 100 nm, so that the induced superconductivity should also overlap with the edge channel profile if it is not directly on the SC edge. In figure 4.5 a) an alternate device layout on the same chip is shown with three Josephson junctions after contact definition etching. On the top and at the bottom in figure 4.5 a), the dark rough areas show where the SC, mask and parts of the Si are removed to separate the JJ leads from another. The Si_3N_4 mask is successfully removed, with only little mask left in the upper design part. However, the micrograph of the device with 4 µm long bridges exhibits a core problem of the first generation JJTLM design. Close to the remaining mask and at the bottom of the JJ dark patches are left. This mass of unknown origin, most probably hardened resist, conceals parts of the Nb contacts, hiding possible short circuits connecting the Nb contacts. This problem is more prominent for short bridges and thus the closer the larger mask areas are, showing that the etching close to the JJ regions strongly impairs the design.

In figure 4.4 b) a Hall measurement as illustrated in figure 4.4 a) is depicted. The Hall data is anti-symmetrized to filter out longitudinal signals. The symmetrized longitudinal measurement of R_{xx} is shown in figure 7.16, exhibiting broad magnetic switching peaks, accompanied by a WL background. A current of 10 nA is applied between the ends of the JJTLM device while sweeping a magnetic field perpendicular to the sample plane. At all investigated temperatures from 15 K to 10 mK a ferromagnetic hysteresis curve is found, saturating to a maximal remanence field of 65 mT. At low temperatures flux focusing will influence the coercive field, artificially lowering the coercive field. The AHE amplitude is only tens of Ohms, which is not surprising given the thickness of the film as well as the low Cr doping in the film. Moreover, a possible doping by the Nb contacts cannot be ruled out. Any influence of the contact pad Nb’s transition to superconductivity is filtered out by the antisymmetrization. The measurement seemingly exemplifies the validity of the JJTLM

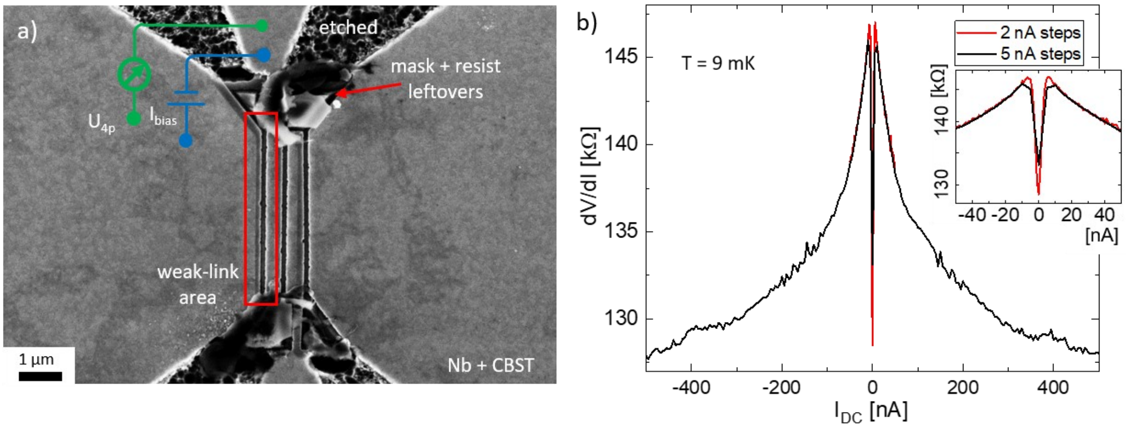

Figure 4.5: First generation device with three weak links in succession. After resist patterning and RIE etching, excess Nb and the mask are removed, creating the etched areas shown in a). Without mask, the JJ region marked in red is visible, contacted as indicated in blue and green in a four-point setup. Irremovable contaminations, most likely baked resist, can be identified close to the left-over SiO_2 pillars, creating short circuit hazards. Differential resistance measurements over an exemplary weak link are shown in b), exhibiting an increase in resistance at low currents. Only closely around zero current can a dip in resistance be identified, enlarged in the inset in b).

design, showing that Hall measurements are possible in the devices while providing Josephson junction devices for investigations of induced superconductivity.

In figure 4.5 b) a measurement over a weak link with 120 nm contact separation is depicted, revealing a trend similar to the results of the previous simple JJ device in the previous subchapter. At the base temperature of 9 mK no superconductivity or critical current is found, but an increase in resistance towards smaller currents. While the results are qualitatively similar, the differential resistance over the weak link is extreme, reaching into the 150 kΩ regime. There seems to again exist a barrier at the interface, creating a low transparency between MTI and SC inhibiting transport of correlated quasiparticles and thus resulting in a high resistivity over the junction. However, in contrast to the device of the previous subchapter, the *in situ* process rules out the formation of an oxidized layer, which could constitute the barrier. Therefore, the magnetism remains as the most probable cause for the low transparency, even though the Cr concentration in the utilized lowCr compound should lead to a smaller magnetic gap compared to the MTI used in the previous subchapter.

In figure 4.5 b) however, in contrast to the data of UCLA sample, a sharp dip in resistance in a range of ±5 nA (±5 mV with a 1 MΩ pre-resistance to define the bias current) can be identified. This finding is akin to measurements performed on Nb-HgTe-Nb junctions in [172]. They show a similar dip in a differential resistance peak at low bias voltage, caused by low transparency due to surface oxidation. The dip is identified as an indication of increased transmission probability of correlated quasiparticles, portending a presence of an induced superconductivity in the weak link. Towards higher bias the resistance levels off due to normal single quasiparticle transport over the weak link, which is not as affected by the low transparency at the interface. With the similarities in resistance characteristics measured in [172] and on the device in his section it can be assumed that the dip in figure 4.5 b) is a sign for an induced SC proximity effect in the Nb-MTI-Nb junction. The fact that this dip did not occur in the previous sample suggests that the lower magnetic doping lead to a higher transparency, allowing for a proximity effect with a short induced SC coherence length at low bias.

Lastly it needs to be mentioned that the high resistance over this weak link poses a problem to the overall approach of the measurement. A voltage was applied over a pre-resistivity of 1 MΩ to define the current flowing over the junction expecting a much smaller, negligible resistance from the device. The device resistance amounts to almost 15% of the pre-resistivity however, meaning the device resistance cannot be neglected compared to the series pre-resistance, necessitating a higher series resistance to be utilized in further measurements.

The results of the first successfully fabricated CBST JJTLM device reveal two highly interesting points. Firstly, the general *in situ* deposited device configuration allows for measurements of the magnetic properties of the underlying MTI film while also being capable of producing devices to investigate induced superconductivity. This fruitful design thus promises many follow-up measurements. After mask and excess SC removal an ALD dielectric could be deposited onto the device, followed by a gate layer enabling even more intricate investigations like gated Hall and gated junction I-V measurements. Secondly, the effect of increased resistance at low currents is also prevalent in this optimized design, which had not been exposed to ambient conditions before SC deposition**.** It is therefore unlikely that the resistance peak appears due to a bad interface from an oxide barrier between the MTI and the Nb, but rather due to the magnetism itself. By inhibiting the transport via Cooper pairs or correlated quasiparticles, the magnetism effectively acts as a barrier, lowering the transparency. Since the magnetic exchange gap is reliant on temperature and vanishes at T_{Curie}, a decrease of peak resistance with higher temperatures is expected, fitting to the data. However, the resistance dip in figure 4.5 b) points towards the existence of a short range induced proximity effect at low bias, a claim supported by the similar results in [172]. However, fabrication issues during patterning and etching could have had an influence on the JJTLM samples. The magnetic field dependent resistance dip feature that is present in the sample from the UCLA (see figure 4.3 a)) could not be unambiguously replicated in the JJTLM, pointing towards a necessary design rework, apart from the etching issues of this first generation JJTLM device.

4.2.2 Second Generation JJTLM

In figure 4.6 a) an angled view of a 2nd generation JJTLM after CBST deposition is depicted. The bridges responsible for the JJ after SC deposition are separated by hundreds of nanometers from disks of 1 µm diameter, which, after HF release, constitute the pillars (blue outline shown in figure 4.6 a)) upon which the mask rests. When removing the excess Nb and etching the mask to reveal the underlying device, only the centers of these circular or ellipsoid pillars need to be removed to dispose of the mask layer. With safety distances ranging from 500 nm to multiple micrometers, the JJs thus are situated away from the aggressive etching processes used during circuit definition and mask removal.

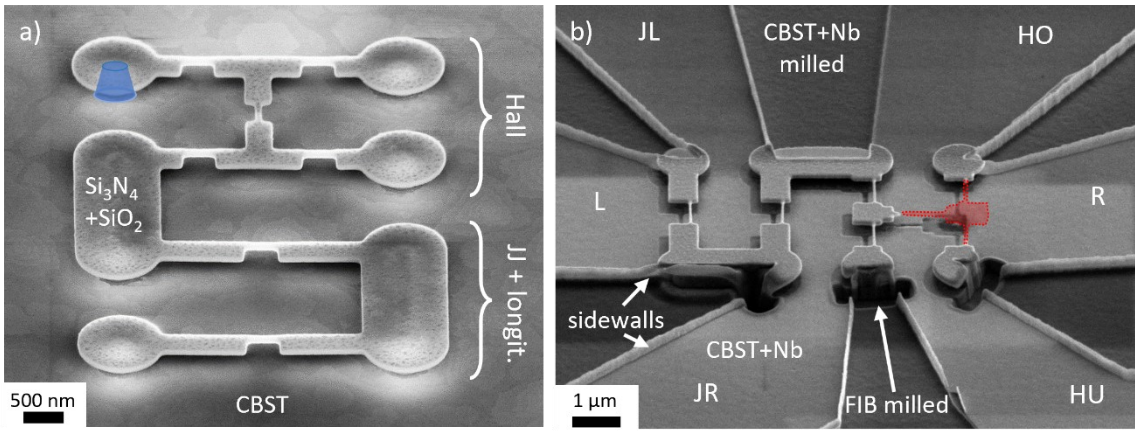

Figure 4.6: Second generation JJTLM devices. The suspended mask in a) is held by SiO_2 pillars (example in blue) at a distance from the junction-forming tapered region and 300 nm above the Si-MTI surface. Spacing pillars and active regions apart promises better etching performance. In b) a device etched with Ar milling is depicted. The milling removes the excess CBST+Nb, but does not release the mask, although a part was lost during cleanroom fabrication (red outline). Side walls are formed, connecting mask to active layer. These connections are later cut via localized focused ion beam (FIB) milling. FIB is performed on all connections, 3 of 8 milling steps were already performed in b). The six contacts are named by their position, right contact R and so on.

Additionally, the Hall configuration is modified into an additional JJ perpendicular to the other junctions and parallel to the current, which would be applied between L and R in figure 4.6 b). In comparison to the first-generation devices this leads to a smaller region of MTI not covered with SC. Only this area will be influenced by the external magnetic field during Hall measurements, the Hall measurements (from HO to HU in figure 4.6 b)) should however still yield hysteresis and Hall signals. The fabrication process is unchanged from generation one devices and the growth process for MTI, Nb and capping can also be maintained. As shown in figure 4.6 a) high quality thin film growth of CBST is possible, with few protruding TI shards on the hard mask. This yields sharp edges during Nb deposition in the following step. To investigate films more alike to those in section 3.2.2, the growth time is however shortened, decreasing the thickness to approximately 8.6 nm of CBST.

Due to prolonged outage of the RIE systems during device fabrication, an ion milling process was chosen to remove the Nb. The samples were milled with Ar ions at an acceleration voltage of 500 V with a current of 120 mA for 5 minutes, with ten alternating 30 second etching and 30 second cooling steps to not burn and harden the UV6 resist, yielding a JJTLM device as shown in figure 4.6 b). In contrast to the RIE etching a much smoother etching profile on the Si is achieved. However, as is indicated in figure 4.6 b) in the left part of the picture, with ion milling side walls are formed, which creates new challenges for device fabrication. The walls are formed by milled Nb and MTI, which are redeposited to the edge of the patterned resist layer. After removal of the resist via acetone and isopropanol, these metallic side walls persist. The side walls would not generally pose a problem in the stencil lithography devices, since the important JJs were covered with protective resist and the side walls are positioned far from them. However, the height of the

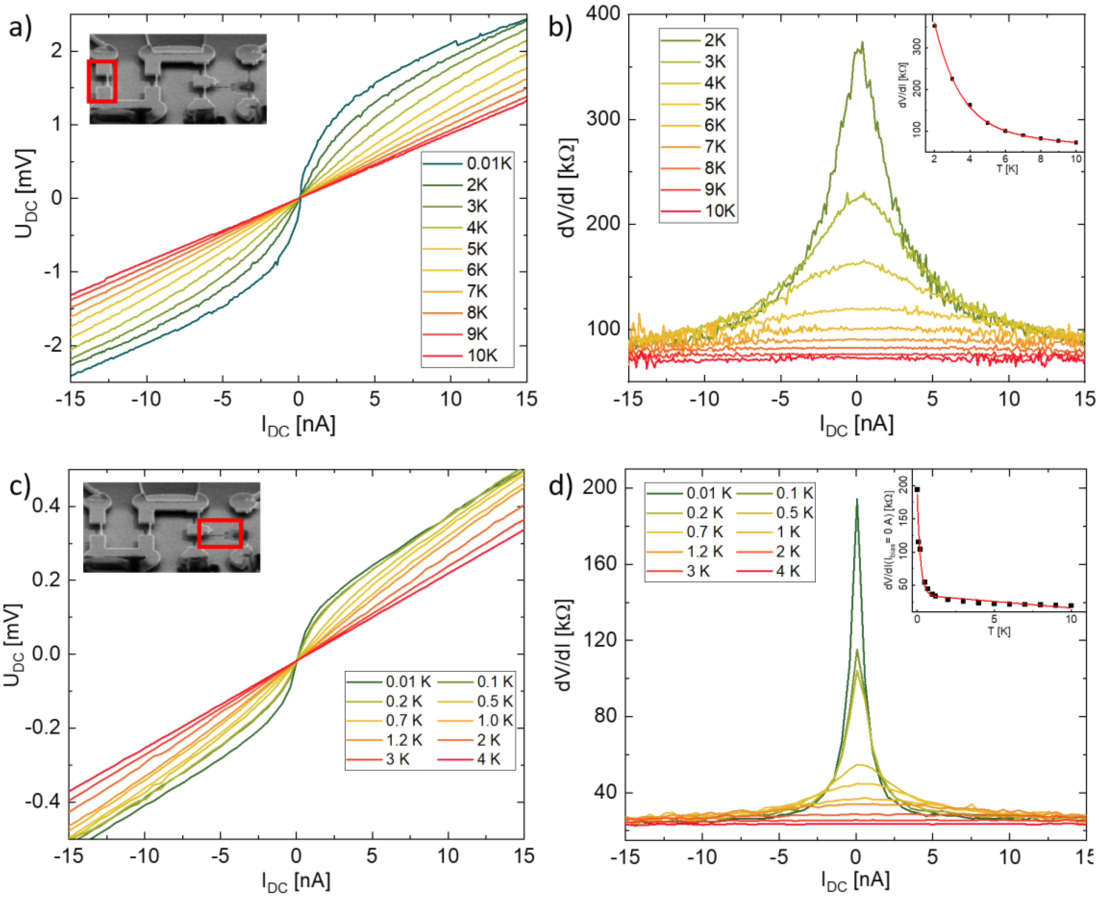

Figure 4.7: I-V and differential resistance of two junctions in the investigated device. The I-V characteristics in a) and c) at the wea links marked in the insets show a steep increase at zero bias current, increasing in slope with decreasing temperature. The differential resistance in b) and d) thus exhibits a sharp peak at zero current bias. The prominent feature reaching into hundreds of kΩ is lost towards higher temperatures, subsiding with the SC of the Nb electrodes, accompanied by thermal softening effects. The difference in resistance between the two junctions on the same chip can be linked to the decreased JJ separation of 80 nm in a) and 60 nm in c). Moreover, due to the device layout there might be additional paths over other contacts involved in c) and d). The inset in d) shows a fit (red) to the temperature dependent peak height, suggesting an exponential behavior at low and a linear behavior at higher temperatures.

walls is unexpectedly tall, connecting the Nb of all contacts via the sidewalls over the mask pillars. The mask and pillars themselves could not be removed within reasonable etching times as visible in the top part of figure 4.6 b).

In order to still measure the devices, the chip is inserted into a focused ion beam (FIB) chamber, capable of using a high energy Ga ion beam to mill in predefined areas. As shown in figure 4.6 b) in case of the bottom four pillars, rectangles are defined onto the connection from the side wall onto the mask. The FIB etches deep holes at these positions, cutting the connection from metal layer to mask. In figure 4.6 b) at the top, three side walls are still connecting both levels.

The contacts are thereafter electrically separated, with the predefined weak links being the positions where the SCs are closest to another. The mask could be removed during this process, but in order to not harm the sample in further process steps, it was decided to leave it standing, accepting flux focusing effects. The sample is glued into a chip carrier, bonded with aluminum wire and inserted into a cryostat, repeating the measurements done on the first generation sample with the second generation sample layout. After cooling down to the base temperature of 10 mK, four-point measurements over two junctions in one device are performed, the respective junctions marked with red rectangles in the insets in figure 4.7 a) and c). The bridge size amounts to 80 nm width x 800 nm length (L-JL) and 60 nm x 800 nm (HO-HU), replicating weak links on the underlying CBST film, which was grown to have a thickness of 6.7 nm, following the recipe for the hiCr compound established in chapter 3.2.2. The hiCr compound with a larger magnetic gap in this optimally fabricated junction is chosen to compare with the lowCr compound of the previous subchapter 4.2.1.

Hall investigations on the device depicted in figure 4.6 b) exhibit hysteretic resistance plateaus unlike the expected AHE hysteresis found in normal Hall bars or the JJTLM device in the previous subchapter (see figure 4.4 b)). Since this chapter is however focusing on the interplay of MTI and induced superconductivity, the Hall data and an extensive explanation of the observed phenomena via magnetic domain switching effects can be found in the appendix in chapter 7.4.

Similar to both previous investigations of SC on MTIs, in all investigated junctions the same peak behavior is measured. I-V and differential resistance graphs of two exemplary junctions are given in figure 4.7 a) and c) as wells as b) and d) respectively. While the increase in resistance between the HO-HU contacts shown in figure 4.7 d) is comparable to that of the previous 1st generation device at 10 mK (figure 4.5 b)), ranging in the 100-200 kΩ regime, the L-JL junction in figure 4.7 b) exhibits a resistance 2.5 times as high. At 2 K the resistance amounts to 370 kΩ, only set to increase further towards lower temperatures. The L-JL junction is wider than the HO-HU junction, a lower resistance is therefore expected. The resistance of the latter could however be additionally decreased by possible additional current paths via the JR or R electrode, involving two weak links each. The insets in figure 4.7 b) and d) show the evolution of peak height at zero bias current with temperature. The fit consists of an exponential and a linear component, suggesting an exponential dominance of the low transparency processes at low temperatures and a linear behavior for higher temperatures, which follows the resistance development in the hiCr MTI with temperature (compare figure 3.8 f)). As in the previous subchapter, a low transparency interface is present, strongly suppressing the penetration of Cooper pairs into the MTI. The absence of a resistance dip at low bias currents suggests that the larger magnetic gap of the hiCr compound decreased the transparency even further, inhibiting any formation of proximitized superconductivity in the MTI as was postulated in chapter 2.2.4.

Thus, in the second generation JJTLMs no dip in the I-V curve close to zero applied bias current could be found, which is present in the previous sample (figure 4.5). This is even though the design and etching process was improved upon. To rule out any fundamental issues in the combination of materials, design concept or fabrication processes an identical JJTLM device with non-magnetic TI is fabricated, see figure 7.19 in the appendix. On this device, regular Josephson junction experiments, akin to those in more simple JJ layouts performed in our group ([105], [162], [173], [174], [175]), with expected critical currents could be performed. This strongly suggests that the JJTLM approach itself is viable and that the low transparency at the interface is indeed caused by the magnetic nature of the employed CBST MTI film and not caused by fabrication issues, which could not be excluded in the previous subchapters.

There are still many possibilities to increase the likelihood of finding a proximity effect in the MTI. Utilizing a penta-layer stack of BST-CBST-BST-CBST-BST instead of a continuously doped layer or a sandwich structure like in chapter 3.2.3 would entail a BST buffer layer between the SC and the magnetically doped compound. This might increase the interface transparency and lead to a higher induced SC coherence length in the MTI. On the other hand, the Cr itself might be the cause of the absence of SC, creating a magnetization gap too large for induced SC and Cooper pairs to form. This possibility will be shortly researched in the next section, where $MnSb_2Te_4$ will be investigated in a JJTLM to compare Cr and Mn based MTIs regarding their SC adaptability.

4.3 Comparison with a $MnSb_2Te_4$ JJTLM

In figure 4.8 a) a finished JJTLM device with a $MnSb_2Te_4$ thin film as the MTI layer after RIE etching is depicted. The device allows for a direct comparison between MTIs with two different magnetic constituents. The MST layer is grown in the BST-MBE chamber following the recipe described in the appendix (chapter 7.1.2), however the substrate temperature is adjusted to fit to a different holder, a vacuum transfer holder. This holder is needed to provide the *in situ* deposition of SC on the MST film device. After growth at T_{sub} = 360°C with a rate of 2 Å/s resulting in an MST film of 10 nm thickness with a stoichiometry of almost pure $MnSb_2Te_4$ (MST 14:1 MnTe via RBS), the vacuum transfer holder is moved *in situ* from the growth chamber into a vacuum suitcase, which can be detached from the chamber while maintaining a vacuum in the 10^{-9} mbar range. The sample is then transferred to the Nanocluster, where it is channeled into the M13 MBE chamber for Nb and subsequent capping deposition, following the established recipes, amounting to 15 nm Nb and 5 nm Al_2O_3. The fabrication then continues as described in section 7.3, with one addition.

In order to reliably remove the bridge and thus decrease the presumed flux focusing effects present in the previously investigated devices, an exfoliation technique is utilized to remove the free standing Si_3N_4 mask. Before RIE etching, the sample is coated with a polymer layer provided by *First Contact*^{TM} (*FC* in the following). *FC* is a tool to clean optical equipment of dust particles by applying a layer of epoxy and, after shortly drying it, pressing it onto a sticky tape, with which the epoxy is exfoliated from the sample. Any contaminations are removed together with the epoxy, leaving only the clean surface of the optical instrument. During the time of this thesis it was discovered that on stencil lithography samples with a design similar to JJTLMs, *FC* can be utilized to remove the Si_3N_4 mask layer. While Si_3N_4 mask pieces attached to SiO_2 directly can remain after exfoliation, as shown in figure 4.8 a), suspended nitride is reliably removed. This technique will to a larger extent be used in the following chapter to enable scanning tunneling microscope measurements on prepatterned samples. For the JJTLM structure the removal

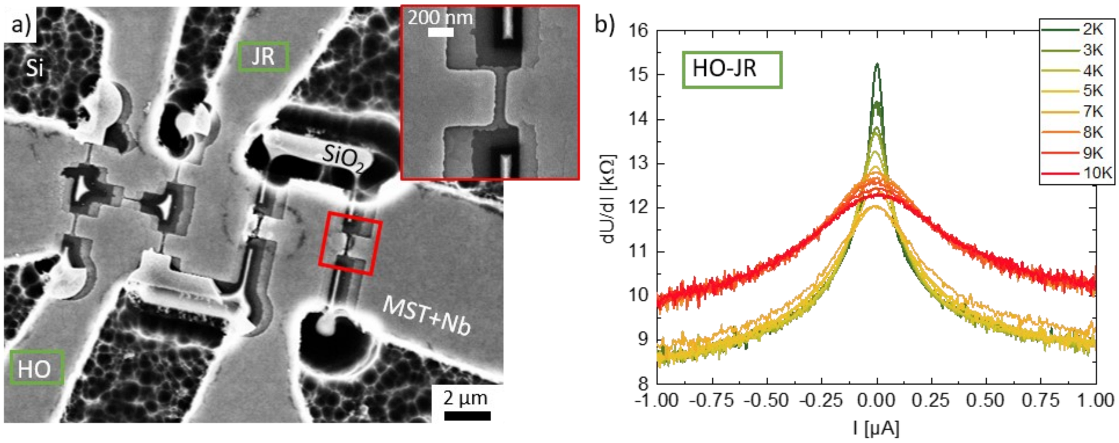

Figure 4.8: a) SEM micrograph of a $MnSb_2Te_4$-Nb-Al_2O_3 JJTLM device. The rough surface reveals etching of the layers down into the silicon, avoiding shorts between contacts. The Si_3N_4 mask has been removed prior to RIE etching with First Contact polymer exfoliation, leaving only SiO_2 stumps. The inset shows a zoom in of the L-JL weak link before RIE etching. The etching caused damage to some JJ, likely due to static between the Nb layers, disqualifying junctions L-JL and JL-JR for measurements. Thus, JR-HO is measured as shown in b). Again, the peak feature known from the CBST compounds is observed. The overall differential resistance is lowered, revealing a drop in resistance when losing SC in the Nb contacts. No indication of induced SC is found.

of large parts of the mask lessens the flux focusing effects of the Nb covered mask while additionally increasing reproducibility in further fabrication steps by eliminating the possibility of side walls and shadowing effects during etching.

The sample is bonded just as the CBST JJTLM devices and inserted into the same cryostat. To test the I-V characteristics, four-point measurements are performed over multiple weak links, with the measurements over HO-JR shown exemplarily in figure 4.8 b) for temperatures between 2 K and 10 K. Strikingly, the behavior is similar to the one seen in the CBST-Nb JJTLM devices, exhibiting a peak in differential resistance towards zero applied voltage. No indications of induced SC are measured in any of the present weak links. The low transparency is therefore independent of the nature of the ferromagnetic dopant, but probably only reliant on the strength of the magnetic exchange energy itself[2]. The lower overall resistance in the equally sized junction compared with the CBST device in chapter 4.2.2 might point towards a weaker magnetic barrier than in the CBST compound. This is proposedly be helped by the layered nature of the MST compound, especially in a thin film.

There are features in the data of figure 4.8 b) not seen in previous investigations. Between 7 K and 8 K the curve shifts by more than 1 kΩ, fitting closely to the superconducting transition temperature of the Nb contacts between 7 K and 7.5 K measured on the contact pads themselves. The shift in resistance thus most likely shows the transition of the contact metal to superconductivity and is more noticeable in the present junction due to the overall lower resistance in the 10 kΩ range, compared to the 100 kΩ range in the CBST devices. Moreover, the peak feature is present, although broadened, also at higher temperatures

---

[2] Recent, in-progress, investigations in our group with V-based MTIs also exhibit the resistance peak, further supporting this claim.

above the T_c of the Nb. An additional weak localization effect is therefore suspected to be present. This WL might occur also in the CBST devices, however it is again more visible at higher temperatures in MST due to the overall lower resistance compared to the CBST JJTLMs investigated.

4.4 Discussion

To summarize, the exaggerated resistance peak is present below the critical temperature of the Nb, however only with magnetic TI thin films, clearly suggesting a connection to the magnetization of the film. As was detailed in the theory of the LRPE in chapter 2.2.4, it is theoretically possible to combine SC and magnetism to form not only induced SC but also p-wave superconductivity [94], [99]. In the presented data, no proximitized region spanning the full weak link and thus no supercurrent over a junction can be measured in the devices. Inquiries into literature on MTI-SC devices reveal one instance of similar behavior measured on a JJ consisting of a $MnBi_2Te_4$ flake proximitized with NbN or Nb separated by 60 nm [176]. A resistance peak at low bias is found, reaching into the kΩ range. Xu *et al.* therein argue that “Lower resistance at greater bias voltage is observed as a result of general tunneling behavior […]” and that at low-bias voltage a reduced barrier height and therefore higher tunnel probability is present [176]. Peak shoulders in the differential resistance in the kΩ range are interpreted as an indication for the tunneling process and for an induced superconducting gap. While the assumption of a tunneling behavior in [176] is disputable, since no supercurrent or dip in resistance is measured, the fact that another comparable experiment on an MTI film contacted in a JJ layout with NbN and Nb shows the resistance peak underlines the difficulties of proximitizing the magnetic layer.

In the scope of this work, multiple optimization steps have been undertaken towards a better proximity effect in MTI-SC hybrid devices. By employing stencil lithography, chemical processes on the MTI surface for device structuring have been avoided via a patterned growth. Performing the metal deposition *in situ,* followed by a capping, promises optimal interfaces by preventing any oxidation of the functional layers. Lastly, design reworks shifted any postprocessing away from the junctions themselves to inhibit contaminations during contact definition. However, still only indications of induced superconductivity have been measured as shown in the previous paragraphs. Therefore, it is important to gather the issues that might inhibit induction of superconductivity in the MTI-SC system in order to efficiently tackle them in future experiments:

1. It is possible that generally no ABS, which mediate the supercurrent in the proximitized regions, can form in the MTI region. Specifically, this would entail that the strong inherent magnetism, i.e. a large magnetic exchange energy, in the ferromagnetic TI breaks up the correlated quasiparticle states immediately as postulated in chapter 2.2.4. This would lead to a low transparency at the interface of the Nb and MTI, leading to a highly resistive junction, similar to S-I-N-I-S devices and as observed in the experiments in this chapter [172].

2. If ABS are generally possible, the range of the induced SC in the MTI might still be shorter than the smallest attainable weak link separation with the stencil lithography technique. As shown in figure 2.7, the strength of the SC ordering parameter decreases much faster for a SC-FM interface than for an SC-semiconductor interface for example. Especially when the magnetic exchange energy becomes large $\Delta_m \gg k_B T$, the decay length of the triplet state $\xi_{S_z=\pm 1}$ reverts from being of the order of $\sqrt{D/2\pi T}$ (see chapter 2.2.4) to $\sqrt{\hbar D/\Delta_m}$, with D the diffusion length [94]. Typical Δ_m of MTI in the meV range would then cause decay lengths of a few nanometers.

3. There are concerns that the properties of (magnetic) TI devices are altered when they are irradiated by high-voltage electrons during SEM or electron beam lithography. Damaged thin films exhibit strong increases in charge carrier density and loss of mobility after exposures at 30 kV and 50 kV. For the patterning of the JJTLM structure, 100 kV are used in electron beam lithography, possibly resulting in yet unknown quality deterioration [177]. The first MTI weak link device in chapter 4.1 had not been exposed to high voltages and is the only device to show hysteretic magnetic field dependent drops in resistance, fitting to possible induced SC during the magnetization switching.

It needs to be stressed that these findings do not mean that the approach of using lateral junctions to investigate the interplay of MTIs and SC is a dead end in general. In fact, lateral JJs on FMs of various scales and layered JJ with thick, but proximitized, FM layers have been realized in literature ([94], [102], [103], [178], [179], [180]). It is therefore possible to create ABS in ferromagnetic TI systems, however more experiments need to be undertaken to fully explore the available parameter space. The bullet points above point towards three main issues that need to be explored in greater detail to increase the transparency and thus enhance the induced superconductivity: the effect of the magnetization strength of the FM MTI layer, the penetration length of possible Cooper pairs into the FM layer and problems regarding the fabrication via electron beam lithography.

In sections 4.1 and 4.2.1 the measurements on the MTI-SC hybrids show signs of induced superconductivity in line with literature ([169], [172]) and portend that the establishment of correlated quasiparticles in the MTI is not fundamentally a problem as suspected in the first bullet point. Rather, the magnetic gap in the MTI causes a low transparency which inhibits sufficiently large induced SC coherence lengths. In [181], Kou *et al.* show that lowering the Chromium concentration results in a smaller magnetic gap while maintaining magnetism in the sample. The data of the first generation JJTLM, where lowCr MTI was grown (Figure 4.5 b)), and the second generation JJTLM, utilizing hiCr MTI (Figure 4.7 d)), at base temperature enable a comparison of the involved Cr concentrations and therefore the magnetic energy gaps. The weak link measurements reveal that only in the lowCr concentration compound dips in the resistance peak at low bias are found. A higher transparency and therefore stronger proximity effect caused by a lower magnetic exchange energy in the MTI can thus be assumed, in line with Maier *et al.* [172]. Moreover, although the peak feature is of similar height in the two devices, the increase towards low bias is only of the order of a factor x1.5 for the lowCr sample, while it is of the order of x9 over the HO-R junction for the hiCr device. This is even though the contact separation in the lowCr device is doubled as given in table 4.1. While there may be influences from the device geometry or fabrication to the resistance that differ between the devices, the lowered resistance nonetheless points towards a lower barrier for SC-MTI interaction with lower magnetic doping in CBST. Therefore, lowering the magnetic dopant content in CBST further could enable induced superconductivity over the full weak link by increasing the induced SC coherence length. Moreover, utilizing heterostructures of CBST/BST or MST/ST might yield fruitful results due to lower magnetic gaps at the FM-SC interface.

Device	Cr content	Junction separation	Junction width	Resistance peak	Resistance increase
1st generation	0.15	120 nm	175 nm	146 kΩ	150%
2nd generation	0.24	60 nm	800 nm	195 kΩ	930%

Tab 4.1: Comparison of the weak links investigated at base temperatures in the first generation and second generation JJTLM devices. Cr content refers to x in $Cr_x(BiSb)_{2-x}Te_3$*. Peak resistance measured at zero bias current. Resistance increase compares peak value with base resistance at high bias derived from Lorentz-fits to the peak value at base temperature.*

If decreasing the magnetic exchange energy alone does not lead to the desired extension of induced SC coherence length, the distance between the JJ contacts should be lowered, as stated in bullet point 2. The weak link separation is limited by the bridge width of the stencil lithography technique. The thinnest bridges realized in our group feature a width of 30 nm, which might suffice to find induced SC. By carefully adjusting the angle of the SC deposition, the shadow of the bridge can however be artificially narrowed, similar to the double deposition in chapter 4.1 (see figure 4.2 a)). This way, contact separation dependent junction measurements can be performed in the future to identify the penetration depth of possible correlated quasiparticles in the MTI. Additionally, locally measuring the induced SC gap profile close to the MTI-SC interface would help to identify the limitations of the induced SC.

Lastly, addressing the third bullet point, fabrication issues due to electron beam lithography can be avoided by changing the way the contacts are patterned after growth of the devices. Since only the first junction device, which was not exposed to electron beam lithography after thin film growth, showed magnetic field dependent resistance dips (figure 4.3 a)) in line with induced superconductivity in magnetic materials [169], further care should be taken during post-growth processes. By altering the mask designs before growth, optically patterned contacts are a possibility, avoiding electron beam radiation. Furthermore, the altered masks can be designed to enable the deposition of gates after contact definition as gate dependent measurements might lead to new insights in the hybrid devices, similar to the investigations performed by Xu *et al.* [176].

In conclusion, while the JJTLM devices established in this chapter do not show the desired induced p-wave superconductivity in the SC-MTI hybrid devices, they successfully point out the directions in which new insights may be achieved. The devices allow for measurements over the *in situ* fabricated weak links capable of Josephson junction measurements and also enable Hall measurements in the same devices, achieving what the structures were designed to do. Two clear indications of induced superconductivity are found, both pointing towards the strength of the magnetic exchange energy as a cause for a low transparency at the MTI-SC interface, which results in high resistances at low bias. The proposed dependency on the magnetic gap illustrates the importance of lower dopant concentration in the MTI or of heterostructure MTIs, promising an improvement of the low transparency.

To gauge to which extent the contact separation needs to be lowered or how far the magnetic gap needs to be decreased, locally measuring the induced and the magnetic gap at the interface of MTI and SC would provide valuable insight. Revealing these qualities on a microscopic level promises many fruitful investigations, is however hard to realize. An instrument capable of such measurements is the scanning tunneling microscope (STM), which measures the local density of states directly via a tunneling current. Capable of probing not only the MTI characteristics but also those of the SC on a miniature scale without additional exposure to high voltage electron beams, STM might provide exactly the tools needed enhance future JJTLM investigations. The obstacles towards the investigation of the SC-MTI interface via STM and their solutions will be laid out in the following chapter, where a variant of stencil lithography is devised to create SC-(M)TI devices tailored to STM experiments.

5 Removable Ultra High Vacuum Lithography and its Application in Scanning Tunneling Microscopy

In the previous chapter it was shown that inducing superconductivity into magnetic topological insulators is inhibited by a bad transparency at the SC-MTI interface. The magnetic exchange energies suppress the formation of pairs of correlated quasiparticles, leading to a heavily diminished induced SC coherence length and to resistance peaks at low bias currents. However, in the work of other groups ferromagnetic JJs even with strong ferromagnets have been achieved [182], [183]. The question is therefore: how large is the induced SC coherence length in MTI-Nb hybrids and what can be done to enlarge it? To answer this question and to be able to more closely inspect the superconducting proximity effect at the interface of the (M)TI and the SC, an investigation with scanning tunneling microscopy (STM) is chosen to be conducted. Creating hybrid structures of MTI and SC *in situ* viable for STM however requires the development of new fabrication techniques. In the beginning the basics of STM will be shortly detailed, followed by a first approach towards realizing SC-(M)TI hybrid devices viable for STM investigations using removable stencil masks. While removable masks hold great potential for STMs with atomic force microscopy (AFM) capabilities, in the subsequent section a new iteration of stencil lithography will be developed, which will be capable of providing the desired interfaces for MTI-SC investigations without the need of AFM, making it more suitable to any commercially available STM. If successful, this approach would open the way to a range of STM experiments capable of detecting and validating MZMs, as detailed in [184].

5.1 Scanning Tunneling Microscopy Basics

STM is a highly surface sensitive measurement, relying directly on quantum mechanics. It maps the local density of states (LDoS) of a surface via the tunneling current from an atomically sharp STM tip to the sample. The tunneling current is determined by the tunneling probability, which itself depends on the distance of sample to tip, the work function of tip and target material and the LDoS on the surface. The current is proportional to

$$I_{tunnel} \propto e^{-2\kappa l}\,, \tag{5.1}$$

with l the distance from tip to sample and $\kappa = \sqrt{2m_e \phi_{\mathrm{avg}}}/\hbar$, where ϕ_{avg} is the average barrier height, depending on the work functions of the materials involved, and m_e the electron mass. The exponential dependence on the distance is key in STM, as a difference of 1 Å in distance can lead to a decrease of current by one order of magnitude. First the sample topography is measured on a small scale with a constant tunneling current and relatively high bias voltage, followed by a scan on the selected surface with a constant distance varying the bias voltage. The tunneling current in this voltage bias sweep depends on the LDoS, yielding an insight into the surface band structure. In contrast to angle resolved photo emission spectroscopy, no momentum dependent measurements can be performed, however by applying positive or negative voltages between tip and sample, the LDoS at energies below and above the Fermi level can be mapped. STM is most efficient at low temperatures, since the LDoS fluctuates heavily with temperature. When assuming $T \rightarrow 0$ K, the differential conductance from tip to sample (or vice versa) is given by

$$\frac{dI}{dV}(V)|_{T=0} \propto N_s(eV), \tag{5.II}$$

with $N_s(eV)$ the density of states at the surface of the sample at the energy eV. Investigating the LDoS this way is called scanning tunneling spectroscopy (STS). For a more detailed explanation the reader is referred to [185]. [186]

5.2 Membrane Mask Lithography Paired with SAG

To investigate the evolution of the induced superconductivity in (magnetic) TIs, first the right sample design needs to be chosen. It has been shown by Jia and Sun in 2017 that by applying a magnetic field perpendicular to the surface of a TI (Bi_2Se_3) which was proximitized by an underlying layer of $NbSe_2$ superconductor, signatures of Majorana Zero modes could be found [85], [187]. These signatures manifested in the centers of the Abrikosov lattice points, made up of magnetic vortices in the surface of the superconducting layer where a magnetic flux penetrates the type 2 superconductor. By employing spin-polarized scanning tunneling microscopy they measured a polarization dependent differential conductance peak at zero bias, in line with theoretical predictions for spin selective Andreev reflections involving Majorana zero modes [188]. Other studies further showed the possibilities to induce SC into the TI surface states [189], [190].

Although their experiments open up to the possibility to directly find signatures of MZMs in SC/TI structures, their approach is limited by the large scale of their samples. A $NbSe_2$ pseudo-substrate is exfoliated and thereafter TI is grown via MBE onto the exfoliated flake. The overgrown flake is then *in situ* transferred to an attached STM to protect the surfaces of the grown films from surface oxidation. This procedure only allows for plain film investigations with random distributions of the Abrikosov vortices. Moreover, only one surface can be studied, either the SC or the TI surface. For studying the proximity effect in detail however it would be beneficial to access the surfaces of both quantum materials with an STM tip. While this is easily achievable with *ex situ* processes by depositing SC materials onto parts of the TI via lithographical methods, these steps involve resist and development processes which may potentially alter the TI surface qualities and render STM studies impossible as argued in the chapters before.

As shown in chapter 4, we can produce *in situ* patterned devices via UHV lithography for different applications. With this technique we are in principle able to create structures of

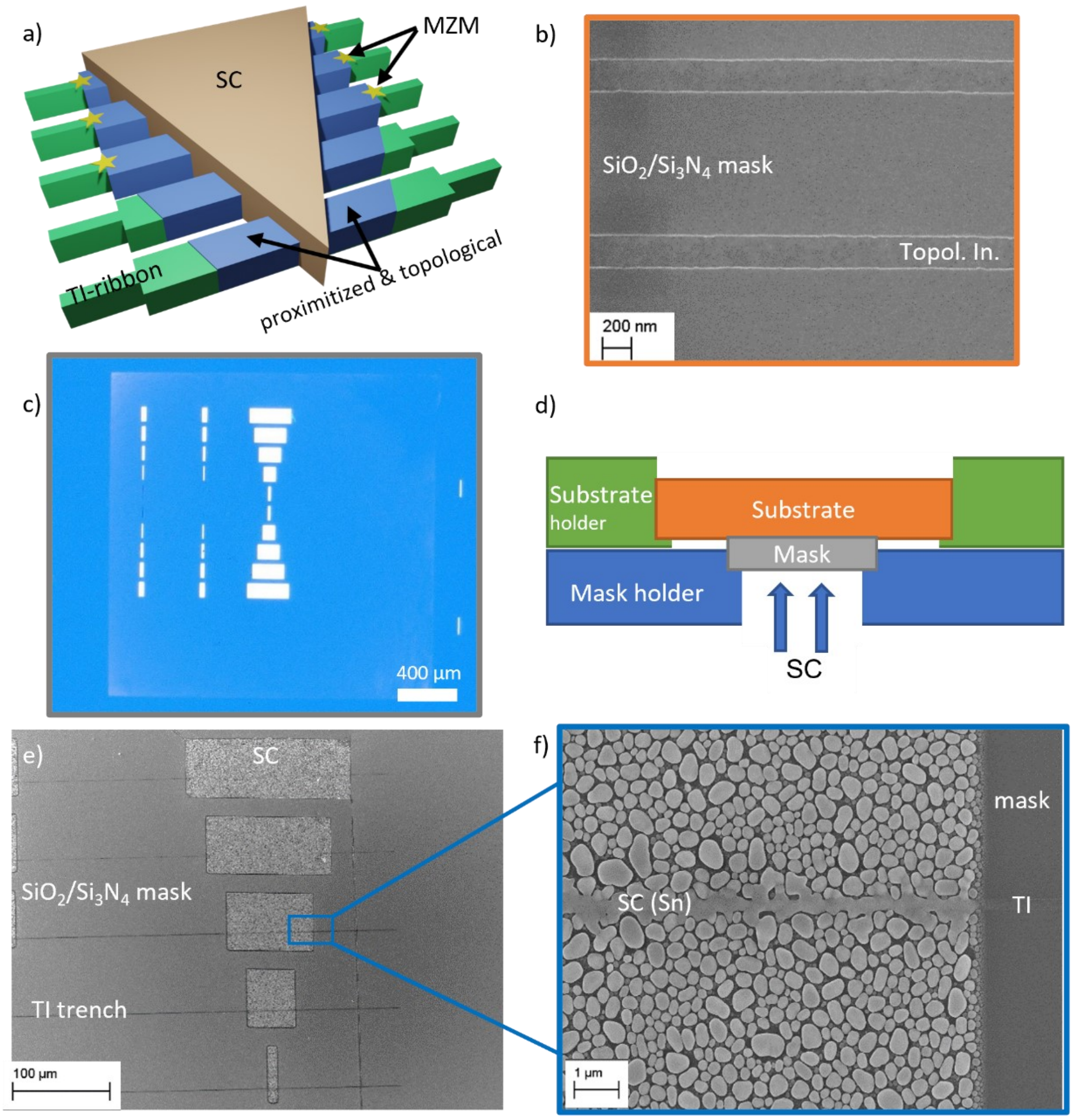

Figure 5.1: Concept and realization of STM-compatible in situ fabricated nano-scale TI ribbons combined with patterned superconductor: a) Schematic depicting the desired structure. Selectively grown TI nanoribbons (green) with changing cross-section are partly covered by a superconducting material (brown), causing proximitized superconductivity in the TI adjacent to the latter (blue). The 1D structure is re-topologized by an in plane magnetic field. When the diameter is changed, a trivial gap is opened again, so that at each end of the topological and superconducting region (blue) a Majorana mode is proposed to exist (stars). b) Selectively grown TI ($(BiSb)_2Te_3$) nanoribbons in prepatterned trenches etched into a SiO_2/Si_3N_4 mask. c) Mask membrane fabricated following [163] *with incrementally widening holes to deposit SC onto the TI nanoribbons as shown in a). d) Configuration of mask, substrates and holders during growth in the MBE chamber. The mask is inserted under the substrate after TI growth to deposit SC selectively. e) and f) Finished samples with SC patches deposited on trenches filled with TI. The enlarged picture in f) illustrates the non-continuous growth of SC due to insufficient cooling capabilities.*

arbitrary size and layout to investigate the interface of TI and SC as desired. However, since STS and STM measurements rely on close proximity of sample and measurement tip, comparatively large structures like those used in chapter 4 pose a problem. Bridge structures with a height of up to 400 nm over the substrate surface inhibit the movement of the STM tip and create a hazard, potentially destroying the tip, which would result in an interruption of measurements. In the lead up to the development of the fixed on-chip mask samples used in chapter 4, another technique was developed utilizing removable stencils, that could be introduced and removed in between growth steps and allowed for selective area epitaxy of TI as well as superconducting films [163], [165], [191], [192]. The deposition through the mask however proved to be not as precise as the on-chip mask due to blurring effects and therefore smeared out edges of the deposited materials, resulting in shorted Josephson junctions. Nonetheless, the process allows for the introduction of multiple masks with varying layout one after each other. Thus, arbitrary stacks of different materials could be deposited in changing patterns *in situ* onto TI that could either be grown as a plain thin film or into prepatterned SAG designs, see figure 5.1.

The latter feature makes this stencil mask technique interesting for STM applications. Since the mask can be removed *in situ* after SC deposition, the STM tip can freely access the structures. This allows for *in situ* fabricated quasi-1D TI structures covered with SC only partly, so that the SC behavior moving from the SC onto the TI can be directly investigated. Close to the interface, proximitized TI forming a topological superconductor should be present, proposedly hosting Majorana physics when an in-plane magnetic field is applied to re-topologize the quasi-1D nanostructure. In the experiments of Jia *et al.* a STM accessible Majorana mode is created at the top surface of the film where the magnetic flux leaves the surface via the vortex [85]. Since Majorana quasiparticles only exist in pairs, a second Majorana mode arises at the other side of the approximately cylindrical vortex threaded area. If one however considers laterally grown ribbons of TI covered partly with SC, the two Majorana modes proposedly exist at both ends of the covered region [193]. Since Majorana quasiparticles are their own anti-particles, when positioned close by each other, the Majorana state wave functions start to hybridize and if brought too close, will annihilate [194], [195]. This behavior of the Majorana modes is characteristic for MZMs and should be observable in STS measurements on these devices by comparing the zero bias peak response of multiple structures of varying SC island length.

The desired structure to test this behavior is shown in figure 5.1 a). It combines TI ribbons with a triangular superconducting patch. The change in diameter of the TI ribbon is used to form topological and non-topological areas. With a specific in plane magnetic field of one flux quantum threading the wire in the wider region, topological and proximitized parts of the TI nanoribbon are formed (blue). The thinner nanoribbon is non-topological (green) with a trivial gap and thus a Majorana mode is proposed to arise at the edge (stars in figure 5.1 a). Due to the tapered form of the SC covering parallel ribbons, the latter are covered by decreasing width of superconducting regions. Thus, the proximitized regions (blue) gradually approach each other. The two ribbons in front in figure 5.1 a) thus do not show a localized Majorana mode, but the latter is smeared out over the TI region. If one shortens the length of the wider region proportionally to the tapered SC patch, the Majorana modes would approach each other accordingly. As explained above, the zero-energy state and associated zero bias conduction peak signature of Majorana modes then splits [88]. In the proposed device the splitting of the Majorana state can be observed directly in scanning tunneling spectroscopy when following the SC edge with the tunneling tip moving towards the SC triangles tip and measuring on the confined proximitized TI region.

To realize a first test structure with TI nano-ribbons, SAE trenches with varying widths (without the changing diameters in in figure 5.1 a)) etched into a mask of 5 nm SiO_2 and 20 nm Si_3N_4 are filled with TI, in this case $(BiSb)_2Te_3$, grown in the BST MBE chamber. Special care has to be taken in this step, not only due to the narrow substrate temperature window for selective growth in general, but also since another silicon substrate needs to be used. In the chapters before, silicon (111) wafers were used as a substrate with resistivities ranging from 2000 up to 10000 Ω·cm. For STM/STS measurements a current must flow from tip to substrate and from the substrate to ground or vice versa. Highly ohmic substrates do not allow for such measurements in single tip scanning tunneling microscopes as the one intended for these measurements in our partner groups. When two tips or more are present, current can be directed from one to another, however with only one tip, the STM stage acts as the ground. Thus, highly conductive silicon substrates with 5 mΩ·cm resistivity are used, which also influences the optimal substrate temperature. By decreasing the substrate temperature by 5 to 10°C depending on the TI material grown, good SAE can be achieved as shown in figure 5.1 b). The pre-growth substrate preparation and cleaning is the same as in the previous chapters.

After selective TI growth, the removable membrane mask cannot be positioned accurately on a structure in the vacuum, as was shown in [163]. This inaccuracy is compensated by the stencil and SAE mask design as shown in figure 5.1 e). By putting parallel trenches onto the substrate and utilizing a mask with rectangular holes wider than the inter-trench distance, it is assured that when depositing SC onto the trenches at least one trench is covered with each stencil mask hole. The utilized mask is shown in figure 5.1 c). Instead of the tapered design shown in the schematic in figure 5.1 a), discrete increases in width are patterned. This is to have a perpendicular arrangement of mask to trench and thus a constant width of the proximitized region. By varying the length of the rectangular holes in the stencil, TI ribbons are covered with SC material of varying length. Figure 5.1 d) illustrates the configuration of substrate and mask in the MBE chamber during growth. Firstly, the patterned substrate is put into a separate sample holder capable of vacuum suitcase transfers, which in turn is inserted into an adapter plate for the growth chamber (not shown in figure 5.1 d)). TI is then deposited into the trenches without any additional removable stencil mask. Utilizing a wobble stick, the separate substrate holder is taken from the adapter plate and kept in vacuum while the mask holder with mask is put into the adapter plate at air. The sample holder is then lowered onto the mask *in situ*, creating the configuration shown in figure 5.1 d) for the deposition of the superconductor. Via the reversed process, the mask can be removed and a capping can be applied to the sample without breaking the vacuum.

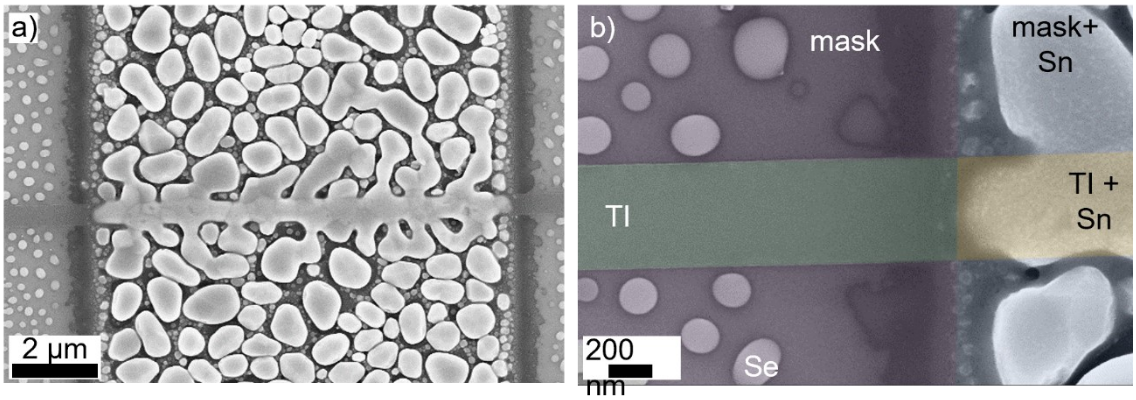

Figure 5.2: SEM micrographs of a TI trench covered with Sn through the mask shown figure 5.1 c) and covered with Se capping after SC deposition. a) Deposition of Sn on the TI filled trench. No formation of a continuous Sn film is observed on the Si_3N_4 mask, however on the TI trench a clearly closed region can be identified. In b) the edge of the Sn on the TI is shown in more detail, different layer stacks indicated by coloration. The blurring of the Sn deposition extends over an area of approximately 200 nm. On the mask Si_3N_4 surface, the amorphous Se capping forms droplets, on TI and Sn a continuous smooth film is formed.

Figure 5.1 e) and f) show the finished patterns. Tin[3] as a superconductor has been evaporated through the mask onto the TI trenches covering decreasing length of the TI trenches thereby realizing the SC part of the design of figure 5.1 a). The Tin was evaporated from a standard Knudsen effusion cell onto the sample, which had been cooled below 0°C. In figure 5.1 f) it is however clearly discernable that the superconducting layer is not continuous on the Si_3N_4 mask surface. This is shown in more detail in figure 5.2 a) and b). In figure 5.2 a) a 500 nm wide trench filled with TI is shown, onto which a 6 µm wide patch of Sn has been deposited. The depicted structure thus constitutes a TI nano-ribbon with a separation of 6 µm of the proposed Majorana modes. The samples were additionally coated with a layer of amorphous Se capping (Se source temperature at 110°C, ~10^6 mbar flux) for protection from ambient conditions when transferring to the STM chamber via ambient conditions. The Se forms droplets on the inert Si_3N_4 surface, on the TI and Sn surface a continuous amorphous layer is formed, protecting the functional surfaces. The different surfaces are shown in figure 5.2 b) color-coded in greater detail. While the shown layout in theory would provide the desired set-up to measure the signatures presented earlier, the discontinuity of the SC Tin layer offers an inadequate surface for the STM measurements. This could be resolved by further decreasing the substrate temperature during Sn deposition, thus withdrawing kinetic energy from the arriving tin molecules and thereby preventing them from coagulating due to lowered mobility on the sample.

As shown in figure 5.2, with this removable stencil lithography process the desired structures can be fabricated fully *in situ*. The choice of superconductor is limited by the availability in the used chamber. In our case only Aluminum or Tin were available. For STM measurements, the samples are transferred after SC deposition either via a vacuum suitcase, which can be moved to an available port at a STM chamber, from where the

---

[3] At the given time, Tin was chosen due to being the most promising SC available in the growth chamber. Issues with $AlTe_x$ were known and thus ruled out the also available Al.

sample is then transported into the scanning position, or by using a protecting Se capping and a transfer via ambient conditions. The Se capping is then removed in the STM chamber, revealing the pristine TI surface and guaranteeing an entirely *in situ* process.

In consultations with our STM partners from the Jiaotong University in Shanghai and the RWTH University in Aachen, it was brought to our attention that though these structures were in principle usable for the desired STM measurements, the available STM systems in both universities, capable of reaching the needed cryogenic temperatures and magnetic fields, only featured maximum scanning ranges of the order of μm and no AFM capabilities. Therefore, no preliminary large-scale scan to map the surface topography of the sample is possible. To measure the LDoS at the TI-SC interface, the tip would have to be positioned on the SC regions to scan onto the TI surface or vice versa, where a tunneling current into the materials would grant access to the distance information between the tip and the sample. On the Si_3N_4 surface of the SAE mask however no tunneling current can flow due to the large gap in the LDoS of insulators at cryogenic temperatures. There, no information on the tip-sample distance can be measured, creating a hazard for tip-crashing, interrupting the measurements.

To counter the issues that arise when working with SAE masks, another way of fabricating the desired structures *in situ* must be found. To do so, four criteria are established:

1. The topological insulator has to be grown in a predetermined pattern without the use of a selective area epitaxy mask consisting of insulators on the substrate directly. That way only TI, SC and Si are allowed to be on the sample surface in the STM chamber.
2. Superconducting material needs to be deposited *in situ* in a way that only destined parts of the TI are covered with SC, guaranteeing access to TI surfaces with induced superconductivity, thus requiring good mask alignment.
3. The surface of the TI must not be exposed to ambient conditions at any point of the fabrication process. Hence, the samples must be vacuum suitcase transferred to the STM chamber or a capping must be provided.
4. The structures must be easily identifiable with the STM, either by markers, large scale or great number of structures.

In the following section, a process to fulfill these four criteria will be introduced using large scale local UHV lithography, similar to the underlying idea of the devices in section 4.2.

Nonetheless, the procedure developed in this section is capable of *in situ* creating large scale structures of multiple materials on prepatterned substrates. Due to the only hardly optimizable alignment of the mask and the underlying substrate, special care needs to be taken when designing the patterns. In scanning tunneling platforms with more than one tip to act as ground or an incorporated AFM possibility to exactly position the tip over the TI structures, the samples developed in this section could still be measured. In cooperation with Prof. Bert Voigtländer and Dr. Arthur Leis of PGI-3 of the Research Center Jülich, a removable mask was employed to identify edge channels of *in situ* deposited TI patches [196], [197], [198].

5.3 Removable Large Scale UHV Lithography

To find a suitable alternative that fulfils the criteria given in the previous section we re-evaluated the on-chip UHV lithography shown in chapter 4.2. As mentioned before, the large-scale coverage of the substrate with the 400 nm mask stack of SiO_2 and Si_3N_4 would pose a problem for STM measurements and would also not comply with the first criterion. However, the development of the local UHV lithography as exhibited in chapter 4.2 opened up new possibilities of *in situ* device fabrication with only a minimal amount of insulating mask material on the Si surface. Moreover, a second development in the fabrication of the local UHV lithography heralded a solution for the problem posed by criterion 1, i.e. the patterned growth without the use of an insulating mask.

To resolve problems with flux-focusing due to SC-covered bridges for Josephson junction fabrication, the bridges are removed by reactive ion etching or with the help of an exfoliatable polymer solution as in chapter 4.2. Utilizing the reliance of local UHV lithography on the SiO_2 pillars and the thus limited points of interconnection between the Si_3N_4 mask and the substrate enabled new ways to realize a removal of the insulating on-chip mask structures without harming the TI or the SC layers. In this way, the first criterion can be fulfilled.

Depositing the TI through the on-chip mask leads to a confined growth of TI film, limited to the directly exposed area plus the area reached due to substrate rotation during growth and the diffusion length of the evaporated materials on the Si. With this method, patterned TI films can be fabricated, however the confinement is not as rigid as with the SAE mask technique in the previous section. In the Josephson junction fabrication process this was utilized to have TI also deposited in the shadowed region, as not to have holes in the thin film layers. However, to pattern the TI into structures on the nm scale as intended for the STM investigations, wider bridges can be used to separate areas of TI intentionally. An advantage of this method is that it is not limited to TIs, but also magnetic TIs and any material that is directionally evaporated can be grown in a patterned manner as shown in chapter 4. The same mask openings to pattern the TI can in a second step be used to also deposit the superconducting material onto the TI. By stopping the rotation and evaporating the SC onto the underlying TI at a distinct angle, only parts of the TI are covered, fulfilling the second criterion.

The local UHV lithography was developed to have a device surrounded by plain SC material, which is to be structured into contacts pad via electron beam lithography and subsequent etching, as shown in the previous chapters (Figure 4.4 & Figure 4.6 b)). For devices for electrical transport, a large number of structures in proximity to each other provides no advantages, as the number of contacts is on one side limited by the available ports of the dilution fridge and on the other side by the area needed for the circuit path on the sample. For STM however these limitations are not necessary, enabling the upscaling of the local UHV lithography to extensive grids instead of small structures. Thereby, the fourth criterion can be fulfilled.

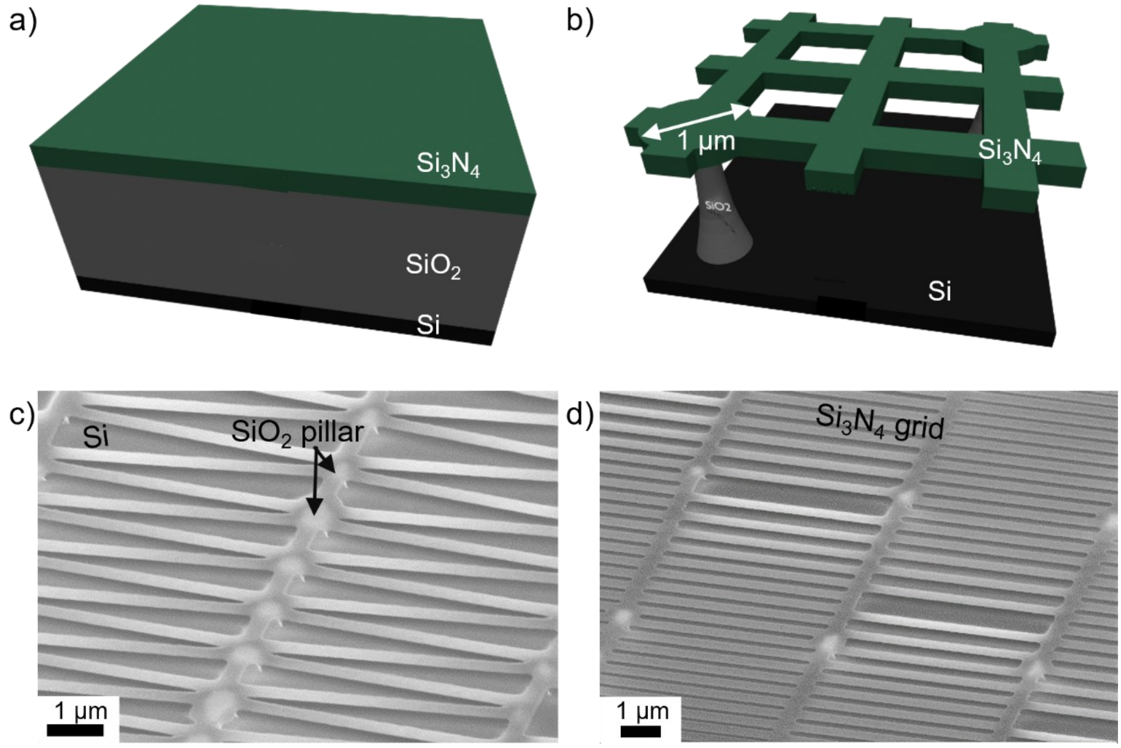

Figure 5.3: Structuring of the large-scale UHV lithography grids. a) shows a schematic of the layer stack of 300nm SiO_2 and 100nm Si_3N_4 deposited via LPCVD onto a low ohmic Si (111) wafer (not to scale). With the resist and RIE processes explained in the main text, the nitride is patterned into the desired layout and via HF the SiO_2 is removed to release the grid and to expose the Si surface as shown in schematic b). SEM micrographs of different layouts establish the stability of the UHV lithography grids with high (c) or low (d) pillar density.

The process of substrate fabrication and the developed structures are shown in figure 5.3 & figure 5.4. A stack of 300 nm SiO_2 and 100 nm Si_3N_4 is first deposited via low pressure chemical vapor deposition on a highly doped 5 mΩ·cm Si (111) 4-inch wafer (figure 5.3 a)). For further fabrication, the wafer is cut into 7x7 mm² pieces, which is the size of the STM sample holders in the group of Prof. Markus Morgenstern at the RWTH University in Aachen. The substrates are then covered via spin coating at 4000 rpm with the negative photo lithography resist AZ 2020 (nLOF), mixed in a ratio of 1:1 with AZ EBR to render the resist sensitive to electron beam lithography. A pre-exposure bake is performed for 5 min at 100°C and the samples are subsequently exposed with a dose of 91 µC/cm² at an acceleration voltage of 100 kV. A post-exposure bake at 110°C for 3 min follows before the sample is developed in AZ MIF 326 for 25 s, succeeded by a rinse in distilled water. Via reactive ion etching with a CHF_3/O_2 plasma (55/5 sccm, 25W, 100W ICP) at 20°C for 185 s the bare 100 nm of Si_3N_4 are removed. This nitride etch is also performed globally on the backside of the substrate in order to ensure electric contact to the STM carrier. Before growth the samples are cleaned in piranha solution and hydrofluoric acid as described in chapter 3. Here however, special care needs to be taken during the HF etching step.

In the local UHV lithography, wider silicon nitride patches were designed to act as pillars for the bridge structures between them (see figure 5.4 b)), which in turn are to be underetched with HF completely. In the large-scale UHV lithography (LUL), the bridges

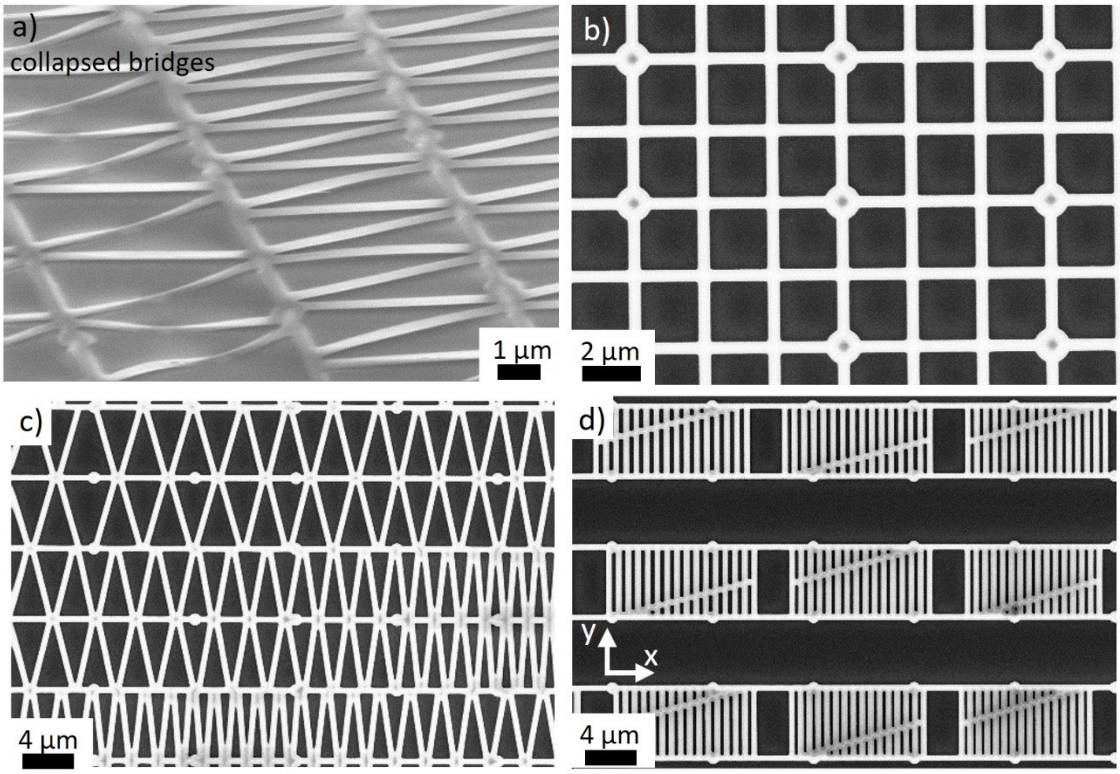

Figure 5.4: Stability limits and chosen designs. In a), diagonal stripes of nitride span between parallel bridges with 8µm separation. The angle between the diagonal bridges varies along the parallel bridges. Thus, the length of the bridges increases with the opening angle. If the bridge extends too far, the bridges collapse, limiting the maximum length of single bridges. In b), c) and d) the chosen pattern designs are depicted in SEM pictures after HF etching.

are designed to inhibit TI growth underneath, while still being underetched. Thus, discs with a diameter of 1 µm are included in the grid designs shown in figure 5.3 b). After the release by HF etching the Si_3N_4 grids are hovering over the Si, only supported by the SiO_2 pillars formed under these discs as shown in figure 5.3 c) and d), illustrating the stability over varying pillar densities. The size of the bridges is altered to test the stability of the bridges depending on width and length. The optimal bridge width for the chosen pillar-top disc diameter of 1 µm was found to be 500 nm. At this width, the SiO_2 under the bridge can be easily removed with a 16:30 minute 1% Hf dip, while simultaneously ensuring stable SiO_2 pillars and bridge length of up to 8 µm between two pillars. Longer bridges of the same width or less wide bridges of the same length were prone to collapsing, see figure 5.4 a), or to being ruptured by the tensile strain of some of the superconducting material deposited on top in later process steps.

Three designs are chosen for the intended STS experiments: simple square designs to test the scope of the induced superconductivity into the TI, triangular and striped structures as shown in figure 5.4 b), c) and d), respectively. The triangular structures are designed as a proof of concept for future experiments utilizing a QAH MTI, which would enable measurements comparable to that of Kezilebieke *et al.* [199] to investigate chiral edge channels. In combination with prepatterned TI stripe structures these would result in a direct translation of the patterns created in section 5.2.

Since the material sources in the MBE chamber are mounted with a 30° angle to the surface normal of the substrate and the mask is 300 nm apart from the Si, all structures extend approximately 175 nm to all sides compared to the designed pattern, providing a minimum width and length of the wires of about 400 nm, when taking to account the minimum mask hole width of 50 nm. When depositing superconducting material in the next step without rotation, the angle can be chosen depending on the desired measurement. To emulate the structures of the first-generation samples, the superconducting material has to be deposited in the long direction of the rectangular holes.

In doing so, the TI ribbon is fully covered with SC, except for one shadowed end, compare figure 5.5 a). There, similar to the ribbons fabricated with SAE and removable mask lithography, see figure 5.2 a), a Majorana mode is proposed to arise at the edge of the proximitized region. Ribbons of varying length provide the possibility to investigate the dependence of the Majorana signature on the distance between the pairs of the quasiparticle modes. Additionally, by depositing the SC material with an angle to the long side of the rectangle, one flank of the TI ribbon is accessible to the STM, enabling a measurement of zero bias signatures along the wire length as shown in figure 5.5 a). Only at the ends of the ribbons, if the ribbon is in a quasi-one-dimensional state, zero bias peaks as signatures for Majorana modes should emerge, reinforcing the signature of the elusive quasiparticle [88].

The designed structures can be linked together to the eponymous large-scale grids. A 1 μm disk is put at every 8 μm in x and 5.6 μm in y direction. Along the x direction, 500 nm wide bridges are designed. In the simple square design, this is also done along the y direction, resulting in a network of perpendicular bridges as shown in figure 5.4 b). For the triangular design as depicted in figure 5.4 c), bridges are set in a zig-zag pattern, decreasing the angle every two bridges from 45° to 8° in steps of first 5°, then 4°. This is mirrored into the next row over the x direction. Through this, X-structures with decreasing angles are formed. In the next two rows, the design is copied but shifted along the x-direction by 24 μm. This mirroring and shifting is employed for better STM tip accessibility. When starting at a random position on the grid, one might want to move to a specific layout size. Without shifting, the closest desired structure is found along the x direction. With design shift, the desired structure might be reached faster along y-direction. In an experimental method like the STM/STS, which is only supplied with a limited scanning range, this increases the chance of finding a specific structure when a random starting point has to be used.

The stripe pattern shown in figure 5.4 d) takes advantage of the same procedure. To create ribbons of varying width and length within a preferably small design, that can be strung together easily, bridges are set along the y direction with a desired spacing (width) between them (vertical bridges in figure 5.4 d)). A horizontal connection is put between the bridges, moving from the horizontal bridge grid towards midway between the horizontal bridge grid (diagonal lines in figure 5.4 d)).

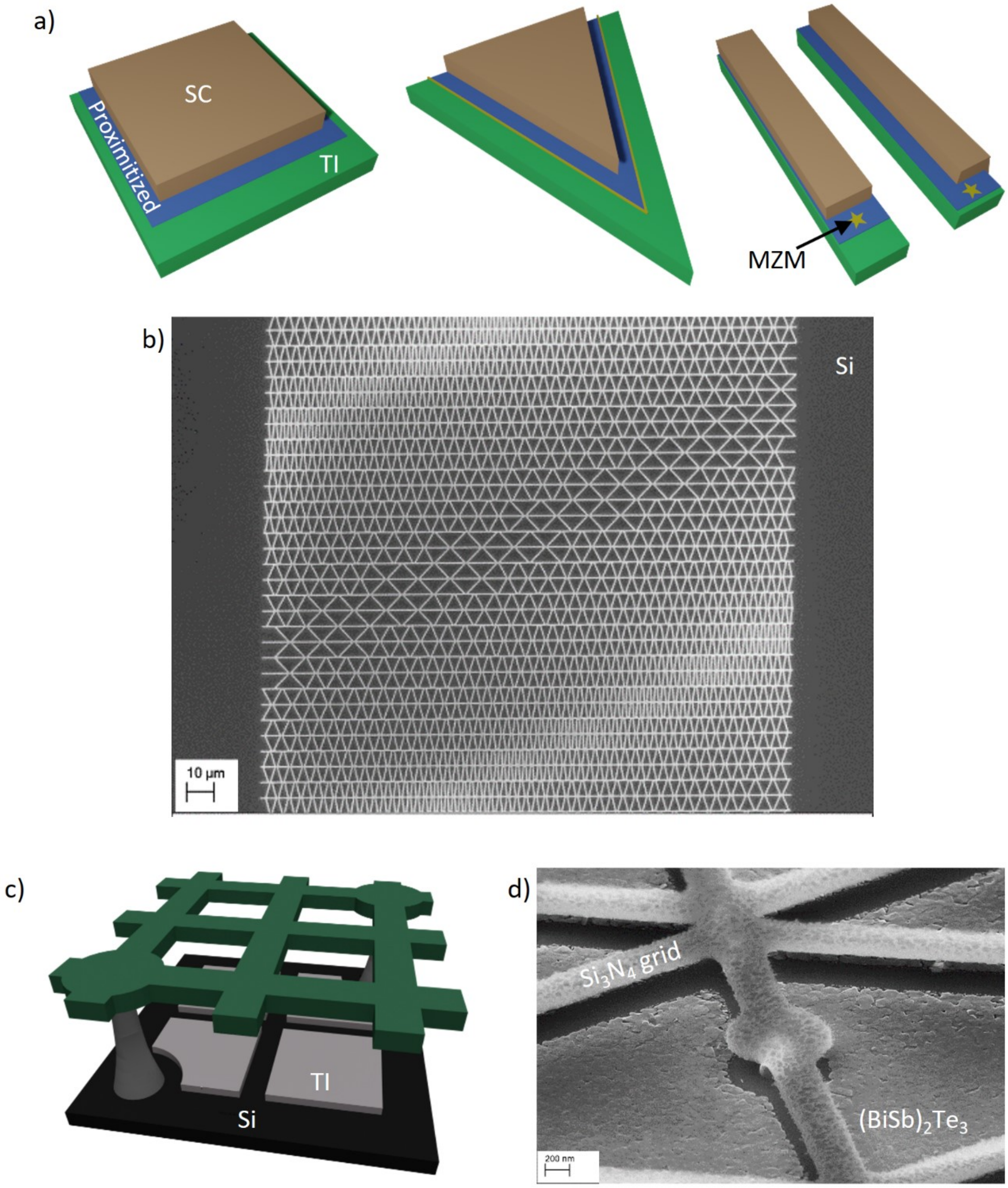

Figure 5.5: a) Schematics of the three designs indicating in blue the proximitized regions of the TI (green) in contact with the superconductor (brown). On the stripe structures a yellow star hints at the position of the localized Majorana mode in the quasi one-dimensional case. By manipulating the deposition angle of the superconductor, the TI stripe can be covered partly or fully with the SC. Figure b) shows an example of a full triangle grid spanning multiple 100 µm, which can however be expanded in all directions. In c) a schema of the grid after TI deposition is shown continuing from figure 5.3 b), in d) the realization of this with $(BiSb)_2Te_3$ is shown in an SEM micrograph for direct comparison.

Thus, each vertical rectangular hole in the mask is separated into two rectangles with length l and $l - y$, where l is the maximum distance between the horizontal bridge grid and y is the extent of the shift of the connecting bridge up to twice $\frac{l}{2}$. The three designs can be combined infinitely and have been realized to an extent of 1x1 mm² large grids resting on solely the SiO_2 pillars as shown in figure 5.5 b). Even larger grids, combinations of different grids and other structures can easily be realized.

As shown in figure 5.5 c) and d), TI is grown onto the cleaned and HF etched substrates following the pattern of the LUL grid. For comparison purposes, $(BiSb)_2Te_3$ is first grown, aiming at the stoichiometry provided in [126]. To do so, the substrate is baked at 700°C for 10 minutes to remove the hydrogen passivation after hydrofluoric acid cleaning and then cooled to a substrate temperature of 220°C over a period of 30 minutes. During the heat up and cooldown, the effusion cell sources are set to the temperature parameters given in the table below.

T [°C]	Cracker / Tip (Bi)	Tube	Reservoir	Resulting flux
Bi	520	-/-	445	$6x10^{-9}$ mbar
Sb	900	570	430	$4x10^{-8}$ mbar
Te	900	600	395	$5.2x10^{-7}$ mbar

Tab. 5.1: TI growth parameters set for the growth of BiSbTe onto the LUL samples for STM investigations. The opening of the tellurium cracker cell valve is set to 60% (maximum).

The TI is deposited with a substrate rotation speed of 15 rpm and a rate of ~0,32 nm/min. The resulting film on plain chips is intended to be about 25 nm thick. In principle, the TI film could also be grown without rotation and thus would directly reproduce the layout of the grid above. However, without rotation, the elements will be deposited spatially separated and not form a compound thin film. Using stoichiometric compounds as source material in the future might allow for directed deposition of TI, however this will not be discussed in the scope of this work.

For the superconductor deposition the rotation is stopped similar to the process in chapter 4. With an electron beam evaporator, superconducting material is supplied onto the sample, on the grid as well as the TI underneath. Niobium is chosen due to its large SC gap, high critical temperature and high critical magnetic field [200], [201]. For a rate of 1.8 A/s a beam current of about 200 mA at a beam voltage of 10 kV is applied to the source material at a substrate temperature of 50°C. The deposition direction depends on the desired Nb-TI configuration as mentioned before, resulting in structures as shown in figure 5.6 a) and c), with a schematic view in b). Due to step and edge effects of the TI surface combined with tensile strain in the Nb, Nb can delaminate partly, see figure 5.6 c) and e).

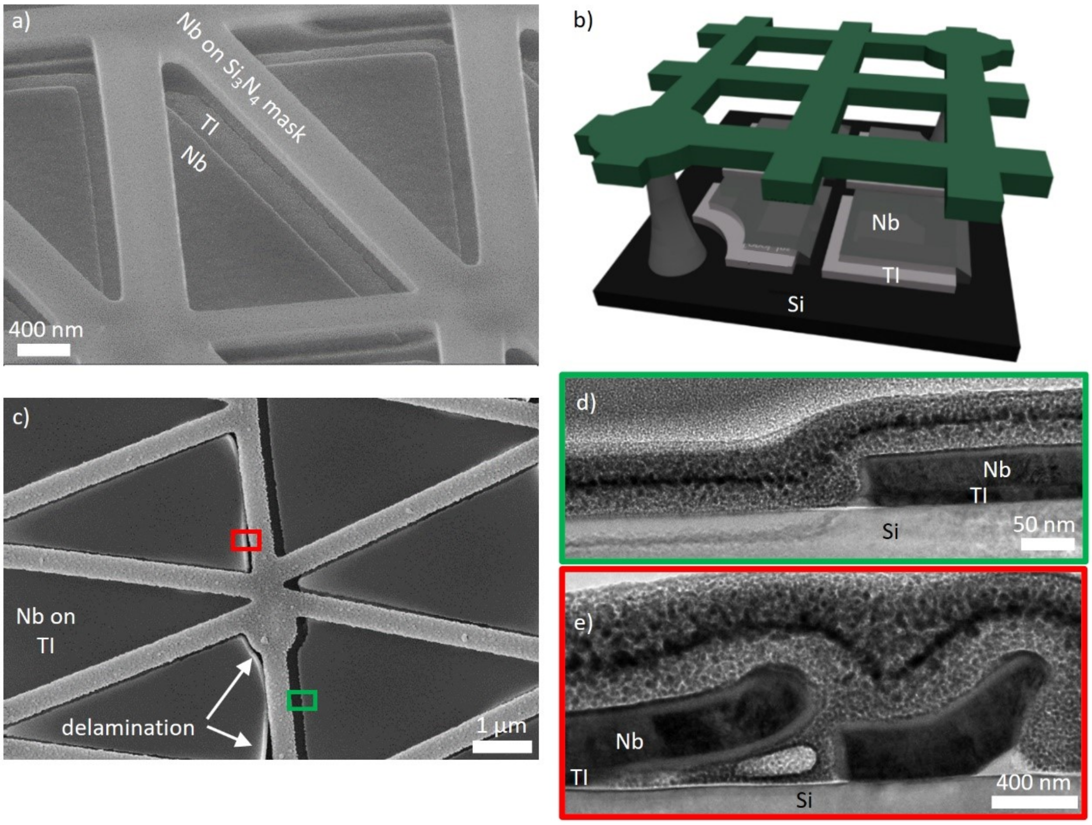

Figure 5.6: LUL grids after TI and SC (Nb) deposition. The tilted view in a) reveals the growth of smooth Nb film on the underlying TI film. On the mask, only smooth Nb without any TI crystallites is present. b) illustrates the step schematically. Strain in the Nb can cause the film to delaminate at edges of the underlying TI. In c) this happened at the edges deposited under the mask due to the deposition angle, where the TI surface can exhibit an edge. On the opposite site, where the Nb is deposited on flat TI, the Nb sticks (d). In extreme cases where Nb is grown over the TI-SC edge, delamination can happen on both surfaces, accompanied by rupturing of the Nb film as visible in the TEM micrograph in e).

At this point, the thin films are arranged as they are needed for the STM investigations, however the grid is still in place. It cannot be removed *in situ*, except for a possible removal via focused ion beam in combination with a nanomanipulator. This method would in turn require the adaptation of the growth process to a suitable sample holder, altering the growth parameters drastically as known from previous experiments. An active removal has only been performed on small bridge devices (like those in chapter 4.2) and it is questionable whether this would even be feasible on large-scale grids. Removing the grid *ex situ* via reactive ion etching would mean that with electron beam lithography a hole in a resist at each supporting pillar needs to be patterned, so that the pillar alone can be etched. As shown in chapter 4.2, though the procedure can be used to remove the grid structures, the area directly beside the pillars is often damaged during the process. Especially the deep holes in the Si can create hazards for the STM tip during measurements. An additional problem arising when using an *ex situ* approach to the grid removal is that the samples need to be capped before exposure to air. In chapter 3 this is already mentioned in respect to transport characteristics, during the sample fabrication for STM it became apparent however just how important the capping is also for the surface morphology of the TI. In the appendix in figure 7.20 the surface of a plain uncapped BST film is shown. Immediately after growth the triangular crystal structure and terraces are clearly discernible. After storage in a N_2 environment this sharp morphology is maintained for days up to some weeks, however slight formation of a rougher surface is already overlaying the step structure. In ambient conditions the films start to build a heavily oxidized surface (stronger for Sb-containing TIs) in a matter of hours [202]. This change materializes in the formation of a grisly layer covering the film, through which the underlying triangular structure is still visible. The prevalence of this phenomenon on Sb-based TIs compared to Bi-based TIs points toward a formation of SbO_x and TeO_x. Thus, capping of the highly surface sensitive STM samples is crucial, even more so than for transport. In samples designated for the latter, protection from heavy oxidation is guaranteed by a 5 nm thick capping layer of Al_2O_3 as shown in chapters 3 and 4. This capping is however a “hard” capping, it cannot and is not destined to be easily removed and forms a stable insulating layer on the thin film devices. For STM or STS investigations the insulating nature of the capping layer poses a tunneling problem. Thus, another capping needs to be found that can be applied *in situ* after TI and SC deposition and which can be removed in a later step in vacuum, best in the STM chamber itself. Regarding the previously stipulated criteria for the desire structures, this narrows the third criterion down to:

3. The surface of the TI must not be exposed to ambient conditions at any point of the fabrication process. Hence, the samples must be *provided with a removable capping, which withstands grid removal processes.*

The criterion was also amended by the requirement that the capping not only needs to be removable but must also protect the *in situ* grown structures during the removal of the on-chip large scale mask or grid.

The fact that the capping needs to be applied *in situ* narrows the available materials down to those accessible in either the Nanocluster, the second MBE chamber or a chamber easily accessible via a vacuum suitcase transfer. Most oxide and metal layers require chemical or physical etching to remove, endangering the crucial surface of the TI. Two materials available in both MBE chambers however promise the desired properties: pure tellurium and selenium. The qualities of pure Te and Se layers as capping materials have been shown in multiple publications, see [203], [204], [205]. Thus, the Se capping has already been used in the previous section, was however not further investigated due to the superior problems of the general approach of the removable mask technique. The capping layers can be removed via annealing at comparatively low temperatures ranging from 150°C to 220°C, where Te, consistent with its higher evaporation temperature, requires slightly higher decapping temperatures. This temperature range, however, is below the temperature at which the TI itself starts to degenerate or re-evaporate rapidly, which starts at or slightly above the growth temperature. Deterioration of the TI surface begins at temperatures higher than 220°C without a suppressing counterpressure of Te. Decapping studies on the samples are performed in greater detail further below.

With this, two possible capping candidates have been found, either Se or Te capping. In figure 5.7 b) and c), samples covered with Se and Te capping are shown. The cappings are deposited with 10 rpm at ~14°C substrate temperature (lowest possible in the used growth

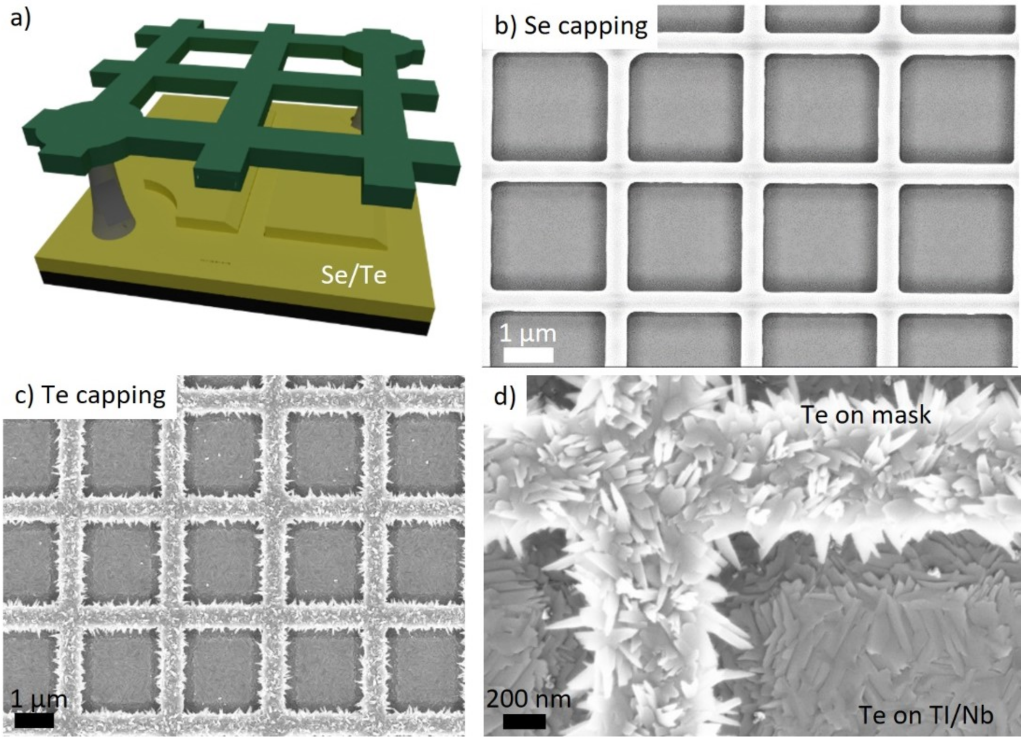

Figure 5.7: Capping with Te or Se promises to protect the sample surfaces from ambient conditions while also providing protection form mask removal processes. a) illustrates the current step schematically. In b), a ~25 nm amorphous Se capping is deposited globally on the sample, creating a smooth film, hiding any height features of the underlying film. The Te capping in contrast, also deposited at ~14°C, forms a polycrystalline film, with sharp edges protruding from all surfaces (c). Enlarging the edge region of a feature in d) shows the crystalline nature of the capping in more detail. The shadowing from crystallites on the mask might cause holes in the capping, detrimental for later processes.

chamber) to create impermeable, at best amorphous, capping layers. Since crystalline capping layers might not growth in the planar growth mode of the TI crystals but can rather form crystallites instead of a closed layer, a crystalline capping might suffer from holes exposing the TI surface. As is shown in figure 5.7 b) Se forms a smooth amorphous layer covering the grid as well as the underlying TI-SC surface completely.

Special care needs to be taken when depositing the Se capping, however. The 14°C are measured close to the heater of the MBE chamber, not on the substrate directly. When evaporating Se for Bi_2Se_3 films, the effusion cell temperatures are set to 230-240°C for the reservoir and 800°C for the cracker. Using these parameters however, no Se capping is present on the chips after growth. Since a flux can be measured and a Se-containing TI could be grown before capping deposition, the reason for the non-existing capping cannot lie with the effusion cell. In the BST MBE chamber, where Se is evaporated from a standard Knudsen cell as opposed by the cracker cell used in the M13 in the Nanocluster, the Se source is heated to only 110°C. It has been shown that in this chamber amorphous Se capping can easily be deposited at comparable substrate temperatures. The most likely difference in growth conditions is given by the cracker. The tip of the Se effusion cell, where the cracker is located, protrudes into the growth chamber and is directed towards the substrate. It can be assumed that the substrate is warmed by the heat radiation of the cracker cell up to a point where the Se is reevaporated or where the substrate is hot enough to not

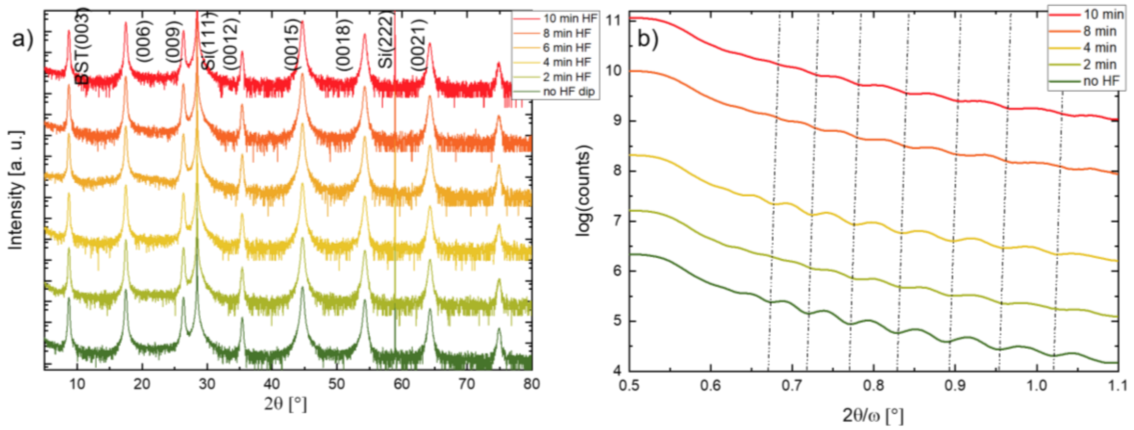

Figure 5.8: Evaluating the stability of Se capping films. In a), XRD curves (shifted for clarity) of a Se capping on a BST TI show no change in the crystal structure of the underlying BST when dipping the sample for up to 10 minutes into 1% HF. The XRR data in b) shows a gradual decrease of oscillation strength, however the oscillation period remains largely the same, indicating some increase in roughness but no decrease in thickness.

allow for Se deposition. To counter this effect, the cracker temperature was lowered drastically as can be extracted from the following tab. 5.2.

T [°C]	Cracker / Tip (Bi)	Tube	Reservoir	Resulting flux
Se	350	-/-	230	2.7x10^{-7} mbar
Te	900	600	395	5.1x10^{-7} mbar

Tab. 5.2: TI growth parameters set for the growth of Se and Te capping onto the LUL samples for STM investigations. The opening of the Selenium and Tellurium cracker cell valve is set to 60% (maximum).

With these parameters, closed amorphous Se films can be deposited as shown in figure 5.7 b). Similarly tested Te capping films formed crystalline layers as shown in figure 5.7 c) and d), which disqualified the Te capping in comparison to the readily depositable Se capping due to the possibility of holes in the crystalline capping. Especially shadowing effects of crystallites on the mask layer as in figure 5.7 d) could lead to hole formation in the underlying layer. In the next section 5.3.2 however, arguments in favor of a Te capping will be revealed, reevaluating its viability.

As shown in figure 5.7 b), soft-capped samples can be fabricated, leaving only the grid removal to be accomplished. In discussions with colleagues, it was brought up that previous work on Se capping had shown it to be resistant to hydrofluoric acid. Plain TI samples with Se capping were grown and dipped into 1% hydrofluoric acid for various times and the thickness and TI quality was evaluated via XRD and XRR. Figure 5.8 shows the dependence of film quality on HF etching time. In a), the XRD response of a TI film covered with a Se capping in monitored, showing no discernible deterioration after 10 min HF, longer than needed to remove the grid with about 5-8 minutes. The XRR measurement on a plain amorphous Se film shows oscillations that do not change in frequency with HF exposure time but become less pronounced. The oscillation frequency determines the overall layer thickness, which therefore does not change. Meanwhile the roughness increases, leading to the decrease in oscillation amplitude. On the whole, the Se capping itself can be regarded as HF resistant for a minimum of 10 minutes in 1% HF.

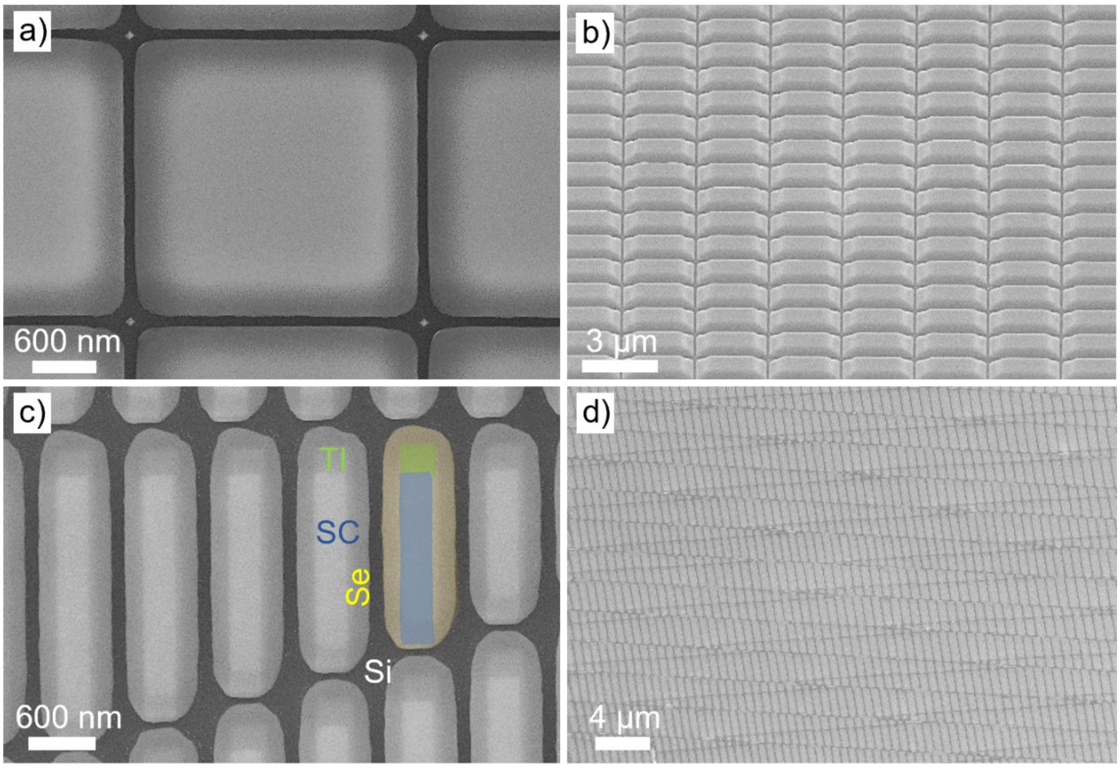

Figure 5.9: Examples of successful Se degridding. a) depicts a square patch of TI and SC, covered with a smooth layer of amorphous Se capping. The grid was removed with HF, also removing the supporting pillars, leaving only miniscule remains. An angled view in b) reveals the conformity on a large scale. c) stripe structures of different length of TI (green) covered partly with SC (blue), capped with Se (yellow), forming exactly the desired structure shown in figure 5.5 a). Only conducting Si is present otherwise, fulfilling criteria 1.-3. Grid removal on stripes is also possible on a large scale (d), complying to criterion 4.

The HF resistance of the Se layer allows for an elegant way of removing the LUL grids: By dipping the samples after TI, SC and Se capping deposition into HF, the SiO_2 pillars supporting the grid can be removed. Due to the protection of the Se capping, no surface of the underlying superconductor or topological insulator layer is exposed to the acid. The choice of Nb as a superconductor for the intended experiments has an additional effect when removing the pillars. The Niobium deposited at 50°C substrate temperature exhibits a tensile strain as was shown in figure 5.6 c) and e). After a pillar has been removed, this tensile strain causes the Si_3N_4/Nb layer to curl, decreasing the risk of having the mask stuck to the functional layers. To further minimize the amount of mask debris, during the HF dip a pipette with deionized water is used to flush away removed mask parts. This resulted in qualitatively high-grade patterns of TI/SC/Se-capping structures, with only low ohmic Si surface between them. The grids and therefore the structures can be designed to be arbitrarily large and complex, thus fulfilling the four criteria. In figure 5.9 examples of finished samples are shown. One can even clearly discern the TI and SC layer underneath the smooth amorphous Se layer in figure 5.9 c).

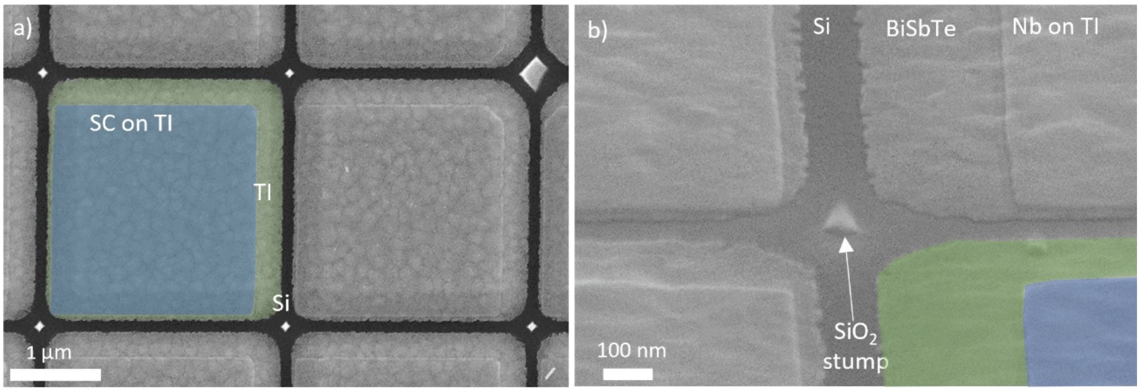

Figure 5.10: Successful decapping of degridded structures. Only miniscule SiO_2 *pillar stumps are present between the TI-SC patches, with some larger* SiO_2 *patches where wider pillar tops where present. The position of the Nb patches, shifted towards the bottom left in a), highlighted by the coloration, leaves a bare TI area of approximately 250 nm width for STM measurements. Sharp edges from Nb onto the TI are visible in b).*

Finally, the decapping capabilities need to be tested. As mentioned before temperatures between 150°C and 250°C are used to remove soft cappings in literature, see [203], [204], [205], where Se is at the lower border. To heat the sample, the substrate is reintroduced into the MBE chamber to anneal the sample with temperatures close to those used in the growth. This also ensures that the substrate temperature does not exceed the growth temperature, which would cause the TI to rapidly re-evaporate. Multiple temperatures have been examined for the removal of the Se capping. When heating the sample too high, damage to the TI is expected, so it was decided to start at the lower temperature limit and move upwards. At too low temperatures the Se capping is not fully removed but coalesces to form droplet like structures while exposing only part of the TI/SC surface. At temperatures of 200°C with an annealing time of 10 minutes the Se capping can be reproducibly removed, exposing the TI and Nb surfaces as shown in figure 5.10.

However, Selenium incorporation poses a significant problem. When depositing materials in MBE even at low temperatures, an intermixing of the deposited layers occurs. Se is known for its tendency to replace Te in TI crystals due to its smaller size and slightly increased electronegativity [206]. Nb forms Nb_xSe_y compounds, most notably $NbSe_2$, a layered transition metal chalcogenide with a critical superconducting temperature of 1 - 4.5 K, depending on thickness [207], [208]. The formation of a layered superconductor with such a high critical temperature due to Se incorporation poses no problem, in contrast to the incorporation of Se into the TI. A quaternary compound is formed at the TI surface consisting of $Bi_{0.3}Sb_{1.7}Te_xSe_{3-x}$, with an unknown ratio of Te to Se. This ratio influences the position of the Fermi level within the topological band gap, resulting in an unknown Fermi level configuration in the decapped samples.

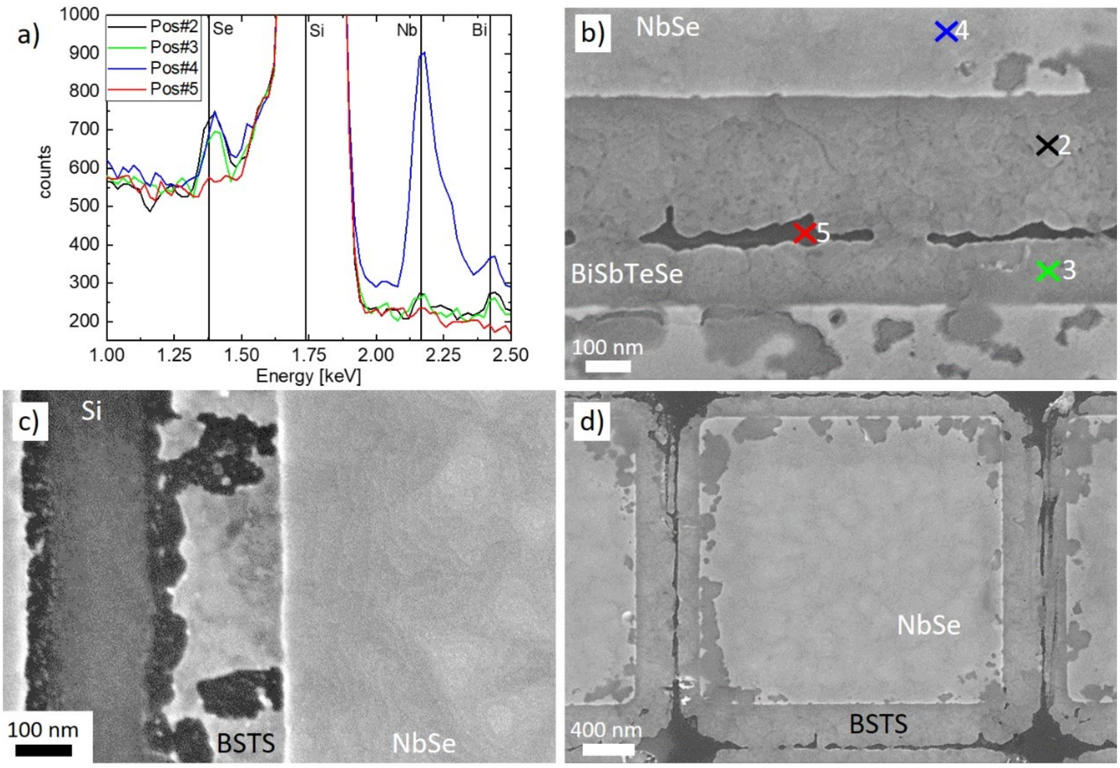

Figure 5.11: Examples of sample deterioration after HF degridding and Se decapping. a) The Se signal, given by the characteristic EDX peak at 1.379 keV, is present on both Nb and TI (Pos#2, 3 & 4), but not on the Si (Pos#5). Se is therefore embedded into the TI and Nb layers, while the Si surface is pristine after decapping. When annealing to ~200°C this leads to surface roughening and loss of the pristine triangular surface structure as in b). In c) an extreme case is shown, where the TI is evaporated in large parts due to too high decapping temperatures, maybe paired with incomplete capping. The latter results in the formation of various oxides from the TI, which are removed in HF. Under the Nb, the original TI structure is visible with clearly visible terraces. In d) the effects of too thin Se capping, also present in b) are shown on a larger scale, with holes in the Nb, where NbO_x formed at bare Nb edges, was removed by HF.

When the surface is uncovered and all Se capping has proposedly been removed, EDX measurements reveal a continuous existence of Se in the TI and the SC layer as shown in figure 5.11 a), also evidenced by [206] in Bi_2Te_3. As explained in the previous paragraph, this alone would not be detrimental, however when comparing the TI surfaces of TI-only samples and those after the Se decapping process, it is obvious that the distinct characteristics of the TI film are lost as shown in figure 5.11 b). SEM pictures reveal no identifiable step structures of the quintuple layered TI film, but a rough surface. The incorporated Se re-evaporates at lower temperatures than the Bi, Sb or Te, causing a deterioration of the TI surface layer, where heavily Se containing regions are removed from the crystal. The resulting TI surface is not suitable for the highly surface sensitive measurements performed in an STM. In extreme cases, the TI film is even entirely removed, leaving only patchy areas as in figure 5.11 c). The latter is most probably a combination of Se incorporation and insufficiently thick Se capping. Due to the triangular growth mode of the TI crystals, edges protruding further under the bridge can potentially form, which cannot be reached by the Se capping. While these regions would not be interesting for the STM measurements, the exposed edges of TI will oxidize and be etched during the grid removal, creating an entry point for the HF under the Se capping. Another effect visible in figure 5.11 b) and d) is an etching of the Niobium by the HF when the Se capping is not thick enough. Steep edges like those of the Nb patches are not fully covered by a thin amorphous Se film, leading to an oxidation of Nb at its edges. NbO_x is easily etched with HF, removing parts of Nb under the Se capping. A thicker Se capping or thinner Nb are however easy solutions to this problem.

Although high quality samples as shown in figure 5.10 were fabricated and similar samples will be examined in STM in chapter 5.4, the persistent challenges when employing HF degridding and utilizing a Se capping described in the previous paragraphs result in a low yield of good samples. While in some instances both processes work flawlessly, as with the samples shown in figure 5.10, the reproducibility is far too low to guarantee a working sample in the STM. In the following, two approaches to mitigate the sample deterioration are presented.

5.3.1 Exfoliation with First Contact^{TM} Polymer

When removing the grid with a dip into hydrofluoric acid, multiple issues are present. On one hand, the issues described in the previous section 5.3 arise, on the other hand the removal time depends significantly on the structure density. The previously shown square grids have a comparably low density of nitride bridges, while structures used for the stripe patterns to form TI ribbons have much more nitride surface per structure area. Even when accounting for the latter and reducing the repetitions in the grid pattern these structures need longer HF etching times to be removed compared to square structures. The required longer etching times only aggravate the existing problems. Moreover, the varying density of patterns in the designs lead to parts of grid that are more easily released than others, which also increases the risk of mask sticking to the substrate, since they are still connected to the denser regions and are therefore not easily blown away by the pipette.

The simplest solution of a much thicker Se capping covering the entire rim of the TI patch is possible, however limited by the bridges. When applying a thick enough Se capping, the Se on the bridges connects with the layer on the TI-SC structures, forming a continuous Se layer that cannot be penetrated by the HF later to remove the grid. Light scratching with cotton swabs removes the grid, but results in damaged Nb layers, increasing the etched Nb areas. Therefore, a method to remove the UHV lithography grids without damaging the Nb/TI/Se surfaces needs to be found which also reduces the necessary HF etching durations irrespective of the structure density.

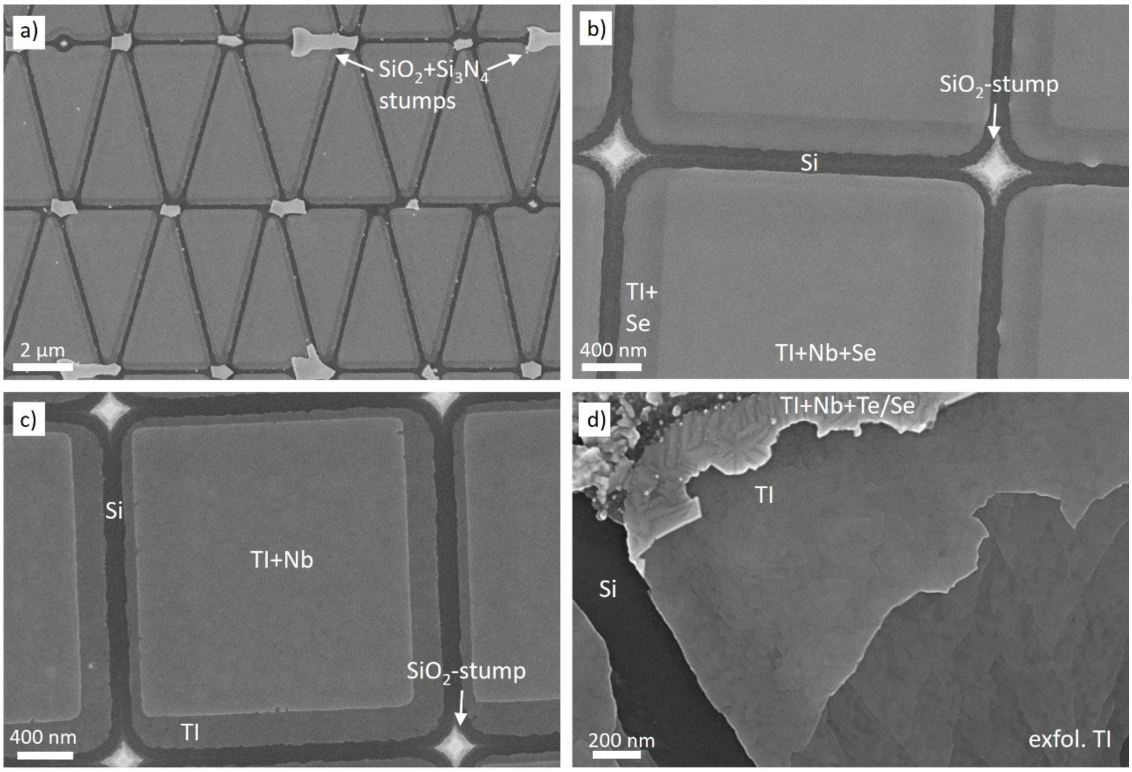

Figure 5.12: a) to c) show a LUL sample after exfoliating the grid (a), after a subsequent HF dip (b) and after decapping of the Se capping (c). In a), stumps where the Si_3N_4 mask is still attached to SiO_2 pillars underneath are still present at each point where the mask structure density is high. The HF dip removes the pillars at their thinnest point, leaving only some SiO_2 stumps without larger nitride parts as in b). The samples are still covered with Se capping. Decapping of the Se reveals good structures, which still suffer from Se incorporation, but no HF etching effects on the functional layers can be identified. In d) a side effect of the exfoliation is shown. Functional layers of structures close to the grid border can be removed together with the grid. In the upper part of the SEM micrograph, remnants of a Te+Se capping are still present. Below, the capping and the Nb have been removed, exposing the TI surface with the characteristic triangular crystal structure. Even further down, layers of the TI were also removed, revealing the crystal structure in the TI itself.

At this time colleagues working on electrical transport devices similar to those in chapter 4.2 switched from using cotton swabs to remove the local UHV lithography to an exfoliatable polymer film. In combination with local UHV lithography, the polymer films showed convincing results, removing the silicon nitride bridges by ripping them off from the SiO_2 pillars underneath. This approach promises a HF-less removal of the bridges also on the LUL samples.

Thus, after growth of the functional layers and Se capping layer, the sample is covered with the polymer film with a brush. Unlike as observed using the cotton swabs, here no damage to the sample has been recorded. The film is then kept at room temperature for 10 minutes to dry the polymer film. A piece of adhesive tape is stuck onto the dried film and thereafter carefully removed. The grids are embedded into the polymer film and removed together with it, leaving only SiO_2 stumps on the sample surface as shown in figure 5.12 a) and b). Thus, the grid is removed without any structural damage to the thin layers.

In some cases, the polymer film not only removes the silicon nitride grids, but on larger areas of capped film without structures can also remove the Se capping, Nb and rarely also parts of the underlying topological insulator as shown in figure 5.12 d). This is of no concern on the larger areas, which will not be measured in the STM, and only rarely happens on the patterns itself, since here the protruding bridge structures form a protective spacer. Minimal amounts of accidentally degridded structures can even be helpful. If for example in the square grid design one of the patches loses the Se capping, or the Nb layer also, these areas can be used to monitor the underlying layers in SEM as in figure 5.12 d) before decapping in the STM chamber.

After degridding with *FC*, only a comparably short dip of up to 3 minutes in HF is needed to remove the SiO_2 stumps of the pillars to achieve a sample with only conducting Si and Se-capped TI/Nb surfaces ready for transfer to the STM chamber. With this approach, grids of all structure densities can be reliably and cleanly relieved of the nitride structures without any large-scale damage to the functional layers and devices as shown in figure 5.12 c). Moreover, the amount of mask debris is minimized by this approach, removing the grids mostly entirely without any remnants of silicon nitride structures.

Thus, using *First Contact™* to exfoliate the grid structures, only a short exposure to acid is needed, decreasing the probability of damage by the etching process. Moreover, damage to the patterns and capping is greatly reduced, firstly because the Si_3N_4 grid is removed completely, and no parts can stick to the sample as was the case with flushing by using a pipette. Secondly, the exfoliation is strong enough to remove also the densest structures, whereby no cotton swab scratching needs to be employed to remove the structures, preventing scratch damage to the capping and functional layers.

5.3.2 Te as a Se-Capping Alternative

The process to remove the grid can be greatly optimized by using *FC* and exfoliating the grid structures, minimizing the damage to the patterns as well as the time needed to expose the front surface of the sample to hydrofluoric acid. As mentioned in the previous sections however, the decapping process of the Se leads to a deterioration of the TI films surface, impeding the desired measurements, since scanning tunneling measurements rely on almost atomically flat surfaces. Moreover, an undetermined Se-containing quaternary compound TI is formed, $Bi_{0.3}Sb_{1.7}Te_xSe_{3-x}$, which exhibits unpredictable shifts in Fermi-energy as well as an uncertain position of the Dirac point in the altered gap structure. These challenges can possibly be overcome by using Te in the capping layer.

As shown in section 5.3, the selenium capping grown in the molecular beam epitaxy chamber M13 in the Nanocluster is deposited as an amorphous layer, covering the functional surfaces almost entirely and protecting it from ambient contaminations and oxidation [205], [206]. Te capping grown at the same, lowest possible substrate temperature on the other hand shows polycrystalline features, which cannot uphold the promise to protect the surface in a patterned device as shown in figure 5.7. A second disadvantage of

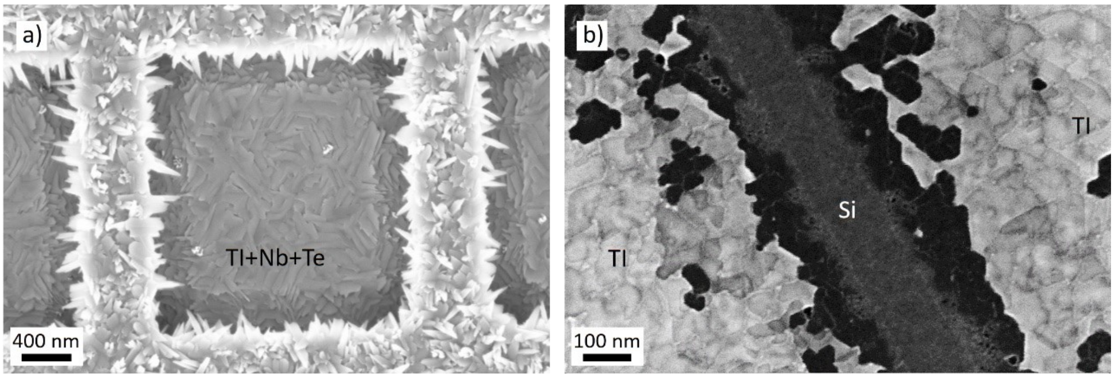

Figure 5.13: Pure Te capping on LUL samples. a) The polycrystalline Te film on the mask is suspected to created holes in the capping on the TI/SC underneath. When decapping the sample after degridding with FC and HF the problems also known from too little Se capping can be identified (b). TI is removed at the edges either due to HF etching of oxides or temperature removal of exposed TI. The only advantage compared to Se capping is a preserved TI surface, exhibiting the expected triangular and step structures, which were lost with Se cappings due to Se incorporation (see figure 5.11 b)).

the Tellurium capping is the formation of TeO_x on the exposed surface. In decapping tests on pure Te films, after they had been exposed to ambient conditions for multiple days, these layers could not be re-evaporated even at temperatures where the TI itself would be re-evaporating. Using even higher temperatures would cause the TI to be removed together with the capping. The prospect of mitigating the incorporation of Se and its consequences however still legitimizes trials of Te capping.

When swiftly transferring the samples to the decapping test chamber after growth, it is possible to re-evaporate the Te as shown in figure 5.13 at only slightly higher temperatures than needed for the Se capping, 200°C for Se compared to 220 – 240°C for the Tellurium capping. This supports the hypothesis that the formation of TeO_x after prolonged exposure to air creates a layer of material on the capping surface, which is stable at higher temperatures and therefore hard to remove. When annealing the Te-capped samples at moderate temperatures to remove the capping, only little Te is re-evaporated from the TI. The TI might even be improved by the annealing step, which is similar to post-growth annealing known from literature [209]. However, exposing these samples to hydrofluoric acid to remove the grid or the pillar leftovers after FC degridding, results in severe damage to the TI regions visible after the decapping process in figure 5.13 b). At the edges of the TI patches dark regions are visible in SEM on the bare TI areas only. When adjusting the SEM contrast to the darker regions, one can see that the TI in these darker regions has been fully removed, seconding the claim that the pure polycrystalline Te capping is not tightly protecting the edges of the patterns. Since the Te deposited on the elevated grid protrudes over the edges of the pattern (figure 5.13 a)), parts of the pattern might not be covered with Te for the full duration of the capping deposition allowing HF to etch exposed and presumably oxidized TI and Nb surfaces. An amorphous Te capping would therefore be desired but could not be deposited in the scope of this thesis. As a silver lining, the remaining TI surface shows better preservation after decapping compared to Se capped samples (compare figure 5.11 b)).

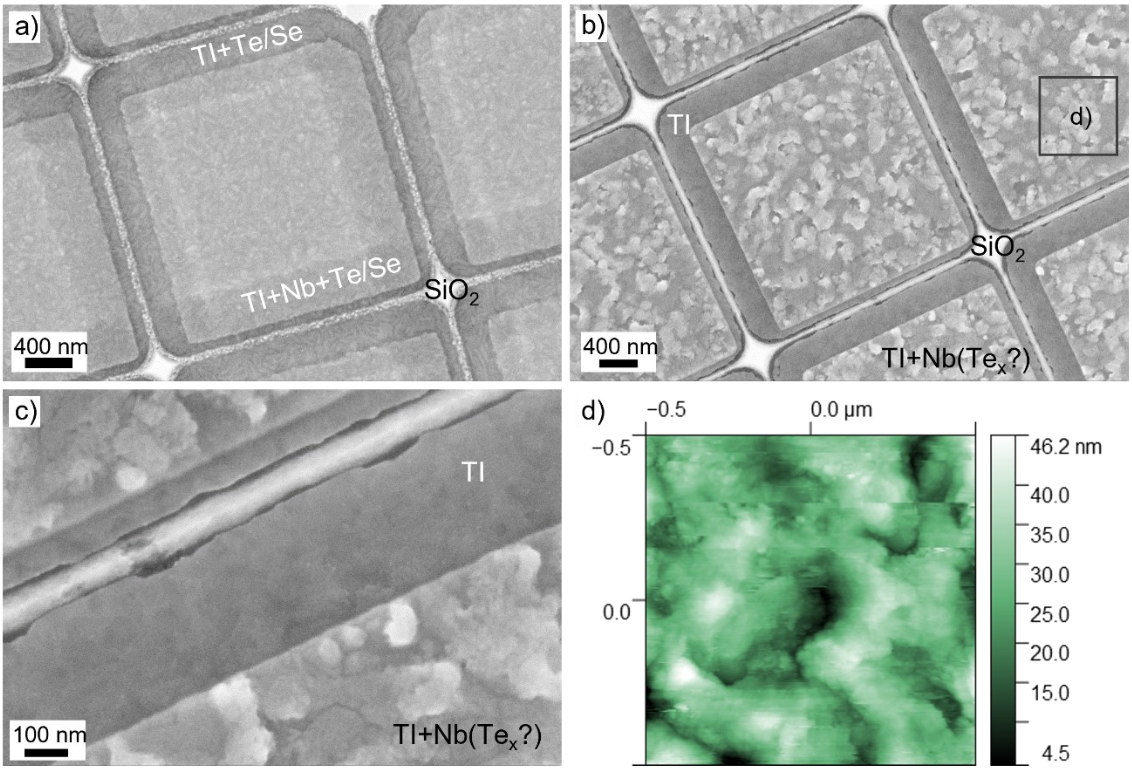

Figure 5.14: LUL samples capped with Te+Se after degridding with FC (a) and after decapping (b). Larger SiO_2 features are still present due to an insufficiently short HF etch before growth. The Te capping does not appear as jagged since it is covered with the smooth Se capping. After decapping no removal or large-scale damage to the TI can be identified (b) and when inspecting the bare TI in c) the surface shows no porous structure (as with Se decapping), but a rather smooth layer. The Te/Se capping combination on the TI therefore yields better results on the TI surface, however on the Nb surface this situation is the opposite. The Nb is rough and multicolored in the SEM picture, indicating an abnormal change in stoichiometry or electronic configuration. AFM measurements in d) on the surface highlighted in b) confirm the rough topography. It is accompanied by an absence of superconductivity in the $NbTe_x$ layer found with STM. The crass height variation is larger than the Nb thickness of ~25 nm.

To cope with these challenges, an alternative approach is to combine the two capping materials in a way that the disadvantages of each are canceled out. With Se and Te capping this is achieved by first growing a thinner layer of Te after the deposition of TI and Nb as a superconductor and following this with a deposition of a Se capping. The result is shown in figure 5.14 a). The Te forms a layer that might exhibit holes due to its polycrystalline structure. Applying a second, thicker capping layer of Se onto the Te aims to fill possible openings in the Te capping. Additionally, the Se layer prevents the Te capping layer from oxidizing and forming the hardly removable TeO_x compounds that previously rendered pure Te unfeasible. The layer of Te on the other hand is expected to impede the incorporation of Se into the TI, thus protecting the TI surface from deterioration when decapping the samples at elevated temperatures. The growth parameters for the cappings are as described in table 5.2 with a substrate temperature of 14°C, limited by the temperature of the cooling water in the system. Samples fabricated with standard TI and Nb parameters and covered with a Te-Se capping are coated with *FC* to remove the grid and then decapped with the process of Te, which is optimal at 240°C for 15 minutes. Degridded and decapped samples are shown in figure 5.14 a) and b) respectively. The degridding works similarly well as with the pure Se capping, the TI surfaces exposed after decapping show the same characteristics as on the plain, Te-only capped samples and distinct triangular TI crystal features are easily identifiable in the decapped regions. Therefore, by combining Te and Se capping the challenges imposed by the TI deterioration after Se-only decapping and by the incomplete HF tightness of the Te-only capping have been overcome.

However, a new problem in connection with the Te capping can be recognized when inspecting the surface of the Niobium after Te-Se decapping as shown in figure 5.14 b) and c). Comparing the topography of Niobium used for the transport measurements shown in chapter 4 (see figure 4.2) with that of the Niobium after Se decapping as shown in figure 5.10 - figure 5.12 no immediate difference can be discerned in SEM. Possibly a layer of $NbSe_x$ has formed, since it is however itself a superconducting material this is of no concern. The Nb surface after Te and Te-Se decapping in contrast shows a profound transformation. The change in SEM contrast suggests either an inhomogeneous incorporation of material into the Nb layer or a stark change in surface roughness, possibly both. The prevalence of this change only in Te capped samples suggests an incorporation of Te into the Nb, similar to the Se incorporation. $NbTe_2$ has been shown to be a layered superconducting material, however at a comparably low critical temperature of 0.5 K [210]. The material formed via Te incorporation however is not stoichiometric $NbTe_2$, and thus assumptions and finding sources about its superconducting behavior are difficult. In [190] Zang *et al.* deposit a similar, but inverted layer stack of Bi_2Te_3 on Nb, resulting in a Bi deficient $NbTe_x$ interlayer, even though both Bi and Te fluxes are supplied continuously. This underlines the tendency of Niobium to absorb the Tellurium.

To inspect the superconducting qualities of the formed compound, plain Te-Se capped samples were introduced into an STM chamber and annealed for 5:30 minutes at ~260°C. A rough surface is measured as shown in figure 5.14 d), consistent with the surface seen in the SEM. The height differences on the Nb layer are extreme. The maximum difference of 40 nm cannot be explained by rough TI alone but suggests a starkly changed topography of the Nb itself due to Te incorporation. In spectroscopic measurements at 640 mK, no continuous superconducting gap is found, additionally suggesting a formation of $NbTe_x$. This alteration of the Nb in contact with the Te capping is found on all fabricated samples. Since the exact stoichiometry of the $NbTe_x$ layer is not clear, compounds with higher Te content might have been formed, which only turn superconductive at reasonable temperatures when high pressures are applied [211], further aggravating the problems with Nb and Te capping.

These findings disqualify the Te capping in combination with Nb as a superconductor. In the scope of this thesis, no other superconducting material was tested as an alternative to Nb. However, for future applications an investigation with Tantalum, Lead or Palladium might be feasible. Therefore, although the Te capping prevents the deterioration of the TI surface during decapping, it is not suitable for application on the TI-Nb LUL samples.

At this point, in discussions with Priyamvada Bhaskar, Prof. Markus Morgenstern and Dr. Marcus Liebman, in charge of the STM at the RWTH in Aachen, a compromise was made to accept the presence of some left-over SiO_2 pillar stumps between the patterns. The probability to strike one of the pillars with the STM tip while approaching the sample surface was deemed reasonably small to take a chance at this procedure.

Thus, the pure Se capping is chosen for the fabrication of further devices. By using *First Contact™* to remove the grid and allowing for minimal SiO_2 on the sample surface, all exposure of the sample front side to hydrofluoric acid after growth can be avoided. Therefore, the damage exhibited in the chapter when exposing the TI surface to the HF acid after degridding can be prevented. Only the incorporation of Se into the TI layer and thus the re-evaporation of the Se during decapping remains a challenge in the fabrication. However, as shown in figure 5.10 and figure 5.12, it is possible to realize high quality samples nonetheless, which will be examined in the next section.

5.4 Scanning Tunneling Microscopy and Spectroscopy Results

Samples fabricated via the process described in sections 5.3 and 5.3.1 were introduced into the STM to check the general viability of the approach. On a first sample, the decapping of the Se capping in the STM chamber was tested with a layerstack of only TI and capping.

In the STM, a current is applied to the low-ohmic substrate to heat the surface and remove the capping layer. By supplying a constant power, the sample is kept at 100-180°C for 2.5 hours. In figure 5.15 a), an exposed TI surface is shown in a topographic scan with atomic resolution, proving the viability of the Se capping, albeit only on small scales due to decapping surface deterioration. Determining the lattice parameter a gives an average of $a = 4.25 \pm 0.09$ Å, in line with values expected for BST and as expected much closer to Sb_2Te_3 TIs [129]. The STS measurement in figure 5.15 b) reveals a tunneling voltage profile closely resembling the LDoS of STS scans on BiSbTe compounds found in literature [212]. Around the Fermi level, at zero bias voltage, a minimum in DOS is present, suggesting a Fermi level in the bulk band gap. Therefore, the Se incorporation is, at least in this sample, not worsening the samples electronic configuration. This is another argument towards using Se as the capping material.

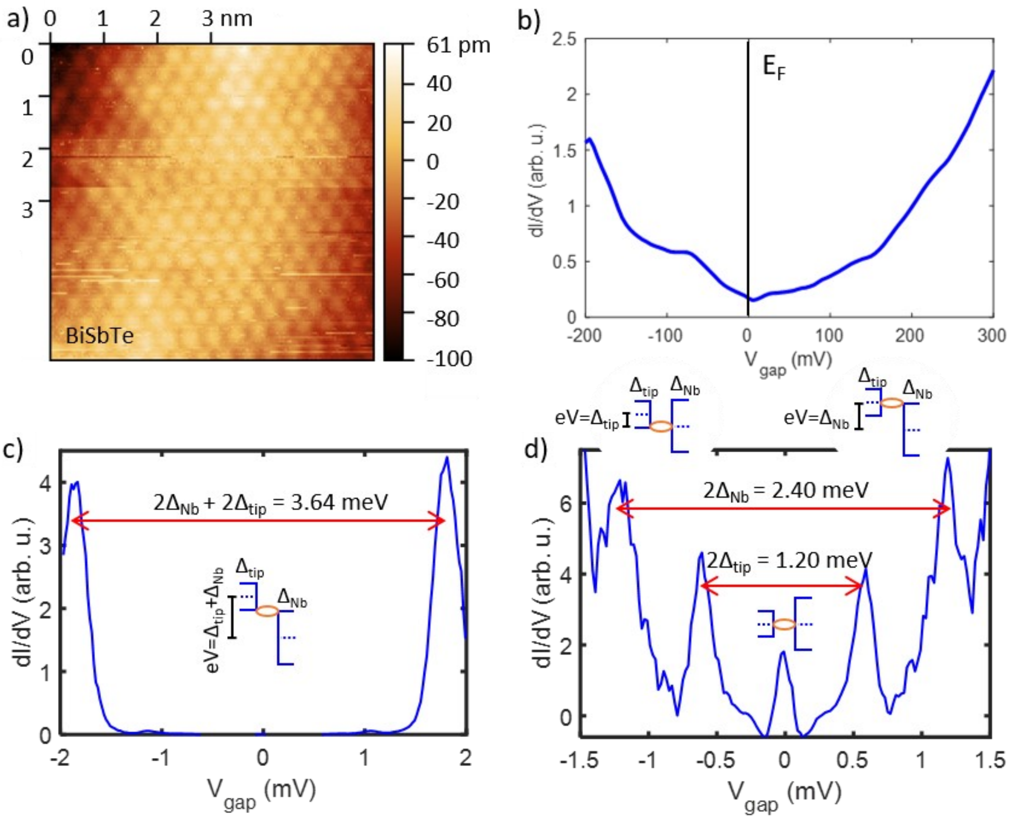

Figure 5.15: a) After annealing the sample for 1 h to 100-120°C, a pristine surface of a TI can be measured with atomic resolution, albeit on small scales. The hexagonal arrangement and interatomic distances fit to the expected values for the BST TI. Moreover, spectroscopic measurements show a conductance behavior resembling literature values [212]*, suggesting a Fermi level in the gap, where the DOS and therefore conductance is lowest (b). c) and the zoom-in in d) show measurements on a second sample with Nb at 640 mK with a superconducting tip due to Nb accumulation. The peaks appear where the occupied high DOS at zero energy and at the SC gap edge of the tip overlap with high DOS on the sample, enabling transport via AR (orange in the insets). At zero bias voltage both SC ground states overlap, increasing bias voltage then leads to overlapping as indicated by the insets, yielding 3 peaks in each direction. Data provided by Priyamvada Bhaskar* [213].

A second sample with Nb and Se capping is introduced into an STM with cryogenic capabilities to evaluate the superconducting gap signatures of the Nb layer after Se capping removal. As shown in figure 5.15 c) and d), measurements performed by Priyamvada Bashkar at the RWTH Aachen on the Niobium at 630 mK reveal a superconducting gap with multiple peaks from overlapping high DOS positions. When approaching the sample, some Nb was collected on the tip, creating a superconducting STM tip. Therefore, both tip and sample exhibit the typical SC LDoS profile with accumulation of states at the gap edges and at zero energy. At zero bias voltage the 0 states overlap, forming a Josephson junction like circuit and thus yielding an increased conduction via AR. By applying a bias voltage and thus moving the tip's DOS upwards, first the DOS at the diminished gap of the tip intersects with the 0 state of the sample, resulting in peaks at ±0.6 meV (see insets in figure 5.15 d)). At higher bias, the 0 state of the tip intersects with the Nb gap edge DOS, giving 1.2 meV for the Nb gap, close to literature values of $2\Delta = 2.32 - 2.91$ meV [38], [200], [214], until lastly the lower tip DOS crosses the upper Nb gap DOS resulting in an increased

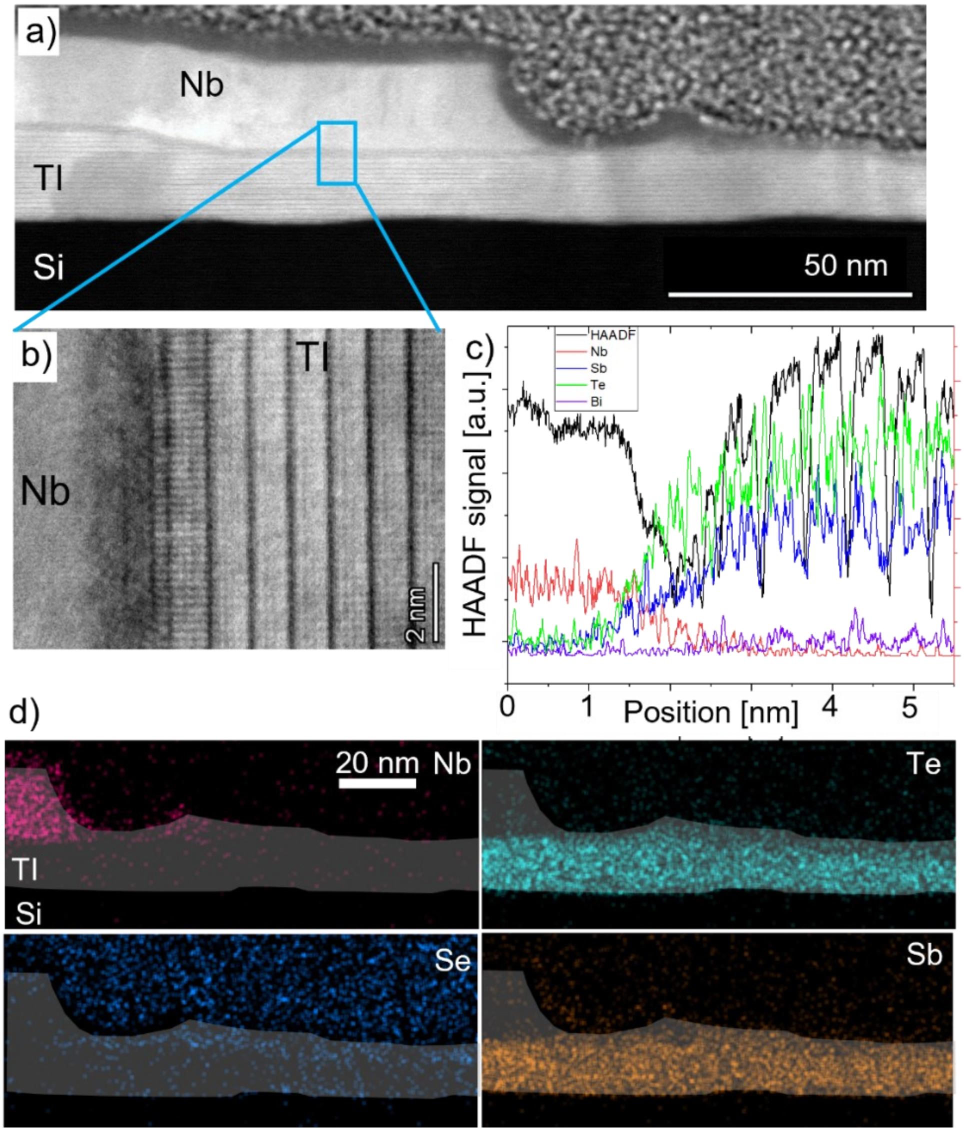

Figure 5.16: TEM and EDX investigation of a lamella extracted from a degridded and decapped LUL sample. In an overview of the lamella is shown, depicting the Nb layer on the TI. The Nb layer exhibits a sharp edge before sloping down onto the TI. At the TI-Nb interface (b) the TI QLs are clearly distinguishable, but a trilayer-like region can be seen at the immediate interface. EDX line measurements show a region of smooth transition from Nb to the TI at about 2 nm where a trillayer of NbTe$_2$ *could be present. EDX maps of the TI surface in d) show the distribution of Nb, Te, Se and Sb, highlighting the Nb-TI layer position in grey. At this specific position, a kernel of Nb is situated about 20 nm from the Nb edge. Te, Sb and Nb show no intermixing, the Se after decapping is accumulating mostly at the TI surface forming a quaternary compound. The Se incorporation into the Nb surface is rather minute.*

conduction at $\Delta_{Nb} + \Delta_{tip}$ (figure 5.15 c)). The measurements thus show that via the employed methods of Se capping and decapping as well as STS on Nb, both desired qualities of the film, topography and DOS can be investigated.

Figure 5.16 a) and b) illustrate TEM microscopy pictures of a finished LUL sample after BST, Nb and Se deposition to examine the interface quality at the TI-Nb interface as well as the surface of the TI. The sample is degridded and decapped by the methods described above and a FIB cut is performed perpendicular to the Nb-BST edge. The shown area is well suited for the investigation of the behavior of the superconducting gap when measuring from Nb onto the TI surface. In figure 5.16 a) the transition from the Nb onto the TI is depicted, exhibiting a steep Nb edge and a thinning of the TI towards the right edge. A closer look at the TI-Nb interface in b) and c) reveals a sharp interface from the Nb (red) to the TI, with the potential formation of a trilayer at the immediate TI-Nb interface. The EDX data in c) is not fully conclusive there, but a smooth transition from the Nb signal to the Te is present. Though this could be explained by a Nb-Te trilayer, a BST layer deeper down in the lamella would show the same EDX profile. $NbTe_2$ has been seen in previous samples in our group exhibiting high transparency with Bi_2Te_3, suggesting a good interface quality of the LUL devices. Investigating the TI surface after decapping with EDX, the Se signal in figure 5.16 d) shows only little intermixing of Nb with Se and a slight aggregation on the TI surface, forming a quaternary compound. Still, the bulk of the Se capping has been entirely removed.

A complete line scan from Nb onto TI is finally performed in the University of Cologne by Dr. Jens Brede on a LUL sample. The data is given in figure 5.17. After BiSbTe, Nb and Se growth the sample was degridded with *FC* and brought to the University of Cologne, where it was inserted into the STM chamber and decapped by annealing. The resulting surface between two square structures is shown in figure 5.17 a) in an AFM mode overview. From left to right there is first the Nb layer on TI, then a thin TI edge, followed by a minute Si gap, a wide TI area exhibiting the expected triangular crystal structure and followed by Nb, confirmed by an AFM line scan along the black line. The shown area is well suited for the investigation of the behavior of the superconducting gap when measuring from Nb onto the TI surface, as was planned after the results of chapter 4.

Such a measurement is performed in figure 5.17 b) over a range of 200x200 nm at 350 mK. The black line scan shows the scan height information, aligning with the AFM measurement in a). Every four nanometers a measurement is performed. The resulting profiles are averaged along the Nb edge direction, which as shown in a) is parallel to the y-direction. Therefore, all measurements in one 4x200 nm column with similar distance to the Nb edge are combined. Since the Nb edge is not fully straight, this results in a slight overlap of Nb and TI surface measurements very close to the edge, affecting 2-3 columns. The measured conductance is normalized by the normal state conductance. The dI/dV map reveals a persistent and strong superconducting gap on the Nb layer with superconducting coherence peaks as depicted in figure 5.15 c). This remains unchanged up to the Nb edge, where the SC gap closes quickly, extending a maximum of 20 nm onto the TI surface. Due to the averaging, this value is probably overestimated. The faint central dip region from about 120 nm onwards is not to be confused with the TI bulk gap, as the latter is two orders of magnitude larger (compare figure 5.15 b)). A small superconducting gap can also be excluded, as this feature shows no coherence peaks and does not exhibit any further distance dependence over 120 nm. This measurement is performed on multiple positions and samples, yielding the same result. As highlighted in blue in the profile measurement in figure 5.17 b), the presence of the SC is lost after about 20 nm, showing no drop to zero conductance, zero bias conduction peak or superconducting coherence peaks. The zero bias conduction line scan (red) also shows a plateau 20 nm after the drop from the Nb layer. A

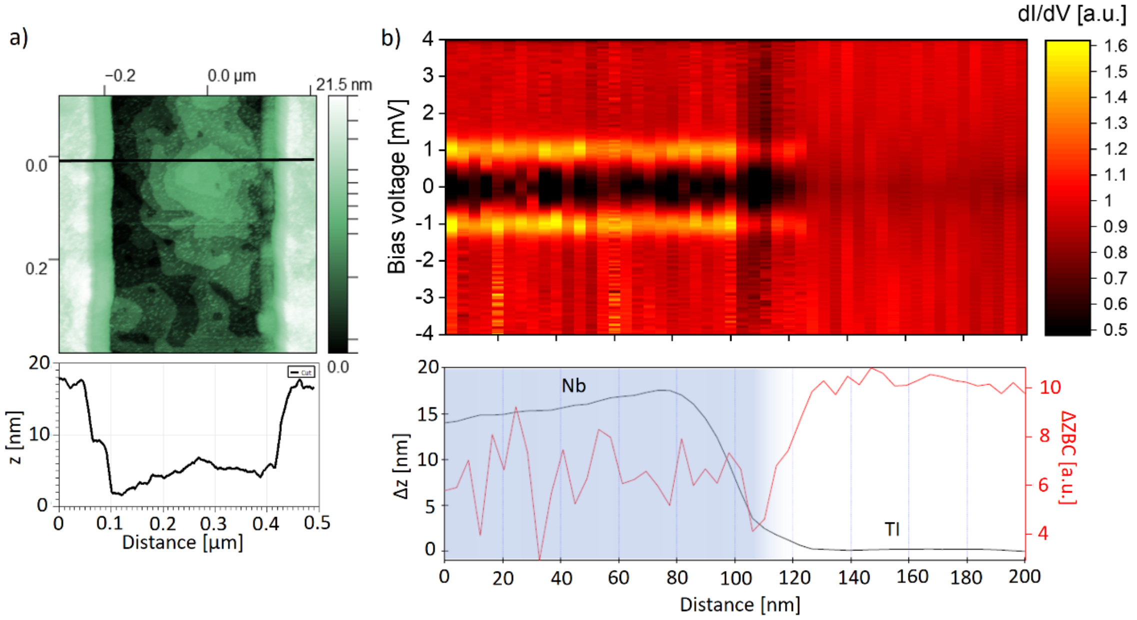

Figure 5.17: a) AFM overview map and line profile of a degridded and decapped LUL sample. Left and right the edges of a Nb patch are visible, with a TI layer in between. The TI exhibits the expected triangular structure and a high surface quality after Se decapping. On the sample of a) a map of the LDoS was measured at 350 mK as shown in b). Every four nm of the map of 200x200 nm, a U_{bias}-dI/dV profile is measured, similar to that in figure 5.15 b)-d), followed by an averaging along the Nb edge. The conductance is normalized to the normal state conductance. The line profile in b) shows the height information Δz and dU/dI at zero bias (ΔZBC). Between 0 to 110 nm the scan is performed on Nb, yielding a superconducting gap and SC coherence peaks as in figure 5.15 c). Over a distance of 20 nm however, at 100 to 120 nm, the gap feature is lost and only a minute dip around zero bias is found on the TI surface. Increasing the bias range at this position yields the profile of the TI LDoS as shown in figure 5.15 b). The SC gap therefore only persists for <20 nm on the TI surface. Data and images provided by Jens Brede.

chemical interface barrier preventing SC from proximitizing the non-magnetic TI is not seen in the TEM and EDX measurements, which would rather suggest a high transparency. This finding thus seems to contradict the measurements done on wider than 20 nm Josephson junctions [105], [215], [216], however the absence of a SC gap does not rule out the presence of correlated quasiparticles in the region, which would carry a current via ABS in the case of a JJ.

Moreover, this measurement does not contradict measurements performed on top-down TI-SC systems, since the TI system proximitized by the SC underneath is less than 10 nm thick [85], [190]. Still, we suspected to see a SC induced into the surface states of the TI on a longer scale than <20 nm [217], [218]. A second, earlier fabricated, sample investigated by Priyamvada Bashkar at the RWTH Aachen had shown similar results as shown in figure 5.18. There however, the TI etching and degradation issues that are present in figure 5.11 were still prominent, hence it could not be determined whether a double tip was present or whether the off-Nb measurement was performed on an exposed Si surface that had been etched bare unintentionally. Due to the surface degradation, no atomic resolution on the TI could be achieved to prove its presence. When measuring spectra in a line moving off the

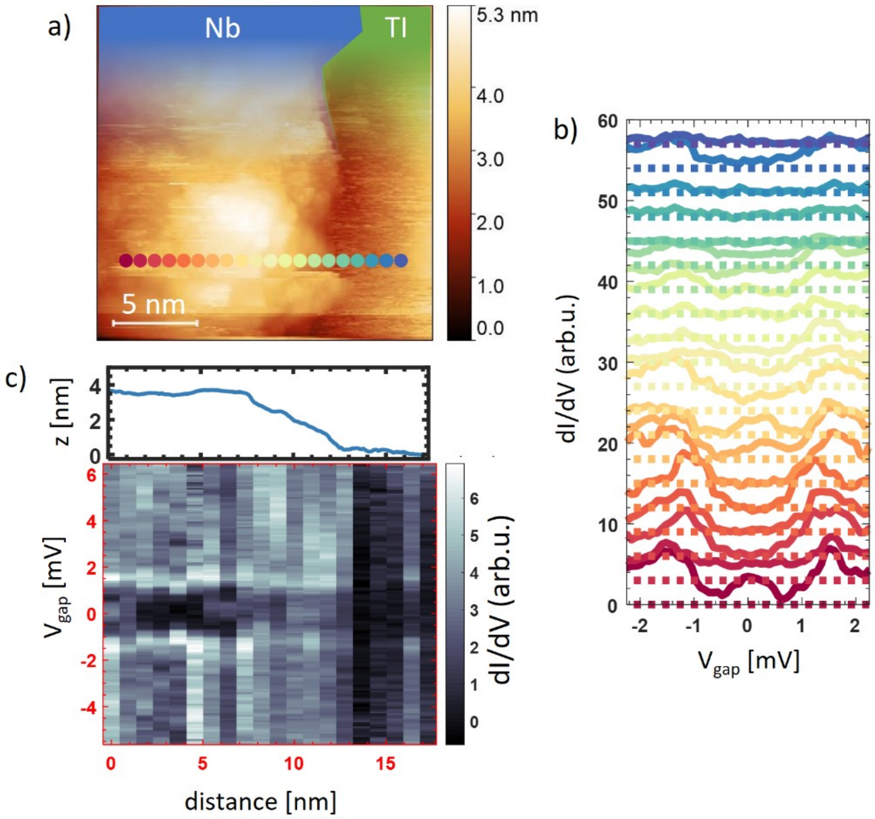

Figure 5.18: STS/STM measurements at 640 mK on an earlier sample, in which the TI etching issues were not solved yet. Due to high noise the surface of the TI could not be resolved. a) As in figure 5.17, a line scan is performed from Nb onto TI, with b) showing dI/dV data at the marked spots in a). The data is shifted for clarity, revealing the loss of a gap and its coherence peaks when moving off the Nb step. In c) a height profile and corresponding gap profile map show the loss of the SC gap feature on an even smaller scale. The gap is lost after 2-4 nm, however the low surface quality of the TI in this sample does not allow for a clear distinction between TI, etched TI and SI surface. Data and images provided by Priyamvada Bhaskar [213].

Nb as shown in figure 5.18 a), the same SC gap to gap-closure behavior is observed as in figure 5.17. The gap vanishes over few nanometers and while some in gap features seem to be present, the general noise does not allow for further investigations of the sample. Still, the same behavior suggests presuming a TI surface is measured when moving off the Niobium is valid in both samples, although no atomic resolution is present in either. The latter would clearly prove the rapid gap closure. Therefore, the LUL technique is still in need of optimization to enable atomic resolution measurements on the TI and SC surface to clearly distinguish the layers. That this is generally achievable has been shown in figure 5.15 a).

The rapid loss of the SC gap indicates that for investigations on MTIs, the edge of the magnetic TI should be near the edge of the SC, similar to the set-up on the left hand side of the AFM micrograph in figure 5.17 a) to ensure SC in the vicinity of the edge state. Although no extended SC gap profile on the TI surface could be measured, all in all, the LUL technique achieves what it has been designed for: the investigation of the development of the SC gap and LDoS at the transition from a patterned SC onto a TI with *in situ* prepared

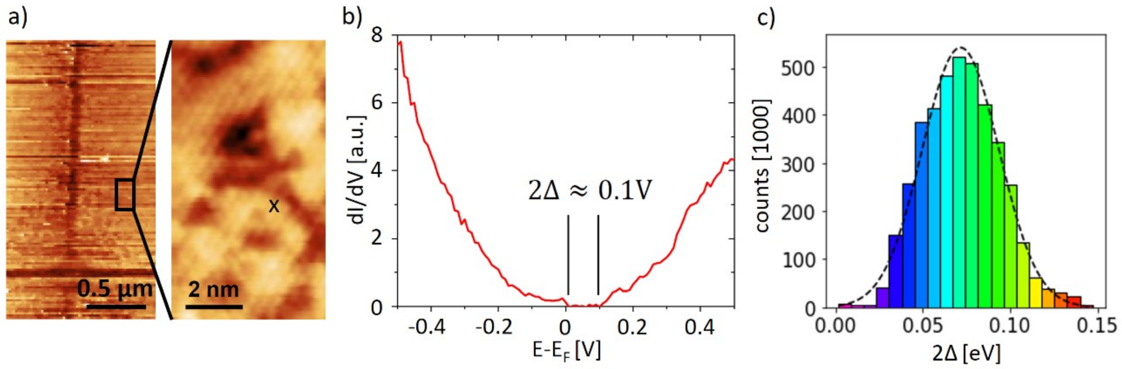

Figure 5.19: STM and STS on CBST. a) A trilayer CBST/BST/CBST structure is deposited on a grid sample and capped with Te and Se as in figure 5.14. After annealing to 230°C for 20 minutes, the sample is cooled to 6K, below the Curie temperature. In STM, the square MTI structures are clearly discernible, however the streaks indicate dirt or leftover capping, making stable STS measurements difficult. High resolution scans show the atomic surface structure, however due to capping leftovers the resolution is not as good as in figure 5.15. At the marked position an STS measurement in b) reveals a 0.1 V gap in the surface state LDoS close to the Fermi level. c) depicts a histogram detailing the distribution of gap magnitude over multiple positions. A Gaussian fit to the approximately normal distribution yields $2\Delta=72\pm22$ meV, in agreement with literature values of magnetic gaps measured on other CBST thin films [159]. *Graphics provided by Felix Lüpke (PGI-3).*

surfaces. More research needs to be performed still on the sample cleanliness after degridding and decapping as well as on the options of other soft cappings. Especially an approach utilizing a Nb/NbTe$_x$/Te-capping stack circumventing the issue of rough NbTe$_x$ formation could enable higher quality TI thin film surfaces. These proposals are still a work in progress, but the measurements of the last paragraph show the viability of the LUL approach clearly.

STM on decapped magnetic TIs

To further show the viability of the developed technique, also regarding the measurements on MTIs, an MTI sample is brought to the group of Dr. Felix Lüpke at the Peter Grünberg Institute 3. On this sample, a Te+Se capping is combined with a thin layer of CBST in a trilayer sandwich structure. The CBST thin film is grown following the recipe of the sandwich sample in chapter 3.2.3. Since no Nb is present on the sample, a Te+Se capping is a viable option to protect the surface states of the Te-based compound. To release the capping, the sample is annealed to 230°C for 20 minutes in a second chamber and then transferred in vacuum to a one-tip STM at 6 K. In figure 5.19 a), a larger AFM mode micrograph of the decapped square structure is shown alongside a zoomed in picture revealing the TI surface with a slightly smeared out atomic resolution, showing a discernable hexagonally packed atomic configuration. At the position marked with an x, a spectroscopic curve is measured, depicted in figure 5.19 b), revealing a conductivity of approximately 0 at zero bias, indicating a gap in the LDoS. As the temperature is below the Curie temperature, a FM configuration should be present, creating a magnetization gap in the sample surface. The measured gap has a width of about $2\Delta = 100$ meV. Measurements on multiple positions yield an approximately normal distribution centered around $2\Delta = 72 \pm 22$ meV determined by a Gaussian fit in figure 5.19 c), which is perfectly in line with values for the magnetic gap of a CBST MTI given in literature [159]. The extent of the measured magnetic gap is an order of magnitude larger than the gap of Nb measured in figure 5.15. Presuming this disparity in gap size is also present in the JJTLM samples in chapter 4, it explains the strongly suppressed induced SC coherence length. Thus, exploring CBST MTIs with lower Cr doping levels are imperative to achieve long SC coherence lengths, as was propounded in chapter 4.4. However, the width of the distribution in figure 5.19 c) is a direct consequence of the random Cr distribution in the film. Thus, when transitioning to less doped thin films, regions with very low magnetic gaps might pose a challenge for the establishment of a homogeneous magnetic phase in these films, especially when considering a QAHI phase. Unfortunately, the sample in in figure 5.19 suffered from contaminations of capping leftovers, impeding repeated measurements on the sample. Therefore, more time needs to be invested into improving the capping and decapping process. However, the fact that a magnetic gap could be measured in the present sample adds another validation step needed to go towards the realization of quasi *in situ* fabricated MTI+SC STM samples.

To summarize, the three measurements shown in figure 5.15, figure 5.17 and figure 5.19 each performed in STMs of different groups establish the high variability of the LUL process and the possibilities of the technique to cater to the requirements of various STM set-ups. In future samples, the capping process needs to be further optimized and a combination of MTI and SC needs to be deposited. These hybrid structures will reveal the interaction between the superconductor and the MTI and will shed light onto the findings of chapter 4. Utilizing various concentrations of magnetic doping should then lead to an understanding of the behavior of the induced SC coherence length, leading to improved device layouts for electrical transport measurements. In the next step, triangular and stripe structures will then be used to investigate features related to spatial confinement to finally move towards studying the physics of MZMs via STM.

In conclusion, the measurements clearly reveal the capabilities of the developed technique. By using a removable capping and large scale UHV lithography, confined patterns of TI thin films and superconductors on a sub-micrometer scale are achievable while also securing that the surfaces of the functional layers are at no point during the fabrication process exposed to ambient conditions. Only in the STM chamber will the desired surfaces be made accessible for measurements, without the presence of insulating and therefore potentially tip damaging material. This quasi *in situ* device fabrication method for arbitrarily patterned structures for STM investigations is a unique approach opening the path to many more possible experiments utilizing the same technique. Especially the ways to distinguish MZMs from trivial excitations discussed in Jäck *et al.* in [184] should be implemented with the LUL technique in coming experiments. It should also be emphasized again that the developed technique is not limited to TIs but can be employed for various quantum materials capable of being grown in an MBE chamber or via any other directional thin film deposition technique. It exemplifies the first atomically resolved STM measurements on patterned thin films not patterned by the STM itself [219], but by outsourcing the electron beam lithography via the stencil lithography step to before the growth and thus avoiding contaminations from cleanroom processing.

6 Conclusion & Outlook

Utilizing topological insulators to create a new, more fault-tolerant route towards quantum computation is the desire of many. This thesis set out to investigate one of the most important steps towards topological quantum computing, which is the interplay of magnetic topological insulators and superconductors. While these states are proposed to exist in TI-SC hybrid devices and first, debated, indications have been found, MTIs and the QAHE arising in them are proposed to host more accessible and stable Majorana states. When transitioning into the quasi-1D regime they allow for Majorana states in confined devices independent of external in-plane magnetic fields. This is a great advantage over nanowires of semiconducting materials, which rely on a magnetic flux along the wire axis to enter into a topological phase in the first place. The combination of an MTI or a QAHI with a SC utilizing the capabilities of *in situ* UHV lithography, an established process at the PGI-9 in the Research Center Jülich, was therefore the declared goal of this thesis.

Previous to the efforts taken in this thesis only non-magnetic topological insulator films had been grown in the institute. These growths had been performed for plain thin films, selectively deposited films as well as combinations of TIs with SCs using the UHV lithography technique. Since Chromium is known to be a viable dopant for TIs to reach the QAHI regime quite reliably, a Cr source was added to the BST MBE system, providing first achievements in CBST thin film growths by showing continuous Cr incorporation and thus no large-scale phase separation of an additional CrTe phase in the thin films. Simultaneously, a second MBE chamber at the HNF Nanocluster, the M13, was put into operation as part of this thesis. The system provides all elements relevant for CBST, as well as multiple metals via electron beam evaporation. Growth optimization in the new system yielded high quality TI thin films (chapter 3.1), providing the basis for multiple publications [146], [157], [162], [220], [221], [222]. Hall devices of CBST films exhibit strong ferromagnetic order and state of the art carrier densities and mobilities (chapter 3.2). By decreasing the CBST film thickness the goal of the QAH insulator draws nearer, evidenced by the increase in anomalous Hall resistivity. While the CBST compounds were characterized, a new species of MTI had gained traction among the MTI community, the intrinsically magnetic TIs in the form of $MnBi_2Te_4$ and $MnSb_2Te_4$. Research performed in parallel to optimizing the CBST in this thesis however finds that $MnBi_2Te_4$ heterolayers form antiferromagnetic parts and trivial TI parts due to uncontrollable layer stacking. MST could be a solution to this problem, as it does not need heterolayer stacking to establish a ferromagnetic order. SQUID measurements as well as investigations of Hall devices showed indications of FM order, however far from quantization (chapter 7.1).

The final breakthrough is brought by adapting a trilayer approach of CBST/BST/CBST, exhibiting quantized Hall resistance and the exact temperature dependent behavior of the longitudinal resistance known from literature to culminate in the QAHE at temperatures in the mK range (chapter 3.2.3). The direct measurement of the QAHE is however impeded by limitations in the measurement setup, reaching only 1.2 K. Nonetheless, the high-quality

MTI compound necessary for the realization of the QAHI-SC system is achieved, opening the way towards experiments with the desired MTI-SC hybrid devices.

Further research building on what was achieved in this thesis regarding MTIs entails improving the quality of the MTI crystals and striving towards a more robust stoichiometry of MST. More complex hetero structures of CBST and BST layers might provide further advantages, for example featuring a magnetically proximitized BST layer at the interface to the superconductor, to not have magnetic dopants immediately at the SC-MTI interface. Even an intermixing of CBST and MST might be feasible to establish FM order in an MST dominant compound. Utilizing ferromagnetic insulators like EuSe or EuS is an additional approach towards the realization of MTI (and even QAHI)-SC hybrids, with which magnetism and SC could be separately induced into an TI layer, creating an overlapping region with both phenomena [223], [224], [225]. Via digital alloying and subsequent annealing of the layers to form a single MTI crystal even the issue of non-functional MTI selective area growth might be solved in the future [226].

The fabrication of two systems of magnetic topological insulator materials has been achieved in the first part of this thesis, with CBST showing strong signs of reaching the QAH phase. The second part thus concentrates on using these MTI compounds and combining them with superconductors in order to study the interplay of MTI and SC. Josephson junctions, which are familiar structures known from investigations of the proximity effect into non-magnetic TIs performed in the PGI-9 previously, were chosen to examine the extent of the proximity effect into the MTI. In literature, weak links with pure and strong ferromagnetic compounds have been shown to exhibit supercurrents, invalidating the argument that magnetism could be generally preventing MTI Josephson junctions ([94], [102], [103], [178], [179], [180]). First investigations of an CBST thin film provided by partners at the UCLA, onto which a layer of Niobium was deposited in Jülich via a UHV stencil lithography mask, showed an unexpected strong increase in resistance at low bias currents (chapter 4.1). This absence of a supercurrent in the MTI can be caused by multiple issues affecting this first SC-MTI hybrid: An oxidized layer between MTI and SC that formed during transport to Jülich could not be excluded, which might potentially form an insulating barrier; multiple damages to the mask layer creating shorts inhibited measurements of various devices; the selectively deposited Josephson junctions provided no means to investigate the magnetic qualities of the CBST film. However, magnetic field dependent measurements revealed hysteretic sharp drops in resistance at the coercive fields, thus when the magnetic exchange gap in the MTI films is briefly diminished. Known from studies on other magnetic JJ in literature, the dips indicate the formation of short ranged induced SC close to the Nb contacts that does not span the full weak link but decreases the resistance [169]. The transparency for correlated quasiparticles is thus increased when the magnetic gap is diminished.

To correlate the magnetic and induced SC gap, a device needed to be designed which allows for investigations into the extent of proximitized superconductivity as well as evaluation of the magnetic response of the MTI film. Since prepatterned selective area growth was shown to be incompatible with the high sticking coefficients of the involved magnetic dopants, a layout was devised utilizing only the suspended UHV lithography technique. Measurements on the resulting, purely *in situ* fabricated, Josephson-junction-transmission-line-measurement devices exhibit a similar bias dependent resistance behavior on Cr- as well as Mn-MTIs (chapters 4.2 and 4.3). Since these samples did not suffer from the possible obstacles detailed in the previous paragraph, only the magnetic exchange energy is left as the source for the low transparency for correlated quasiparticles. This claim is corroborated by a separately but identically fabricated JJTLM with non-magnetic TI and Nb, where regular expected supercurrents were observed (see figure 7.19). Hall measurements in the MTI devices show domain formation dependent processes due to screening effects but nonetheless enable measurements of the coercive field via Hall signals, validating the JJTLM design further (chapter 7.4). Comparing the two *in situ* CBST JJTLM devices illustrates that only in the device with a lower Cr concentration a drop in resistance at low bias is present. In accordance to results in literature on JJs [172], this dip is another sign of a short ranged induced SC and an increased transparency, as was the case for the dips in the magnetic field dependent measurements before. The dip's presence only in the lower doped CBST compound further identifies a large magnetic exchange energy as the main obstacle, causing low transparency and thus impeding a strong proximization of MTI, and points towards the use of lower magnetic gap materials for future devices. The absence of a supercurrent in the MTIs did not allow for measurements of indications of Majorana physics. Future experiments utilizing UHV lithography and MTIs should target thinner bridges and thus smaller weak link contact separations as well as smaller magnetic gaps, increasing the transparency and thus the likelihood of Andreev bound states spanning the weak link. A rework of the Hall part of the JJTLM device might also be beneficial in order to have more distinctive Hall signals. Nonetheless, the JJTLM devices are the culmination of the efforts undertaken to reach the goal of this thesis, the *in situ* integration of MTIs and SC into a hybrid structure, achieving first indications of SC in the MTI devices.

In the third part an extremely local approach to investigate the induced SC into (M)TIs is given in the form of scanning tunneling microscopy investigations, enabling local measurements of the induced superconducting gap on TI compounds. Nano- to micrometer sized structures with partly overlapping SC material would be needed to investigate the induced SC in a device like setup. UHV lithography can provide such devices, the insulating hard mask however poses an insuperable risk to the delicate STM tip. Therefore, the removable stencil lithography is developed, providing large scale, fully in UHV created repetitive patterns of (M)TI-SC hybrids (chapter 5.3). Two soft cappings, Te and Se are explored and their properties compared, while simultaneously evaluating wet etching and exfoliation based removal of the hard mask grids. The result is a reliable technique for the STM investigation of hybrid devices, not limited to (M)TI-SC hybrids, entailing full protection of the functional surfaces from any ambient conditions. Only in the STM chamber itself is the soft capping removed via annealing, uncovering pristine surfaces. First results show the superconducting gap of Nb and high-quality density of states profiles of TIs after decapping, but a line scan from superconducting Nb onto the TI reveals a rapid loss of a SC gap when transitioning onto the TI surface over a distance of less than 20 nm (chapter 5.4). The gap closing is seen in multiple samples and shows that for SC-MTI samples, the SC layer needs to be deposited close to the MTI edge to provide a SC gap to the MTI's edge state. Moreover, the results call for narrower JJ in future MTI-JJTLM designs. Lastly the magnetic gap of CBST films after decapping is examined and magnetic gap values comparable to literature are found. A large disparity between the SC and magnetic gap sizes measured in STM again suggests that the Chromium doping level in the investigated CBST MTIs is too high, separating the correlated quasiparticles and thus yielding low transparency and low induced SC coherence lengths. Therefore, the next step is to combine MTI thin films of various Cr doping levels with SCs and measure the development of the SC gap when transitioning from the SC onto the (proximitized) MTI. First, this would be done on larger patterns before proceeding to nanometer scale structures. The extracted gap profile will be used to improve the JJTLM design in order to evaluate the proximity effect also in electrical transport. To utilize the more promising Te capping also with a superconducting material, an alternative for Nb might have to be found. This alternative should ideally also provide robust 2e periodicity instead of Nb's observed 1e periodicity when measuring the parity of superconducting islands, which is proposedly caused by sub-gap states in the Niobium's superconducting gap [227], [228]. Ta or Al (with a diffusion-preventing interlayer [220]) could be viable candidates towards robust Majorana physics, however their stability in the magnetic fields of the MTI need to be evaluated. Moreover, an intentionally grown $NbTe_x$ layer on the pure Nb might prevent the formation of the extremely rough self-forming $NbTe_x$ layer after Te capping. Lastly, the biggest hindrance for this promising technique is the issue of surface contamination by capping left-overs and surface deterioration during degridding. Solving these issues would lead to more stable STM tip operation, enabling line scans and STS mapping with atomic resolutions. Whether this can be achieved by multilayer-cappings, alternative decapping or new degridding approaches is still research in progress.

Looking into the future, the materials and techniques developed in the three parts of this thesis provide a toolkit for a plethora of further MTI and MTI-SC interaction research. As it was set out in this thesis' title, this toolkit of *in situ* techniques can be used to investigate how and if superconductivity is induced into magnetic topological insulators, be it via electric transport or scanning tunneling measurements. Apart from the installation and commissioning of the new MBE tool M13 in the HNF Nanocluster, the establishment of MTIs in general and specifically CBST as a host material for the QAHE at the PGI-9 offers a manifold of further experiments, also for other research fields like spintronics. Advancement of $MnSb_2Te_4$ will provide further tools to the toolkit by procuring a second possible QAH material. But $MnBi_2Te_4$ should not be disregarded, since the antiferromagnetism in the compound enables investigations into the extensive field of axion insulators. The next tool, the JJTLM device, fabricated via *in situ* patterning with stencil lithography, provides insights into the MTI-SC compatibility, working towards the goal set for this thesis. It shows that by engineering the magnetic exchange gap in the MTI, indications of induced superconductivity can be found in CBST-Nb hybrid devices calling for further experiments with lower magnetic exchange gaps. These will go hand in hand with local investigations of the gaps utilizing the last tool developed in this thesis, the innovative large scale UHV lithography technique. It provides an instrument capable of reliably creating patterned, STM-compatible samples with combinations of arbitrary quantum materials for *in situ* measurements in ways unprecedented in STM.

I hope the results garnered in these chapters and the toolkit I provide with this thesis will help future generations of postgraduates in their endeavors to achieve the irrefutable verification of the elusive Majorana mode in fully proximitized MTI-SC hybrid devices, bringing us all a large step closer towards topological quantum computing.

7 Appendix

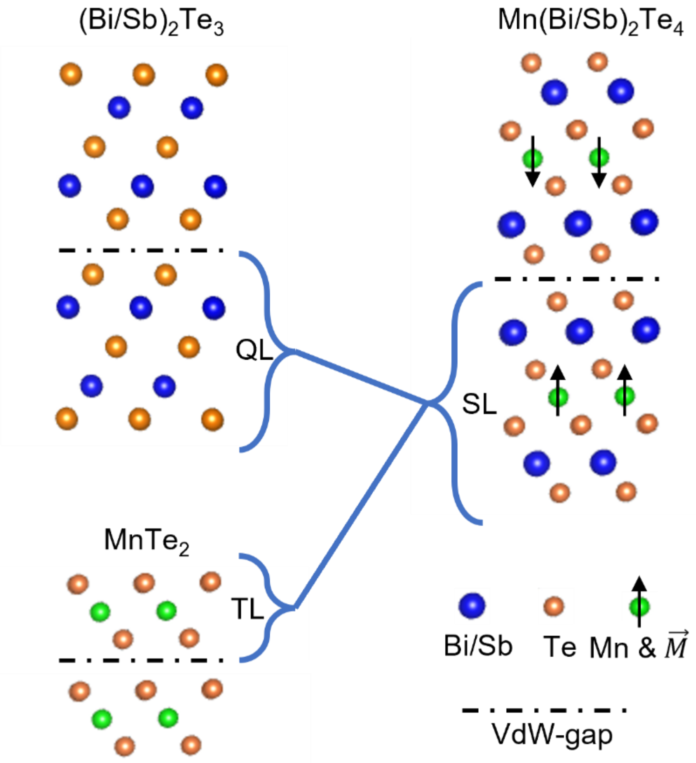

Figure 7.1: Septuple MnBiTe/MnSbTe layers (SL) made from QLs and trilayers (TLs), bound together by van der Waals forces. The SL can be visualized as a Te-Mn-Te trilayer substituting the middle Te layer in the QLs. Three SL with 60° rotation between layers (ABC stacking) form a unit cell with lattice parameters a =4.334 Å and c = 40.91 Å (MBT), each SL therefore having a thickness of 13.64 Å [229]. *The magnetization in the SL is carried by the Mn atoms, which arrange antiferromagnetically between SLs in MBT.*

7.1 Intrinsic MTIs: Septuple-layered Manganese Compounds

When magnetic TIs commenced to be explored as a system in which the quantum anomalous Hall effect could be realized, the focus was almost exclusively put onto magnetically doped TIs and, although more rarely, TIs in contact to a magnetic compound to induce magnetism into the TI. Magnetic dopants include Cr, V, Fe and also Mn to varying success, although forms of stable magnetism could be established in all of them. While in Cr- and V-doped samples rather soon stable QAH states were found [53], [230], in Fe and Mn doped samples the effect is still searched for [141], [231].

This changed drastically for Mn when it was found in 2019 by Gong *et al.*, Li *et al.* and Otrokov *et al.* [115], [232], [233] that at higher concentrations of Mn in the crystal, septuple layers emerged by a fixed arrangement of the Mn atoms in the middle of a Bi_2Te_3 quintuple layer (which is also proposed by ab initio calculations for vanadium in the form of VBi_2Se_4 [234], [235]). As shown in figure 7.1, the septuple layered (SL) structure of the intrinsic magnetic TI $MnBi_2Te_4$ (MBT) can be understood as a combination of the QLs of the ordinary TIs, combined with a single layer of the antiferromagnetic compound $MnTe_2$ [236]. A Te-Mn-Te building block is inserted into each Te-Bi-Te-Bi-Te QL in the middle position, resulting in a Te-Bi-Te-Mn-Te-Bi-Te SL structure. The intrinsic magnetism of the $MnTe_2$ is transferred to the SL compound, while the topological nature of the Bi_2Te_3 is also maintained. The resulting compound exhibits a large topological gap of 220 meV in the bulk. On all side surfaces the gap is closed by a TSS as expected for a topological material, however on the surfaces perpendicular to the out-of-plane magnetization a magnetic gap is opened due to TRS breaking. The magnetic gap created at the Dirac point amounts to up to 88 meV, evoking a large energy window in which the QAH state can be found when gating the Fermi level into this gap [233]. But not only the gap size promises a more stable QAH platform, the fixed position of the magnetic moments in the layers suppresses magnetic gap variations over the sample surface, in contrast to doped MTIs. The compound thus promises a large parameter space to investigate the interplay of MTI and SCs.

However, while a single layer of MBT is a trivial ferromagnet, a stack of MBT follows the antiferromagnetic coupling of the $MnTe_2$ as indicated by arrows in figure 7.1. The antiferromagnetically ordered MBT is not a QAHI, but an axion insulator [50]. In order to observe the QAHE in layer stacks of MBT SLs, two approaches can be taken. Either the number of layers must be odd, resulting in an uncompensated SL, turning the full layer stack minutely FM, or a large external magnetic field is applied aligning the magnetization in the full stack to form an “artificial” FM [237]. This artificial FM might then be gated into the QAHI regime.

These two requirements pose crucial hindrances for the MBE growth of MBT and the examination of devices. While smooth, large-scale terraces of MBE grown film are possible, it is impossible to guarantee a continuous single height of the TI film so that the odd SL number is maintained for one whole device. Due to the predominantly Volmer-Weber growth type in the examined TIs, that is growth via a formation of islands that coalesce into large thin films, there will always be regions with more or fewer SLs. The even/odd layer configuration for the investigation of QAHE in MBT is thus only realizable in exfoliated flakes with a controlled, continuous thickness. The alignment of magnetization of all layers in the MBT stack on the other hand undermines a crucial advantage of MTIs for device investigations. When examining quasi-1D structures of TI in the form of nanowires, in-plane magnetic fields are needed to close the arising confinement gap [65]. These need to be sufficiently precise to apply a magnetic flux of half a flux quantum through each ribbon which is required to be topological. Additionally, when moving towards braiding, operating schemes involve the control of the superconducting phase in the proximitizing SC to be adjusted via out-of-plane magnetic fields penetrating SQUID structures [26]. While ribbons made of MBT might not need the in-plane component, the necessary out-of-plane field to stabilize the FM QAH state (9 T in [237]) will heavily impact the possibilities to realize Majorana devices from the film.

There were however workarounds found with which the aFM structure of MBT can be avoided and FM order in arbitrarily thick stacks can be achieved. Thus, the viability of

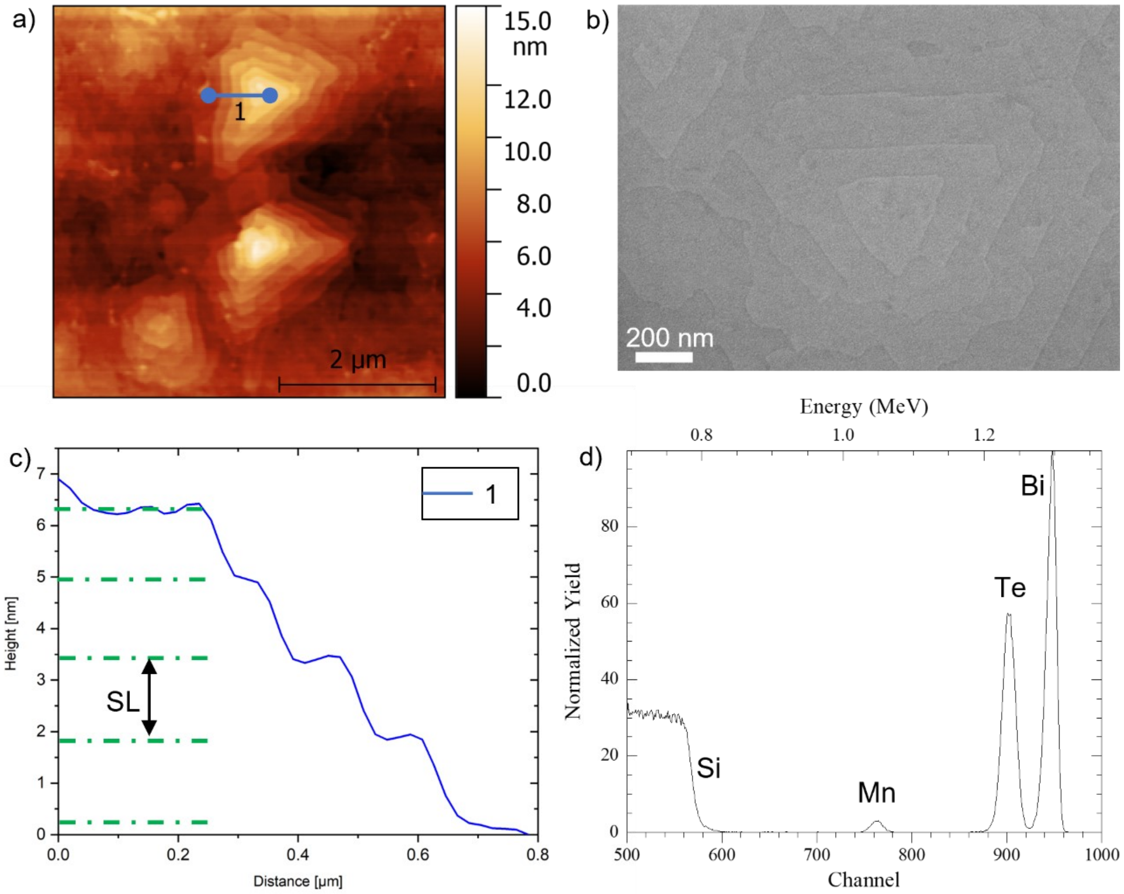

Figure 7.2: MnBiTe films grown in the BST-MBE on Si(111) substrates. In a) an atomic force micrograph is shown, exhibiting high triangular crystalline mounds, surrounded by flatter surfaces as shown in the SEM micrograph in b). These mounds arise frequently in the Mn compounds at random points, probably at substrate surface contaminations or edges. A scan along the marked line is given in c), showing the SL steps in the mound with a height of approximately 1.4 nm, fitting to literature values [229]. *RBS measurements (d) confirm the presence of Mn in the grown layers and are utilized to determine the stoichiometry. A) adapted from* [240].

MBT as an QAH MTI can be re-established, raising hopes to realize SC-MBT hybrid structures. These workarounds and the general fabrication and growth of MBT will be investigated in further detail in the following section.

After MBT was discovered as the first intrinsic magnetic TI, it was proposed to mix Sb into the compound to influence the Fermi level position in hopes to reach a charge neutral compound following the example of $(BiSb)_2Te_3$ [238]. The results were promising, showing a charge neutrality at around 31% Sb content and an influence of the Sb ratio on the magnetism of the film. Ultimately however, while pure $MnSb_2Te_4$ was shown to also be antiferromagnetic, it is also topologically trivial [239], rendering it for the most part uninteresting for QAHI research.

In 2021, Wimmer *et al.* [241] showed that these assumptions made due to DFT calculations are only true for a perfectly ordered MST crystal. Depending on the synthesis procedure, intermixing of Sb and Mn will occur, which in turn heavily influences the magnetism and topology of the material. At low rates of intermixing, around 2.5%, the purely SL MST will not only turn ferromagnetic, but topological. The resulting $MnSb_2Te_4$ compound thus promises to exhibit FM order and a Fermi level close to the magnetic gap, all while being topologically non-trivial [241]. This compound will be further investigated, grown and examined in section 7.1.2.

7.1.1 The Manganese Bismuth Telluride system

The following results on the growth and characterization of $MnBi_2Te_4$ were collected together with Robert Müller in the scope of the supervision of his Master's thesis studies.

The first decision that had to be taken before the growth of MBT compounds could commence was to choose a MBE chamber to introduce Mn into and how to evaporate it, via Knudsen thermal effusion cells or via electron beam evaporation. Due to the availability of a plethora of other materials for further processing, the newer M13 chamber was chosen, however only an e-beam evaporation crucible was available. Compared to Cr, Mn is expected to exhibit high enough beam fluxes to facilitate growth at temperatures around 750°C due to its relatively low vapor pressure, while Cr evaporation only starts at 1000°C. This causes problems for the e-beam evaporation, since only very low powers are needed to generate fluxes, so low, that no stable control of the fluxes was possible. The result were discontinuous, rough growths of low crystal quality. Therefore, further growths of manganese compounds were shifted to the BST-MBE, in which one effusion cell was equipped with manganese. The far better adjustable flux of material via thermal control resulted in high quality crystalline MBT thin films as exhibited in figure 7.2.

Figure 7.2 a) depicts an AFM measurement on a MBT film grown at 300°C substrate temperature with $T_{Bi} = 480\ °C, T_{Te} = 330\ °C$ and $T_{Mn} = 751\ °C \pm 3\ °C$, resulting in a Te:Bi:Mn flux ratio of 300:20:1, maintaining a Te surplus to avoid defects. The Mn cell's temperature is not exact, but is driven by a constant set voltage, causing the temperature to vary slightly. The flux ratio however is largely maintained. Figure 7.2 a) shows large, protruding crystalline mounds next to a comparably flat thin film. The surrounding thin film is shown in a SEM micrograph in figure 7.2 b), where the triangular structure of the TI film terraces is clearly discernable, exhibiting up to 200 nm wide flat terrace areas. These larger mounds in a) can be found randomly on the film and might be due to contaminations of the flat substrate before growth, at which nucleation happens more frequently and robustly, causing larger islands to form. The mounds, although generally preferred to be avoided, can be used in AFM to investigate the step height of the vdW layers. A line scan along the blue line named in figure 7.2 a) is depicted in figure 7.2 c), clearly showing the steps in the vdW material. The steps show an average height of 1.39 ± 0.04 nm, which is in accordance with literature values for the septuple layered material [229]. In BiSbTe compounds, the QL steps amount to 1 nm per QL. Thus, already by the AFM it can be concluded that a septuple compound has been formed when Mn was introduced.

Ratio	Exemplary measurement	Compound	Allotted/left-over percentage points	Ratio in full film
2Mn% < Bi%	Mn% = 8,9% Bi % = 32,9% Te% = 58,2%	$MnBi_2Te_4$	8,9 : 17,8 : 35,6 -> 1 : 2 : 4	about 9 MBT SL : 7 BT QL
		Bi_2Te_3	15,1 : 22,6 -> 2 : 3	
2Mn% = Bi%	Mn% = 13,8% Bi % = 29% Te% = 57,2%	$MnBi_2Te_4$	13,8 : 27,6 : 55,2 -> 1 : 2 : 4	Pure in range of RBS error
2Mn% > Bi%	Mn% = 18,9% Bi % = 25,3% Te% = 55,7%	$MnBi_2Te_4$	12,6 : 25,3 : 50,6 -> 1 : 2 : 4	about 12 MBT SL : 6 MnTe
		MnTe	6,3 : 5,1	

Tab. 7.1: Classification of different RBS stoichiometry results with examples. When the ratio of Bi is greater than twice the ratio of Mn, a mixture of MBT and BiTe layers is formed (first row). The opposite case (bottom row) results in a MBT and MnTe layer stack. In both cases, the maximum value of buildable SLs with a 1Mn:2Bi:4Te ratio is allotted, the left-over percentage points make up the 2Bi:3Te or 1Mn:1Te layers, resulting in the given layer ratios (last column). Only in the case of 2Mn%=Bi%, a pure MBT compound is grown (middle row).

RBS measurements further confirm the presence of Mn in the layers as shown in figure 7.2 d). When increasing the Mn flux relative to the Bi flux, two regimes can be distinguished in RBS as shown in table 7.1. At lower Mn fluxes, the elemental percentages given by RBS can be separated into $MnBi_2Te_4$ and Bi_2Te_3, which means when subtracting twice the amount of Mn percentage points from the Bi percentage and four times the amount of $Mn\%$ from the Te percentage, following the $MnBi_2Te_4$ stoichiometry, the left over Bi and Te percentages have a ratio of 2:3, suiting the Bi_2Te_3 compound. This is given in the first line in table 7.1, when $2Mn\% < Bi\%$. At higher Mn fluxes, the Mn percentage in the grown film exceeds the necessary Bi available, $2Mn\% > Bi\%$, as given in the bottom row in table 7.1. In this case, when adding half of the amount of $Bi\%$ from the $Mn\%$ and twice the $Bi\%$ from the $Te\%$ to form $MnBi_2Te_4$, the left-over $Te\%$ and $Mn\%$ have a ratio of 1:1, resulting in a mixture of MBT and MnTe. With careful adjustments of the Mn flux in relation to the supplied Bi, a Mn ratio between the two regimes of about 14.2 % can be achieved, which is the ratio expected for a pure $MnBi_2Te_4$ crystal. Exemplary RBS results for such a measurement in the range of RBS errors ($\pm 0.4\%$) are given in the middle row in table 7.1, when $2Mn\% = Bi\%$.

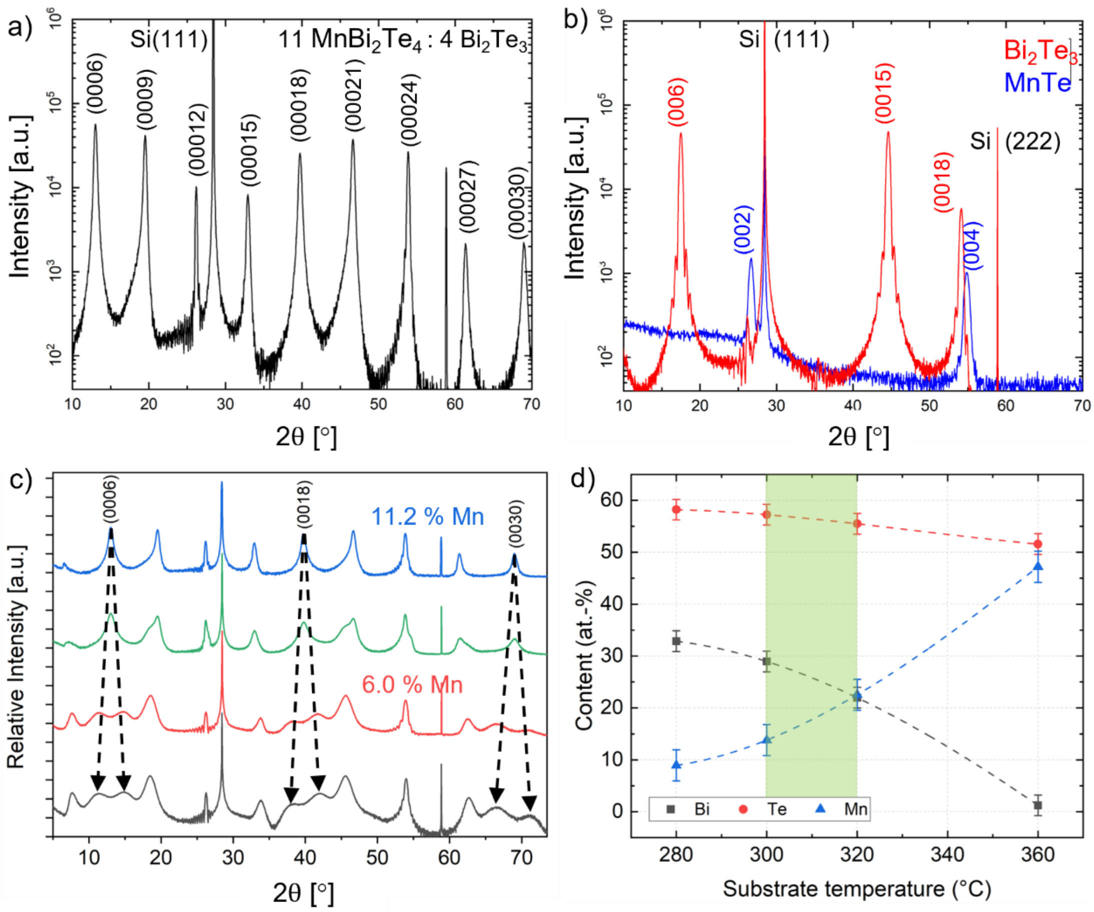

Figure 7.3: Comparison of XRD results of $MnBi_2Te_4$ (a), Bi_2Te_3 (b, red) and MnTe (b, blue). The (0006) peak of the MBT compound divides into the (003) and (006) compounds of Bi_2Te_3 the more Bi_2Te_3 quintuple layers are incorporated into the MBT:BT compound. In the case of a) the ratio is 11:4, or 11.2% Mn, corresponding to the blue curve in c). The splitting of three MBT peaks is shown in c) when decreasing the Mn ratio, ultimately leading to pure Bi_2Te_3. Possible MnTe peaks as in b) can only hardly be identified in pure MBT due to the overlap of the (00012) -(002) and (00024)-(004) peaks. d) depicts the evolution of Mn content with substrate temperature while the material fluxes are kept constant. c) adapted from [240].

The existence of Bi_2Te_3 and MnTe surplus in the respective compounds points towards an interesting circumstance. The surplus, which stoichiometrically fits to vdW layered compounds, suggests that interlayers of the respective compounds exist in the SL structure of the MBT. This superlattice structure should be visible in X-ray diffractometry, as the interlayers provide a change in lattice parameters, especially along the z-axis in the crystalline *c* direction. In figure 7.3 a), the characteristic XRD pattern of SL MBT (11 MBT : 4 BiTe) are plotted, in b) the peaks of Bi_2Te_3 and MnTe are given. Of high interest are the MBT (0 0 0 6) peak at about $2\theta = 13°$ and the (0 0 0 18) peak at about $2\theta = 39.6°$, which each split up into two superlattice satellite peaks when increasing the amount of surplus Bi_2Te_3 in the compound. As shown in figure 7.3 c), the degree of splitting increases the more Bi_2Te_3 QLs are introduced into the system. Via this method, the QL:SL ratio can be roughly estimated [242], the estimation via stoichiometry however tends to be more exact, as will be seen later in the TEM investigations. In the extreme case of very low Mn content, the diffraction pattern defaults to the pattern of Bi_2Te_3, as there are only QL left in the thin film then. The MBT (0 0 0 6) peak for example thus continuously splits up into the Bi_2Te_3 (0 0 3) and (0 0 6) at $2\theta = 8.7°$ and $17.5°$ respectively.

Figure 7.3 d) illustrates that the substrate temperature during growth has an unusually strong effect on the stoichiometry of the film when the material fluxes are kept constant. This behavior emerged during the growth series for the XRD peak splitting investigation. The region marked in green between 300°C and 320°C is best suited to grow MBT compounds in the BST-MBE, with FWHM of the MBT XRD peaks down to 50 arcsec. At substrate temperatures lower than the green zone, polycrystalline films with small domains form, unsuited for further investigations. Above the green zone in figure 7.3 d), the thin films develop holes, which enlarge with substrate temperature, until only singular islands are formed. When increasing the temperature starting at 300°C with Mn constantly at 13.8% power, the Mn content increases steadily towards equilibrium with Bi, for which the share decreases likewise. The Te content also decreases, as more and more MnTe is formed. An increase in Bi desorption during growth at elevated substrate temperature and the thusly decreased growth rate and altered stoichiometry has also been observed in previous work in the same chamber. It is therefore important to control the substrate temperature more tightly for stoichiometric MBT compounds compared to BST compounds. The higher desorption of Bi at elevated temperatures, while Mn increases and Te is almost constant due to its overabundance, foreshadows a challenge when trying to grow the compound selectively. Selectivity is maintained when the desorption from the amorphous mask is higher than the absorption while the opposite has to apply to the Si surface. If Mn is still adhering at temperatures where the Bi is desorbing, there might be many Mn nucleation clusters on the Si_3N_4 mask. The possibility of SAG of MBT is further investigated in chapter 3.3.

When supplying too little Mn flux for the stoichiometric compound, Bi_2Te_3 interlayers will proposedly form, which fits to the elemental ratios from RBS and the peak development in XRD. This behavior can be capitalized on regarding the magnetism of the compound. As mentioned in the introduction to this chapter, MBT is inherently an antiferromagnetic compound, not suited to provide a QAHI platform at low magnetic fields. As has been shown by Kagerer *et al.* and Klimovskikh *et al.* in 2020 this can be influenced by the ratio of SL to QL [147], [242]. To clearer identify the relation between both, the compound is written as $(MnBi_2Te_4)(Bi_2Te_3)_n$ or the equivalent $MnBi_{2+2n}Te_{4+3n}$. In the following, n will mark the number of QL between each SL, as suggested by the former notation. Each SL is in itself a ferromagnet, but the SLs couple antiferromagnetically over short distances. By inserting non-magnetic QLs between SLs, the aFM coupling is diminished. For $n = 0, 1$ and 2 Klimovskikh showed that the $(MnBi_2Te_4)(Bi_2Te_3)_n$ system is still antiferromagnetic, however with increasing n lower magnetic fields are needed to align the magnetization directions in the compounds, signaling a decrease in aFM coupling strength. At $n = 3$, the compound is considered to be ferromagnetic, yielding a promising route to realize the QAHE in an intrinsic magnetic heterostructure TI. Higher n compounds should theoretically also exhibit FM due to the vanishing aFM coupling strength, however there the SL are rather described as fully uncoupled magnetic layers with no alignment of the

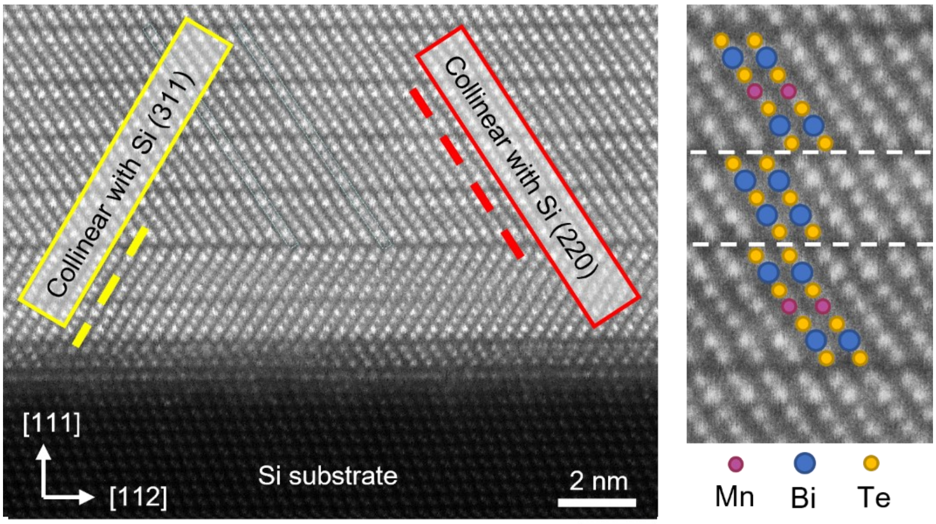

Figure 7.4: Scanning TEM of MnBiTe showing the septuple layered nature of the MBT compound. Two twisted domains can be identified. On the Si(111) surface, first a BiTe/MBT layer collinear to the Si(311) direction is present, which is then overgrown by a layer collinear to Si(220). Directly at the Si interface, a trilayer can be identified, possibly a local MnTe layer. The proposed positions of the elements are marked in the zoomed in picture on the right. The position of the heavier Bi can be discerned quite well, while the Te and Mn positions cannot be differentiated. A QL is also incorporated, supporting the claim of a SL:QL mixing when Mn% is lower than ~14%. Modified from [240].

magnetizations. Thus, the $n = 3$ case is the most promising and therefore sought after. In 2021, Deng *et al.* recorded the QAHE in a $n = 4$ MBT-BT compound grown as a single crystal via the Bridgman method, which was additionally irradiated with electrons to manipulate the charge carrier density, up to temperatures of 1.9 K, further underlining the prospects of the superlattice approach [160].

The next step towards the identification of the magnetization and Hall effect nature in the fabricated MBT samples would be the fabrication of Hall devices from capped, less than 10 nm thin films and their investigation. In order to examine the development of the magnetization with $= 1,2,3 \ldots$, first thicker films with the desired stoichiometries are fabricated. These are investigated via scanning transmission electron microscopy (STEM) to control the stacking order of SL:QL directly, in contrast to indirectly via XRD or RBS. In figure 7.4, the interface of an MBE grown MBT film with $n \approx 0$ is shown in an STEM micrograph. Multiple SLs and their atomic composition are visible, in the zoomed-in picture on the right the specific elements and vdW gaps are additionally highlighted. The growth of septuple layered $MnBi_2Te_4$ with Mn from a Knudsen effusion cell is successful and yields high quality MBT thin films, as was evidenced by RBS and XRD, see figure 7.2 d) and figure 7.3 a). A single QL is wedged between the SLs in the zoom-in, proving that the assumption of the existence of a QL-SL heterostructure in our samples is correct. Moreover, two rotated twin domains can be distinguished, with one overgrowing the other. As marked in the figure, the bottom two layers, one QL and one SL, are collinear to the Si (311) orientation, while the upper SLs are collinear to the Si (220) orientation. The lamella for the STEM investigation was prepared as noted along the Si (112) direction. The graphic

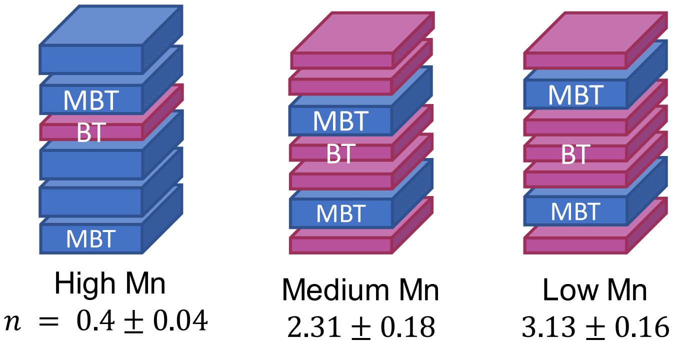

Figure 7.5: Visualization of the different MBT stoichiometries and therefore stacking orders grown for investigation of the magnetization behavior. The SL ratio n was determined by RBS stoichiometry measurements.

shows that locally the ratio of QL to SL can be clearly determined to compare with the XRD and RBS measurements.

For the planned Hall bar devices, MBT films with three compositions depicted in figure 7.5 are deposited to compare the magnetic behavior. For the high and medium Mn compounds, $n \approx 0 \,\&\, 2$, aFM is expected, for the low Mn compound with $n \approx 3$ one expects FM order. Before Hall devices of these compounds are however investigated, the stacking order is evaluated via STEM and EDX in order to ensure that the measured magnetic response can be rightfully attributed to the proposed decreasing aFM coupling. In figure 7.6 a)-c) TEM micrographs together with corresponding EDX scans of the layers are depicted. The Bi_2Te_3 layers are marked purple, blue denotes the MBT SLs. In the EDX spectra, the blue curves describe the Mn content along the lamella, starting at the Si substrate. Distinct peaks show nicely how the Mn is positioned mainly in the middle of the SLs. The high Mn compound in figure 7.6 c) shows a ratio of 14 SLs to 3 QL, which is a little less than the $n = 0.4$ suggested by the RBS measurement, which would give a QL for roughly every third septuple layer. In this particular extract of the prepared lamella $n = 0.2$, however this is only a narrow, local measurement of the layer stack, while RBS averages over an area of multiple mm². Figure 7.6 c) therefore already illustrates a hindrance for the approach towards FM via SL-QL stacking. If in parts of the samples more QLs are present than in others, or vice versa, magnetic domains with varying magnetism are bound to arise. This could theoretically be solved by forcing QL growth by closing the Mn shutter periodically, so that SL are grown at fixed positions. Figure 7.6 a) and b) however suggest that this solution might also not be applicable.

In figure 7.6 a) and b) the low and medium Mn containing compounds are depicted. Compared to c), fewer SLs are present due to the decreased Mn flux. In the given sections of the lamellas, the ratio n is $n = 2.2 \,\&\, 1.2$ for a) “low” and b) “medium”, respectively. These ratios are not in line with those determined by RBS, however as mentioned before, the TEM only shows a small excerpt of the full film. Much more significantly, the layers show a bunching of QLs towards the substrate. In b), this effect is only minute, with a four-layer stack of QL at about 11 to 15 nm, but the tendency of the QLs to amass close to the substrate becomes more evident when examining figure 7.6 a).

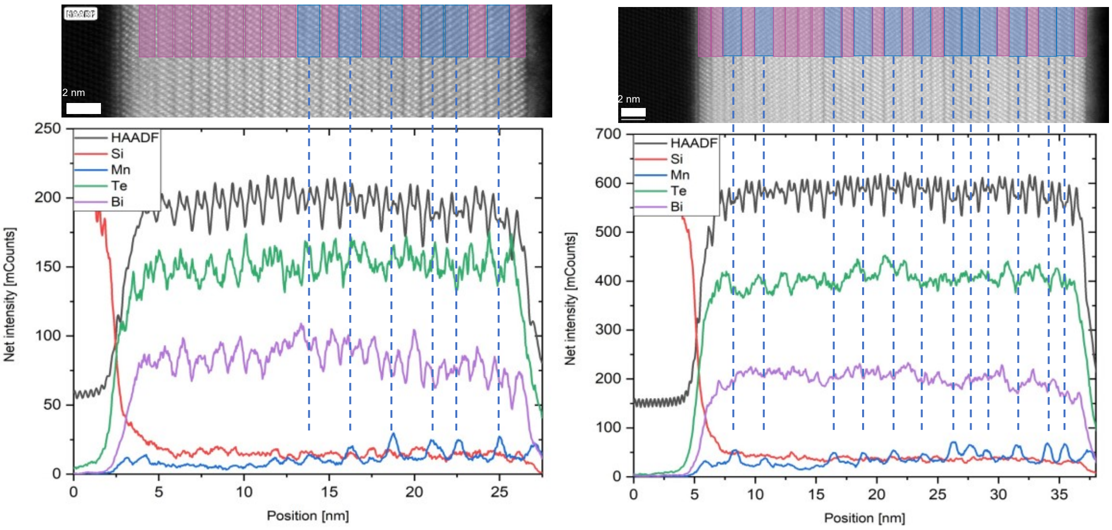

a) low Mn

b) medium Mn

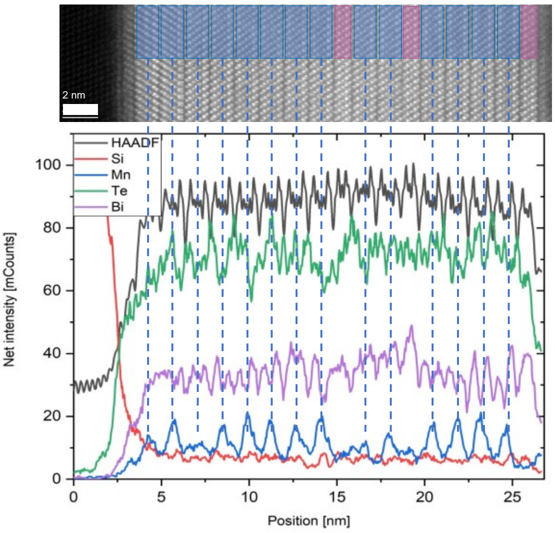

c) high Mn

Figure 7.6: TEM and related EDX profiles along the lamellas extracted from the three MBT:BT compounds. In purple and blue, the QL and SLs are highlighted in the TEM respectively, with the Mn position aligning well with the Mn peaks in the EDX profiles (blue dotted lines). In the EDX spectra the intensity of the respective elements is shown in color code. While the high Mn compound in c) shows only few QLs as expected, in b) and a) the amount of QL increases as planned. However, the stacking order is not following the SL:QL ratio, but the SLs accumulate at the thin film surface. This is most noticeable in a). The Mn flux during growth did not change, suggesting a propagation of Mn during growth in the films.

SLs are only present in the second half of the grown film, with EDX spotting only doping-level amounts of Mn in the first 10 of 21 layers, with slight accumulations at the Si-MTI interface, proving that the Mn shutter was opened for the full growth duration. The flux of Mn before and after growth is compared for all compounds and shows no significant increase towards the end of the growth. In all three compositions however a Mn peak at the thin film surface is visible, which cannot be attributed to a SL. The layer bunching can therefore be appointed rather to the Mn SLs than to the QLs, which means Mn is driven to the top of the film in compounds with low Mn contents, creating more SLs towards the top layer. This effect was not reported on in MBT single crystals fabricated via Bridgman method [239] or MBE thin films [147], [242], [243], however in these publications there is either no TEM employed or only small sections of films are shown with which no statement regarding the full film can be made. The absence of SLs in the low Mn compound is measured over the full lamella, indicating a fundamental issue when growing SL-QL heterostructures. The non-uniformity of the stacking sequence and bunching of MBT SL are detrimental to the FM approach, as they create an aFM layer of MBT on top of a regular Bi_2Te_3 TI. The fact that the Mn tends to accumulate towards the surface of the MTI moreover impairs the prospects of manually controlling the position of the SLs by utilizing the shutter. Even in this approach, the position of the MBT SLs might not be well affixed.

A possible explanation is a minimum amount of accessible Mn atoms on the sample surface required to form a SL. Due to the low Mn rate necessary to create the $n \geq 2$ compounds, some Mn needs to be deposited on the sample first before enough material is present to form a SL. This explanation would be supported by the presence of doping-level Mn in the QLs and the absence of the problem in Bridgman single crystals. However, towards the surface one would then suspect SLs still separated by QL due to part of the accessible Mn being built into the SL, leaving not enough to form another SL immediately. This effect would intensify for lower Mn fluxes, in figure 7.6 a) however there is a consistent, almost $n = 1$ pattern of SLs after the first SL at 12-14 nm. A second explanation is highly mobile Mn and a slightly more energetically favorable configuration into Bi_2Te_3 rather than MBT. Since the substrate is heated from the back, the interface of the Si to the MTI is the hottest part, slightly decreasing in temperature towards the sample surface. This would cause the Mn to float on the surface of the grown film, until a given thickness and temperature decrease is given, at which Mn is incorporated into the TI. The surplus of Mn at the top of the sample could also be explained by this approach. The temperature gradient through the film of 20-30 nm magnitude thickness should however be rather small, making this effect more unlikely.

Though the goal to manufacture a FM MBT compound via stacking becomes an improbable approach due to the revelation of hardly controllable stacking orders and a tendency of the Mn to accumulate at the sample surface, Hall devices were fabricated of the high and medium Mn compounds from thinner films of 11.5 nm and 10.5 nm thickness, respectively. Figure 7.7 a) shows the hysteresis curves of each compound at 1.2K and zero top gate voltage. The raw data exhibited a large influence of the symmetric longitudinal resistance in the Hall signal in both samples, which was filtered from the exhibited data by antisymmetrization. Charge carrier concentrations of $n_{2D} = 2.6 \cdot 10^{13}\ \mathrm{cm}^{-2}$ for the high Mn and $n_{2D} = 5.2 \cdot 10^{13}\ \mathrm{cm}^{-2}$ for the medium sample are determined. A reason for the twice as high concentration in the medium compound was given by [244], who determined via DFT simulations that the formation energy for Bi antisite defects in MBT-BT stacks is lower than in pure MBT due to strain, backed by strain investigations done in the scope of the Master's thesis of Robert Müller [240].

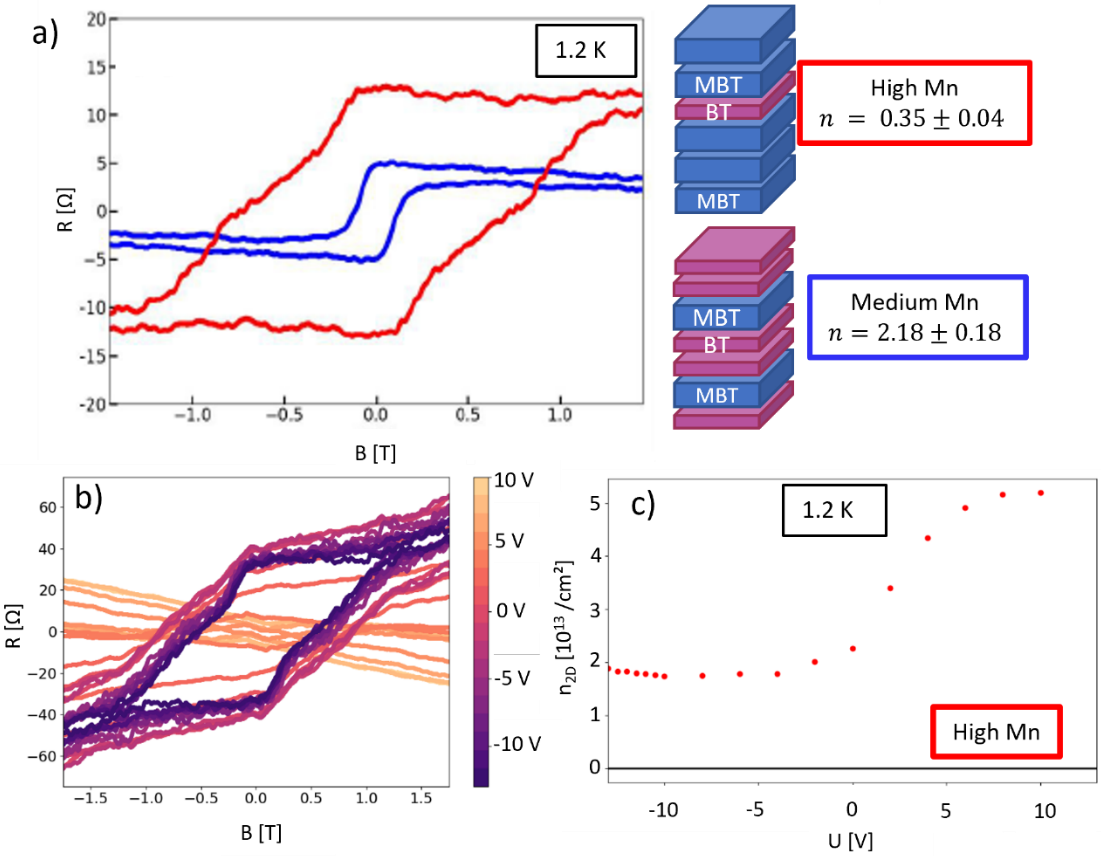

Figure 7.7: Hall characterization of $MnBi_2Te_4$:Bi_2Te_3 compounds. In a) the magnetic response of the Hall signal shows a hysteresis for both compounds depicted on the right at 1.2 K. In the high Mn compound (red) hysteresis kinks can be identified at ~0.5 T, pointing towards aFM signatures in the compound. Following the expectations for $n \geq 2$ compounds, these kinks are not present in the medium Mn compound. Gating of the high Mn compound reveals a strong dependency of the AHE on the charge carriers (b), which increase strongly towards positive gate voltages (c). This suggests a gating into the conduction band, diluting the surface state electrons presumably mediating the magnetism in the compound.

The Hall data at 1.2 K in figure 7.7 a) also illustrate the hysteresis behavior of the MBT Hall devices. Both the high and medium Mn compounds show signatures of the anomalous Hall effect, therefore proving a magnetic order is established in the crystals. However, while the medium Mn compound exhibits a singular step in resistance and a coercive field of ±0.1 T, comparable to the CBST Hall measurements, the high Mn compound features second step at ±0.5 T. A hysteresis with multiple steps and hysteresis loops is expected of aFM compounds, signaling a switching of magnetization of separate domains or layers, while in a FM compound the full stack switches at once [245], [246]. The present data show a mix of both signals and therefore competing aFM and FM effects. Nonetheless, the two devices show the expected behavior, with a weak, but established FM order in the medium compound and a competing FM and aFM switching in the almost pure MBT layer stack. SQUID measurements on the high Mn compound further proved aFM behavior in thicker films due to a stagnant ZFC magnetization (see appendix figure 7.18).

Gate dependent measurements of the high Mn device shown in figure 7.7 b) and c) reveal an increase in charge carriers at gate voltages higher than 3.6 V, accompanied by a stark decrease in AH hysteresis. At gate voltages below -4 V the carrier density stagnates at $1.7 \cdot 10^{13}\,\mathrm{cm}^{-2}$ while the slope of the Hall signal superimposed on the hysteresis changes sign. This might indicate the position of the bulk band gap. With higher concentrations the hysteresis diminishes drastically, suggesting that the magnetism is strongly dependent on the charge carrier density, which points towards the RKKY interaction as a mediator of magnetism in this sample. This effect has also been found in MnBiTeSe crystals, where the Curie temperature increases with the chemical potential closing in on the Dirac point. In [247], Checkelsky *et al.* argue that the magnetism in this system is mostly mediated by the surface Dirac electrons in the bulk band gap, which are largely independent of the gating, in contrast to the bulk carriers. Due to the low signal level at higher gate voltages, no statements can be made about the effect of gating on the fate of the stepwise magnetization switching of the competing aFM and FM contributions. The samples showed no indications of a QAH behavior, especially when noting the low resistivity of the thin film.

To summarize, $MnBi_2Te_4$ is an intrinsically magnetic, however antiferromagnetic, topological insulator, which promises a large and conform magnetic gap. When intercalated with non-magnetic Bi_2Te_3 layers, FM order can be achieved. This prospect is unfortunately dulled by the fact that the stacking sequence cannot be accurately controlled in MBE growth, but the MBT SLs tend to accumulate at the thin film surface, inhibiting planned periodic heterostructures. Moreover, for the QAHE the films needed would have to be less than 10 nm thick. For an $n = 3$ compound and the typical SL and QL thicknesses, this would result in two SLs and 6-7 QLs, which only allows for minute magnetic stability. Due to the fact that the compound itself can however be grown in a high quality via MBE, many groups are still actively investigating the compound. Its aFM order might moreover open up experiments towards axion insulators, which proves that further investigations into this MTI are worthwhile [248].

7.1.2 The Manganese Antimony Telluride system

Not long after the discovery of $MnBi_2Te_4$ as the first intrinsic magnetic TI, Sb was doped into the compound to influence the Fermi level position to optimize the material. Pure $MnSb_2Te_4$ however was not an immediate candidate, as it was predicted to be non-topological in its pure and perfectly crystalline form. Only in 2020 it was shown by Wimmer *et al.* that topology is re-established when the defects in the crystal, predominantly Mn-Sb intermixing, are considered, leading to a non-trivial topology and a ferromagnetic response [241], [249]. When the stacking problems regarding the MBT-BT heterostructures became clear, somewhat disqualifying MBT as a candidate for an intrinsic MTI Majorana platform via MBE, an alternative needed to be found. The fabrication of $MnSb_2Te_4$ (MST) requires similar parameters to MBT. Since moreover no stacking sequences are needed in MST to establish FM order, the development of MST as an alternative intrinsic MTI suggests itself.

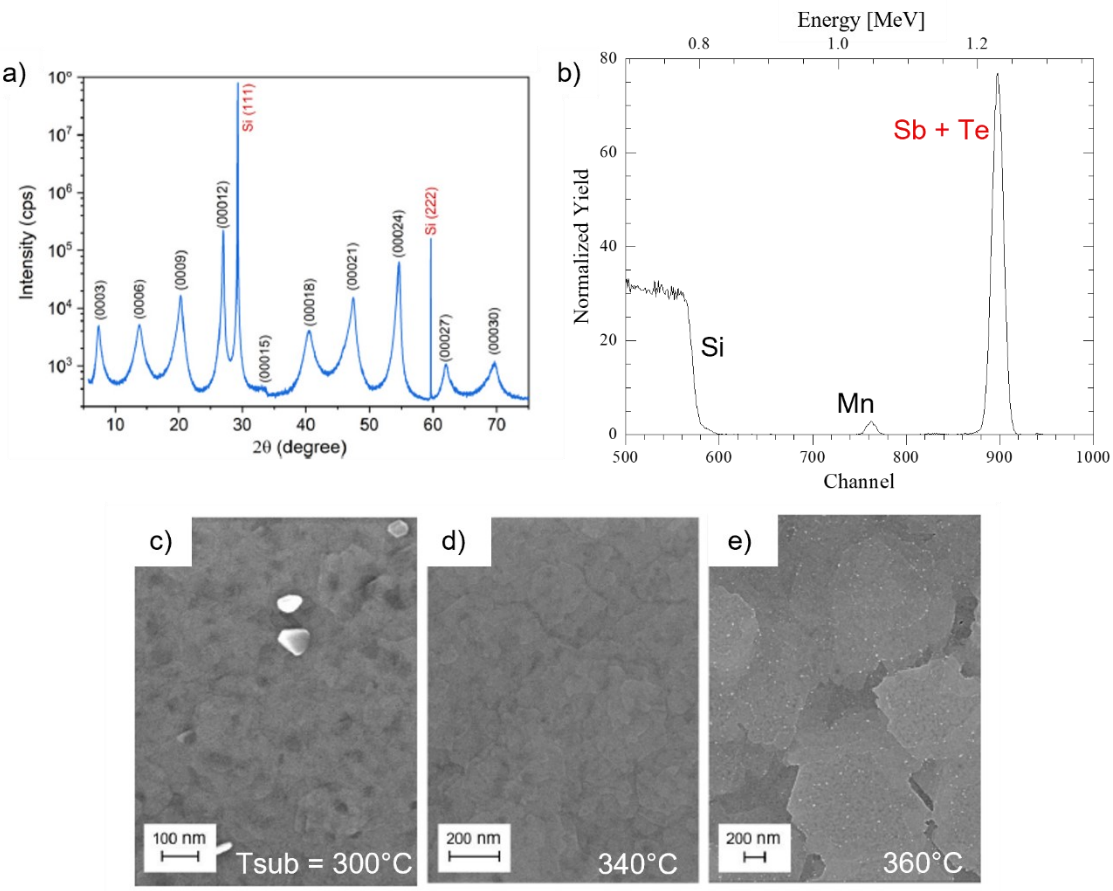

Figure 7.8: $MnSb_2Te_4$ characterization with XRD (a), RBS (b) and SEM (c)-(e). XRD exhibits SL peaks similar to MBT, but with a characteristic suppressed (00015) peak. The RBS measurement in b) reveals the incorporation of Mn in the thin film. Due to their similar weight, the RBS peaks of Sb and Te are combined and the stoichiometry must be extracted mathematically. d)-f) show SEM micrographs of MST growth at varying substrate temperatures, 300°C, 340°C and 360°C respectively. At lower temperatures, crystallites form on the film, while at higher temperatures the deposited films do not coalesce and smaller crystallites form along the edges. These might be indications of MnTe forming at higher T_{sub}, especially when considering the Mn behavior in MBT. c)-e) modified from [240].

The transition to MST was facilitated by the similarity of MBT and MST in their crystal structure and the known parameters for the growth of Sb_2Te_3. First, by setting the cell temperatures of Te and Sb to $T_{Te} = 330°C$ (fixed) and T_{Sb} = 420-460°C, material fluxes of $1.2 \cdot 10^{-6}$ mbar and $\sim 8 \cdot 10^{-8}$ mbar were employed, respectively. Sb flux is changed in the given range to stabilize the flow. The Mn is set to $T_{Mn} = \sim 760°C$, resulting in a flux of $\sim 3.5 \cdot 10^{-9}$ mbar, with slight variations due to the given control by power only, without a PID-controlled feedback loop. The flux ratio magnitudes are thus given by Mn:Sb:Te ~1:20:400, indicating the clear Te overpressure regime to suppress Te antisite defects. Resulting thin films show septuple layered XRD peaks and clear signals of the Mn in RBS measurements as shown in figure 7.8 a) and b).

To determine the stoichiometry from the RBS data, the analysis proceeds similar to the MBT evaluation, however here the percentages of Sb and Te are superimposed, since their elemental weights are only one unit apart. The calculation is however similar to the MBT

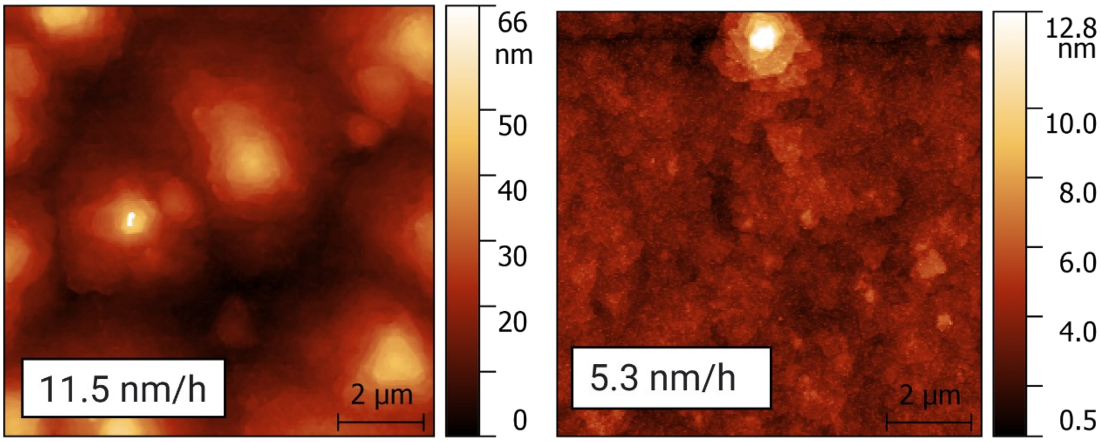

Figure 7.9: Decreasing the MST growth rate yields smoother film topographies as evidenced by AFM measurements. At 11.5 nm/h, a high density of strongly protruding mounds forms instead of a smooth film with large terraces, yielding a rough surface. Decreasing the growth rate results in increasingly smooth films, in which the extreme mounds can only be found at contamination sites that were present before growth. In each picture one of these contamination mounds can be seen in bright white. Modified from [240].

procedure. If $Mn\% \approx 14.3\%$ of the total compound and the Sb and Te ratios are twice or four times that percentage, a pure MST film has been grown. For $\%Mn < 14.3\%$, $\%Sb_{SL} = \%SbTe - 2 \cdot \%Mn$ and $\%Te_{SL} = \%SbTe - 4 \cdot \%Mn$ are needed to build the MST SLs, while the leftover $\%SbTe$ is used to build Sb_2Te_3 QLs. For $\%Mn > 14.3\%$ the stoichiometry can be calculated by three equations that are $\%Mn = \%Mn_{SL} + \%Mn_{MnTe}$, $\%SbTe = \%Sb_{SL} + \%Te_{SL} + \%Te_{MnTe}$ and $\%Mn_{SL} = 2 \cdot \%Sb_{SL} = 4 \cdot \%Te_{SL}$. The equations utilize the assumption that there are only SL and MnTe layers, with the Sb being used up entirely to form SLs. By combining the equations, one gets $5 \cdot \%Mn_{SL} = \%SbTe - \%Mn$, from which all other percentages can be derived. Simulating RBS measurements for the calculated stoichiometries and including the sample thickness yields fits closely resembling the measured data. The desired amount of Mn in the compound given by [241] is slightly above the pure MST with 14.3%, but should not exhibit a significant number of MnTe layers. Thus, small deviations from 14.3% can indicate a relevant contribution of Mn_{Sb} intermixing. Only then, the slight surplus of Mn in the compound yielding ferromagnetism and non-trivial topology can be achieved.

After establishing the presence of Mn in the compound via RBS and XRD, growth optimization is performed to fabricate high-quality thin films as was done with MBT. In figure 7.8 c) – f), SEM micrographs of MST thin films grown at substrate temperatures of 300°C, 340°C and 360°C are shown exemplarily. At lower T_{sub}, randomly oriented crystallites tend to form on the underlying MTI layer, standing brightly in a). Increasing the substrate temperature to 340°C in figure 7.8 b) results in a smooth film with rocking curves exhibiting a FWHM of 50-70 arcsec. Even higher temperatures of 360°C in c) lead to a formation of islands with varying height with sharp edges between them, showing a reluctancy to coalesce to a smooth thin film. Moreover, small crystallites form at the step edges. These crystallites mainly form at high Mn fluxes and could consist of MnTe, especially with the phenomenon of increased Mn density at the MTI surface of the MBT

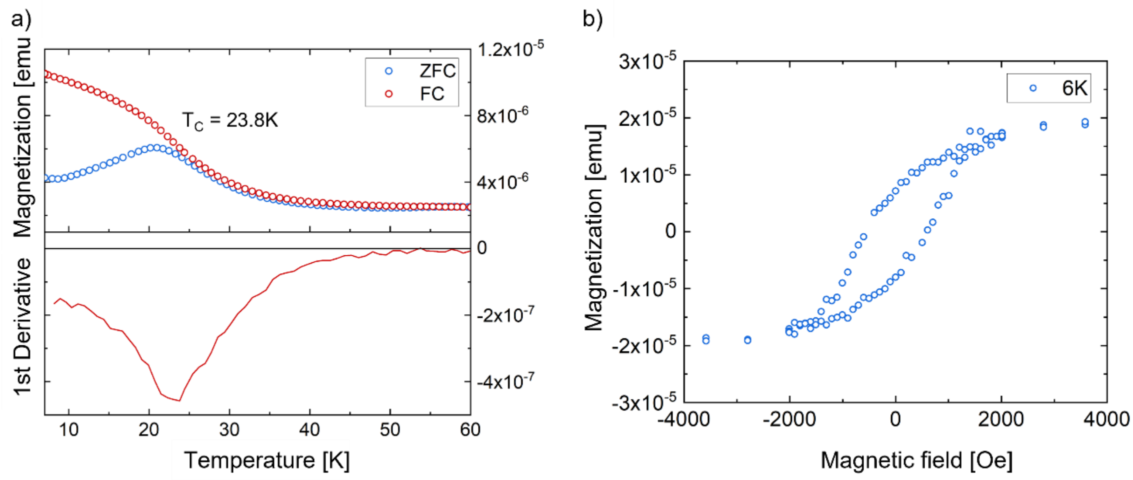

Figure 7.10: SQUID results on MST. The (zero) field cooling curves reveal an increase of magnetization in the film with temperature for the ZFC fitting to FM behavior [250]. *A Curie temperature of 23.8 K is given by the peak in the derivate curve. When driving an outer magnetic field at 6K, a FM hysteresis is found for the magnetization, which was not present for CBST films. Adapted from Robert Müllers Master's Thesis* [240].

layers in mind, which were found in the TEM investigation. The substrate temperatures cannot be directly linked to those given in chapter 7.1.1 for MBT, as these films were grown on another substrate holder. Later experiments on the same holder as for MBT showed a T_{sub} window of optimized growth, similar to the 340°C example in figure 7.8 b), for 280°C.

A second way to optimize the quality of the grown thin films is to vary the growth rate of the MTI film. Varying the growth rate by lowering the Mn and Sb fluxes, while keeping their ratio at ~1:20, results in vastly different films as shown in the AFM measurements in figure 7.9. At high to moderate growth rates of > 10 nm/h, strongly protruding islands form, indicating a largely Vollmer-Weber growth mode. When decreasing the growth rate at otherwise equivalent growth parameters, smooth films are grown with only seldom protruding islands, which are rather caused by contaminations present before the growth. Furthermore, by employing low growth rates the formation of small crystallites at the step edges is inhibited. This can be attributed to the extended time given to the material on the sample surface to rearrange while providing the same mobility via the constant substrate temperature. In contrast to BST and MBT films, where lower rates also provided a way to control the extent of rotational twin domains in the film, this was not achievable in the MST films, where the contributions of both domains remained constant with decreasing growth rate. The reduction was however also not achieved for pure Sb_2Te_3 and thus seems inherent to Sb-containing TIs. By carefully adjusting the substrate temperature and material fluxes and thus the growth rates, high quality MTI thin films of MST can be fabricated, exhibiting rocking curves with FWHMs comparable to those achieved in MBT. The reduction of surface roughness and number of protruding islands furthermore facilitates the growth of sub-10 nm films for later Hall samples.

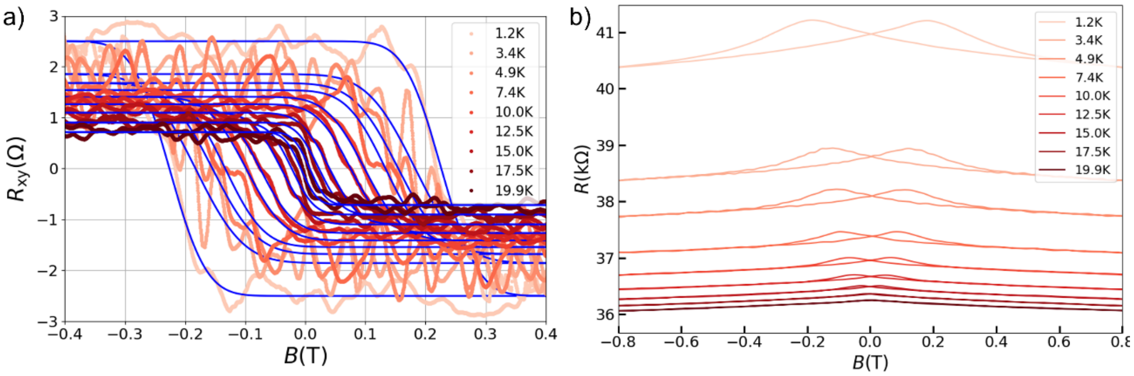

Figure 7.11: Hall characterization of an MST:MT Hall device. The symmetrized Hall signal has a low signal to noise ratio due to the low Hall resistances. Blue lines indicating fits to the data reveal a AHE of 2.5 Ω with a remanence of $B_c = 226\,mT$. *A thickness of 14 nm paired with a suboptimal stoichiometry can be linked to the low hysteresis, also explaining the high* R_{xx} *and low μ of 5.3 cm²/Vs and high* n_{2D} *of* $9.1x10^{14}/cm^2$. *However, a magnetic response is clearly measurable, suggesting even an FM response.*

To evaluate the magnetic response of the fabricated MST thin films, as was done with the CBST and MBT layer stacks, SQUID measurements were employed on a purely MST SL sample, determined by XRD. As shown in figure 7.10 a), the zero-field cooling and field cooling M-T curves exhibit a distinct FM behavior, similar to that measured in some CBST SQUID samples (figure 7.17 b)) [250]. The peak in the first derivative of the M-T curve identifies a Curie temperature of the compound of $23.8 \pm 1\,K$, which is slightly below literature values, ranging from 25 K to 46 K [241], [251], [252]). Additionally, when sweeping the out-of-plane magnetic field, a ferromagnetic hysteresis is measured at 6 K, with a coercive field of $800\,Oe = 80\,mT$. No such clear hysteresis curves could be measured for either CBST or MBT, promising a well-defined ferromagnetic order in the thin film.

In order to directly compare the three investigated MTI compounds, Hall devices were fabricated from a 14 nm thin $MnSb_2Te_4$ film capped with 3 nm of AlO_x, which was oxidized natively, following the steps described in the following chapter 7.2. The stoichiometry of the MST is determined by RBS to $(MnSb_2Te_4)_3$:$(MnTe)_1$. The MST Hall devices exhibit FM behavior in the longitudinal as well as the Hall signal, with a hysteresis in both measurements as shown in figure 7.11 a) and b). At 1.2 K the remanence is about twice that of the CBST thin films with 0.226 T compared to ~0.1 T and present over the full investigated temperature range, as expected from the SQUID investigation (T_C = 23.8 K). However, the Hall data, symmetrized in figure 7.11 a), only shows a small AHE of only 2.5 Ω and is overshadowed by noise. The progression of AHE and remanence with temperature are nonetheless plausible and the remanence at 5 K is comparable to that given by the SQUID data in figure 7.10 b). The longitudinal signal shows a large resistance, only increasing with lower temperatures, comparable to what is measured in the lowCr CBST sample in figure 3.8 d).

In conclusion, while the values for the resistance are far from any QAH signatures, a magnetic response has been measured in the MST compound in SQUID as well as a Hall device, both indicating a FM behavior. The low signal to noise ratio in figure 7.11 a) might however hide aFM characteristics, which need to be resolved in future studies of MST. A thinner film with less Mn content as well as an improvement of film quality is required to further investigate the viability of the intrinsically magnetic MST as an alternative to the more established CBST. The work by Wimmer *et al.*[241] strongly suggests so and reaching a QAH regime in MST would be a great achievement, providing an additional route towards QAHI-SC hybrid devices. A recent study has also investigated MST/ST hetero structures exhibiting a FM response, which depends on SL to QL ratio similar to MBT/BT, however a bunching of SL cannot be ruled out [253]. A study with scanning tunneling spectroscopy on the other hand has shown that even the septuple layered Mn-MTI compounds can have issues with an inhomogeneous magnetic gap distribution, which needs to be investigated further in order to create robust QAH states [254].

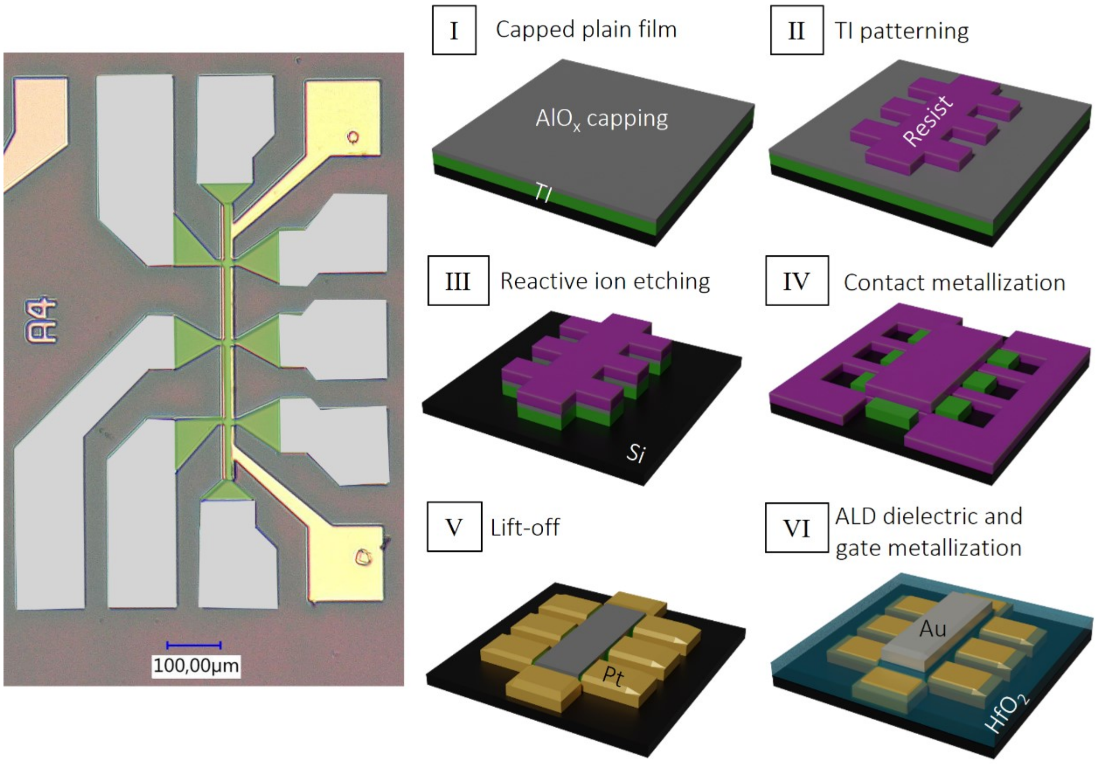

Figure 7.12: Micrograph of a finished Hall bar and schematic of the process of Hall bar fabrication. An AlO_x capped TI film (I) is covered with resist (II), which is patterned by chemical processes revealing only the surfaces to be etched via reactive ion etching (III). The structured TI Hall bar (III) is again covered with resist and only the areas for contact deposition are laid bare (IV), removing the capping in these areas. Contact metals are deposited, followed by cleaning of the sample (V) and subsequent dielectric deposition (HfO_2) via atomic layer deposition (VI). Lastly, patterned resist as in IV is used to deposit gate metal (Au) onto the Hall bar/HfO_2 only (VI).

7.2 Hall Device Fabrication

The Hall devices are prepared via optical lithography in the cleanroom facilities of the HNF in the Jülich Research Center. The process is performed on 10x10 mm² high ohmic, phosphorous-doped n-type (>2000 Ω · cm) Si (111) samples, which become insulating when cooled to cryogenic temperatures, onto which plain films of (M)TI material has been grown. To protect the TI and its surface states from ambient conditions and contaminations [255], an additional capping layer of AlO_x is deposited on the grown TI *in situ*. It has been shown that such a capping can maintain pristine TI surfaces after prolonged exposure to air and after cleanroom processes [256]. The process of capping differs between the two MBE chambers. In M13, stoichiometric Al_2O_3 is provided from the EBV and is deposited at 50°C substrate temperature with a rate of about 6 nm/min. In the BST MBE, a 3 nm layer of Al is deposited with a rate of 0.7 nm/min (1150°C Al cell temperature), which later oxidizes natively to form a protective, but not stoichiometric, AlO_x layer. The latter growth has to be performed at substrate temperatures below 0°C to minimize Al incorporation into the TI.

Starting the Hall bar fabrication, the capped thin films (figure 7.12 I) are covered with positive optical resist AZ5214E via spin coating at 4000 rpm for 30 seconds, which is baked out at 90°C for 5 minutes. With a mask-less aligner (MLA100) by Heidelberg Instruments, the bar mesa of the device is patterned into the resist. The MLA uses a laser with a wavelength of 365 nm, supplying a dose of 300 mJ/cm². The illuminated resist is removed in a 35 s dip into AZ MIF 326 developer, yielding figure 7.12 II. By a reactive ion etching (RIE) step with 25 W forward power, 100 W inductively coupled plasma power, 55 sccm CHF_3 and 5 sccm O_2 for 4 minutes at 20°C the TI exposed after the development is removed, leaving only the Hall bar covered with resist (figure 7.12 III). For the next steps, the resist is removed by a 5 min rinse in acetone and isopropanol each. If thereafter resist is still visible in optical microscopy, a Gigabatch plasma ashing step with 600 sccm O_2 at 600 W for up to 5 min is performed. Next, electrical contact pads are provided to the Hall bar, since the TI is only hardly bond-able due to the weakly adhering QL, prone to flaking. Thus, as in figure 7.12 IV via the same optical lithography steps described above, resist is patterned to expose the contact areas of the Hall bar mesa. The development step is prolonged by 10 to 15 s to remove the AlO_x capping together with the resist, so that a good electrical contact is enabled between the TI layer and the deposited contact metals, without an insulating barrier in between[4]. 50 nm of Ti as a sticking layer and 100 nm of Pt are deposited by EBV in the cleanroom as contact material on the patterned resist. The excess metal and underlying resist are removed via a lift-off process by immersing the sample in acetone for a minimum of 5 min, revealing only the designed contacts, shown in figure 7.12 V. Though the samples are at this point ready for B-field dependent measurements, being able to gate the films and thus manipulate the Fermi level is crucial for the investigation of the TI and later the QAHI. Hence, illustrated in figure 7.12 VI, a 15 nm HfO_2 layer is deposited globally via atomic layer deposition (ALD) as a gate dielectric. For the gate and gate contacts, the process of the contact deposition and lift-off is repeated (figure 7.12 IV + V), without the additional development time. The devices are now finished, the sample is diced into pieces fitting into the measurement cryostat and then glued with silver paste and bonded with aluminum wire onto a chip carrier.

7.3 JJTLM Device Fabrication

The JJTLMs are fabricated from LPCVD silicon oxide (300 nm) and nitride (100 nm) layers on the high ohmic Si (111) wafers that were also used for the growth of the MTIs. After dicing into 6x6 mm² pieces, substrates are spin coated at 4000 rpm with the negative photo lithography resist AZ 2020 (nLOF), mixed in a ratio of 1:1 with AZ EBR to render the

---

[4] The employed AZ MIF 326 developer is based on highly diluted TMAH, a base conveniently capable of etching Al_2O_3.

resist sensitive to electron beam lithography. A pre-exposure bake is performed for 5 min at 100°C and the samples are subsequently exposed with a dose of 91 µC/cm² at an acceleration voltage of 100 kV. Electron beam alignment markers, for future writing of contact or gate layers, are written simultaneously. A post-exposure bake at 110°C for 3 min follows before the sample is developed in AZ MIF 326 for 25 s, succeeded by a rinse in distilled water. Via reactive ion etching with a CHF_3/O_2 plasma (55/5 sccm, 25W, 100W ICP) at 20°C for 185s the bare 100 nm of Si_3N_4 are removed. For growth the samples are then cleaned as in chapter 3, however with a 16:30 min HF acid dip to ensure removal of all unnecessary SiO_2, leaving only the desired SiO_2 under the mask. Next, the samples are quickly (<20 mins) transferred into vacuum. As with plain (M)TI growth, in the growth chamber the samples are first annealed to 700°C to remove possible water or other contaminations as well as the hydrogen passivation. After growth of CBST with rotation, the rotation is stopped to deposit Nb with electron beam evaporation. Thereafter, 5 nm Al_2O_3 is deposited as capping on the full sample under rotation.

The devices are then extracted from the vacuum and spin coated for 30 s with UV6 positive electron beam lithography resist at 4000 rpm. After a 1 min soft bake at 130°C the desired contacting pattern is written via e-beam lithography with a dose of 80 µC/cm². The samples are post-exposure baked at 140°C for 5 min and developed with MF-CD 26 for 60 s. After patterning, the resist protects the Nb that is used for contacting as well as the device itself, covering the entire midsection of the JJTLM device. The larger Si_3N_4 areas acting as bridge suspension are not protected and supposed to be etched together with the excess Nb surrounding the device. The sample is inserted into a RIE chamber, where a three-step recipe given in the table below is used to remove the bare Nb and Nb/Si_3N_4. The parameters were refined together with Max Vaßen-Carl during his Master's thesis [111].

Step	Time [s]	Gas flow SF_6/Ar [sccm]	RF/ICP power [W]
Al_2O_3 etching	8	30 / 80	100 / 2000
Nb etching	9	20 / 10	10 / 500
Si_3N_4 etching	40	100 / 8	100 / 0

Three-step RIE recipe parameters for Nb and Si_3N_4 mask etching for JJTM devices.

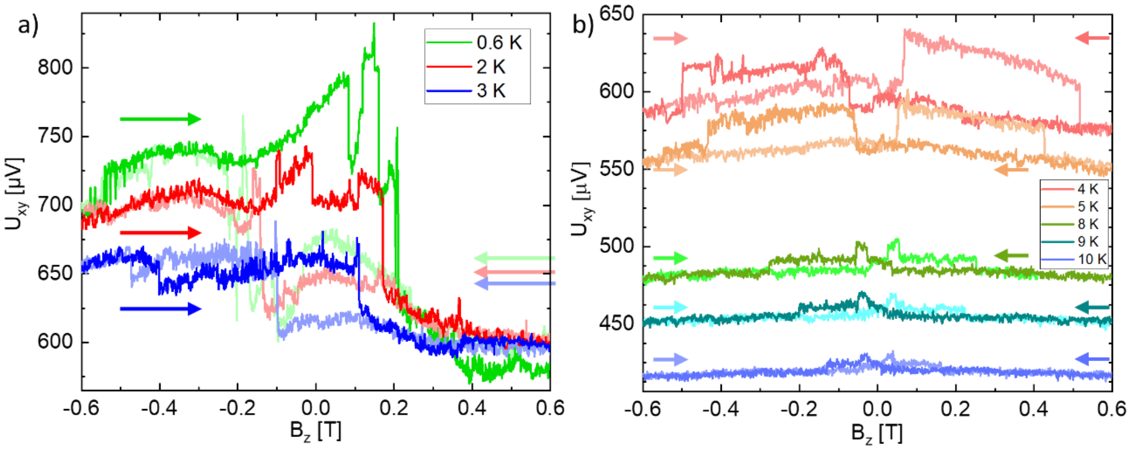

Figure 7.13: Hall investigations between the contacts HO-HU as labelled in figure 4.6 b). In a), hysteresis curves, offset by an underlying longitudinal resistance, show a steady increase of the remanence field with lower temperatures. The sweep directions of the external out of plane magnetic field are given by the accordingly colored arrows. Flux fluctuations due to the surrounding Nb SC likely result in localized sharp dips/peaks. Investigations at higher temperatures in b) reveal an unexpected behavior, exhibiting drops back onto a "ground" level when crossing a certain magnetic field level. The plateaus of high resistance shrink in size and extension with temperature. Unknown from previous Hall data, these features possibly originate from magnetic domain formations.

7.4 Second Generation JJTLM: Hall Investigations

Figure 7.13 illustrates temperature dependent Hall measurements performed between the contacts HO-HU of the second generation JJTLM device in figure 4.6 a) while a current of 50 nA is applied between contacts L and R. In a) at temperatures below 4 K a hysteresis is measured in the Hall (U_{xy}) data when sweeping the magnetic field between ± 0.6 T. Peculiarly, the remanence field is enlarged compared to the measurements of similar CBST thin films in chapter 3.2, where the remanence converges to ~0.1 T. Moreover, longitudinal U_{xx} measurements do not show any magnetization switching peaks, as in for example figure 3.12. Flux focusing would lead to smaller external remanence fields, locally increased at the Hall bar, thus yielding narrower hysteresis curves. Release of trapped fluxes is a likely explanation for sharp local resistance jumps in figure 7.13 a) but does not explain the enlarged remanence. The data would at first glance suggest that, similar to the findings in the previous section, the JJTLM device is capable of providing Hall data, revealing the desired magnetic properties of the investigated film. However, the data is purposefully not (anti-)symmetrized or converted into Hall resistance, resulting in a jumping of the hysteresis not between $\pm R_{AHE}$ at the critical field, but between elevated Hall voltage levels. This is to compare the data with the Hall measurements in figure 7.13 b), but also due to the fact that the effect might not actually result from a simple hysteresis switch as seen in chapter 3 or in the previous subchapter.

This concern manifests when examining the Hall data for higher temperatures in figure 7.13 b). Instead of a fading AHE and thus diminishing remanence field, an essentially flat

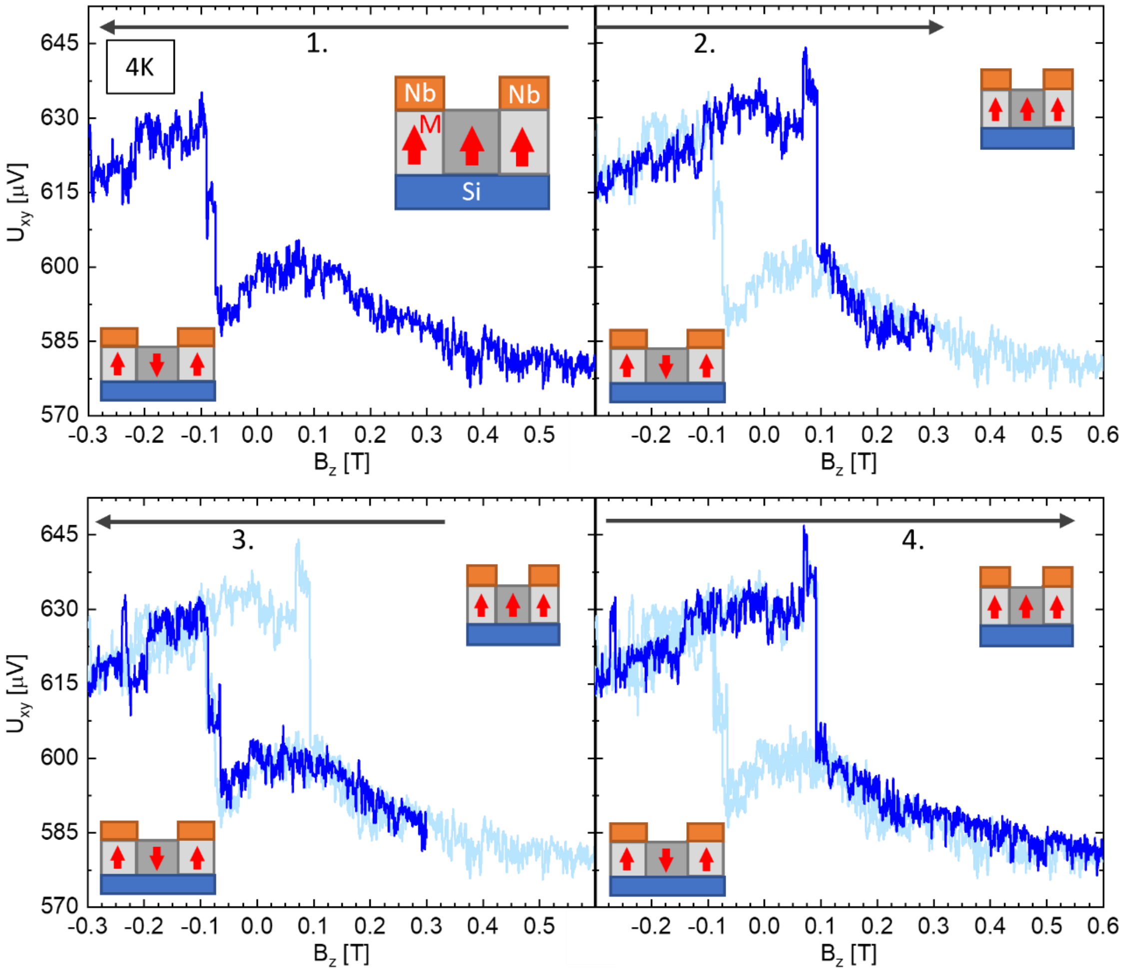

Figure 7.14: Examining four steps of the progression of the plateau effect exemplary at 4K. By first sweeping the magnetic field from high positive to medium negative values (1.), the hysteresis behavior corresponds to those measured previously, see figure 3.7. The flux screening of the Nb however need to be considered when trying to explain the drop back to level 0 at higher negative magnetic fields shown in figure 7.13 b). At -0.09 T the non-SC covered region switches magnetization (red arrows), creating an interface of non-aligned magnetic domains leading to scattering and thus higher resistance. This is maintained until +0.09 T is reached in the second step (2.), where both magnetizations are aligned again. Circling the smaller loop (3.) and returning to the intimal field (4.) shows the reproducibility of the feature.

voltage trend is measured, with only a slight indication of a WL effect due to longitudinal components present in the data. More strikingly however, plateaus are present, symmetric around zero magnetic field dependent on sweep direction. The plateaus are present for all investigated temperatures from 4 K onwards, but the step heights increase with decreasing temperatures. The magnetic field needed for a plateau transition increases similarly with lower temperatures. At temperatures above 5 K a second plateau step close to zero magnetic field appears, see figure 7.13 b) suggesting a three-level voltage, or rather resistance, system. How can this transition from expected hysteresis to plateau structure be understood?

The interpretation of the data becomes clearer when examining the 4 K data closely. Examining figure 7.13 b), sweeps performed on the full range of ±0.6 T cause a behavior similar to that at higher temperatures with plateaus symmetric around zero magnetic field.

An exactly opposite trend, the formation of a ferromagnetic hysteresis curve similar to those in figure 7.13 a) for lower temperatures, is found when the sweep is performed from 0.6 T only to -0.3 T and back shown in figure 7.14. In fact, a magnetic field loop between ±0.3 T at 4 K reveals a clear, repeatable hysteresis, not present in the full range sweeps of figure 7.13 b). When starting at negative fields as in figure 7.15 a) and sweeping towards +0.3 T, the hysteresis jump can be inverted. This means that when sweeping from high fields (±0.6 T) towards low opposite fields (∓0.3 T), the proposedly AHE resistance always switches to a higher resistive state.

In figure 7.15 b) the full range and small range 4 K field sweeps are displayed together. In both sweeps, the initial down sweeps overlap entirely, with the small range (bright red) staying on the plateaus at -0.3 T, while the full range scan (bright blue) jumps off the plateau at approximately -0.5 T. The following up-sweep thus starts at two distinct levels, 0 (ground level, bold blue) and 1 (first plateau, bold red). Strikingly, at approximately 0.1 T, the two measurements cross and swap places. The curves then coalesce again at about 0.5 T, when the full range sweep switches back 1 → 0. There therefore seem to exist two stable levels of resistance, for which specific external magnetic fields determine the transition, while the initial magnetic field sets the plateau position.

As shown in figure 7.14 and figure 7.15 a), the ansatz utilizing the flux screening by the superconducting Nb contacts might help to understand the data of the JJTLM sample. Since the effects rely heavily on the field screening of the SC, the switching behavior is not measured in the non-SC Hall devices of the previous chapter. A possible explanation of the effect relies on the assumption that a current is flowing between the two involved contacts, which is not the case for the intended Hall set up. With the complex structure of the examined Hall device (see figure 4.6) and the close proximity of the Hall contacts HO-HU (60 nm) it is however highly likely that a current is flowing over the HO-HU weak link. This would mean that the present U_{xy} measurement is not a classical Hall voltage measurement, in which only a voltage is measured. In figure 7.13 to figure 7.15, the measured value is thus deliberately given in voltage, since a transformation to Hall resistance would not be correct when a current is flowing between the Hall contacts. Dividing the measured “Hall” voltage by the applied longitudinal current of 50 nA, a resistance of the order of 8 to 17 kΩ is present, depending on temperature. This is in line with the longitudinal measurements over the junction given in figure 4.7 d) (HO-HU), although at 50 nA, further supporting that a current is flowing through the HO-HU. When examining the (symmetrized) longitudinal measurement of the Hall configuration in the previous subchapter in figure 7.16, this effect might also have been present, explaining the increased coercive fields, which did not line up with the corresponding Hall measurements in figure 4.4.

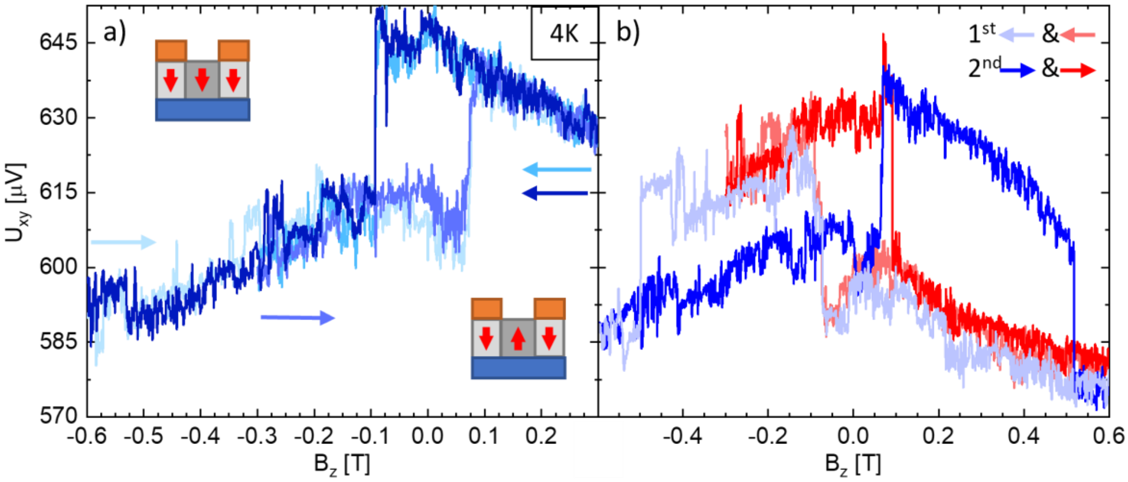

Figure 7.15: In a), the loop performed in figure 7.14 is repeated, but commencing at -0.6 T, showing the reversibility of the process (sweep directions chronologically light blue → dark blue). In b), both full range (blue) and short range (red) loops starting at +0.6 T are superimposed. The initial down sweep (1.) is shown in bright colors, the back sweep (2.) in bold colors. Thereby the exact alignment of the two levels of voltage independent of initial sweep direction is revealed.

To explain the process occurring in the measurement, one has to consider the center region of the Hall area between the HO-HU contacts (dark grey in the insets in figure 7.14 and figure 7.15 a)) as an area with a magnetization that switches separately from the CBST covered by Nb (light grey). This is due to screening effects in the Nb, which lead to the formation of domain walls between the antiparallelly magnetized domains. When the center region is antiparallel to the screened areas, a current flowing from one contact to the other would need to perform two spin flips, significantly increasing the resistance compared to the parallel aligned case. Thus, when commencing a measurement at high positive fields as in figure 7.14, the CBST film is fully aligned and a low voltage/resistance is measured, the weak link is at voltage level 0. At - 0.09 T the magnetization in the center region is inverted by the external magnetic field, fitting to the results for the coercive field of CBST in chapter 3.2, creating the domain walls. This is stable up to a breakthrough field of, in the case of the 4K measurement, approximately -0.5 T. There, the fluxes penetrating the type-II superconducting Nb are strong enough to align the buried MTI layer, aligning the MTI magnetization parallel to the center region and thus decreasing the resistance [200].

Reversing the magnetic field sweep at fields lower than the breakthrough field, for example for 4 K at -0.3 T as done in figure 7.15 b) (red curves), upholds the antiparallel alignment up to +0.09 T, where the coercive field of the center region is exceeded and the Hall area realigns. As can be seen in figure 7.15 b), by stitching together the elevated level 1 resistances given by different measurement cycles a continuous curve is formed, with decreasing resistance towards higher fields due to a WL background. The breakthrough field as well as the coercive field of the CBST decrease with higher temperature, which explains the progression of the plateau size when examining figure 7.13 b) and figure 7.15 b). With that in mind, reexamining the measurements in figure 7.13 a) reveals that the breakthrough field below 4 K might not have been exceeded. The hysteresis there is thus a jump from level 0 to 1 and back, not a hysteresis loop in the usual Hall measurement sense. The data however still reveals the coercive field, influenced by screening of the Nb.

This approach to understand the plateaus in the Hall measurement is viable up to 5 K, at higher temperatures as in figure 7.13 b) no screening effects due to superconductivity are present. Lower coercive fields and thus domain reversal effects might explain the jumps in voltage in these measurements. Also, a possible connection between this plateau switching behavior and the magnetic field sweep induced dips in figure 4.3 a) cannot be excluded. Further investigations are thus required to understand these features.

7.5 Supplementary Appendix

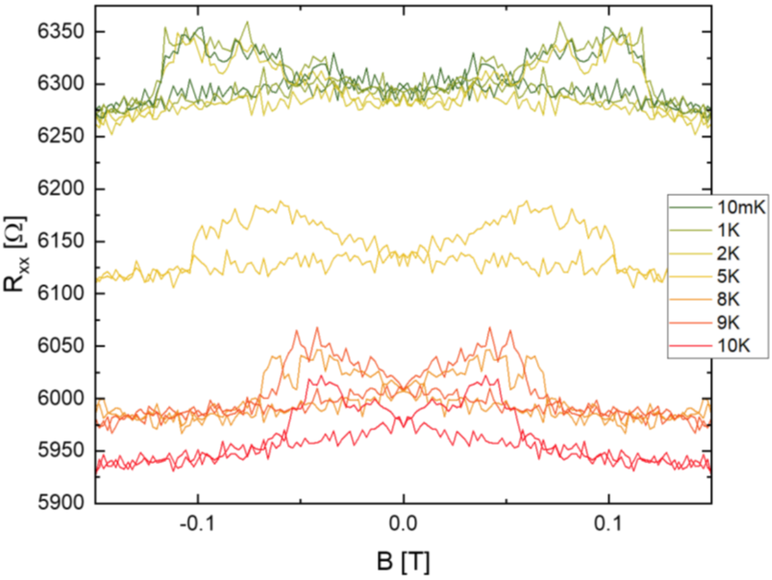

Figure 7.16: Symmetrized longitudinal resistance of the device shown in Figure 4.4. Although they are enlarged, the data shows the magnetization switching peaks expected for the longitudinal Hall measurements of CBST as shown in chapter 3.2. The maximum value of 110 mT at 10 mK moreover fits to the expected values for CBST as established earlier. A WL background as evidenced in chapter 3.2 is also observable.

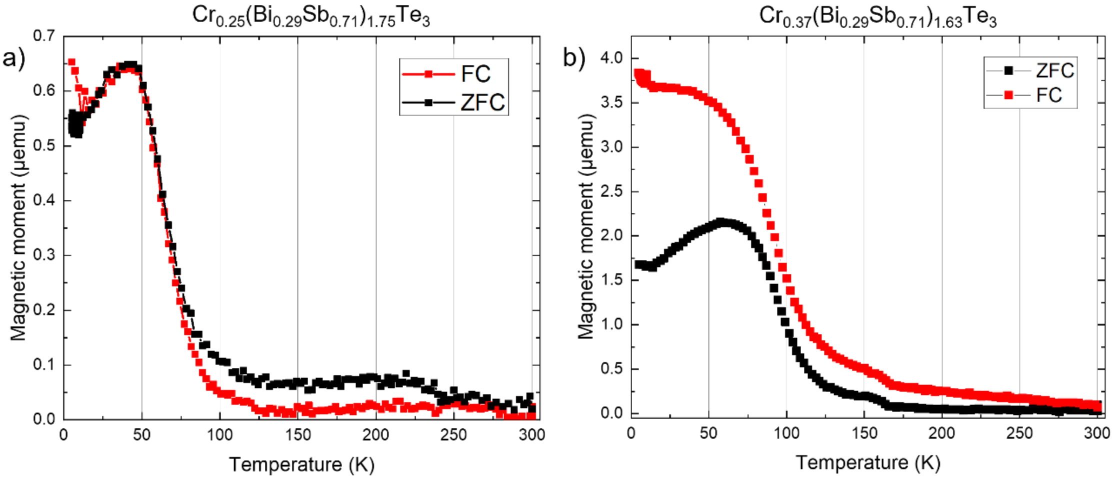
$Cr_{0.25}(Bi_{0.29}Sb_{0.71})_{1.75}Te_3$

$Cr_{0.37}(Bi_{0.29}Sb_{0.71})_{1.63}Te_3$

Figure 7.17: SQUID data with zero-flied cooling (ZFC) and field-cooling (FC) for two CBST compounds of different Cr concentration. While all curves show an increase in magnetic moment towards lower temperatures, the characteristic split between ZFC and FC only appears in b), however at highly elevated temperatures, suggesting critical temperatures far above the expected 15-25 K. The compound in a) contains less Cr (closer to those investigated in chapter 3.2) and exhibits a more reasonable critical temperature of 64 K, determined by the first derivative. Large background signals from the substrate, possible CrTe incorporation in these thicker films (60-80 nm) and non-agreement with the Hall data however casts doubt on the viability of the SQUID data. Adapted from the Master's thesis of Max Vaßen-Carl [111].

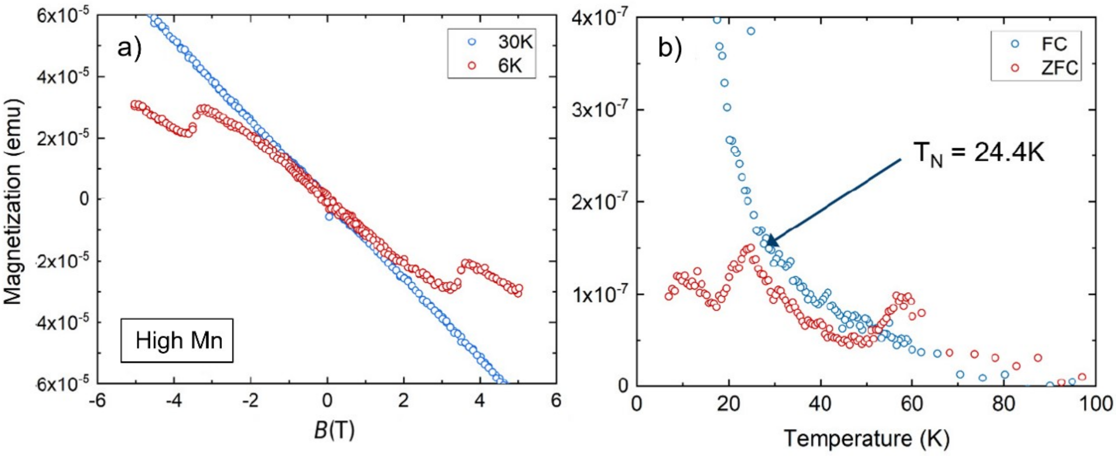

Figure 7.18: SQUID measurements on MBT with high Mn content. a) At 30 K only the diamagnetic response of the substrate is measured. At lower temperatures a deviation from a strictly linear behavior is observed, indicating aFM. Above 3 T perpendicular external field the kink in magnetization suggests an alignment of spins to a FM arrangement. The formation of an aFM phase can also be extracted from the ZFC curve in b), which unlike the FC, only increases slightly up to 24.4 K and then stagnates. This marks the Neel temperature of 24.4 K, in accordance with values from literature for pure MBT [257]. *Adapted from the Master's thesis of Robert Müller* [240].

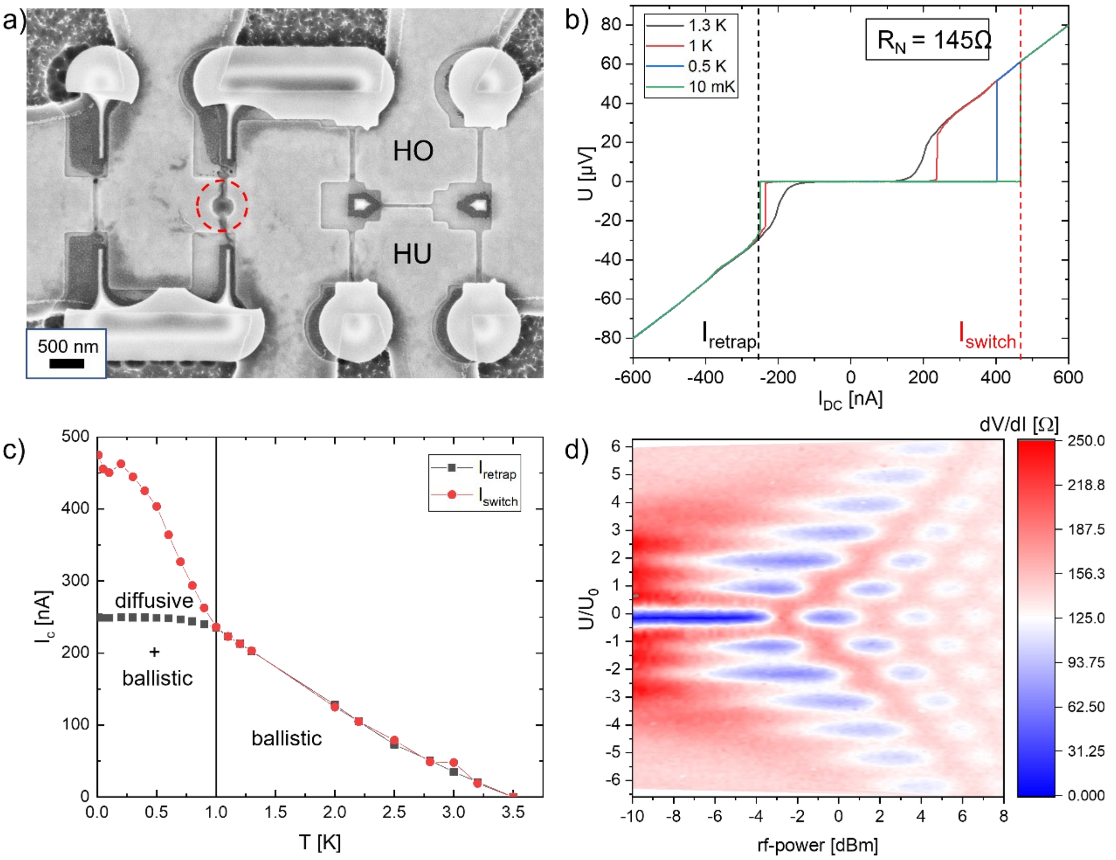

Figure 7.19: JJTLM device utilizing non-magnetic BST film. The device in a) is fabricated as a control device to test the viability of the JJTLM approach with a known non-magnetic compound. The fabrication process is equal to that of the MST JJTLM device in chapter 4.3. During RIE etching static effects caused local melting of the otherwise electrically separated contact pads at their closest distance, highlighted by the red circle. b) I-V measurements between HO-HU reveal a vanishing resistance and thus a critical current at temperatures below 3.5 K. At 10 mK base temperature a maximum critical current of 250 nA is determined, utilizing the retrapping current I_{retrap}. *This results in a* I_cR_N *product of 36.25 µeV. The* R_N *of 145 Ω is determined by a fit to the linear slope of the I-V curve at higher currents. This value is in line with findings of our group on earlier, similar samples, consisting of only a simple JJ however* [105], [106]. *The existence of a sensible critical current in a device using the same fabrication method as for the MTI JJTLMs supports that the JJTLM approach is feasible and that the absence of SC in MTI-SC devices stems from magnetism related effects. Plotting* I_{retrap} *and* I_{switch} *over the temperature in c) results in a distinct curve exhibiting a kink in the slope. At temperatures below 1 K the junction exhibits additional diffusive contributions to the critical current. For further reading on and interpretation of this curve the reader is referred to* [105]. *Lastly, Shapiro measurements involving an external radio frequency (rf) excitation of 4.6 GHz by an antenna in the measurement setup at base temperature are plotted. The scaling to the Shapiro step width* $U_0 = f_{rf}*h/2e$ *reveals the presence of all Shapiro steps, even and odd. For 4π periodicity only even Shapiro steps are expected. Here, the first step is diminished in size compared to the following, hypothesizing a 2π+4π superposition* [105]. *By performing the same Shapiro measurement in the exclusively ballistic regime at temperatures above 1 K, overshadowing 2π periodic components could be filtered out in future measurements, presumably revealing a stronger diminishing of the first odd step.*

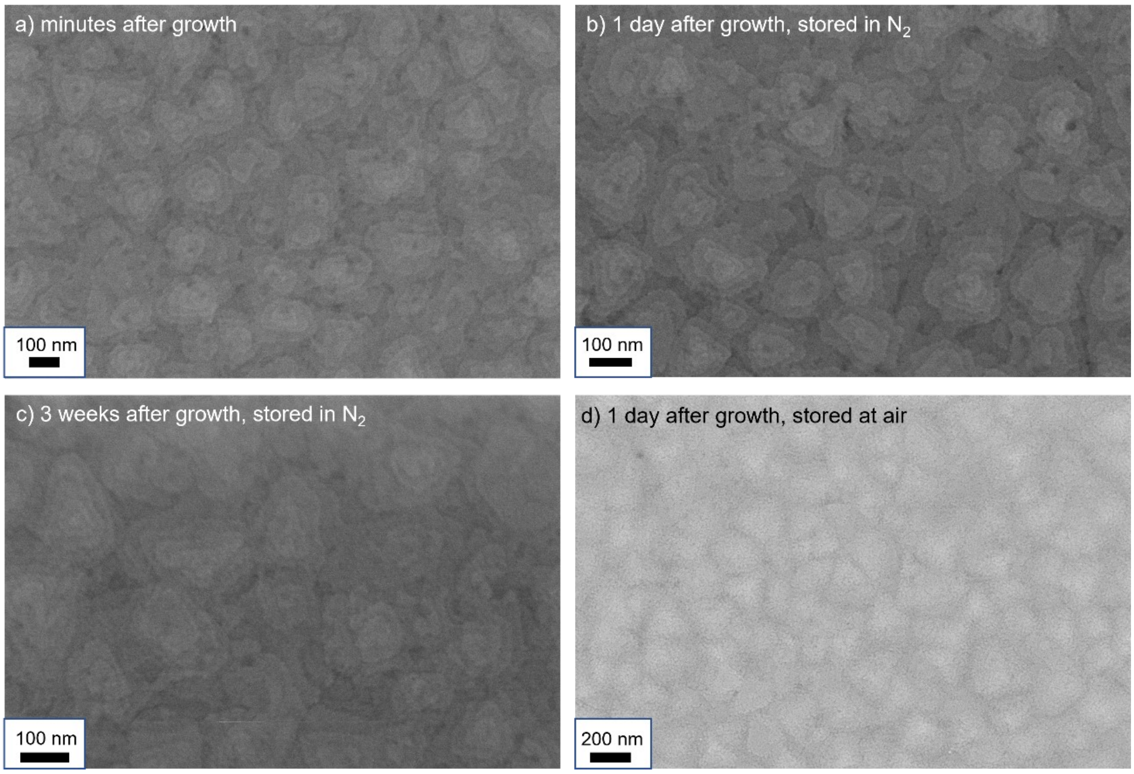

Figure 7.20: $(BiSb)_2Te_3$ surface degradation due to oxidation. a) shows the surface of the TI after an immediate transfer to SEM after growth. Terraces can be clearly resolved, showing flat steps as far as SEM can resolve. After one day in nitrogen atmosphere (b) the surface exhibits no discernible changes, after three weeks (c) in same storage the surface is slightly less resolvable, but terraces and steps are still well observable. Storing the samples at ambient conditions however causes rapid oxidation even after one day, covering the film with a rough surface oxide, which obscures the underlying crystal structure. Due to differences in brightness the crystal-islands can still be discerned in SEM when zooming out as shown in d). The shown effect is observed to happen more aggressively with increasing Sb content in the TI crystal.

List of Abbreviations

ABS	Andreev Bound State
AFM	Antiferromagnetism
aFM	Atomic Force Microscopy
AHE	Anomalous Hall Effect
ALD	Atomic Layer Deposition
AR	Andreev Reflection
BCS	Bardeen-Cooper-Schrieffer
BdG	Bogoliubov-de-Gennes
BEP	Beam Equivalent Pressure
BST	$(BiSb)_2Te_3$
CBST	$Cr_x(BiSb)_{2-x}Te_3$
C(M)EM	Chiral (Majorana) Edge Mode
CNP	Charge Neutrality Point
CP	Cooper Pair
DFT	Density-Functional Theory
(L)DoS	(Local) Density of States
EBV	Electron Beam eVaporator
EDX	Energy Dispersive X-ray spectroscopy
FC	*First Contact*^{TM}
(Z)FC	(Zero) Field Cooling
FFLO	Fulde-Ferrell-Larkin-Ovchinnikov
FIB	Focussed Ion Beam
FM	Ferromagnetism
FWHM	Full Width Half Maximum
HF	Hydrofluoric Acid
HNF	Helmholtz-Nano-Facility
JJ	Josephson Junction
JJTLM	Josephson Junction-Transmission Line Measurement
LPCVD	Low Pressure Chemical Vapor Deposition
LRPE	Long Range Proximity Effect
LUL	Large Scale UHV Lithography
MST	$MnSb_2Te_4$
MTI	Magnetic Topological Insulator
MZM	Majorana Zero Mode
NC	NanoCluster
NSC	Non-SuperConductor
PECVD	Plasma Enhanced Chemical Vapor Deposition
PGI	Peter Grünberg Institute
QAHE	Quantum Anomalous Hall Effect
QC	Quantum Computation
QHE	Quantum Hall Effect
QL	Quintuple Layer
QSHE	Quantum Spin Hall Effect
RBS	Rutherford Backscattering Spectrometry
RIE	Reactive Ion Etching
RKKY	Ruderman-Kittel-Kasuya-Yosida
RSJ	Resistively Shunted Junction
SAG/SAE	Selective Area Growth / Epitaxy
SC	SuperConductor
SEM	Scanning Electron Microscope
SL	Septuple Layer
SOC	Spin Orbit Coupling
SQUID	Superconducting Quantum Interference Device
STM	Scanning Tunneling Microscope
STS	Scanning Tunneling Spectroscopy
(S)TEM	(Scanning) Tunneling Electron Microscopy
TI	Topological Insulator
TRS	Time Reversal Symmetry
UCLA	University of California Los Angeles
UHV	Ultra High Vacuum
vdW	van der Waals
VTI	Variable Temperature Insert

MBE	Molecular Beam Epitaxy	W(A)L	Weak (Anti-) Localization
MBS	Majorana Bound State	XRD	X-Ray Diffraction
MBT	$MnBi_2Te_4$	XRR	X-Ray Reflectometry

References

[1] A. Patrizio, “The coronavirus pandemic turned Folding@Home into an exaFLOP supercomputer,” *arstechnica*, 2020. Accessed: Feb. 05, 2024. [Online]. Available: https://arstechnica.com/science/2020/04/how-the-pandemic-revived-a-distributed-computing-project-and-made-history/

[2] “Folding@Home,” https://foldingathome.org/?lng=en.

[3] “Computational predictions of protein structures associated with COVID-19,” https://www.deepmind.com/open-source/computational-predictions-of-protein-structures-associated-with-covid-19.

[4] A. Robert, P. K. Barkoutsos, S. Woerner, and I. Tavernelli, “Resource-efficient quantum algorithm for protein folding,” *npj Quantum Inf*, vol. 7, no. 1, Dec. 2021, doi: 10.1038/s41534-021-00368-4.

[5] G. Popkin, “Quest for qubits,” *Science (1979)*, vol. 354, no. 6316, pp. 1090–1093, Dec. 2016, doi: 10.1126/science.354.6316.1090.

[6] M. Freedman, A. Kitaev, M. Larsen, and Z. Wang, “Topological quantum computation,” *Bulletin of the American Mathematical Society*, vol. 40, no. 1, pp. 31–38, Oct. 2002, doi: 10.1090/S0273-0979-02-00964-3.

[7] B. Lian, X. Q. Sun, A. Vaezi, X. L. Qib, and S. C. Zhang, “Topological quantum computation based on chiral Majorana fermions,” *Proc Natl Acad Sci U S A*, vol. 115, no. 43, pp. 10938–10942, 2018, doi: 10.1073/pnas.1810003115.

[8] A. Kitaev, “Anyons in an exactly solved model and beyond,” *Ann Phys (N Y)*, vol. 321, no. 1, pp. 2–111, Jan. 2006, doi: 10.1016/j.aop.2005.10.005.

[9] D. P. Arovas, R. Schrieffer, F. Wilczek, and A. Zee, “Statistical mechanics of anyons,” *Nucl Phys B*, vol. 251, pp. 117–126, Jan. 1985, doi: 10.1016/0550-3213(85)90252-4.

[10] V. Lahtinen and J. K. Pachos, “A Short Introduction to Topological Quantum Computation,” May 2017, doi: 10.21468/SciPostPhys.3.3.021.

[11] D. Litinski and F. Von Oppen, “Braiding by Majorana tracking and long-range CNOT gates with color codes,” *Phys Rev B*, vol. 96, no. 20, Nov. 2017, doi: 10.1103/PhysRevB.96.205413.

[12] A. D. Scheppe and M. V. Pak, “Complete description of fault-tolerant quantum gate operations for topological Majorana qubit systems,” *Phys Rev A (Coll Park)*, vol. 105, no. 1, Jan. 2022, doi: 10.1103/PhysRevA.105.012415.

[13] B. Van Heck, A. R. Akhmerov, F. Hassler, M. Burrello, and C. W. J. Beenakker, “Coulomb-assisted braiding of Majorana fermions in a Josephson junction array,” *New J Phys*, vol. 14, Mar. 2012, doi: 10.1088/1367-2630/14/3/035019.

[14] E. Majorana, “Teoria simmetrica dell’elettrone e del positrone,” *Il Nuovo Cimento*, vol. 14, no. 4, pp. 171–184, Apr. 1937, doi: 10.1007/BF02961314.

[15] C. W. J. Beenakker, “Search for majorana fermions in superconductors,” *Annu Rev Condens Matter Phys*, vol. 4, no. 1, pp. 113–136, 2013, doi: 10.1146/annurev-conmatphys-030212-184337.

[16] L. Fu and C. L. Kane, “Superconducting proximity effect and majorana fermions at the surface of a topological insulator,” *Phys Rev Lett*, vol. 100, no. 9, pp. 1–4, 2008, doi: 10.1103/PhysRevLett.100.096407.

[17] N. R. Ayukaryana, M. H. Fauzi, and E. H. Hasdeo, “The quest and hope of Majorana zero modes in topological superconductor for fault-tolerant quantum computing: An introductory overview,” in *AIP Conference Proceedings*, American Institute of Physics Inc., Aug. 2021. doi: 10.1063/5.0059974.

[18] D. Aasen *et al.*, “Milestones toward Majorana-based quantum computing,” *Phys Rev X*, vol. 6, no. 3, pp. 1–28, 2016, doi: 10.1103/PhysRevX.6.031016.

[19] O. Viyuela, S. Vijay, and L. Fu, “Scalable fermionic error correction in Majorana surface codes,” *Phys Rev B*, vol. 99, no. 20, May 2019, doi: 10.1103/PhysRevB.99.205114.

[20] X.-C. Yao *et al.*, “Experimental demonstration of topological error correction,” *Nature*, vol. 482, no. 7386, pp. 489–494, Feb. 2012, doi: 10.1038/nature10770.

[21] J. Sau, S. Simon, S. Vishveshwara, and J. R. Williams, “From anyons to Majoranas,” Dec. 01, 2020, *Springer Nature*. doi: 10.1038/s42254-020-00251-9.

[22] R. M. Lutchyn, J. D. Sau, and S. Das Sarma, “Majorana fermions and a topological phase transition in semiconductor-superconductor heterostructures,” *Phys Rev Lett*, vol. 105, no. 7, Aug. 2010, doi: 10.1103/PhysRevLett.105.077001.

[23] M. Leijnse and K. Flensberg, “Introduction to topological superconductivity and Majorana fermions,” *Semicond Sci Technol*, vol. 27, no. 12, pp. 1–21, 2012, doi: 10.1088/0268-1242/27/12/124003.

[24] L. Fu, C. L. Kane, and E. J. Mele, “Topological insulators in three dimensions,” *Phys Rev Lett*, vol. 98, no. 10, pp. 1–4, 2007, doi: 10.1103/PhysRevLett.98.106803.

[25] M. Z. Hasan and C. L. Kane, “Colloquium: Topological insulators,” *Rev Mod Phys*, vol. 82, no. 4, pp. 3045–3067, 2010, doi: 10.1103/RevModPhys.82.3045.

[26] T. Hyart, B. Van Heck, I. C. Fulga, M. Burrello, A. R. Akhmerov, and C. W. J. Beenakker, “Flux-controlled quantum computation with Majorana fermions,” *Phys Rev B Condens Matter Mater Phys*, vol. 88, no. 3, pp. 1–17, 2013, doi: 10.1103/PhysRevB.88.035121.

[27] S. Plugge, A. Rasmussen, R. Egger, and K. Flensberg, “Majorana box qubits,” *New J Phys*, vol. 19, no. 1, Jan. 2017, doi: 10.1088/1367-2630/aa54e1.

[28] A. Cook and M. Franz, “Majorana fermions in a topological-insulator nanowire proximity-coupled to an s-wave superconductor,” *Phys Rev B Condens Matter Mater Phys*, vol. 84, no. 20, Nov. 2011, doi: 10.1103/PhysRevB.84.201105.

[29] J. Manousakis, A. Altland, D. Bagrets, R. Egger, and Y. Ando, “Majorana qubits in a topological insulator nanoribbon architecture,” *Phys Rev B*, vol. 95, no. 16, pp. 1–9, 2017, doi: 10.1103/PhysRevB.95.165424.

[30] T. Schäpers, *Semiconductor Spintronics*. De Gruyter, 2021. doi: 10.1515/9783110639001.

[31] J. H. Bardarson and R. Ilan, “Transport in Topological Insulator Nanowires,” pp. 93–114, 2018, doi: 10.1007/978-3-319-76388-0_4.

[32] Y. Zeng, C. Lei, G. Chaudhary, and A. H. Macdonald, “Quantum anomalous Hall Majorana platform,” *Phys Rev B*, vol. 97, no. 8, Feb. 2018, doi: 10.1103/PhysRevB.97.081102.

[33] D. Burke, D. Heffels, K. Moors, P. Schüffelgen, D. Grützmacher, and M. R. Connolly, “Robust Majorana bound states in magnetic topological insulator nanoribbons with fragile chiral edge channels,” Feb. 2023, [Online]. Available: http://arxiv.org/abs/2302.10982

[34] P. Mandal, N. Taufertshöfer, L. Lunczer, M. P. Stehno, C. Gould, and L. W. Molenkamp, “Finite Field Transport Response of a Dilute Magnetic Topological Insulator-Based Josephson Junction,” *Nano Lett*, 2021, doi: 10.1021/acs.nanolett.1c04903.

[35] Q. L. He *et al.*, “RETRACTED ARTICLE: Chiral Majorana fermion modes in a quantum anomalous Hall insulator–superconductor structure,” *Science (1979)*, vol. 357, no. 6348, pp. 294–299, 2017, doi: 10.1126/science.aag2792.

[36] H. Zhang *et al.*, “RETRACTED ARTICLE: Quantized Majorana conductance,” *Nature*, vol. 556, no. 7699, pp. 74–79, Apr. 2018, doi: 10.1038/nature26142.

[37] M. Kayyalha *et al.*, “Absence of evidence for chiral Majorana modes in quantum anomalous Hall-superconductor devices,” *Science (1979)*, vol. 367, no. 6473, pp. 64–67, 2020, doi: 10.1126/science.aax6361.

[38] R. Gross and A. Marx, *Festkörperphysik*. De Gruyter, 2018. doi: 10.1515/9783110559187.

[39] K. v. Klitzing, G. Dorda, and M. Pepper, “New Method for High-Accuracy Determination of the Fine-Structure Constant Based on Quantized Hall Resistance,” *Phys Rev Lett*, vol. 45, no. 6, pp. 494–497, Aug. 1980, doi: 10.1103/PhysRevLett.45.494.

[40] C. L. Kane and E. J. Mele, “Quantum Spin Hall Effect in Graphene,” *Phys Rev Lett*, vol. 95, no. 22, p. 226801, Nov. 2005, doi: 10.1103/PhysRevLett.95.226801.

[41] C. L. Kane and E. J. Mele, “Z_2 Topological Order and the Quantum Spin Hall Effect,” *Phys Rev Lett*, vol. 95, no. 14, p. 146802, Sep. 2005, doi: 10.1103/PhysRevLett.95.146802.

[42] B. A. Bernevig, T. L. Hughes, and S.-C. Zhang, “Quantum Spin Hall Effect and Topological Phase Transition in HgTe Quantum Wells,” *Science (1979)*, vol. 314, no. 5806, pp. 1757–1761, Dec. 2006, doi: 10.1126/science.1133734.

[43] D. Hsieh *et al.*, “A topological Dirac insulator in a quantum spin Hall phase,” *Nature*, vol. 452, no. 7190, pp. 970–974, Apr. 2008, doi: 10.1038/nature06843.

[44] H. Zhang, C.-X. Liu, X.-L. Qi, X. Dai, Z. Fang, and S.-C. Zhang, “Topological insulators in Bi_2Se_3, Bi_2Te_3 and Sb_2Te_3 with a single Dirac cone on the surface,” *Nat Phys*, vol. 5, no. 6, pp. 438–442, Jun. 2009, doi: 10.1038/nphys1270.

[45] Y. Xia *et al.*, “Observation of a large-gap topological-insulator class with a single Dirac cone on the surface,” *Nat Phys*, vol. 5, no. 6, pp. 398–402, Jun. 2009, doi: 10.1038/nphys1274.

[46] M. Morgenstern, “Introduction to Topological Insulator Materials,” in *Topological Matter - Topological Insulators, Skyrmions and Majoranas*, vol. 139, S. Blügel, Y. Mokrousov, T. Schäpers, and Y. Ando, Eds., Jülich: Forschungszentrum Jülich GmbH, 2017, ch. B Topological Solids, p. B1.1-B1.30. Accessed: Feb. 07, 2022. [Online]. Available: http://hdl.handle.net/2128/22133

[47] C.-X. Liu, X.-L. Qi, X. Dai, Z. Fang, and S.-C. Zhang, “Quantum Anomalous Hall Effect in $Hg_{1-y}Mn_yTe$,” *Phys Rev Lett*, vol. 101, no. 14, p. 146802, Oct. 2008, doi: 10.1103/PhysRevLett.101.146802.

[48] E. H. Hall, “XVIII. *On the ‘Rotational Coefficient’ in nickel and cobalt*,” *The London, Edinburgh, and Dublin Philosophical Magazine and Journal of Science*, vol. 12, no. 74, pp. 157–172, Sep. 1881, doi: 10.1080/14786448108627086.

[49] F. D. M. Haldane, “Model for a Quantum Hall Effect without Landau Levels: Condensed-Matter Realization of the ‘Parity Anomaly,’” *Phys Rev Lett*, vol. 61, no. 18, pp. 2015–2018, Oct. 1988, doi: 10.1103/PhysRevLett.61.2015.

[50] Y. Tokura, K. Yasuda, and A. Tsukazaki, “Magnetic topological insulators,” *Nature Reviews Physics*, vol. 1, no. 2, pp. 126–143, 2019, doi: 10.1038/s42254-018-0011-5.

[51] X. Kou, Y. Fan, M. Lang, P. Upadhyaya, and K. L. Wang, “Magnetic topological insulators and quantum anomalous hall effect,” *Solid State Commun*, vol. 215–216, no. 1, pp. 34–53, 2015, doi: 10.1016/j.ssc.2014.10.022.

[52] C. Z. Chang and M. Li, “Quantum anomalous Hall effect in time-reversal-symmetry breaking topological insulators,” *Journal of Physics Condensed Matter*, vol. 28, no. 12, 2016, doi: 10.1088/0953-8984/28/12/123002.

[53] C. Z. Chang *et al.*, “Experimental observation of the quantum anomalous Hall effect in a magnetic topological Insulator,” *Science (1979)*, vol. 340, no. 6129, pp. 167–170, 2013, doi: 10.1126/science.1234414.

[54] M. Mogi *et al.*, “Magnetic modulation doping in topological insulators toward higher-temperature quantum anomalous Hall effect,” *Appl Phys Lett*, vol. 107, no. 18, 2015, doi: 10.1063/1.4935075.

[55] Y. Deng *et al.*, “Quantum anomalous Hall effect in intrinsic magnetic topological insulator $MnBi_2Te_4$,” *Science (1979)*, vol. 367, no. 6480, pp. 895–900, 2020, doi: 10.1126/science.aax8156.

[56] J. König, H.-H. Lin, and A. H. MacDonald, “Theory of Diluted Magnetic Semiconductor Ferromagnetism,” *Phys Rev Lett*, vol. 84, no. 24, pp. 5628–5631, Jun. 2000, doi: 10.1103/PhysRevLett.84.5628.

[57] D. J. Priour, E. H. Hwang, and S. Das Sarma, “Disordered RKKY Lattice Mean Field Theory for Ferromagnetism in Diluted Magnetic Semiconductors,” *Phys Rev Lett*, vol. 92, no. 11, Mar. 2004, doi: 10.1103/PhysRevLett.92.117201.

[58] K. He, Y. Wang, and Q. K. Xue, “Quantum anomalous hall effect,” Mar. 01, 2014, *Oxford University Press*. doi: 10.1093/nsr/nwt029.

[59] R. Yu, W. Zhang, H.-J. Zhang, S.-C. Zhang, X. Dai, and Z. Fang, “Quantized Anomalous Hall Effect in Magnetic Topological Insulators,” *Science (1979)*, vol. 329, no. 5987, pp. 61–64, Jul. 2010, doi: 10.1126/science.1187485.

[60] X. Kou, “Magnetic Topological Insulators and Quantum Hall Effect,” PhD Thesis, University of California, Los Angeles, 2015.

[61] C.-Z. Chang *et al.*, “Thin Films of Magnetically Doped Topological Insulator with Carrier-Independent Long-Range Ferromagnetic Order,” *Advanced Materials*, vol. 25, no. 7, pp. 1065–1070, Feb. 2013, doi: 10.1002/adma.201203493.

[62] G. Moore and N. Read, “Nonabelions in the fractional quantum hall effect,” *Nucl Phys B*, vol. 360, no. 2–3, pp. 362–396, Aug. 1991, doi: 10.1016/0550-3213(91)90407-O.

[63] Y. Oreg, G. Refael, and F. Von Oppen, “Helical liquids and Majorana bound states in quantum wires,” *Phys Rev Lett*, vol. 105, no. 17, Oct. 2010, doi: 10.1103/PhysRevLett.105.177002.

[64] V. Kaladzhyan, J. Despres, I. Mandal, and C. Bena, “Majorana fermions in finite-size strips with in-plane magnetic fields,” *European Physical Journal B*, vol. 90, no. 11, pp. 1–9, 2017, doi: 10.1140/epjb/e2017-80103-y.

[65] J. H. Bardarson, P. W. Brouwer, and J. E. Moore, “Aharonov-Bohm oscillations in disordered topological insulator nanowires,” *Phys Rev Lett*, vol. 105, no. 15, Oct. 2010, doi: 10.1103/PhysRevLett.105.156803.

[66] C. Z. Chen, Y. M. Xie, J. Liu, P. A. Lee, and K. T. Law, “Quasi-one-dimensional quantum anomalous Hall systems as new platforms for scalable topological quantum computation,” *Phys Rev B*, vol. 97, no. 10, pp. 1–5, 2018, doi: 10.1103/PhysRevB.97.104504.

[67] H. Kamerlingh Onnes, “The Superconductivity of Mercury,” *Leiden Commun.*, vol. 120b, 1911.

[68] J. Bardeen, L. N. Cooper, and J. R. Schrieffer, “Theory of Superconductivity,” *Physical Review*, vol. 108, no. 5, pp. 1175–1204, Dec. 1957, doi: 10.1103/PhysRev.108.1175.

[69] H. Froehlich, “Interaction of electrons with lattice vibrations,” *Proc R Soc Lond A Math Phys Sci*, vol. 215, no. 1122, pp. 291–298, Dec. 1952, doi: 10.1098/rspa.1952.0212.

[70] J. Bardeen and D. Pines, “Electron-Phonon Interaction in Metals,” *Physical Review*, vol. 99, no. 4, pp. 1140–1150, Aug. 1955, doi: 10.1103/PhysRev.99.1140.

[71] Y. S. Hor *et al.*, “Superconductivity in $Cu_xBi_2Se_3$ and its Implications for Pairing in the Undoped Topological Insulator,” *Phys Rev Lett*, vol. 104, no. 5, p. 057001, Feb. 2010, doi: 10.1103/PhysRevLett.104.057001.

[72] S. Sasaki *et al.*, “Topological Superconductivity in $Cu_xBi_2Se_3$,” *Phys Rev Lett*, vol. 107, no. 21, p. 217001, Nov. 2011, doi: 10.1103/PhysRevLett.107.217001.

[73] M. P. Smylie *et al.*, “Robust odd-parity superconductivity in the doped topological insulator $Nb_xBi_2Se_3$,” *Phys Rev B*, vol. 96, no. 11, p. 115145, Sep. 2017, doi: 10.1103/PhysRevB.96.115145.

[74] K. Kobayashi, T. Ueno, H. Fujiwara, T. Yokoya, and J. Akimitsu, “Unusual upper critical field behavior in Nb-doped bismuth selenides,” *Phys Rev B*, vol. 95, no. 18, p. 180503, May 2017, doi: 10.1103/PhysRevB.95.180503.

[75] D. Rosenbach, “Quantum transport and induced superconductivity in selectively deposited topological insulator devices,” PhD Thesis, RWTH Aachen, Aachen, 2020. doi: 10.18154/RWTH-2021-06366.

[76] P. G. DE GENNES, “Boundary Effects in Superconductors,” *Rev Mod Phys*, vol. 36, no. 1, pp. 225–237, Jan. 1964, doi: 10.1103/RevModPhys.36.225.

[77] T. Schäpers, *Superconductor/Semiconductor Junctions*, vol. 174. Berlin, Heidelberg: Springer Berlin Heidelberg, 2001. doi: 10.1007/3-540-45525-6.

[78] B. D. Josephson, “Possible new effects in superconductive tunnelling,” *Physics Letters*, vol. 1, no. 7, pp. 251–253, Jul. 1962, doi: 10.1016/0031-9163(62)91369-0.

[79] I. O. Kulik, “Macroscopic Quantization and the Proximity Effect in S-N-S Junctions ,” *Soviet Journal of Experimental and Theoretical Physics*, vol. 30, p. 944, 1969.

[80] R. Hoonsawat and I. M. Tang, “Andreev reflection at a NS interface for non-normal angle of incidence,” *Phys Lett A*, vol. 127, no. 8–9, pp. 441–443, Mar. 1988, doi: 10.1016/0375-9601(88)90214-9.

[81] N. A. Mortensen, K. Flensberg, and A.-P. Jauho, “Angle dependence of Andreev scattering at semiconductor–superconductor interfaces,” *Phys Rev B*, vol. 59, no. 15, pp. 10176–10182, Apr. 1999, doi: 10.1103/PhysRevB.59.10176.

[82] S. Shapiro, “Josephson Currents in Superconducting Tunneling: The Effect of Microwaves and Other Observations,” *Phys Rev Lett*, vol. 11, no. 2, pp. 80–82, Jul. 1963, doi: 10.1103/PhysRevLett.11.80.

[83] N. Read and D. Green, “Paired states of fermions in two dimensions with breaking of parity and time-reversal symmetries and the fractional quantum Hall effect,” *Phys Rev B*, vol. 61, no. 15, pp. 10267–10297, Apr. 2000, doi: 10.1103/PhysRevB.61.10267.

[84] J. Alicea, “New directions in the pursuit of Majorana fermions in solid state systems,” Feb. 2012, doi: 10.1088/0034-4885/75/7/076501.

[85] H. H. Sun and J. F. Jia, “Detection of Majorana zero mode in the vortex,” *NPJ Quantum Mater*, vol. 2, no. 1, pp. 1–9, 2017, doi: 10.1038/s41535-017-0037-4.

[86] H. H. Sun *et al.*, “Majorana Zero Mode Detected with Spin Selective Andreev Reflection in the Vortex of a Topological Superconductor,” *Phys Rev Lett*, vol. 116, no. 25, Jun. 2016, doi: 10.1103/PhysRevLett.116.257003.

[87] C. Nayak, S. H. Simon, A. Stern, M. Freedman, and S. Das Sarma, “Non-Abelian anyons and topological quantum computation,” *Rev Mod Phys*, vol. 80, no. 3, pp. 1083–1159, Sep. 2008, doi: 10.1103/RevModPhys.80.1083.

[88] S. M. Albrecht *et al.*, “Exponential protection of zero modes in Majorana islands,” *Nature*, vol. 531, no. 7593, pp. 206–209, Mar. 2016, doi: 10.1038/nature17162.

[89] F. Domínguez *et al.*, “Josephson junction dynamics in the presence of 2π - And 4π -periodic supercurrents,” *Phys Rev B*, vol. 95, no. 19, May 2017, doi: 10.1103/PhysRevB.95.195430.

[90] B. S. Chandrasekhar, “A NOTE ON THE MAXIMUM CRITICAL FIELD OF HIGH-FIELD SUPERCONDUCTORS,” *Appl Phys Lett*, vol. 1, no. 1, pp. 7–8, Sep. 1962, doi: 10.1063/1.1777362.

[91] A. Stellhorn, “Interplay of proximity effects in superconductor/ferromagnet heterostructures,” PhD Thesis, RWTH Aachen, Aachen, 2021.

[92] M. Eschrig, “Spin-polarized supercurrents for spintronics,” *Phys Today*, vol. 64, no. 1, pp. 43–49, Jan. 2011, doi: 10.1063/1.3541944.

[93] A. I. Buzdin, “Proximity effects in superconductor-ferromagnet heterostructures,” *Rev Mod Phys*, vol. 77, no. 3, pp. 935–976, Sep. 2005, doi: 10.1103/RevModPhys.77.935.

[94] V. V. Ryazanov, V. A. Oboznov, A. Y. Rusanov, A. V. Veretennikov, A. A. Golubov, and J. Aarts, “Coupling of two superconductors through a ferromagnet: Evidence for a π junction,” *Phys Rev Lett*, vol. 86, no. 11, pp. 2427–2430, Mar. 2001, doi: 10.1103/PhysRevLett.86.2427.

[95] F. S. Bergeret, A. F. Volkov, and K. B. Efetov, “Long-range proximity effects in superconductor-ferromagnet structures,” *Phys Rev Lett*, vol. 86, no. 18, pp. 4096–4099, Apr. 2001, doi: 10.1103/PhysRevLett.86.4096.

[96] K. Halterman, O. T. Valls, and P. H. Barsic, “Induced triplet pairing in clean s-wave superconductor/ferromagnet layered structures,” *Phys Rev B*, vol. 77, no. 17, p. 174511, May 2008, doi: 10.1103/PhysRevB.77.174511.

[97] M. Houzet and A. I. Buzdin, “Long range triplet Josephson effect through a ferromagnetic trilayer,” *Phys Rev B Condens Matter Mater Phys*, vol. 76, no. 6, Aug. 2007, doi: 10.1103/PhysRevB.76.060504.

[98] J. Linder, T. Yokoyama, and A. Sudbø, “Theory of superconducting and magnetic proximity effect in S/F structures with inhomogeneous magnetization textures and spin-active interfaces,” *Phys Rev B*, vol. 79, no. 5, p. 054523, Feb. 2009, doi: 10.1103/PhysRevB.79.054523.

[99] W. M. Martinez, W. P. Pratt, and N. O. Birge, “Amplitude Control of the Spin-Triplet Supercurrent in S /F /S Josephson Junctions,” *Phys Rev Lett*, vol. 116, no. 7, Feb. 2016, doi: 10.1103/PhysRevLett.116.077001.

[100] M. Eschrig, J. Kopu, J. C. Cuevas, and G. Schön, “Theory of Half-Metal/Superconductor Heterostructures,” *Phys Rev Lett*, vol. 90, no. 13, p. 4, 2003, doi: 10.1103/PhysRevLett.90.137003.

[101] J. Linder and J. W. A. Robinson, “Superconducting spintronics,” Apr. 08, 2015, *Nature Publishing Group*. doi: 10.1038/nphys3242.

[102] R. S. Keizer, S. T. B. Goennenwein, T. M. Klapwijk, G. Miao, G. Xiao, and A. Gupta, “A spin triplet supercurrent through the half-metallic ferromagnet CrO_2,” *Nature*, vol. 439, no. 7078, pp. 825–827, Feb. 2006, doi: 10.1038/nature04499.

[103] M. S. Anwar, M. Veldhorst, A. Brinkman, and J. Aarts, “Long range supercurrents in ferromagnetic CrO_2 using a multilayer contact structure,” *Appl Phys Lett*, vol. 100, no. 5, p. 052602, Jan. 2012, doi: 10.1063/1.3681138.

[104] F. S. Bergeret and I. V. Tokatly, “Spin-orbit coupling as a source of long-range triplet proximity effect in superconductor-ferromagnet hybrid structures,” *Phys Rev B Condens Matter Mater Phys*, vol. 89, no. 13, Apr. 2014, doi: 10.1103/PhysRevB.89.134517.

[105] P. Schüffelgen *et al.*, “Selective area growth and stencil lithography for in situ fabricated quantum devices,” *Nat Nanotechnol*, vol. 14, no. 9, pp. 825–831, 2019, doi: 10.1038/s41565-019-0506-y.

[106] D. Rosenbach *et al.*, “Reappearance of first Shapiro step in narrow topological Josephson junctions,” *Sci Adv*, vol. 7, no. 26, pp. 1–10, 2021, doi: 10.1126/sciadv.abf1854.

[107] Y. Lu and T. T. Heikkilä, “Proximity effect in superconducting heterostructures with strong spin-orbit coupling and spin splitting,” *Phys Rev B*, vol. 100, no. 10, p. 104514, Sep. 2019, doi: 10.1103/PhysRevB.100.104514.

[108] F. Zhang, C. L. Kane, and E. J. Mele, “Surface states of topological insulators,” *Phys Rev B Condens Matter Mater Phys*, vol. 86, no. 8, Aug. 2012, doi: 10.1103/PhysRevB.86.081303.

[109] B. Lian, J. Wang, and S. C. Zhang, “Edge-state-induced Andreev oscillation in quantum anomalous Hall insulator-superconductor junctions,” *Phys Rev B*, vol. 93, no. 16, Apr. 2016, doi: 10.1103/PhysRevB.93.161401.

[110] C. Visani *et al.*, “Equal-spin Andreev reflection and long-range coherent transport in high-temperature superconductor/half-metallic ferromagnet junctions,” *Nat Phys*, vol. 8, no. 7, pp. 539–543, 2012, doi: 10.1038/nphys2318.

[111] M. Vaßen-Carl, “Signature of induced superconductivity in magnetic topological insulators,” Master’s thesis, RWTH Aachen, Aachen, 2021.

[112] S. B. Chung, X. L. Qi, J. MacIejko, and S. C. Zhang, “Conductance and noise signatures of Majorana backscattering,” *Phys Rev B Condens Matter Mater Phys*, vol. 83, no. 10, Mar. 2011, doi: 10.1103/PhysRevB.83.100512.

[113] B. Lian, J. Wang, X. Q. Sun, A. Vaezi, and S. C. Zhang, “Quantum phase transition of chiral Majorana fermions in the presence of disorder,” *Phys Rev B*, vol. 97, no. 12, Mar. 2018, doi: 10.1103/PhysRevB.97.125408.

[114] D. Culcer, A. Cem Keser, Y. Li, and G. Tkachov, “Transport in two-dimensional topological materials: Recent developments in experiment and theory,” 2020, *IOP Publishing Ltd*. doi: 10.1088/2053-1583/ab6ff7.

[115] Y. Gong *et al.*, “Experimental Realization of an Intrinsic Magnetic Topological Insulator,” *Chinese Physics Letters*, vol. 36, no. 7, 2019, doi: 10.1088/0256-307X/36/7/076801.

[116] K. G. Günther, “Aufdampfschichten aus halbleitenden Ill-V-Verbindungen,” REIMER, 1958.

[117] K. S. Novoselov, “Graphene: Materials in the Flatland (Nobel lecture),” Jul. 25, 2011. doi: 10.1002/anie.201101502.

[118] A. Richardella, A. Kandala, J. S. Lee, and N. Samarth, “Characterizing the structure of topological insulator thin films,” *APL Mater*, vol. 3, no. 8, Aug. 2015, doi: 10.1063/1.4926455.

[119] P. Ngabonziza, M. P. Stehno, H. Myoren, V. A. Neumann, G. Koster, and A. Brinkman, “Gate-Tunable Transport Properties of In Situ Capped Bi_2Te_3 Topological Insulator Thin Films,” *Adv Electron Mater*, vol. 2, no. 8, p. 1600157, Aug. 2016, doi: 10.1002/aelm.201600157.

[120] T. P. Ginley, Y. Wang, and S. Law, “Topological insulator film growth by molecular beam epitaxy: A review,” *Crystals (Basel)*, vol. 6, no. 11, pp. 1–26, 2016, doi: 10.3390/cryst6110154.

[121] S. Borisova, J. Krumrain, M. Luysberg, G. Mussler, and D. Grützmacher, “Mode of growth of ultrathin topological insulator Bi_2Te_3 films on Si (111) substrates,” *Cryst Growth Des*, vol. 12, no. 12, pp. 6098–6103, 2012, doi: 10.1021/cg301236s.

[122] S.-W. Chen, S.-T. Lu, and J.-S. Chang, “Bi-In-Te phase diagram,” *J Alloys Compd*, vol. 722, pp. 499–508, 2017, doi: 10.1016/j.jallcom.2017.06.144.

[123] J. Kampmeier, S. Borisova, L. Plucinski, M. Luysberg, G. Mussler, and D. Grützmacher, “Suppressing twin domains in molecular beam epitaxy grown Bi_2Te_3 topological insulator thin films,” *Cryst Growth Des*, vol. 15, no. 1, pp. 390–394, 2015, doi: 10.1021/cg501471z.

[124] L. Hu, T. Zhu, X. Liu, and X. Zhao, “Point defect engineering of high-performance bismuth-telluride-based thermoelectric materials,” *Adv Funct Mater*, vol. 24, no. 33, pp. 5211–5218, Sep. 2014, doi: 10.1002/adfm.201400474.

[125] S. K. Lim, M. Y. Kim, and T. S. Oh, “Thermoelectric properties of the bismuth-antimony-telluride and the antimony-telluride films processed by electrodeposition for micro-device applications,” *Thin Solid Films*, vol. 517, no. 14, pp. 4199–4203, May 2009, doi: 10.1016/j.tsf.2009.02.005.

[126] J. Kellner *et al.*, “Tuning the Dirac point to the Fermi level in the ternary topological insulator $(Bi_{1-x}Sb_x)_2Te_3$,” *Appl Phys Lett*, vol. 107, no. 25, Dec. 2015, doi: 10.1063/1.4938394.

[127] X. He, H. Li, L. Chen, and K. Wu, “Substitution-induced spin-splitted surface states in topological insulator $(Bi_{1-x}Sb_x)_2Te_3$,” *Sci Rep*, vol. 5, 2015, doi: 10.1038/srep08830.

[128] C. Weyrich *et al.*, “Growth, characterization, and transport properties of ternary $(Bi_{1-x}Sb_x)_2Te_3$ topological insulator layers,” *Journal of Physics Condensed Matter*, vol. 28, no. 49, Oct. 2016, doi: 10.1088/0953-8984/28/49/495501.

[129] A. N. Mansour, W. Wong-Ng, Q. Huang, W. Tang, A. Thompson, and J. Sharp, “Structural characterization of Bi_2Te_3 and Sb_2Te_3 as a function of temperature using neutron powder diffraction and extended X-ray absorption fine structure techniques,” *J Appl Phys*, vol. 116, no. 8, 2014, doi: 10.1063/1.4892441.

[130] K. Nagasaka *et al.*, “Synchrotron powder X-ray diffraction and structural analysis of $Eu_{0.5}La_{0.5}FBiS_{2-x}Se_x$,” in *Journal of Physics: Conference Series*, Institute of Physics Publishing, Jul. 2017. doi: 10.1088/1742-6596/871/1/012007.

[131] E. Zimmermann *et al.*, “Universal conductance fluctuations in a $Bi_{1.5}Sb_{0.5}Te_{1.8}Se_{1.2}$ topological insulator nano-scaled Hall bar structure,” *Semicond Sci Technol*, Jan. 2023, doi: 10.1088/1361-6641/acb45f.

[132] R. A. Smith, *Semiconductors*, 2d ed. Cambridge University Press, 1978.

[133] J. Teller, “Towards the Quantum Anomalous Hall Effect in Magnetic Topological Insulators,” Master’s Thesis, RWTH Aachen, Aachen, 2022.

[134] J. Zhang *et al.*, “Band structure engineering in $(Bi_{1-x}Sb_x)_2Te_3$ ternary topological insulators,” *Nat Commun*, vol. 2, no. 1, 2011, doi: 10.1038/ncomms1588.

[135] Y. Y. Li *et al.*, “Intrinsic topological insulator Bi_2Te_3 thin films on Si and their thickness limit,” *Advanced Materials*, vol. 22, no. 36, pp. 4002–4007, Sep. 2010, doi: 10.1002/adma.201000368.

[136] R. Yoshimi *et al.*, “Dirac electron states formed at the heterointerface between a topological insulator and a conventional semiconductor,” *Nat Mater*, vol. 13, no. 3, pp. 253–257, 2014, doi: 10.1038/nmat3885.

[137] R. Yoshimi *et al.*, “Quantum Hall effect on top and bottom surface states of topological insulator $(Bi_{1-x}Sb_x)_2Te_3$ films,” *Nat Commun*, vol. 6, pp. 1–6, 2015, doi: 10.1038/ncomms7627.

[138] N. V. Tarakina *et al.*, “Microstructural characterization of Cr-doped $(Bi,Sb)_2Te_3$ thin films,” *CrystEngComm*, vol. 19, no. 26, pp. 3633–3639, 2017, doi: 10.1039/c7ce00872d.

[139] J. M. Zhang *et al.*, “Stability, electronic, and magnetic properties of the magnetically doped topological insulators Bi_2Se_3, Bi_2Te_3, and Sb_2Te_3,” *Phys Rev B Condens Matter Mater Phys*, vol. 88, no. 23, pp. 1–10, 2013, doi: 10.1103/PhysRevB.88.235131.

[140] M. Winnerlein *et al.*, “Epitaxy and structural properties of $(V,Bi,Sb)_2Te_3$ layers exhibiting the quantum anomalous Hall effect,” *Phys Rev Mater*, vol. 1, no. 1, pp. 1–5, 2017, doi: 10.1103/PhysRevMaterials.1.011201.

[141] J. Teng, N. Liu, and Y. Li, “Mn-doped topological insulators: A review,” *Journal of Semiconductors*, vol. 40, no. 8, 2019, doi: 10.1088/1674-4926/40/8/081507.

[142] Y. Wu *et al.*, “Stabilizing the Fermi Level of Cr-Doped Magnetic Topological Insulators by Al Passivation,” *Journal of Physical Chemistry C*, vol. 123, no. 6, pp. 3823–3828, 2019, doi: 10.1021/acs.jpcc.8b09661.

[143] J. E. Simpkins, P. Mioduszewski, and L. W. Stratton, “Studies of chromium gettering,” *Journal of Nuclear Materials*, vol. 111–112, pp. 827–830, Nov. 1982, doi: 10.1016/0022-3115(82)90314-2.

[144] Z. Zhou, Y. J. Chien, and C. Uher, “Thin film dilute ferromagnetic semiconductors $Sb_{2-x}Cr_xTe_3$ with a Curie temperature up to 190 K,” *Phys Rev B Condens Matter Mater Phys*, vol. 74, no. 22, 2006, doi: 10.1103/PhysRevB.74.224418.

[145] M. M. Stasova, “X-ray investigation of some bismuth and antimony chalcogenides,” *Journal of Structural Chemistry*, vol. 5, no. 5, pp. 731–732, 1965, doi: 10.1007/BF00744068.

[146] E. Zimmermann *et al.*, “Fourier transformation based analysis routine for intermixed longitudinal and transversal hysteretic data for the example of a magnetic topological insulator,” Jul. 2023, [Online]. Available: http://arxiv.org/abs/2307.16450

[147] I. I. Klimovskikh *et al.*, “Tunable 3D/2D magnetism in the $(MnBi_2Te_4)(Bi_2Te_3)_m$ topological insulators family,” *NPJ Quantum Mater*, vol. 5, no. 1, pp. 1–3, 2020, doi: 10.1038/s41535-020-00255-9.

[148] M. Mogi *et al.*, “A magnetic heterostructure of topological insulators as a candidate for an axion insulator,” *Nat Mater*, vol. 16, no. 5, pp. 516–521, May 2017, doi: 10.1038/nmat4855.

[149] X. Kou *et al.*, “Scale-invariant quantum anomalous hall effect in magnetic topological insulators beyond the two-dimensional limit,” *Phys Rev Lett*, vol. 113, no. 3, pp. 1–5, 2014, doi: 10.1103/PhysRevLett.113.137201.

[150] X. Feng *et al.*, “Thickness Dependence of the Quantum Anomalous Hall Effect in Magnetic Topological Insulator Films,” *Advanced Materials*, vol. 28, no. 30, pp. 6386–6390, 2016, doi: 10.1002/adma.201600919.

[151] Y. Ji *et al.*, “Thickness-Driven Quantum Anomalous Hall Phase Transition in Magnetic Topological Insulator Thin Films,” *ACS Nano*, vol. 16, no. 1, pp. 1134–1141, Jan. 2022, doi: 10.1021/acsnano.1c08874.

[152] B. Li, Q. Fan, F. Ji, Z. Liu, H. Pan, and S. Qiao, “Carrier dependent ferromagnetism in chromium doped topological insulator $Cr_y(Bi_xSb_{1-x})_{2-y}Te_3$,” *Physics Letters, Section A: General, Atomic and Solid State Physics*, vol. 377, no. 31–33, pp. 1925–1929, 2013, doi: 10.1016/j.physleta.2013.05.020.

[153] M. Liu *et al.*, “Crossover between weak antilocalization and weak localization in a magnetically doped topological insulator,” *Phys Rev Lett*, vol. 108, no. 3, pp. 1–5, 2012, doi: 10.1103/PhysRevLett.108.036805.

[154] G. Lippertz, A. Bliesener, A. Uday, L. M. C. Pereira, A. A. Taskin, and Y. Ando, “Current-induced breakdown of the quantum anomalous Hall effect,” pp. 17–21, 2021, [Online]. Available: http://arxiv.org/abs/2108.02081

[155] M. Kawamura *et al.*, “Current scaling of the topological quantum phase transition between a quantum anomalous Hall insulator and a trivial insulator,” *Phys Rev B*, vol. 102, no. 4, p. 41301, 2020, doi: 10.1103/PhysRevB.102.041301.

[156] M. Eschbach *et al.*, “Realization of a vertical topological p-n junction in epitaxial Sb_2Te_3/Bi_2Te_3 heterostructures,” *Nat Commun*, vol. 6, Nov. 2015, doi: 10.1038/ncomms9816.

[157] E. Zimmermann *et al.*, “Current-induced magnetization switching in a magnetic topological insulator heterostructure,” Aug. 2023, [Online]. Available: http://arxiv.org/abs/2308.07657

[158] M. Kawamura, R. Yoshimi, A. Tsukazaki, K. S. Takahashi, M. Kawasaki, and Y. Tokura, “Current-Driven Instability of the Quantum Anomalous Hall Effect in

Ferromagnetic Topological Insulators," *Phys Rev Lett*, vol. 119, no. 1, Jul. 2017, doi: 10.1103/PhysRevLett.119.016803.

[159] I. Lee *et al.*, "Imaging Dirac-mass disorder from magnetic dopant atoms in the ferromagnetic topological insulator $Cr_x(Bi_{0.1}Sb_{0.9})_{2-x}Te_3$," *Proc Natl Acad Sci U S A*, vol. 112, no. 5, pp. 1316–1321, 2015, doi: 10.1073/pnas.1424322112.

[160] H. Deng *et al.*, "High-temperature quantum anomalous Hall regime in a $MnBi_2Te_4/Bi_2Te_3$ superlattice," *Nat Phys*, vol. 17, no. 1, pp. 36–42, 2021, doi: 10.1038/s41567-020-0998-2.

[161] A. R. Jalil *et al.*, "Selective Area Epitaxy of Quasi-1-Dimensional Topological Nanostructures and Networks," *Nanomaterials*, vol. 13, no. 2, p. 354, Jan. 2023, doi: 10.3390/nano13020354.

[162] T. W. Schmitt *et al.*, "Integration of Topological Insulator Josephson Junctions in Superconducting Qubit Circuits," *Nano Lett*, vol. 22, no. 7, pp. 2595–2602, Apr. 2022, doi: 10.1021/acs.nanolett.1c04055.

[163] M. Schleenvoigt, "Quality Improvement of Molecular Beam Epitaxy Grown Topological Insulator Thin Films and in situ Fabrication of Devices," Master's Thesis, RWTH Aachen, Aachen, 2017.

[164] O. Kwon, Y. Lin, J. Boeckl, and S. A. Ringel, "Growth and properties of digitally-alloyed AlGaInP by solid source molecular beam epitaxy," *J Electron Mater*, vol. 34, no. 10, pp. 1301–1306, Oct. 2005, doi: 10.1007/s11664-005-0253-8.

[165] P. Schüffelgen, "Exploiting Topological Insulators for Majorana Devices and Physics via Molecular Beam Epitaxy," PhD Thesis, RWTH Aachen, Aachen, 2018.

[166] J. Niemayer, " ," *PTB Mitteilungen*, vol. 84, no. 251, 1974.

[167] G. J. Dolan, "Offset masks for lift-off photoprocessing," *Appl Phys Lett*, vol. 31, no. 5, pp. 337–339, 1977, doi: 10.1063/1.89690.

[168] H. G. Wild, "Josephson Junctions with Ferromagnetic Interlayer," Ph.D. Thesis, TU, München, 2012.

[169] G. Qiu *et al.*, "Concurrent Ferromagnetism and Superconductivity in Fe(Te,Se) van der Waals Josephson Junctions," Mar. 2023, doi: 10.1038/s41467-023-42447-4.

[170] B. Li *et al.*, "Superconducting spin switch with infinite magnetoresistance induced by an internal exchange field," *Phys Rev Lett*, vol. 110, no. 9, Feb. 2013, doi: 10.1103/PhysRevLett.110.097001.

[171] J. Strunz *et al.*, "Interacting topological edge channels," *Nat Phys*, vol. 16, no. 1, pp. 83–88, Jan. 2020, doi: 10.1038/s41567-019-0692-4.

[172] L. Maier *et al.*, "Induced superconductivity in the three-dimensional topological insulator HgTe," Oct. 2012, doi: 10.1103/PhysRevLett.109.186806.

[173] M. Veldhorst *et al.*, "Magnetotransport and induced superconductivity in Bi based three-dimensional topological insulators," *Physica Status Solidi - Rapid Research Letters*, vol. 7, no. 1–2, pp. 26–38, Feb. 2013, doi: 10.1002/pssr.201206408.

[174] M. Bai *et al.*, “Novel self-epitaxy for inducing superconductivity in the topological insulator $(Bi_{1-x}Sb_x)_2Te_3$,” *Phys Rev Mater*, vol. 4, no. 9, Sep. 2020, doi: 10.1103/PhysRevMaterials.4.094801.

[175] B. De Ronde, C. Li, Y. Huang, and A. Brinkman, “Induced topological superconductivity in a $BiSbTeSe_2$-based Josephson junction,” *Nanomaterials*, vol. 10, no. 4, Apr. 2020, doi: 10.3390/nano10040794.

[176] W. Z. Xu *et al.*, “Proximity-induced superconducting gap in the intrinsic magnetic topological insulator $MnBi_2Te_3$,” *Phys Rev B*, vol. 105, no. 18, May 2022, doi: 10.1103/PhysRevB.105.184515.

[177] M. P. Andersen *et al.*, “Low-damage electron beam lithography for nanostructures on Bi_2Te_3-class topological insulator thin films,” Jan. 2023, [Online]. Available: http://arxiv.org/abs/2301.11900

[178] T. S. Khaire, W. P. Pratt, and N. O. Birge, “Critical current behavior in Josephson junctions with the weak ferromagnet PdNi,” *Phys Rev B Condens Matter Mater Phys*, vol. 79, no. 9, Mar. 2009, doi: 10.1103/PhysRevB.79.094523.

[179] K. R. Jeon *et al.*, “Long-range supercurrents through a chiral non-collinear antiferromagnet in lateral Josephson junctions,” *Nat Mater*, vol. 20, no. 10, pp. 1358–1363, Oct. 2021, doi: 10.1038/s41563-021-01061-9.

[180] Y. Jungxiang, R. Fermin, K. Lahabi, and J. Aarts, “Triplet supercurrents in lateral Josephson junctions with a half-metallic ferromagnet,” Mar. 2023, [Online]. Available: http://arxiv.org/abs/2303.13922

[181] X. Kou *et al.*, “Interplay between different magnetisms in Cr-doped topological insulators,” *ACS Nano*, vol. 7, no. 10, pp. 9205–9212, Oct. 2013, doi: 10.1021/nn4038145.

[182] V. M. Krasnov *et al.*, “Planar S-F-S Josephson junctions made by focused ion beam etching,” *Physica C: Superconductivity and its Applications*, vol. 418, no. 1–2, pp. 16–22, Jan. 2005, doi: 10.1016/j.physc.2004.11.004.

[183] L. Ai *et al.*, “Van der Waals ferromagnetic Josephson junctions,” *Nat Commun*, vol. 12, no. 1, Dec. 2021, doi: 10.1038/s41467-021-26946-w.

[184] B. Jäck, Y. Xie, and A. Yazdani, “Detecting and Distinguishing Majorana Zero Modes with the Scanning Tunneling Microscope,” Mar. 2021, [Online]. Available: http://arxiv.org/abs/2103.13210

[185] B. Bhushan, Ed., *Springer Handbook of Nanotechnology*. Berlin, Heidelberg: Springer Berlin Heidelberg, 2010. doi: 10.1007/978-3-642-02525-9.

[186] I. Dayton, “MEASURING PROXIMITY INDUCED EFFECTS IN TOPOLOGICAL INSULATORS USING SCANNING PROBE MICROSCOPY TECHNIQUES,” PhD thesis, Michigan State University, 2016.

[187] B. Jäck, Y. Xie, J. Li, S. Jeon, B. A. Bernevig, and A. Yazdani, “Observation of a Majorana zero mode in a topologically protected edge channel,” *Science (1979)*, vol. 364, no. 6447, pp. 1255–1259, 2019, doi: 10.1126/science.aax1444.

[188] H.-H. Sun *et al.*, “Observation of Majorana fermions with spin selective Andreev reflection in the vortex of topological superconductor,” *arXiv.org*, vol. cond-mat.s, p. arXiv:1603.02549, 2016, [Online]. Available: http://arxiv.org/abs/1603.02549v1

[189] D. Flötotto *et al.*, “Superconducting pairing of topological surface states in bismuth selenide films on niobium,” 2018. [Online]. Available: https://www.science.org

[190] Y. Zang *et al.*, “Competing Energy Scales in Topological Superconducting Heterostructures,” *Nano Lett*, vol. 21, no. 7, pp. 2758–2765, Apr. 2021, doi: 10.1021/acs.nanolett.0c04648.

[191] O. Vazquez-Mena, L. Gross, S. Xie, L. G. Villanueva, and J. Brugger, “Resistless nanofabrication by stencil lithography: A review,” Jan. 25, 2015, *Elsevier B.V.* doi: 10.1016/j.mee.2014.08.003.

[192] O. Vazquez-Mena, V. Savu, K. Sidler, G. Villanueva, M. A. F. Van Den Boogaart, and J. Brugger, “Sub-100 nm-scale Aluminum nanowires by stencil lithography: Fabrication and characterization,” in *3rd IEEE International Conference on Nano/Micro Engineered and Molecular Systems, NEMS*, 2008, pp. 807–811. doi: 10.1109/NEMS.2008.4484447.

[193] S. Vaitiekėnas, Y. Liu, P. Krogstrup, and C. M. Marcus, “Zero-bias peaks at zero magnetic field in ferromagnetic hybrid nanowires,” *Nat Phys*, vol. 17, no. 1, pp. 43–47, Jan. 2021, doi: 10.1038/s41567-020-1017-3.

[194] F. Keidel, P. Burset, and B. Trauzettel, “Tunable hybridization of Majorana bound states at the quantum spin Hall edge,” *Phys Rev B*, vol. 97, no. 7, Feb. 2018, doi: 10.1103/PhysRevB.97.075408.

[195] G. Sharma, C. Zeng, T. D. Stanescu, and S. Tewari, “Hybridization energy oscillations of Majorana and Andreev bound states in semiconductor-superconductor nanowire heterostructures,” *Phys Rev B*, vol. 101, no. 24, Jun. 2020, doi: 10.1103/PhysRevB.101.245405.

[196] A. Leis *et al.*, “Room temperature in-situ measurement of the spin voltage of a $BiSbTe_3$ thin film,” *Sci Rep*, vol. 10, no. 1, pp. 1–8, 2020, doi: 10.1038/s41598-020-59679-9.

[197] A. Leis *et al.*, “Lifting the spin-momentum locking in ultra-thin topological insulator films,” 2021, doi: 10.1002/qute.202100083.

[198] A. Leis *et al.*, “Probing Edge State Conductance in Ultra-Thin Topological Insulator Films,” *Adv Quantum Technol*, Sep. 2022, doi: 10.1002/qute.202200043.

[199] S. Kezilebieke *et al.*, “Topological superconductivity in a van der Waals heterostructure,” *Nature*, vol. 588, no. 7838, pp. 424–428, 2020, doi: 10.1038/s41586-020-2989-y.

[200] D. K. Finnemore, T. F. Stromberg, and C. A. Swenson, “Superconducting Properties of High-Purity Niobium,” *Physical Review*, vol. 149, no. 1, pp. 231–243, Sep. 1966, doi: 10.1103/PhysRev.149.231.

[201] S. Abhirami, E. P. Amaladass, K. Vinod, A. V. Thanikai Arasu, R. Baskaran, and A. Mani, “Superconducting properties of Nb, NbN, and MoN thin films grown on topological insulator $Bi_{1.95}Sb_{0.05}Se_3$: A comparative study,” *Supercond Sci Technol*, vol. 35, no. 9, Sep. 2022, doi: 10.1088/1361-6668/ac7899.

[202] A. A. Volykhov *et al.*, “Rapid Surface Oxidation of Sb_2Te_3 as Indication for a Universal Trend in the Chemical Reactivity of Tetradymite Topological Insulators,” *Chemistry of Materials*, vol. 28, no. 24, pp. 8916–8923, Dec. 2016, doi: 10.1021/acs.chemmater.6b03325.

[203] K. Hoefer, C. Becker, S. Wirth, and L. Hao Tjeng, “Protective capping of topological surface states of intrinsically insulating Bi_2Te_3,” *AIP Adv*, vol. 5, no. 9, Sep. 2015, doi: 10.1063/1.4931038.

[204] K. Virwani *et al.*, “Controlled removal of amorphous Se capping layer from a topological insulator,” *Appl Phys Lett*, vol. 105, no. 24, Dec. 2014, doi: 10.1063/1.4904803.

[205] J. Dai *et al.*, “Restoring pristine Bi_2Se_3 surfaces with an effective Se decapping process,” *Nano Res*, vol. 8, no. 4, pp. 1222–1228, Apr. 2015, doi: 10.1007/s12274-014-0607-8.

[206] K. Virwani *et al.*, “Controlled removal of amorphous Se capping layer from a topological insulator,” *Appl Phys Lett*, vol. 105, no. 24, pp. 1–5, 2014, doi: 10.1063/1.4904803.

[207] M. M. Ugeda *et al.*, “Characterization of collective ground states in single-layer $NbSe_2$,” *Nat Phys*, vol. 12, no. 1, pp. 92–97, Jan. 2016, doi: 10.1038/nphys3527.

[208] H. Wang *et al.*, “High-quality monolayer superconductor $NbSe_2$ grown by chemical vapour deposition,” *Nat Commun*, vol. 8, no. 1, Dec. 2017, doi: 10.1038/s41467-017-00427-5.

[209] Q. X. Guo *et al.*, “Effects of post-annealing on crystalline and transport properties of Bi_2Te_3 thin films,” *Chinese Physics B*, vol. 30, no. 6, Jun. 2021, doi: 10.1088/1674-1056/abee6c.

[210] S. Nagata, T. Abe, S. Ebisu, Y. Ishihara, and K. Tsutsumi, “Superconductivity in the metallic layered compound $NbTe_2$,” *Journal of Physics and Chemistry of Solids*, vol. 54, no. 8, pp. 895–899, Aug. 1993, doi: 10.1016/0022-3697(93)90215-D.

[211] X. Yang *et al.*, “Pressure induced superconductivity bordering a charge-density-wave state in $NbTe_4$ with strong spin-orbit coupling,” *Sci Rep*, vol. 8, no. 1, Dec. 2018, doi: 10.1038/s41598-018-24572-z.

[212] L. N. Lukyanova, I. V. Makarenko, O. A. Usov, and P. A. Dementev, “Scanning tunneling spectroscopy of the surface states of Dirac fermions in thermoelectrics based on bismuth telluride,” *Semicond Sci Technol*, vol. 33, no. 5, Mar. 2018, doi: 10.1088/1361-6641/aab538.

[213] P. Bhaskar, “Fabrication and investigation of ultrahigh vacuum compatible interfaces of topological insulators and superconductors,” Ph.D. Thesis, RWTH University, Aachen, 2023.

[214] D. Bonnet, S. Erlenkämper, H. Germer, and H. Rabenhorst, “A new measurement of the energy gap in superconducting niobium,” *Phys Lett A*, vol. 25, no. 6, pp. 452–453, Sep. 1967, doi: 10.1016/0375-9601(67)90076-X.

[215] W. X. Wu *et al.*, “Gate Tunable Supercurrent in Josephson Junctions Based on Bi2Te3Topological Insulator Thin Films,” *Chinese Physics Letters*, vol. 38, no. 3, Mar. 2021, doi: 10.1088/0256-307X/38/3/037402.

[216] J. Kölzer *et al.*, “Supercurrent in Bi_4Te_3 Topological Material-Based Three-Terminal Junctions,” *Nanomaterials*, vol. 13, no. 2, Jan. 2023, doi: 10.3390/nano13020293.

[217] I. M. Dayton *et al.*, “Scanning tunneling microscopy of superconducting topological surface states in Bi_2Se_3,” *Phys Rev B*, vol. 93, no. 22, p. 220506, Jun. 2016, doi: 10.1103/PhysRevB.93.220506.

[218] C. Kittel, *Introduction to Solid State Physics*, 8th ed. John Wiley & Sons, Inc, 2005.

[219] C. R. K. Marrian and E. A. Dobisz, “High-resolution lithography with a vacuum STM,” *Ultramicroscopy*, vol. 42–44, pp. 1309–1316, Jul. 1992, doi: 10.1016/0304-3991(92)90440-U.

[220] T. W. Schmitt *et al.*, “Anomalous temperature dependence of multiple Andreev reflections in a topological insulator Josephson junction,” *Supercond Sci Technol*, vol. 36, no. 2, Feb. 2023, doi: 10.1088/1361-6668/aca4fe.

[221] K. Janßen *et al.*, “Single in situ Interface Characterization Composed of Niobium and a Selectively Grown $(Bi_{1-x}Sb_x)_2Te_3$ Topological Insulator Nanoribbon,” Dec. 2023, [Online]. Available: http://arxiv.org/abs/2312.07325

[222] G. Behner *et al.*, “In-plane magnetic field-driven conductance modulations in topological insulator kinks,” Oct. 2023, [Online]. Available: http://arxiv.org/abs/2310.06924

[223] Z. Jiang, C.-Z. Chang, C. Tang, P. Wei, J. S. Moodera, and J. Shi, “Independent Tuning of Electronic Properties and Induced Ferromagnetism in Topological Insulators with Heterostructure Approach,” *Nano Lett*, vol. 15, no. 9, pp. 5835–5840, Sep. 2015, doi: 10.1021/acs.nanolett.5b01905.

[224] F. Katmis *et al.*, “A high-temperature ferromagnetic topological insulating phase by proximity coupling,” *Nature*, vol. 533, no. 7604, pp. 513–516, May 2016, doi: 10.1038/nature17635.

[225] J. Wang *et al.*, “Energy gap of topological surface states in proximity to a magnetic insulator,” *Commun Phys*, vol. 6, no. 1, p. 200, Aug. 2023, doi: 10.1038/s42005-023-01327-5.

[226] W. Sun, C.-K. Tan, and N. Tansu, “III-Nitride Digital Alloy: Electronics and Optoelectronics Properties of the InN/GaN Ultra-Short Period Superlattice Nanostructures,” *Sci Rep*, vol. 7, no. 1, p. 6671, Jul. 2017, doi: 10.1038/s41598-017-06889-3.

[227] A. M. Savin *et al.*, “Parity effect in Al and Nb single electron transistors in a tunable environment,” *Appl Phys Lett*, vol. 91, no. 6, 2007, doi: 10.1063/1.2768897.

[228] O. Sharon, A. A. Shaulov, J. Berger, A. Sharoni, R. Berkovits, and Y. Yeshurun, “Current-Induced Crossover of Flux Periodicity from h/2e to h/e in a Superconducting Nb Nano-Ring,” *Nano Lett*, vol. 18, no. 12, pp. 7851–7855, Dec. 2018, doi: 10.1021/acs.nanolett.8b03617.

[229] B. Lian, Z. Liu, Y. Zhang, and J. Wang, “Flat Chern Band From Twisted Bilayer $MnBi_2Te_4$,” Aug. 2019, doi: 10.1103/PhysRevLett.124.126402.

[230] C. Z. Chang *et al.*, "High-precision realization of robust quantum anomalous Hall state in a hard ferromagnetic topological insulator," *Nat Mater*, vol. 14, no. 5, pp. 473–477, May 2015, doi: 10.1038/nmat4204.

[231] W. Niu *et al.*, "Intrinsic ferromagnetism and quantum transport transition in individual Fe-doped Bi_2 Se_3 topological insulator nanowires," *Nanoscale*, vol. 9, no. 34, pp. 12372–12378, 2017, doi: 10.1039/C7NR02807E.

[232] J. Li *et al.*, "Intrinsic magnetic topological insulators in van der Waals layered $MnBi_2Te_4$-family materials," *Sci Adv*, vol. 5, no. 6, pp. 1–8, 2019, doi: 10.1126/sciadv.aaw5685.

[233] M. M. Otrokov *et al.*, "Prediction and observation of an antiferromagnetic topological insulator," *Nature*, vol. 576, no. 7787, pp. 416–422, Dec. 2019, doi: 10.1038/s41586-019-1840-9.

[234] T. V. Bezryadina and S. V. Eremeev, "Heterostructures Based on Magnetic and Topological Insulators," *Russian Physics Journal*, vol. 61, no. 11, pp. 1964–1970, Mar. 2019, doi: 10.1007/s11182-019-01625-y.

[235] H. Li *et al.*, "Antiferromagnetic topological insulator $MnBi_2Te_4$: Synthesis and magnetic properties," *Physical Chemistry Chemical Physics*, vol. 22, no. 2, pp. 556–563, 2020, doi: 10.1039/c9cp05634c.

[236] P. Burlet, E. Ressouche, B. Malaman, R. Welter, J. P. Sanchez, and P. Vulliet, "Noncollinear magnetic structure of $MnTe_2$," *Phys Rev B*, vol. 56, no. 21, pp. 14013–14018, Dec. 1997, doi: 10.1103/PhysRevB.56.14013.

[237] C. Liu *et al.*, "Robust axion insulator and Chern insulator phases in a two-dimensional antiferromagnetic topological insulator," *Nat Mater*, vol. 19, no. 5, pp. 522–527, May 2020, doi: 10.1038/s41563-019-0573-3.

[238] J. Q. Yan, S. Okamoto, M. A. McGuire, A. F. May, R. J. McQueeney, and B. C. Sales, "Evolution of structural, magnetic, and transport properties in $MnBi_{2-x}Sb_xTe_4$," *Phys Rev B*, vol. 100, no. 10, Sep. 2019, doi: 10.1103/PhysRevB.100.104409.

[239] B. Chen *et al.*, "Intrinsic magnetic topological insulator phases in the Sb doped $MnBi_2Te_4$ bulks and thin flakes," *Nat Commun*, vol. 10, no. 1, pp. 1–8, 2019, doi: 10.1038/s41467-019-12485-y.

[240] R. Müller, "MBE Growth and Characterization of Mn-Containing Intrinsic Magnetic Topological Insulators," Master's Thesis, PGI-9, Aachen, 2021.

[241] S. Wimmer *et al.*, "Mn-rich $MnSb_2Te_4$: A topological insulator with magnetic gap closing at high Curie temperatures of 45-50 K," pp. 1–51, 2020, [Online]. Available: http://arxiv.org/abs/2011.07052

[242] P. Kagerer *et al.*, "Molecular beam epitaxy of antiferromagnetic $(MnBi_2Te_4)(Bi_2Te_4)$ thin films on $BaF_2(111)$," *J Appl Phys*, vol. 128, no. 13, pp. 1–7, 2020, doi: 10.1063/5.0025933.

[243] E. D. L. Rienks *et al.*, "Large magnetic gap at the Dirac point in $Bi_2Te_3/MnBi_2Te_4$ heterostructures," *Nature*, vol. 576, no. 7787, pp. 423–428, 2019, doi: 10.1038/s41586-019-1826-7.

[244] M. Du, J. Yan, V. R. Cooper, and M. Eisenbach, “Tuning Fermi Levels in Intrinsic Antiferromagnetic Topological Insulators $MnBi_2Te_4$ and $MnBi_4Te_7$ by Defect Engineering and Chemical Doping,” *Adv Funct Mater*, vol. 31, no. 3, p. 2006516, Jan. 2021, doi: 10.1002/adfm.202006516.

[245] M. M. Shirolkar, M. Li, and H. Wang, “Magnetic and ferroelectric properties of sol - Gel synthesized rhombohedral phase $AlFeO_3$ nanoparticles,” in *Journal of Physics: Conference Series*, Institute of Physics Publishing, Aug. 2017. doi: 10.1088/1742-6596/864/1/012009.

[246] K. Khan, Z. Iqbal, H. Abbas, A. Hassan, and K. Nadeem, “Ferrimagnetic to antiferromagnetic transition and complex impedance analysis of Cr-doped magnesium ferrite nanoparticles,” *Journal of Materials Science: Materials in Electronics*, vol. 31, no. 11, pp. 8578–8588, Jun. 2020, doi: 10.1007/s10854-020-03393-9.

[247] J. G. Checkelsky, J. Ye, Y. Onose, Y. Iwasa, and Y. Tokura, “Dirac-fermion-mediated ferromagnetism in a topological insulator,” *Nat Phys*, vol. 8, no. 10, pp. 729–733, 2012, doi: 10.1038/nphys2388.

[248] K. He and Q. K. Xue, “Quantum anomalous Hall heterostructures,” Mar. 01, 2019, *Oxford University Press*. doi: 10.1093/nsr/nwy157.

[249] W. Ge, P. M. Sass, J. Yan, S. H. Lee, Z. Mao, and W. Wu, “Direct evidence of ferromagnetism in $MnSb_2Te_4$,” *Phys Rev B*, vol. 103, no. 13, Apr. 2021, doi: 10.1103/PhysRevB.103.134403.

[250] P. A. Joy, P. S. A. Kumar, and S. K. Date, “The relationship between field-cooled and zero-field-cooled susceptibilities of some ordered magnetic systems,” *Journal of Physics: Condensed Matter*, vol. 10, no. 48, pp. 11049–11054, Dec. 1998, doi: 10.1088/0953-8984/10/48/024.

[251] T. Murakami *et al.*, “Realization of interlayer ferromagnetic interaction in $MnSb_2Te_4$ toward the magnetic Weyl semimetal state,” *Phys Rev B*, vol. 100, no. 19, Nov. 2019, doi: 10.1103/PhysRevB.100.195103.

[252] D. Y. Yan *et al.*, “Site mixing induced ferrimagnetism and anomalous transport properties of the Weyl semimetal candidate $MnSb_2Te_4$,” *Phys Rev B*, vol. 103, no. 22, Jun. 2021, doi: 10.1103/PhysRevB.103.224412.

[253] I. Levy *et al.*, “Compositional Control and Optimization of Molecular Beam Epitaxial Growth of $(Sb_2Te_3)_{1-x}(MnSb_2Te_4)_x$ Magnetic Topological Insulators,” *Cryst Growth Des*, vol. 22, no. 5, pp. 3007–3015, May 2022, doi: 10.1021/acs.cgd.1c01453.

[254] F. Lüpke *et al.*, “Anti-site defect-induced disorder in compensated topological magnet MnBi2-xSbxTe4,” *Commun Mater*, vol. 4, no. 1, p. 82, Oct. 2023, doi: 10.1038/s43246-023-00408-w.

[255] L. U. Liang *et al.*, “Protected long-time storage of a topological insulator,” *AIP Adv*, vol. 11, no. 2, Feb. 2021, doi: 10.1063/5.0037751.

[256] M. Lang *et al.*, “Revelation of topological surface states in Bi_2Se_3 thin films by in situ Al passivation,” *ACS Nano*, vol. 6, no. 1, pp. 295–302, Jan. 2012, doi: 10.1021/nn204239d.

[257] J. Choe *et al.*, “Electron–Phonon and Spin–Lattice Coupling in Atomically Thin Layers of $MnBi_2Te_4$,” *Nano Lett*, vol. 21, no. 14, pp. 6139–6145, Jul. 2021, doi: 10.1021/acs.nanolett.1c01719.

Acknowledgments

Many people helped and supported me during my studies and my time in Jülich and in this section, I want to thank them for their support.

First and foremost, I want to thank Prof. Detlev Grützmacher for allowing me to write my thesis at his institute and being my first examiner. But I also want to thank him for all the opportunities he gave us Master's and PhD students, like all the conferences and research stays you allowed us to go on, even when I had just started in my positions. Your always on-point criticism and helpful tips and ideas especially regarding growth topics was and is always welcome.

I want to thank Prof. Markus Morgenstern for being my second examiner, for enabling me to start the work on my STM samples together with Priya and for helpful discussions online or during retreats.

Peter Schüffelgen, what can I say, this thesis would not exist if it wasn't for him. For multiple reasons, starting from the fact that he took me in as a Master's student and kept the position so fun and interesting that I just did not want to leave. I admire your thirst for new knowledge and projects and your talent for managing a group. I have seen our group go from three people to now >15 and it is prospering. With your never-ending well of ideas you gave me all the pushes into the right directions to go on with my thesis. All the good times we had on conferences and in Jülich make great memories that I will forever fondly remember.

Tobias, my office partner almost since the beginning. When you asked Prof. Schäpers about Master's thesis projects and I just piggy backed, I did not think that ride would go on for more than six years. Thank you for all the support and great ideas you had, it was always fun reflecting on measurements or concepts with you. The way you internalized the physics we were working with, how you knew about every TI topic and always had a paper ready is still stunning to me. Our times on business trips together with Peter and Daniel will never be forgotten.

Jalil, the man the myth. You jumped back from the grave to go to work so many times, they should make you a german Ehrenbürger. I have never met someone so disappointed by an upcoming holiday as you, just because it meant you could not continue working. The way you help just everybody and are part of almost every work group in the FZ and beyond is just amazing to me. Plus, your knowledge about crystal growth is never-ending, and although you always say you learned it from me because I was in the FZ two month earlier than you, I think we can agree that the student surpassed the teacher already for a long time. I wish you all the best, especially for your health, and that you may always evade the wild boars.

From the large group of colleagues at the PGI-9 I especially want to thank Benjamin Benneman for all the help with the MBEs, even when they were not his to care for, and with growths at the metal MBE. Thanks for teaching me about much technical know-how, although for you it probably was just the bare basics. On a personal level too, you were always a pleasure to be with and you can always come by my home on one of your bike tours.

I want to thank Christoph Ringkamp for being a fellow sufferer at the MBE, for the many fruit- and helpful discussions and for your support at the XRD and in the Nanocluster.

I want to thank my first Master's Student Max Vaßen-Carl for the support with the establishment of the CBST and the fun times we had together at the MBE trying to understand what went wrong again this time. We went through the pandemic together and that made the whole ordeal much more enjoyable. I wish you all the best for your PhD and hope to see the QAHI in all your samples!

My second Masters student, Robert Müller, I want to thank for the great time we had together finding out how MnBiSbTe works and how it doesn't work. I think you still owe me a beer for putting the sample into the mask aligner at exactly 0°.

I want to thank Erik Zimmermann for his help with measuring the MTI samples and providing me the data for my MTI chapter. Also, I would like to thank you for being such an ambitious writer, making use of the many samples I grew in my Ph.D. time. Additionally, I want to thank Prof. Thomas Schäpers for the fruitful discussions and being a swell guy and Justus Teller for his measurements on the CBST samples and the nice graphs for my thesis.

Thanks also to Benedikt Frohn, Jan Karthein and Jonas Buchhorn for the help with measurements and measurements they performed for me.

Thank you, Roudy Hanna, for being a great guy who it's always fun to be around. Thanks for updating me on Lebanese inner workings and letting me win some dice games. Your work ethic and your ideas to enhance the UHV lithography process together with your understanding of all the concepts we are confronted with plus your multi-mediality make you a great PhD and I cannot wait to see your experiments work out even better than they already are.

I would like to thank Kristof Moors for helping me understand theoretical concepts I could not wrap my head around and providing me with ideas for graphics to help my readers wrap their heads around the complex physics that is TIs and SCs.

I want to thank Katja Palmen and Jürgen Schubert for their support with RBS measurements and their interpretation.

Gregor Mussler I want to thank for providing the coffee keeping me awake and for maintaining the x-ray machines to check on my films.

During my work on this thesis I cooperated with many different institutes, one of them the PGI-3 in Jülich. I would like to thank Arthur Leis and Prof. Bert Voigtländer there for the great cooperation we had on TIs grown on SOI substrates and the application of the removable mask. Working with you was always refreshingly uncomplicated, although at some point we should consider putting wheels on the vacuum suitcase. I also want to thank Felix Lüpke for the opportunity to measure MTIs in his STM.

From the PGI-7 in Jülich I would like to thank Oleg Petracic, Anika Stellhorn and Mai Hussein, who allowed us to use, and introduced us to, their SQUID system and helped us understand the data we were generating.

From the RWTH Aachen I would like to greatly thank Priyamvada Baskhar, or Priyanka as I once wrongfully claimed, for all the great work we did together. How often did we think our work was cursed when again another mask broke or a sample didn't look good. It is always nice to suffer such drawbacks not alone but with two people, makes the whole thing a lot more bearable.

From the Universtiy of Cologne I want to thank Jens Brede, Adrian Greichgauer and Oliver Breunig for the work done on the LUL samples and the nice results we got from there. Especially Jens I want to thank for being extremely helpful, always easy to work with and open for new ideas, providing great comments all around.

From the HNF in Jülich I want to thank the whole cleanroom staff for all their work to make the place great to fabricate samples in. I want to especially thank Florian Lentz and Stefan Trellenkamp for their E-beam Lithography, of which they are artists. They were always helpful whenever a design needed changing or a total overhaul, because my idea of the design was bad again or the AutoCAD was refusing to cooperate. Also, I want to thank Elmar Neumann for his help with FIB and at the SEMs. Lastly, I want to give a big thank you to Stephy Bunte, it was always fun to do EDX with you, just talk in the corridor or banter about the other users.

Finally, there are many more people I would like to thank for accompanying me during my PhD time at the PGI 9 and that made my time there a pleasure.

These include Daniel Rosenbach (as with Peter and Tobias, our trips together will never leave my memories), Anne Schmidt, Joscha Domnick, Dennis Heffels, Abbas Espiari, Sarah S. Schmitt (my unofficial first Master's student and university study partner), Nils van den Driesch, Mane Kaladzhian, Johanna Jansen, Albert Hertel, Jinhee Bae and Hans Lüth.

I want to thank my family and friends for their support during my thesis, especially Gregor, Janis and Yannik, with whom I spent many great days and nights playing games, drinking or philosophizing.

And last but certainly not least I want to thank Jenny Schleenvoigt, who over the course of this thesis supported me in every way possible and first became my fiancé and then my wife during the work on this thesis, giving me the strength to continue and always putting a smile on my face.